Universitat Politècnica de València

Instituto de Tecnología Química (UPV-CSIC)

Supported well-defined metals as catalysts for industrially relevant hydrogenation/coupling reactions

PhD in Sustainable Chemistry

(Programa de doctorado en Química Sostenible)

Doctoral Candidate:

Matea Bacic

Directed by:

Dr. Antonio Leyva Pérez

Dra. Judit Oliver Meseguer

Valencia, June 2025

Dr. ANTONIO LEYVA PÉREZ, Investigador Científico del Instituto Universitario Mixto de Tecnología Química (UPV-CSIC), y Dra. JUDIT OLIVER MESEGUER, Investigadora Ramón y Cajal del Instituto Universitario Mixto de Tecnología Química (UPV-CSIC).

CERTIFICAN: Que la presente tesis doctoral, titulada: *Supported well-defined metals as catalysts for industrially relevant hydrogenation/coupling reactions*, ha sido desarrollada por MATEA BACIC bajo mi supervisión, en el marco del Programa de Doctorado de Química Sostenible, en el Instituto Universitario Mixto de Tecnología Química (UPV-CSIC) de la Universitat Politècnica de València.

Dr. Antonio Leyva Pérez **Dra. Judit Oliver Meseguer**

"Look up at the stars and not down at your feet. Try to make sense of what you see and wonder about what makes the universe exist. Be curious."

Stephen Hawking

"C'est le temps que tu as perdu pour ta rose qui fait ta rose si importante."

Antoine de Saint-Exupéry

Acknowledgements

This section might be the hardest to write, not because I lack words, but because no words feel quite enough. How do I thank the people who helped carry me through one of the most challenging and transformative periods of my life? As I sit down to write this, countless faces, voices, and memories come to mind. So many people have made it possible for me to reach this point, finishing a PhD thesis. People who have shared all kinds of moments with me, from the brightest to the most difficult, and who, simply by being part of my life, have helped me grow and become a better version of myself.

Me gustaría comenzar expresando mi más sincero agradecimiento a mis directores de tesis, Antonio Leyva y Judit Oliver, por acompañarme en este camino con tanta dedicación, paciencia y cercanía. Gracias por confiar en mí desde el principio, por estar siempre disponibles para orientarme y por enseñarme a mirar más allá de los resultados, recordándome la importancia de preguntarse siempre el porqué de las cosas, salgan como uno espera o no. A lo largo de estos años ha habido momentos de duda, de frustración y de sentir que no avanzaba. En todos ellos, vuestra actitud ha sido clave: habéis sabido darme el impulso necesario para seguir, ya fuera con nuevas ideas, con otra forma de ver los problemas o, simplemente, con palabras de ánimo. Esa manera de acompañar ha dejado una huella profunda en mi forma de entender y vivir la ciencia. Os estaré siempre agradecida por ello.

También quiero expresar mi agradecimiento al Instituto de Tecnología Química (ITQ) por haber puesto a mi disposición sus instalaciones y recursos durante estos años. Gracias a todo el personal técnico (especial a Carmen, por enseñarme tanto sobre las cromas; a Mer, mi compañera de pilates), así como al personal administrativo, de taller (especialmente del taller mecánico y de reactores) e investigadores, cuyo trabajo diario hace posible el funcionamiento de este centro y crea un entorno tan enriquecedor para desarrollar investigación. Gracias también a la increíble gente de la sala de técnicos (Ester, Amparo, Helena, Miriam y Madalina) por estar siempre ahí, con una sonrisa. Y por supuesto, a Karen, Pablo y Abde: gracias por hacer que incluso los días más largos tuvieran su momento de humor

Han sido muchas las personas que me han ayudado a lo largo del doctorado, tanto en el ámbito científico como en el personal, y sin ellas, mi paso por el ITQ no habría sido tan especial ni tan humano.

Esta etapa no hubiera sido la misma sin todos los compañeros de doctorado con los que he compartido estos años. A mi grupo de investigación, repleto de personas con un talento increíble, de quienes he ido recogiendo inspiración día a día: Adrian, Alex, Alejandro, Amravati, Belen, Cris, Dani, Jordi, Fra, Fran, Giusi, Katerina, Lluis, Marta, Miquel, Paloma, Sergio, Silvia, Susi, Yongkun. También quería agradecer a los adoptivos en el grupo de Cristina/Yongkun: Hilario, Juanan, Jordi, Miguel, Nacho;por hacerme sentir parte del equipo. Y a Ilaria, Nilufar, Minjie, Fran, Silvia y Cris, por ese congreso en Lyon tan especial y lleno de momentos inolvidables. Del grupo de Fotoquímica, gracias a María y Pilar por todos los "chismes" que tanto voy a echar de menos; a Ander, the Basque Guy; a Carlos, por las risas y las fiestas; y a Claudia, Mati, Lorena, Alberto y Antonio, por tantos buenos momentos compartidos.

Nunca me imaginé que acabaría encontrando en el laboratorio algo más que compañeros; se convirtieron en mi familia en Valencia. Tampoco imaginé que encontraría a mis almas gemelas, mis hermanas gitanas, a mi Doctora Muerte, Bea, que roba cebollas, y a la reina de las fiestas, Miriam, que al principio ni quería hablar conmigo porque no hablaba español. Gracias a los genios les coquers y a los mejores tres calvos, Carles, Luis y Camilo, y por supuesto a Maik, el genio de la química orgánica, por salvarme la vida tantas veces y enseñarme el mundo de la purificación, las columnas y muchas más cosas chulas de la orgánica. Tampoco me imagino mis días sin Mori, gracias por darme las mejores aplicaciones de la historia, como alicates – " tijeras que no son tijeras". Y también gracias a Gonzalo, Óscar, Marcos, Pau (El millor faller del món), Dani y Patri por todos los momentos compartidos fuera del trabajo, por ser amigos de verdad. No me olvido del resto del mejor laboratorio del mundo, el B3: Astrid, Camille, Fercho, José Miguel, y los franceses Jordan y Clément. Y no puedo estar más agradecida por haber encontrado a mis caris, Lucía y José Luis, lo mejor que me llevo de aquí: No podría haber deseado mejores personas para compartir todos los momentos, los buenos y los malos, de estos años.

Porque no todo ha sido tesis, química y congresos… gracias a mis amigos "de fuera" por recordarme que hay vida más allá del laboratorio (y que a veces había que salir a vivirla). Más que nada, estoy agradecida por haber encontrado a mis cucarachas (mis princesas): Emily, Mathi, Matea, Francesca y Zara. Hemos crecido tanto durante estos años… aprendimos español juntas (hablar, escribir y hasta discutir), aunque siendo sinceras, fue Emily la que obligó a todo el mundo a hablar español sí o sí. *Pasamos de salir de St.Pat casi todos los días a ser responsables y trabajar (bueno… más o menos). No me imagino mis días sin vosotras y nuestras tonterías. También quiero mencionar a Michaela, mi primera compañera de piso por accidente y Hafsa, mi compañera de piso, y ahora parte de mi historia en Valencia; a Mila, mi cómplice en todos los crímenes; y a Elcy, mi compañera de gimnasio, y, por supuesto, a Deej , mi canım, thank you for your love y por estar always close even when you're far. Seni çok seviyorum, siempre. No podría haber tenido mejores compañeros. Espero que, aunque esta etapa esté llegando a su fin para mí, pueda conservaros en mi vida muchos años más.*

I naravno, ništa od ovoga ne bi bilo isto bez moje balkanske ekipe u Valenciji (Anđela, Bane, Boris, Carling, Darko, Katarina, Karolina, Ksenija, Lena, Luka Plavi, Luka Crni, Marko). Hvala vam što ste bili tu za sve, kave, tračeve, smijeh, roštilje, rakije i ono kad ti samo treba netko tvoj. Bili ste moj mali Balkan usred Španjolske i baš ste mi donijeli osjećaj doma gdje god da smo bili. A posebno hvala mojoj habibti, Eni. Hvala ti što si uvijek bila tu , da me guraš kad nisam mogla sama, da me smiriš kad sve gori, da se smiješ i plačeš sa mnom kao da je sve i tvoje. Imati tebe u svom životu je jedan od onih darova koje nikad ne uzmeš zdravo za gotovo. Ne znam kako bih sve ovo prošla bez tebe.

Et un grand merci à toi, Nadjib, pour tous tes conseils, ton aide précieuse, et pour avoir patiemment écouté toutes mes plaintes, sur tout, sur rien, et sur ce qu'il y a entre les deux. Je promets qu'à partir de maintenant, ce sera uniquement des "produits purs" : plus de plaintes, sans additifs, sans poisons ! (Well..I will try)

Tea, Jeja, Vendi, Karla, Karla, Laura, Ena, Noni, Kika, Doria, Tomi&Hari… i svi ostali koji ste me nosili kroz sve emocije, one lijepe, one teške i one koje ni sama nisam znala objasniti. Vaše poruke, fore, "ajde kad ćeš doma" komentari, i face time kave bile su moj spas. Hvala što ste uvijek bile moj glas razuma i moj smijeh u istom pakiranju.

I naravno, neizmjerna hvala mojoj obitelji i svima koji su bili uz mene tijekom ovog puta. Posebno mojim kumama, Ani i Koki, mami Aniti i sestri Karli (i naravno najdražem članu obitelji – Kai). Vi ste moj oslonac i snaga kroz sve ove godine. Hvala vam na bezuvjetnoj ljubavi, podršci i vjeri u mene, čak i onda kad ja nisam vjerovala. Bez vas ne bih uspjela doći dovde. Nosim vas uvijek u srcu. I posebno hvala mojoj Noni Ani, mojoj svakodnevnoj inspiraciji i snazi. Tvoja ljubav i podrška bile su mi svjetlo u najtežim trenucima i motivacija da uvijek idem dalje.

Finally, I want to thank everyone who has been part of this journey, whether near or far. Each of you has left a mark on this chapter of my life, and I carry your support and kindness with me as I move forward. This thesis is not just my achievement, but ours. Thank you from the bottom of my heart.

Valencia ha sido mi hogar lejos de casa. Estos años aquí, con su gente y su cultura, me han hecho sentir siempre bienvenida. No importa a dónde vaya, Valencia siempre tendrá un lugar especial en mi corazón.

TABLE OF CONTENTS

Abstracts

Abbreviations

Chapter 1. Introduction

Chapter 2. Objectives

Chapter 3. Methodology

Chapter 4. Catalytic Transformation of Biomass-Derived Ketones and Alcohols into Jet Fuel Precursors via Hydrogen-Borrowing Coupling Reactions

Chapter 5. Pd and Pd–Au Catalysts on MOF and Zeolite Supports for Selective Acetylene Semi-Hydrogenation in Ethylene-Rich Feedstocks

Chapter 6. Aromatisation of Linear Alkenes over Few-Atom Ruthenium Oxide Clusters at 300 °C: Mechanistic Insights and Catalytic Performance

Chapter 7. General Conclusions

Publications

Abstracts

La industria petroquímica desempeña un papel vital en la economía global, ya que proporciona materiales esenciales para sectores como la energía, el transporte, el embalaje, los textiles y la construcción. En el centro de esta industria se encuentra la nafta, una fracción de destilación del petróleo crudo que sirve como materia prima clave para la producción de productos de alto volumen como olefinas, aromáticos y precursores de polímeros. Sin embargo, los procesos tradicionales para convertir la nafta, como el craqueo por vapor y el reformado catalítico, son energéticamente muy demandantes y perjudiciales para el medio ambiente. A medida que aumentan las presiones regulatorias y ambientales, surge una necesidad urgente de soluciones catalíticas innovadoras que puedan reducir las emisiones, mejorar la eficiencia y ofrecer una mayor flexibilidad en el uso de materias primas.

Esta tesis se centra en el desarrollo y la evaluación de tres métodos que utilizan catálisis con metales nobles soportados para transformar de manera sostenible los intermedios derivados de la nafta en productos químicos valiosos. Cada método está diseñado para un sector específico de la industria petroquímica: combustibles para aviación, materias primas para polímeros y monómeros aromáticos, mientras se avanza en los objetivos de eficiencia de proceso, circularidad y descarbonización. Se destaca el uso de sistemas catalíticos basados en paladio y rutenio, que ofrecen alternativas energéticamente eficientes y con bajas emisiones para estas transformaciones en el sector petroquímico.

El estudio comienza en el Capítulo 4, donde se investiga la mejora catalítica del aceite KA, una mezcla de ciclohexanol y ciclohexanona derivada del benceno, como una vía prometedora para la producción de combustible de aviación sostenible (SAF, por sus siglas en inglés). Utilizando un catalizador de paladio sobre carbono (Pd/C), el proceso opera bajo condiciones suaves y sin disolventes

mediante un mecanismo de transferencia de hidrógeno. Este proceso de conversión genera hidrocarburos C_8–C_{15} adecuados para aplicaciones en combustible para aviones, logrando una alta economía atómica y eliminando la necesidad de fuentes externas de hidrógeno. La investigación pone especial énfasis en la selectividad de la reacción, la minimización de subproductos y la escalabilidad de este método dentro de las infraestructuras de refinerías existentes. Además, en el Capítulo 5, el enfoque se desplaza hacia la purificación del etileno, un producto clave del craqueo por vapor, mediante la semihidrogenación selectiva de impurezas de acetileno. Este capítulo examina el rendimiento de catalizadores bimetálicos de paladio (Pd) y paladio-oro (Pd–Au) soportados en zeolitas y marcos metal-orgánicos (MOFs). La incorporación de oro mejora la sintonía electrónica y optimiza la estructura del soporte para reducir la sobrehidrogenación a etano, al tiempo que mejora la durabilidad del catalizador. Este enfoque es crucial para las líneas de producción de polietileno, ya que incluso pequeñas cantidades de acetileno pueden desactivar los catalizadores de polimerización. Finalmente, el Capítulo 6 se dedica a la isomerización y aromatización catalítica de olefinas terminales, específicamente 1-octeno, en benceno, tolueno y xilenos (conocidos colectivamente como BTX). Estos compuestos aromáticos desempeñan un papel fundamental en la producción de PET, poliuretanos y otros materiales de alta demanda. El proceso emplea catalizadores basados en rutenio soportados en carbono y zeolitas, utilizando una secuencia en un solo reactor que integra isomerización, ciclación y deshidrogenación. Este enfoque proporciona una alternativa de baja temperatura al reformado convencional de nafta, con una mayor eficiencia energética, selectividad y modularidad del proceso. Se presta especial atención a la optimización de la estructura del catalizador para mejorar el rendimiento de compuestos monoaromáticos y reducir la formación de coque.

En conjunto, estos catalizadores innovadores demuestran cómo los sistemas dirigidos de metales nobles pueden hacer que la producción petroquímica sea más sostenible, modular y circular. Al combinar una alta selectividad con compatibilidad para materias primas renovables y las infraestructuras existentes, estos sistemas ofrecen soluciones prácticas para reducir emisiones, mejorar la eficiencia energética y mejorar el rendimiento económico. Esto posiciona a la catálisis como un elemento central en la transformación hacia un futuro industrial con bajas emisiones de carbono.

La indústria petroquímica exerceix un paper vital en l'economia global, ja que proporciona materials essencials per a sectors com l'energia, el transport, l'embalatge, els tèxtils i la construcció. En el centre d'aquesta indústria es troba la nafta, una fracció de destil·lació del petroli cru que serveix com a matèria prima clau per a la producció de productes d'alt volum com a olefines, aromàtics i precursors de polímers. No obstant això, els processos tradicionals per a convertir la nafta, com el craqueig per vapor i el reformat catalític, són energèticament molt demandants i perjudicials per al medi ambient. A mesura que augmenten les pressions reguladores i ambientals, sorgeix una necessitat urgent de solucions catalítiques innovadores que puguen reduir les emissions, millorar l'eficiència i oferir una major flexibilitat en l'ús de matèries primes.

Aquesta tesi se centra en el desenvolupament i l'avaluació de tres mètodes que utilitzen catàlisis amb metalls nobles suportats per a transformar de manera sostenible els intermedis derivats de la nafta en productes químics valuosos. Cada mètode està dissenyat per a un sector específic de la indústria petroquímica: combustibles per a aviació, matèries primes per a polímers i monòmers aromàtics, mentre s'avança en els objectius d'eficiència de procés, circularitat i descarbonització. Es destaca l'ús de sistemes catalítics basats en pal·ladi i ruteni, que ofereixen alternatives energèticament eficients i amb baixes emissions per a aquestes transformacions en el sector petroquímic.

L'estudi comença en el Capítol 4, on s'investiga la millora catalítica de l'oli KA, una mescla de ciclohexanol i ciclohexanona derivada del benzé, com una via prometedora per a la producció de combustible d'aviació sostenible (SAF, per les seues sigles en anglés). Utilitzant un catalitzador de pal·ladi sobre carboni (Pd/C), el procés opera en condicions suaus i sense dissolvents mitjançant un mecanisme de transferència d'hidrogen. Aquest procés de conversió genera hidrocarburs C_8–

C_{15} adequats per a aplicacions en combustible per a avions, aconseguint una alta economia atòmica i eliminant la necessitat de fonts externes d'hidrogen. La investigació posa especial èmfasi en la selectivitat de la reacció, la minimització de subproductes i l'escalabilitat d'aquest mètode dins de les infraestructures de refineries existents. A més, el Capítol 5 s'enfoca a la purificació de l'etilé, un producte clau del craqueig per vapor, mitjançant la semihidrogenació selectiva d'impureses d'acetilé. Aquest capítol examina el rendiment de catalitzadors bimetàl·lics de pal·ladi (Pd) i pal·ladi-or (Pd–Au) suportats en zeolites i marcs metall-orgànics (MOFs). La incorporació d'or millora la sintonia electrònica i optimitza l'estructura del suport per a reduir la sobrehidrogenación a età, al mateix temps que millora la durabilitat del catalitzador. Aquest enfocament és crucial per a les línies de producció de polietilé, ja que fins i tot xicotetes quantitats d'acetilé poden desactivar els catalitzadors de polimerització. Finalment, el Capítol 6 es dedica a la isomerització i aromatització catalítica d'olefines terminals, específicament 1-octé, en benzé, tolué i xilens (coneguts col·lectivament com BTX). Aquests compostos aromàtics exerceixen un paper fonamental en la producció de PET, poliuretans i altres materials d'alta demanda. El procés empra catalitzadors basats en ruteni suportats en carboni i zeolites, utilitzant una seqüència en un sol reactor que integra isomerització, ciclació i deshidrogenació. Aquest enfocament proporciona una alternativa de baixa temperatura al reformat convencional de nafta, amb una major eficiència energètica, selectivitat i modularitat del procés. Es presta especial atenció a l'optimització de l'estructura del catalitzador per a millorar el rendiment de compostos monoaromáticos i reduir la formació de coc.

En conjunt, aquests catalitzadors innovadors demostren com els sistemes dirigits de metalls nobles poden fer que la producció petroquímica siga més sostenible,

modular i circular. En combinar una alta selectivitat amb compatibilitat per a matèries primes renovables i les infraestructures existents, aquests sistemes ofereixen solucions pràctiques per a reduir emissions, millorar l'eficiència energètica i millorar el rendiment econòmic. Això posiciona a la catàlisi com un element central en la transformació cap a un futur industrial amb baixes emissions de carboni.

The petrochemical industry plays a vital role in the global economy, providing essential materials for sectors such as energy, transportation, packaging, textiles, and construction. Central to this industry is naphtha, a distillation fraction of crude oil that serves as a key feedstock for producing high-volume products like olefins, aromatics, and polymer precursors. However, the traditional processes for converting naphtha, such as steam cracking and catalytic reforming, are both energy-intensive and environmentally detrimental. As regulatory and environmental pressures increase, there is a pressing need for innovative catalytic solutions that can reduce emissions, enhance efficiency, and offer greater feedstock flexibility.

This thesis focuses on developing and evaluating three methods that utilise supported noble metal catalysis to transform naphtha-derived intermediates into valuable chemical products sustainably. Each method is designed for a specific sector of the petrochemical industry, jet fuels, polymer feedstocks, and aromatic monomers, while advancing the goals of process efficiency, circularity, and decarbonization. It highlights the use of palladium- and ruthenium-based catalytic systems, which offer energy-efficient and low-emission alternatives for these transformations in the petrochemical sector.

The study commences in Chapter 4, where the catalytic upgrading of KA oil, a blend of cyclohexanol and cyclohexanone derived from benzene, is investigated as a promising avenue for the production of sustainable aviation fuel (SAF). Utilising a palladium-on-carbon (Pd/C) catalyst, the process operates under mild, solvent-free conditions via a hydrogen-borrowing mechanism. This conversion process generates C_8–C_{15} hydrocarbons suitable for jet fuel applications, while achieving high atom economy and eliminating the necessity for external hydrogen sources. The research places special emphasis on reaction selectivity,

the minimisation of by-products, and the scalability of this method within existing refinery infrastructures. Further, in Chapter 5, the focus shifts to the purification of ethylene, a key product of steam cracking, through the selective semihydrogenation of acetylene impurities. This chapter examines the performance of palladium (Pd) and palladium-gold (Pd–Au) bimetallic catalysts supported on zeolites and metal-organic frameworks (MOFs). Incorporating gold improves electronic tuning and optimises the support structure to reduce over-hydrogenation to ethane while enhancing catalyst durability. This approach is crucial for polyethylene production pipelines, as even small amounts of acetylene can deactivate polymerisation catalysts. Finally, Chapter 6 is devoted to the catalytic isomerisation and aromatisation of terminal olefins, specifically 1-octene, into benzene, toluene, and xylenes (collectively referred to as BTX). These aromatic compounds play a vital role in the production of PET, polyurethanes, and other materials in high demand. The process employs ruthenium-based catalysts supported on carbon and zeolites, utilising a one-pot sequence that integrates isomerisation, cyclisation, and dehydrogenation. This approach provides a low-temperature alternative to conventional naphtha reforming, resulting in improved energy efficiency, selectivity, and process modularity. Special attention is given to optimising the catalyst structure to enhance the yield of mono-aromatic compounds while reducing the formation of coke.

Together, these innovative catalysts demonstrate how targeted noble metal systems can make petrochemical production more sustainable, modular, and circular. By combining high selectivity with compatibility for renewable feedstocks and existing infrastructure, these systems provide practical solutions for reducing emissions, improving energy efficiency, and enhancing economic

performance. This positions catalysis as a central element in the transformation toward a low-carbon industrial future.

Petrokemijska industrija ima ključnu ulogu u globalnom gospodarstvu, osiguravajući temeljne materijale za sektore poput energetike, prometa, ambalaže, tekstila i građevinarstva. U središtu ove industrije nalazi se nafta (naphtha), frakcija dobivena destilacijom sirove nafte (crude oil), koja služi kao osnovna sirovina za proizvodnju velikih količina olefina, aromatskih spojeva i prekursora za polimere. Međutim, konvencionalni procesi prerade nafte, poput parnog krekiranja (steam cracking) i katalitičke reformacije (catalytic reforming), izrazito su energetski zahtjevni i štetni za okoliš. U uvjetima sve strožih ekoloških i regulatornih zahtjeva, nužna su inovativna katalitička rješenja koja mogu smanjiti emisije, povećati učinkovitost i omogućiti veću fleksibilnost u izboru sirovina.

Ova disertacija bavi se razvojem i ispitivanjem triju postupaka koji koriste katalizatore na bazi plemenitih metala za održivu pretvorbu međuprodukata dobivenih iz nafte u kemijske proizvode. Svaka je metoda usmjerena na konkretan segment petrokemijske industrije, zrakoplovna goriva (jet fuels), sirovine za polimere (polymer feedstocks) i aromatske monomere (aromatic monomers), uz istovremeno promicanje učinkovitosti procesa, kružnog gospodarstva i dekarbonizacije. U središtu istraživanja nalaze se katalitički sustavi temeljeni na paladiju i ruteniju, koji nude energetski učinkovite i niskougljične alternative tradicionalnim metodama.

U četvrtom poglavlju istražuje se katalitička nadogradnja tzv. KA-ulja, smjese cikloheksanola i cikloheksanona dobivene iz benzena, kao potencijalnog izvora za proizvodnju održivog zrakoplovnog goriva (sustainable aviation fuel, SAF). Proces koristi paladij na ugljičnoj podlozi (Pd/C) i odvija se pod blagim uvjetima, bez upotrebe otapala, putem mehanizma prijenosa vodika (hydrogen-borrowing mechanism). Rezultirajući C_8–C_{15} ugljikovodici prikladni su za upotrebu u

mlaznim gorivima, uz visoku atomsku učinkovitost (atom economy) i bez potrebe za dodatnim izvorima vodika. Poseban naglasak stavlja se na selektivnost reakcije, smanjenje nusprodukata i mogućnost integracije procesa u postojeću rafinerijsku infrastrukturu.

U petom poglavlju pažnja se usmjerava na pročišćavanje etilena, ključne sirovine u proizvodnji polietilena, selektivnom poluhidrogenacijom (selective semihydrogenation) tragova acetilena. Analizira se učinkovitost paladijevih (Pd) i bimetalnih paladij-zlatnih (Pd–Au) katalizatora poduprtih na zeolitima i metalno-organskim okvirima (metal-organic frameworks, MOFs). Uvođenjem zlata poboljšavaju se elektronska svojstva katalizatora i optimizira struktura nosača, čime se smanjuje prekomjerna hidrogenacija u etan i povećava trajnost katalizatora. Ovaj je pristup ključan za osiguranje kvalitete etilena, jer čak i male količine acetilena mogu deaktivirati katalizatore za polimerizaciju.

Završni dio petog poglavlja posvećen je katalitičkoj izomerizaciji i aromatizaciji terminalnih olefina, posebice 1-oktena, u benzen, toluen i ksilene (benzene, toluene, xylenes – BTX). Ovi aromatski spojevi ključni su za proizvodnju PET-a (polyethylene terephthalate), poliuretana (polyurethanes) i drugih traženih materijala. Proces se temelji na katalizatorima s rutenijem, poduprtima na ugljiku i zeolitima, i odvija se u jednoj reakcijskoj posudi kroz sekvencu izomerizacije, ciklizacije i aromatizacije. Time se postiže energetski učinkovitija, niskotemperaturna alternativa konvencionalnoj reformaciji nafte (naphtha reforming), uz veću selektivnost i modularnost procesa. Posebna pažnja posvećuje se optimizaciji katalizatora kako bi se povećao prinos monoaromatskih spojeva i smanjilo stvaranje koksa.

Sveukupno, ovi inovativni katalitički sustavi pokazuju kako ciljana primjena plemenitih metala može unaprijediti održivost, fleksibilnost i kružnost petrokemijske proizvodnje. Visoka selektivnost, kompatibilnost s obnovljivim sirovinama i mogućnost primjene u postojećoj infrastrukturi čine ih iznimno pogodnima za smanjenje emisija, povećanje energetske učinkovitosti i poboljšanje gospodarske isplativosti. Kataliza se na taj način potvrđuje kao ključni čimbenik u prijelazu prema industriji s niskim emisijama ugljika (low-carbon industrial future)

Abbreviations

a.u.	*Arbitrary units*
AcOEt	*Ethyl acetate*
Arom.	*Aromatisation*
ASTM	*American Society for Testing and Materials (ASTM International)*
Atm.	*Atmosphere*
BAS	*Brønsted acid sites*
BASF	*Badische Anilin und Soda Fabrik*
BE	*Binding energy*
BET	*Brunauer-Emmett-Teller (surface area analysis method)*
BTX	*Aromatic hydrocarbons (benzene, toluene, and xylenes)*
C-alk.	*Carbon-linked alkylation*
CO-FTIR	*CO adsorption measured by Fourier transform infrared spectroscopy.*
Conv.	*Conversion*
Cycl.	*Cyclisation*
DFT	*Density functional theory*
DRX	*Powder X-ray diffraction*
E.A.	*Elemental analysis*

e.g.	*Lat. Exempli gratia* (for example)
E_a	*Activation energy*
EDX	*Energy Dispersive X-ray Analysis*
E_g	*UV-vis absorption edge energy*
Equiv.	*Equivalents*
ESI	*Electrospray ionization*
EXAFS	*Extended X-ray Absorption Fine Structure*
FT	*Fourier transform*
FWHM	*Full-width at half maximum*
GC	*Gas chromatography*
GC-MS	*Gas chromatography coupled with mass spectrometry*
HAADF	*High-angle-annular dark-field*
HAADF-STEM	*Dark-field scanning transmission electron microscopy with a high-angle annular dark-field detector*
HB	*Hydrogen borrowing*
HBC	*Hydrogen-borrowing condensation*
H-BETA	*Protonic zeolite of the BETA type*
HRSTEM	*High-resolution scanning transmisión electron microscopy*

HRTEM	*High-resolution transmisión electron microscopy*
H-USY	*Protonic zeolite of the USY type*
H-ZSM-5	*Protonic zeolite of the ZSM-5 type*
ICP-AES	*Inductively coupled plasma atomic emisión spectroscopy*
ICP-AES	*Inductively coupled plasma spectrometry*
ICP-OES	*Inductively coupled plasma optical emission spectroscopy.*
IR-ATR	*Attenuated total reflectance infrared spectroscopy*
Isom.	*Isomerisation*
IUPAC	*International Union of Pure and Aplied Chemistry*
J	*Coupling constant*
KA oil	*Ketone-alchohol oil*
KE	*Kinetic energy*
LAS	*Lewis acid sites*
LCA	*Life cycle assessment*
m-	*Substituent in the* meta *position of the aromatic ring*
MDI	*Methylene diphenyl diisocyanate*

Me	*Methyl*
MeOH	*Methanol*
MOF	*Metal-organic framework*
NMR	*Nuclear magnetic resonance*
NMR MAS	*Magic Angle Spinning Nuclear Magnetic Resonance*
NPs	*Nanoparticles*
o-	*Substituent in the* ortho *position of the aromatic ring*
O-alk.	*Oxygen-linked alkylation*
P	*Pressure*
p-	*Substituent in the* para *position of the aromatic ring*
PET	*Polyethylene terephthalate*
Ph	*Phenyl*
PhOH	*Phenol*
PU	*Polyurethanes*
Py-FTIR	*Pyridine adsorption Fourier-transform infrared spectroscopy*
rpm	*Revolutions per minute*
SAAs	*Single-atom alloys*

SABIC	*Saudi Basic Industries Corporation*
SAC	*Single-atom catalysis*
SAFs	*Sustainable aviation fuels*
SAR	*Structure–activity relationships*
T	*Temperature*
TDI	*Toluene diisocyanate*
TEM	*Transmission electron microscopy*
TGA	*Thermogravimetric analysis*
TON	*Turnover number*
UV-Vis	*Ultraviolet–visible spectroscopy*
VOCs	*Volatile organic compounds*
WHSV	*Weight hourly space velocity*
XANES	*X-ray Absorption Near-Edge Structure*
XAS	*X-ray Adsorption Spectroscopy*
XPS	*X-ray Photoelectron Spectroscopy*
ΔG	*Gibbs free energy change*
ΔH	*Enthalpy change*

Chapter 1.

Introduction

Index

1.1. Introduction

The global chemical industry finds itself at a crucial crossroads. With the intensification of climate change and rapid depletion of natural resources, traditional fossil-based industrial models are being subjected to urgent reevaluation. The chemical sector, especially petrochemicals, continues to serve as a cornerstone of the global economy, providing essential inputs for polymers, fuels, pharmaceuticals, fertilisers, and numerous materials integral to everyday life. However, it is also one of the largest industrial contributors to greenhouse gas emissions and a significant consumer of energy and water.[1,2]

According to the International Energy Agency (IEA), petrochemical production represents approximately 10% of global final energy demand and is expected to emerge as the largest driver of oil demand by 2030.[3] Despite its economic significance, the environmental externalities associated with petrochemical operations have prompted widespread calls for decarbonization, material circularity, and innovative processes. These challenges are further exacerbated by growing public pressure, increasingly stringent regulations, such as the EU Emissions Trading Scheme[4] and U.S. Clean Energy Incentives[5], and evolving investor expectations concerning Environmental, Social, and Governance (ESG) performance.[6]

In response to evolving market demands, leading chemical manufacturers are redefining their growth strategies. Prominent global corporations such as BASF[7], Dow[8], SABIC[9], LyondellBasell[10], and Shell Chemicals[11] have set ambitious sustainability targets, including carbon neutrality, renewable feedstock integration, and electrification of production processes. Furthermore, new market entrants and clean-tech startups are emerging with the intent to commercialise

groundbreaking technologies, including CO_2 utilisation, bio-based monomers, and the depolymerisation of waste plastics.[12] Investment in green chemical technologies has experienced significant growth, with over $60 billion USD directed toward sustainable materials and low-emission chemicals from 2020 to 2024. Notably, bio-based fuels and specialty catalysts are identified as key growth segments within this investment landscape.[6,12] Petrochemical activities are also associated with significant air and water pollution, including the emission of volatile organic compounds (VOCs), particulate matter, and heavy metals, which have direct impacts on human health and ecosystems.[13,14]

In the context of these structural shifts, catalysis has evolved from a supportive tool to a pivotal force enabling the industry's transition. More than 90% of chemical manufacturing processes utilise catalysts, which play a vital role in improving energy efficiency, selectivity, and reducing emissions.[15,16] These processes can lower reaction temperatures, eliminate hazardous reagents, minimise waste, and unlock new reaction pathways not achievable with traditional methods.[17] Such capabilities are essential for creating economically viable and environmentally sustainable manufacturing platforms. These attributes are essential for the development of next-generation manufacturing platforms that are both economically viable and environmentally sustainable.

1.1.1. Green and Sustainable Chemistry: Principles and Context

As industrial systems move toward greater environmental responsibility, the role of chemistry, especially catalysis, has evolved into a key driver of sustainable innovation. Green catalysis has emerged as a vital approach, enabling efficient and selective chemical transformations with minimal environmental harm.[18] It encourages the use of safer reagents and solvents, lowers reaction temperatures, and enhances atom economy while reducing energy consumption.[19] Unlike traditional methods that address waste after it is generated, green catalysis strives to eliminate waste at the source by incorporating sustainability principles in the design of both molecules and processes.[20] This proactive approach is essential for the future of the chemical industry. The focus of green catalysis is to improve molecular transformations while minimising waste and hazardous inputs, while also optimising energy and material use right from the outset. This strategy aligns with broader ecological and societal goals.[19,20]

The theoretical and practical foundations of green catalysis are anchored in the 12 Principles of Green Chemistry (see Figure 1-1), formulated by Paul Anastas and John Warner in 1998.[21,22] These principles offer a comprehensive framework for constructing environmentally sustainable chemical processes. They encompass the entire lifecycle of a chemical process, addressing aspects such as feedstock selection, reagent choice, energy input, product design, degradation, and end-of-life considerations. Since their introduction, these principles have received widespread acclaim in academic, regulatory, and industrial sectors as both evaluative benchmarks and strategic designs for sustainable chemistry. Far from being a static checklist, the principles of green chemistry are increasingly recognised as interconnected guidelines that embody a systems-level perspective. The prevention of waste (Principle 1) is a cornerstone of green chemistry,

emphasising the importance of optimising processes at the outset rather than relying on remediation. Atom economy (Principle 2) underscores the necessity of maximising the incorporation of all materials into the final product, thereby enhancing efficiency and minimising raw material consumption. Furthermore, these principles advocate for the use of less hazardous chemical syntheses (Principle 3), the design of safer chemicals (Principle 4), and the reduction or elimination of auxiliary substances, such as solvents (Principle 5). In the realm of industrial energy demands, Principle 6 underscores the importance of energy efficiency by promoting processes that function at ambient temperature and pressure whenever feasible. This strategy effectively reduces the environmental impacts associated with heating, cooling, and pressurisation. Principle 7 advocates for a shift away from depleting fossil resources towards renewable feedstocks, such as biomass or materials sourced from waste. Additionally, Principle 8 recommends avoiding unnecessary derivatisation steps, such as the use of protecting groups, which often increases chemical waste and energy usage. Principle 9 emphasises catalysis as a preferred method of activation, enabling reactions to occur with fewer reagents, generating fewer by-products, and achieving improved selectivity. Furthermore, the integration of real-time analytical techniques, as outlined in Principle 11, enhances process control and safety. Finally, Principle 12 promotes the concept of inherently safer design, advocating for the use of materials and conditions that minimise the risks of explosions, fires, or toxic releases.[21]

Figure 1-1 Schematic representation of the Twelve Principles of Green Chemistry as defined by Anastas and Warner.[21]

The emergence of sustainable chemistry represents a significant conceptual and practical evolution of green chemistry, extending its focus beyond process-level efficiency to encompass full-system considerations such as lifecycle assessment, economic feasibility, regulatory alignment, and resource circularity.[23] This broadened perspective reflects a shift toward integrating environmental, social, and economic dimensions within chemical innovation.[24] Rather than emphasising harm reduction alone, sustainable chemistry promotes the design of regenerative systems, those capable of renewing resources, minimising waste, and maintaining resilience under shifting industrial and ecological conditions.[25, 26]

Central to this framework is the adoption of strategies that simultaneously support environmental stewardship and economic performance. These include the valorisation of biomass and waste-derived inputs, the selection of recyclable or

renewable feedstocks[24,27], and the design of catalysts that are robust, selective, and readily regenerable.[28] By increasing reaction selectivity and reducing auxiliary inputs, such systems enhance material and energy efficiency while mitigating the generation of hazardous by-products. In this regard, catalysis continues to play a pivotal role, not merely by accelerating reactions but by enabling entirely new pathways that align with sustainability targets. Its capacity to operate under mild conditions, facilitate multi-functional transformations, and support process intensification renders it indispensable to sustainable chemical manufacturing.

This integrative approach holds particular significance in petrochemical refining and downstream production, where entrenched reliance on fossil feedstocks, high thermal demands, and complex separations present persistent environmental and economic challenges. In these high-impact domains, catalysis serves as a transformative platform for implementing green chemistry principles at scale. Strategic catalyst development, coupled with judicious feedstock selection and advanced reaction engineering, enables a shift away from resource- and energy-intensive practices toward cleaner, more circular models of production.[27]

The catalytic systems examined herein, spanning biomass upgrading, acetylene hydrogenation, and aromatic hydrocarbon synthesis, exemplify how these concepts can be operationalised. Each system reflects a deliberate alignment with sustainability metrics, not as an add-on, but as an intrinsic element of the reaction design process. By integrating performance optimisation with environmental responsibility, these case studies highlight the feasibility of embedding sustainable chemistry principles into the foundations of modern industrial practice.[29]

Recent developments indicate a significant redefinition of chemical innovation. The field is increasingly defined not just by maximising output, but by a systemic approach that emphasises durability, adaptability, and ecological compatibility. In this context, sustainable chemistry is no longer optional; it has become an essential scientific methodology for advancing technological progress within the limits of our planet.[30] This transformation is most effectively expressed through the lens of catalysis, which offers a pathway to align industrial productivity with environmental integrity in an era marked by constraints and complexity.

1.1.2. Catalysis

The term "catalysis" was introduced in 1835 by Swedish chemist Jöns Jacob Berzelius. A clearer definition emerged in 1894 when Professor Wilhelm Ostwald described it as "the acceleration of a slow chemical process by an external material," known as a catalyst.[31] This substance remains unchanged during the reaction and does not affect the overall stoichiometry. Ostwald's groundbreaking work earned him the Nobel Prize in Chemistry in 1909, recognising his contributions to both catalysis and chemical equilibria.[32]

Following these early developments, catalysis began to be recognised as an independent scientific discipline in the early 20th century.[33] Its importance has since expanded significantly. Today, catalytic processes are employed in the majority of industrial chemical transformations. It is estimated that approximately 95% of chemical products produced by the industry are synthesised using catalysts, which contribute to nearly 80% of the sector's total added value.[34]

In a catalytic reaction, a catalyst enables an alternative pathway that has a lower activation energy barrier (E_a). As illustrated in Figure 1-2, this function is

achieved by decreasing the energy required to reach the transition state, thus accelerating the reaction rate without altering the system's thermodynamic properties. This principle facilitates the effective conversion of reactants into products under milder conditions than would otherwise be necessary, enhancing both the selectivity and speed of chemical transformations.[35,36]

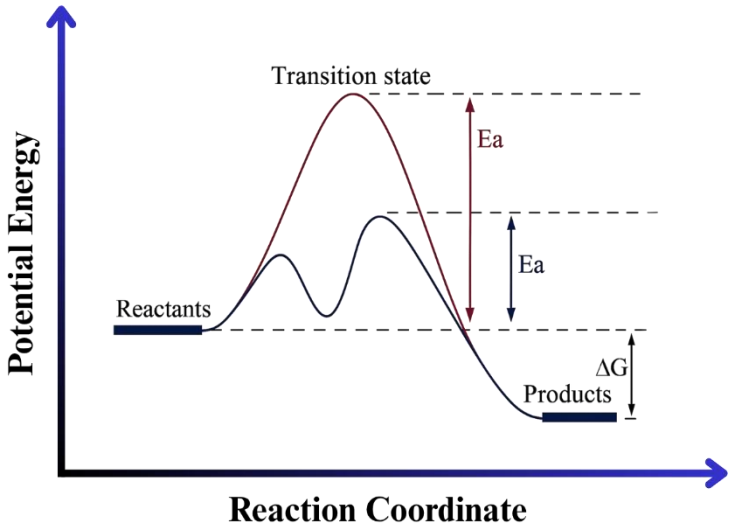

Figure 1-2 Schematic representation of the catalytic effect on reaction energy profile, illustrating the reduction in activation energy (E_a) through an alternative pathway with a catalyst.

The introduction of catalysts has not only made previously unattainable reactions possible but has also significantly improved the efficiency, selectivity, and sustainability of chemical processes. These advancements have resulted in reduced costs, minimised waste, and enhanced compliance with environmental regulations in industrial operations.

Catalytic processes can be categorised based on the energy source employed to drive the reaction. Traditionally, they are classified as thermocatalytic, electrocatalytic, or photocatalytic, depending on whether thermal energy, electrical input, or light serves as the driving force.[37] Additionally, catalysis can be distinguished by the physical phase relationship between the catalyst and the reactants. In homogeneous catalysis, both the catalyst and the reactants exist in the same phase (typically liquid). In contrast, heterogeneous catalysis involves a catalyst that is in a different phase (usually solid) from the reactants. Biocatalysis refers specifically to catalytic processes mediated by enzymes, representing a biologically derived subset of homogeneous catalysis characterised by highly specific activity under mild conditions.[37] These classifications not only illuminate mechanistic differences but also inform catalyst design, process engineering, and the selection of suitable operating conditions for implementation at both industrial and laboratory scales. A more detailed discussion of these catalytic modes will follow in the subsequent sections.

1.1.2.1. Homogeneous vs Heterogeneous Catalysis

Catalytic processes are commonly classified according to the physical state of the catalyst relative to the reactants. The two primary categories, homogeneous and heterogeneous catalysis, differ in their mechanisms, operational benefits, and practical limitations. Each type offers distinct advantages depending on the specific application and scale of the process.[38]

In homogeneous catalysis, the catalyst and reactants exist in the same phase, typically in a liquid medium. This arrangement promotes efficient interactions, leading to faster reaction rates and better product formation. The uniform

distribution of the catalyst minimises mass transfer limitations, allowing for precise control over reaction rates by adjusting factors like ligand environments and solvent polarity. This type of catalysis is especially useful in fine chemical synthesis and pharmaceuticals, where controlling enantioselectivity and regioselectivity is crucial.[39] However, challenges include the difficulty of separating and recovering the catalyst from the mixture, which can be complex and costly on an industrial scale. Additionally, some homogeneous catalysts may lack stability during prolonged use or at high temperatures, affecting their reusability and long-term effectiveness.[35,36]

Heterogeneous catalysis involves catalysts and reactants that exist in different phases, typically with solid catalysts interacting with liquid or gaseous substrates.[40] This arrangement offers several operational advantages, including simplified catalyst separation, enhanced thermal and mechanical stability, and the ability to reuse catalysts across multiple cycles. Consequently, heterogeneous catalysis is often the preferred method for large-scale industrial processes such as hydrocracking, steam reforming, and catalytic oxidation.[41] However, the effectiveness of heterogeneous systems may be influenced by surface phenomena, including limitations in mass transport, accessibility of active sites, and catalyst deactivation caused by sintering or fouling. Factors such as surface morphology, particle size, and the porosity of the catalytic material play crucial roles in determining the efficiency and selectivity of these reactions.[42]

The choice between homogeneous and heterogeneous catalysis is influenced by various factors, including the type of reaction, the desired product, production scale, and economic considerations. Homogeneous systems typically offer enhanced precision and finely tuned reactivity. In contrast, heterogeneous catalysts are recognised for their superior processability and long-term

operational stability. Furthermore, there is a growing interest in hybrid approaches, such as supported molecular catalysts or phase-transfer systems, that aim to integrate the benefits of both catalysis types. This integration broadens the applicability of catalytic science in the pursuit of sustainable chemical production.[37,43,44]

1.1.2.2. Supported Catalysts in Heterogeneous Catalysis

In heterogeneous catalysis, the properties of catalyst supports play a crucial role in the performance of active metal species. The effectiveness of a catalyst, measured by its activity, selectivity, and resistance to deactivation, relies heavily on the support material as well as the catalytic phase. Therefore, catalyst design increasingly focuses on optimising support characteristics, such as porosity, surface area, acidity, and thermal stability, to meet the needs of specific reactions.[45,46] Various support architectures, including activated carbon, different oxides, zeolites with defined microporosity (like FAU and MFI topologies), and metal-organic frameworks (MOFs), are implemented to enhance the performance of noble metals such as palladium, gold, and ruthenium.[47–49] These materials are utilised in diverse applications, including sustainable fuel synthesis, olefin purification, and aromatic compound production. Importantly, no single support material can fulfil all catalytic requirements. Each class of support presents distinct properties that can be strategically leveraged based on the particular reaction environment and desired outcomes.

Activated carbon has traditionally been selected for applications requiring a chemically inert and redox-neutral platform. Its impressive thermal conductivity and wide pore distribution render it effective for facilitating transformations

under relatively mild conditions. However, its structural confinement is somewhat limited, and the absence of acid-base functionalities restricts its effectiveness in reactions that benefit from protonic activity. Despite these drawbacks, activated carbon remains a valuable resource in hydrogen-borrowing and condensation systems, where suppressing side reactions and ensuring uniform metal dispersion are critical.[50–53]

Zeolites are utilised when precise structural and acidic characteristics are required.[54] Their crystalline frameworks impose selective size and shape constraints on reactant molecules, facilitating highly specific interactions with active sites. The solid architecture of zeolites provides excellent thermal stability, and their Brønsted acid sites enable a diverse range of proton-mediated reactions. However, this acidity may also lead to unwanted side reactions, particularly in hydrothermal environments or under conditions prone to coking. As a result, it is crucial to carefully manage process parameters and implement effective regeneration strategies.[55–57]

Metal-organic frameworks (MOFs) have recently emerged as a highly versatile alternative to conventional supports, thanks to their structural tunability. By modularly assembling organic linkers and metal nodes, MOFs offer remarkable flexibility in designing both pore environments and local electronic structures. Their ability to incorporate single atoms or bimetallic dimers within defined cavities facilitates atomic-level control over active site behaviour. While earlier generations of MOFs were prone to moisture and thermal sensitivity, recent advancements in framework design, especially those that involve zirconium clusters, have significantly improved their stability, allowing these materials to withstand the rigorous demands of catalytic processing.[58–60]

When evaluating these materials across various criteria, the distinctions between them become more apparent. Activated carbon is commonly preferred for its high surface area and inertness, though it provides limited control over reaction microenvironments. Zeolites, on the other hand, offer a balance of thermal resilience and shape selectivity, but may require optimisation to minimise coke formation and catalyst degradation. MOFs, which are still under extensive development, provide the greatest degree of architectural tunability. This allows for site-specific catalysis and the integration of hybrid functionalities that are difficult to achieve with inorganic supports alone. (A comprehensive comparison is available in Table 1-1., and Figure 1-3)

Table 1-1 Comparative Properties of Common Catalyst Supports[55, 61, 62]

Feature	Activated Carbon	Zeolites (e.g., MFI, FAU)	MOFs (e.g., UiO-66)
Structure	Amorphous carbon network	Crystalline aluminosilicate framework	Crystalline coordination polymer
Surface Area	High (500–1500 m^2/g)	Moderate to high (300–800 m^2/g)	Very high (>1000 m^2/g)
Porosity	Mesoporous/macro porous, tunable	Uniform micropores	Tunable micro/mesopores
Acidity	Generally inert (non-acidic)	Strong Brønsted and/or Lewis acidity	Variable, depending on linker and node
Thermal Stability	High (except in oxidising environments)	Very high	Moderate to high (Zr-based MOFs preferred)
Shape Selectivity	None	Strong (due to defined pore geometry)	Moderate, customizable
Metal Dispersion	High via surface anchoring	Confined within channels or cages	Atomic-level achievable in pores or cages
Common Limitations	Low confinement, oxidative instability	Coking, acid-driven side reactions	Moisture/thermal sensitivity (improving)
Best Suited For	Redox reactions, mild hydrogenation	Hydrocarbon transformations, selective hydrogenation	Tandem catalysis, fine-tuned reactivity

As the complexity of catalytic processes increases, encompassing not only activity and selectivity but also integration, renewability, and scalability, the imperative for rational support design becomes more critical. There is a notable transition towards hybrid supports that amalgamate the benefits of various support classes. Advanced materials, including carbon-coated MOFs, hierarchical zeolite frameworks, and mesoporous composites, are being meticulously engineered to combine the chemical inertness, structural definition, and tunable functionalities that individual supports often lack. These innovations in supported catalysts are poised to address the rising challenges in sustainable and high-performance chemical manufacturing.[63–65]

The interfacial chemistry between the metal and its support is fundamentally influential in shaping catalytic performance. Key factors such as support polarity, pore architecture, and surface functionalization significantly affect electron transfer dynamics, metal particle size, and resistance to sintering phenomena.[66, 67] For instance, palladium-gold (Pd–Au) systems supported on MFI zeolites exhibit superior electronic communication, effectively lowering activation energy barriers in acetylene conversion.[67,68] In contrast, palladium on carbon (Pd/C) systems primarily rely on uniform dispersion and accessibility to active sites.[69]

When employing ruthenium, non-acidic oxide supports have been strategically utilised to balance redox activity with thermal stability, facilitating low-temperature aromatisation while mitigating coke formation.[70,71]

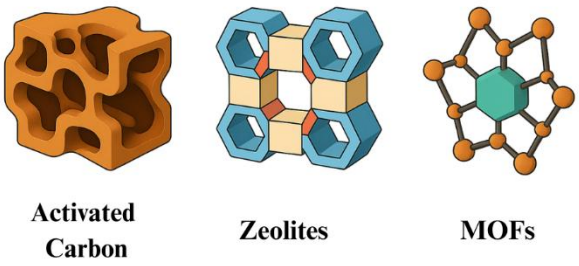

Figure 1-3 Schematic Overview of Key Supports in Heterogeneous Catalysis

Future developments in heterogeneous catalyst design are expected to focus on hybrid supports that combine the best characteristics of current systems. New composite materials, including carbon-coated MOFs, mesostructured oxides, and hierarchical zeolites, are being developed to address issues related to stability, selectivity, and effective metal anchoring.[72,73] These advancements aim to prolong catalyst lifespan and improve atomic efficiency by allowing configurations of single atoms or dimers, especially important for noble metal catalysts, given the need for resource conservation.[74,75] Despite these advancements, heterogeneous catalytic systems still encounter significant challenges that limit their industrial application. Catalyst deactivation from coke buildup, metal leaching, and insufficient stability under high-temperature or high-pressure conditions are persistent issues.[76] In processes like olefin aromatisation, the creation of oligomeric by-products can block active sites, complicating the reaction. Additionally, scaling up these systems raises practical challenges in heat and mass transfer, reactor compatibility, and process consistency. Recent progress in synthesis techniques and regeneration methods is aimed at overcoming these obstacles. By optimising support morphology and

incorporating dopants, researchers are enhancing the stability and reusability of catalysts.[76] This makes supported metal catalysts essential for developing sustainable heterogeneous catalysis, providing a framework for environmentally friendly and economically viable chemical processes. These solid supports not only improve catalyst performance but also affect reaction pathways, promoting mechanisms such as hydrogen transfer and isomerisation.[76,77] Heterogeneous catalytic systems are particularly valued for their resilience in harsh industrial settings, such as catalytic cracking, and their compatibility with various feedstocks, including biomass and olefin-rich streams.[38]

1.1.3. Catalysis in Modern Petrochemical Refining

Modern petrochemical refining encompasses a series of interconnected catalytic processes that transform crude oil into fuels and valuable chemical intermediates. The process commences with atmospheric distillation, wherein crude oil is separated into distinct fractions based on their boiling ranges. Key outputs from this distillation include light gases, naphtha, kerosene, and light gas oils.[78] Naphtha, a light distillate with a boiling range of approximately 30–200 °C, is an essential feedstock due to its diverse molecular composition and reactivity. It serves as a precursor for two critical transformations: steam cracking, which yields light olefins[79] and catalytic reforming, which produces aromatic hydrocarbons (BTX: benzene, toluene, xylenes).[78,80] The conversion of these fractions, particularly those that generate ethylene, BTX aromatics, and cyclohexanol/cyclohexanone (KA oil), is crucial for minimising the environmental impact of the chemical industry and meeting low-carbon regulations.

1.1.3.1. Selective Hydrogenation of Acetylene: Catalytic Precision in Ethylene Purification

In the broader context of modern petrochemical refining, the production of polymer-grade ethylene is a fundamental aspect of global chemical manufacturing. Ethylene is primarily produced through the steam cracking of naphtha and serves as the essential building block for a wide variety of downstream products, such as polyethylene, ethylene oxide, and polyvinyl chloride.[81] With annual global demand exceeding 200 million tons, the purity of ethylene streams is vital for maintaining the integrity of polymerisation processes and ensuring the quality of the final products.[82,83]

The steam cracking process operates at temperatures of approximately 800 °C, involving the thermal decomposition of light hydrocarbons extracted from the upper portion of the atmospheric distillation column.[83,84] This process produces light olefins, such as ethylene and propylene.[85] However, a significant challenge arises from the co-production of acetylene, which typically occurs in concentrations below 1%. While its quantity is minimal, acetylene's high reactivity and strong adsorption affinity present serious issues. It has the potential to irreversibly deactivate polymerisation catalysts, promote the formation of undesirable oligomeric by-products commonly known as "green oil," and create localised hot spots due to its exothermic reaction characteristics. To address these risks, a selective hydrogenation step is employed to convert acetylene into ethylene or ethane, depending on the specific process conditions and economic priorities. Although this purification step involves only a small volume, it plays a crucial role in maintaining the continuity and safety of large-scale ethylene production. The success of this step depends on the catalytic system's ability to balance activity and selectivity, achieving a high conversion rate of acetylene

while minimising over-hydrogenation to ethane, which could otherwise reduce product yield and economic viability.[86,87]

Historically, palladium-based catalysts supported on porous carriers such as alumina or carbon have been utilised for this purpose. While these catalysts demonstrate effectiveness, they often encounter selectivity limitations, particularly under front-end conditions where hydrogen partial pressures are elevated. Excessive hydrogenation can lead to the undesired formation of ethane, diminishing atom efficiency and increasing the load on downstream separation units. Furthermore, frequent regeneration of these catalysts is required due to deactivation caused by coke deposition or metal sintering, adversely affecting overall process economics.[88–90]

Recent advancements have highlighted the potential of bimetallic Pd–Au alloy catalysts, which offer substantial enhancements in selectivity and stability. The addition of gold modifies the electronic properties of palladium, influencing hydrogen adsorption strength and inhibiting deep hydrogenation pathways. These improvements increase the selectivity of acetylene to ethylene, decrease ethane formation, and prolong the catalyst's lifespan.[89,91,92] Moreover, supports such as zeolites and MOFs have been explored to further refine reaction environments through shape selectivity and metal confinement.[93,94] These innovations not only boost performance but also resonate with several Principles of Green Chemistry. Enhanced selectivity and minimised over-hydrogenation relate to Principle 1 (Waste Prevention) and Principle 2 (Atom Economy). The preference for catalysts over stoichiometric reagents exemplifies Principle 9, while reduced hydrogen and energy requirements support Principle 6 (Energy Efficiency). Additionally, the use of operando techniques, such as in situ transmission electron microscopy (TEM) and X-ray absorption spectroscopy (XAS), has yielded real-

time insights into active site dynamics, aligning with Principle 11 (Real-Time Analysis for Pollution Prevention) and promoting the rational design of catalysts.[28,95]

From an industrial and economic perspective, optimising the hydrogenation of acetylene is essential. Improved catalyst performance not only reduces hydrogen demand but also lowers operating temperatures and extends maintenance intervals due to enhanced durability. Collectively, these factors increase plant throughput, decrease operational costs, and elevate profit margins, outcomes that are especially critical in light of rising energy prices and increasingly stringent environmental regulations.[96–98] Although the selective hydrogenation of acetylene is relatively modest in scale compared to the overall volume of ethylene production, it is a vital component of petrochemical operations, as poor control can result in operational problems, catalyst poisoning, and costly process interruptions.[98] The ongoing refinement in this area illustrates how advancements in catalyst technology, grounded in a thorough understanding of molecular mechanisms and sustainability principles, can transform a necessary purification step into a platform for process optimisation, energy efficiency, and environmental stewardship.[96,99] As demand for ethylene continues to grow alongside global urbanisation and industrialisation, the strategic enhancement of this catalytic process will remain central to the competitiveness and sustainability of the polymer value chain.[97,100]

1.1.3.2. Aromatic Hydrocarbon Production

Aromatic hydrocarbons, benzene, toluene, and xylenes, collectively referred to as BTX, are pivotal to the global chemical economy. These compounds serve as vital intermediates in the production of a range of materials, including polyethylene terephthalate (PET), polyurethanes (PU), styrenics, and high-octane fuels. For instance, *p*-xylene is oxidised to yield terephthalic acid, a key monomer in PET production. In addition, toluene and benzene act as precursors for the isocyanates essential for manufacturing polyurethanes, specifically toluene diisocyanate (TDI) and methylene diphenyl diisocyanate (MDI).[101,102] The global demand for these materials is significant: annual benzene production exceeds 50 million tons, while ethylbenzene (used for styrene) and *p*-xylene (for PET) add approximately 47 million tons and 30 million tons, respectively.[102,103] This scale of production highlights the economic and strategic importance of BTX, particularly within industries such as packaging, automotive, textiles, and construction.

The naphtha fraction, obtained from the midsection of the atmospheric distillation column (with a boiling range of approximately 30–200 °C), has historically been the primary feedstock for catalytic reforming, the predominant industrial method for producing BTX aromatics.[104,105] This process involves a series of reactions, including dehydrogenation, isomerisation, cyclisation, and aromatisation, all catalysed by platinum supported on chlorinated alumina, and takes place at temperatures between 480 and 520 °C under moderate pressures.[106] Despite its long-standing efficiency and high throughput, catalytic reforming presents notable sustainability and operational challenges. The significant energy input leads to considerable CO_2 emissions, while the use of chlorinated supports raises concerns of corrosion and necessitates frequent catalyst regeneration due to coke

formation. These factors not only complicate operations but also increase the environmental impact, highlighting the need for more sustainable alternatives. A parallel method known as Friedel–Crafts alkylation produces BTX derivatives by alkylating benzene with light olefins. While early implementations relied on liquid acid catalysts such as aluminium chloride ($AlCl_3$) or hydrofluoric acid (HF), modern systems have shifted to solid acid zeolites, including H-ZSM-5 and H-Beta.[107] These solid catalysts offer advantages such as shape selectivity, reusability, and a cleaner waste profile. However, these systems are not without their challenges. They require high-purity feedstocks and operate under harsh conditions, typically at temperatures between 200 and 400 °C and at elevated pressures.[107] Furthermore, catalyst deactivation can occur due to coke accumulation and olefin polymerisation within the micropores. Additionally, both reforming and alkylation processes are primarily optimised for fossil-derived hydrocarbons, posing integration challenges as the industry increasingly transitions toward bio-based, olefin-rich, or oxygenate-containing feedstocks.[101,108,109]

To tackle these constraints, research is increasingly shifting towards alternative catalytic platforms that provide enhanced feedstock flexibility, improved energy efficiency, and better alignment with green chemistry principles. One of the most promising strategies involves the direct aromatisation of long-chain α-olefins, such as 1-octene, using ruthenium-based catalysts supported on carbon or oxide materials (for example, SiO_2 and Al_2O_3) or bifunctional zeolites like HZSM-5.[110,111] These olefins, which can be sourced from ethylene oligomerisation, Fischer–Tropsch synthesis, or renewable biomass streams, undergo isomerisation, cyclisation, and dehydrogenation in a single reactor step at moderate temperatures (approximately 300 °C).[110,112–114] Unlike traditional

reforming methods that require multiple steps and significant energy input, the Ru-catalysed approach presents a coke-resistant, halogen-free, and regenerable alternative. Crucially, this process produces mono-alkyl aromatics that can be selectively adjusted (for instance, to yield either toluene or xylene) based on the catalyst structure and reaction conditions. This versatility enables targeting specific downstream markets, such as TDI for polyurethane foams or PET for packaging applications.

From a mechanistic standpoint, Ru catalysts enable a "cascade reaction," where terminal alkenes first isomerise into internal alkenes, followed by cyclisation and aromatisation, often generating hydrogen gas as a byproduct.[115–117] This process operates efficiently without the need for Brønsted acids, chlorinated promoters, or multi-stage reactor designs, thereby reducing environmental risks and streamlining process integration. These advancements provide significant benefits in terms of sustainability, economic viability, and process adaptability. Lower operational temperatures lead to decreased furnace usage and CO_2 emissions, extending catalyst lifetimes and reducing the frequency of regeneration. The absence of corrosive additives is in line with Principles 4 and 5 of green chemistry (Designing Safer Chemicals and Safer Auxiliaries), while atom-efficient pathways and the potential for hydrogen co-generation uphold Principles 1, 2, and 6 (Waste Prevention, Atom Economy, and Energy Efficiency).[28] Moreover, the capability to process unconventional or renewable feedstocks makes Ru-based aromatisation particularly attractive in a decarbonising economy, where diversifying raw material sources is both a technical and regulatory imperative.[118,119] Operationally, these systems can either be retrofitted into existing aromatics production infrastructure or deployed in modular units located near bio-feedstock sources. This decentralisation lowers

capital intensity and facilitates on-site production of aromatics, minimising logistical and environmental constraints. From a market perspective, this modularity supports the sustained growth of aromatic demand within both traditional fossil-based and emerging green chemical value chains.

1.1.3.3. Catalytic Upgrading of KA Oil: A Pathway to Sustainable Aviation Fuel

In the realm of modern petrochemical reforming, there is an increasing emphasis on the strategic revaluation of intermediates that are already produced in significant volumes within the chemical supply chain. One notable candidate in this regard is KA oil, a mixture of cyclohexanol and cyclohexanone, which is primarily used in the production of adipic acid for nylon-6,6.[120–123] KA oil can be derived from the oxidation of cyclohexane, an output of benzene hydrogenation, or through the processing of cycloparaffins within the kerosene distillation range.[121,124,125] With global production exceeding 8 million tons annually, KA oil is not only abundant but also logistically accessible and chemically versatile.[121] As the aviation sector faces increasing pressure to reduce carbon emissions, given that it accounts for approximately 2–3% of global CO_2 emissions, attention has shifted toward Sustainable Aviation Fuels (SAFs) as a promising alternative to fossil-derived jet fuels.[126] The International Air Transport Association (IATA) suggests that SAFs could contribute up to 65% of the total emissions reductions needed to achieve net-zero aviation by 2050. However, current production of SAFs remains minimal compared to the anticipated demand of over 400 million tonnes per year, highlighting the urgent need for scalable, renewable, and economically viable production solutions.[127,128]

In this context, the upgrading of KA oil via hydrogen-borrowing condensation (HBC) catalysed by palladium on carbon (Pd/C) has emerged as a promising approach. This redox-neutral mechanism features internal hydrogen transfer steps, thereby eliminating the need for external hydrogen gas and aligning with Principle 6 (Energy Efficiency) and Principle 2 (Atom Economy).[129,130] During the process, the alcohol component of KA oil undergoes dehydrogenation to form a carbonyl. This is followed by C–C bond formation through aldol-type condensation, after which the compound is rehydrogenated using the "borrowed" hydrogen, yielding only water as a by-product.[130,131] This method effectively minimises waste and eliminates the need for additional oxidants or reductants, adhering to Principle 1 and Principle 8 (Reduce Derivatives). The reaction occurs under mild conditions, around 130 °C, and is solvent-free, using liquid reactants that enhance safety and reduce the need for auxiliary inputs, aligning with Principle 5 (Safer Solvents and Auxiliaries). Additionally, incorporating biomass-derived alcohols like ethanol, *n*-butanol, and furfuryl alcohol as co-reactants promotes the use of renewable feedstocks, supporting Principle 7.[131] Catalytic performance can be adjusted through ligand engineering on the Pd surface, particularly using electron-rich phosphines, which influence dehydrogenation rates and product distribution. This adaptability aligns with Principle 9 (Catalysis), favouring catalytic methods for better selectivity and efficiency.[132] The ability to control the product profiles, including linear, branched, or cyclic hydrocarbons, ensures compliance with Jet A-1 fuel specifications.

In practical terms, the Pd/C catalyst system is recyclable and maintains its activity over multiple reaction cycles, improving both catalyst life and process economics.[133] Furthermore, gram-scale demonstrations confirm the process's

scalability and reproducibility in industrial settings. The industrial implications are considerable. Repurposing KA oil, an already abundant feedstock, provides nylon producers and chemical manufacturers with a new opportunity to enter the SAF market. This strategy can diversify revenue streams and enhance asset flexibility. Additionally, since KA oil can be sourced from bio-based benzene or through biochemical pathways to produce adipic acid, transitioning to SAF via this route could ultimately facilitate net-zero carbon fuel cycles.[134] Moreover, the process necessitates minimal adjustments to the current infrastructure. The compatibility of KA oil upgrading with existing refining and distribution systems allows for swift integration, low capital investment, and modular implementation. This makes it particularly attractive for regions that have well-established petrochemical operations but limited renewable fuel infrastructure.[133]

1.1.3.4. Converging Catalytic Innovations for a Low-Carbon Petrochemical Future

The catalytic systems discussed in Sections 1.1.3.1 to 1.1.3.3 (see Figure 1-4) represent a unified strategic approach to modernising petrochemical manufacturing. Though each process addresses a distinct sector within the chemical value chain, they converge in both purpose and design: to enable high-performance chemical transformations with reduced environmental impact. Central to this integration is the deliberate use of noble metals, such as Pd, Ru and Au, which collectively offer tunable reactivity, high selectivity, and thermal resilience under industrial conditions.[129] A defining feature across these systems is their sophisticated handling of hydrogen dynamics. In acetylene hydrogenation, hydrogen is selectively activated to remove trace impurities

without degrading valuable ethylene. In the conversion of KA oil to jet fuel, hydrogen is internally cycled in a redox-neutral environment to drive C–C bond formation, eliminating the need for external hydrogen. In olefin aromatisation, controlled dehydrogenation is employed to generate aromatic hydrocarbons, with hydrogen emerging as a useful co-product. These differing roles, activation, borrowing, and release, demonstrate the catalytic precision required to manage hydrogen pathways effectively across diverse chemical environments.

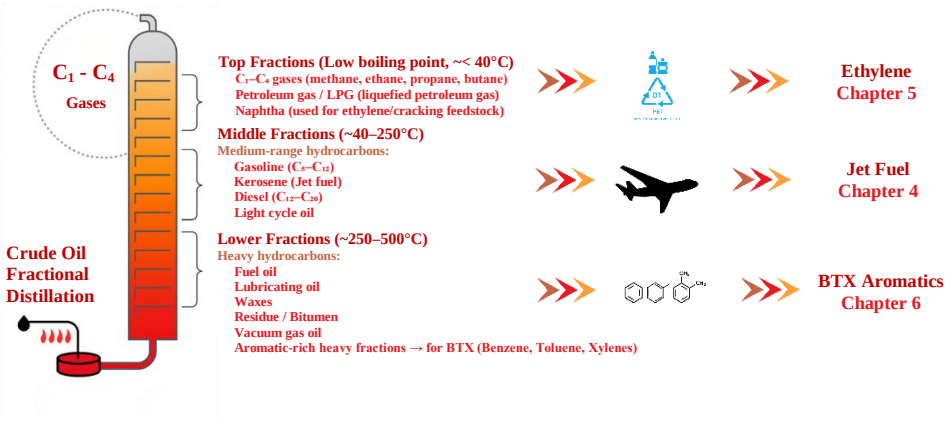

Figure 1-4 Conversion of Naphtha into Jet Fuel Precursors, Ethylene, Acetylene, and BTX

Beyond the intricacies of reaction mechanisms, each of these catalytic platforms presents a reimagined valuation of intermediate feedstocks. KA oil, traditionally limited to nylon production, is now being redefined as a renewable precursor for SAF. Acetylene, previously considered a contaminant, is recognised as a valuable component that can be chemically upgraded to yield polymer-grade ethylene. Long-chain α-olefins, often viewed as low-value byproducts from refinery

processes or synthetic gas conversions, are emerging as promising starting materials for BTX aromatic production, thereby eliminating the necessity for high-temperature naphtha reforming. Collectively, these transformations redefine the hierarchy of feedstocks and underscore the vital role of catalysis in converting underutilised streams into strategic assets.

It is crucial to consider the compatibility of these processes with existing infrastructure. Each system has been designed with modularity in mind, facilitating seamless integration into current facilities with minimal disruption. Pd–Au catalysts can be effectively employed in existing hydrogenation reactors, while Pd/C systems for KA oil upgrading align well with downstream refinery units.[129,135] Furthermore, Ru-based aromatisation modules can be retrofitted into or operated alongside reformers. This design approach minimises capital investment and accelerates commercial adoption, an essential advantage in an industry marked by tight margins and stringent environmental regulations. The industrial synergy of these catalytic technologies becomes even more compelling when viewed in light of global market trends. Ethylene, BTX aromatics, and aviation fuels serve as the backbone of major sectors such as packaging, transportation, textiles, and construction. Recent forecasts suggest that the SAF market is projected to reach USD 131 billion by 2040, driven by decarbonization mandates within the aviation sector. Additionally, the polyethylene market is anticipated to exceed USD 267 billion by 2032, with polymer-grade ethylene purification playing a vital role. Simultaneously, BTX derivatives, which are essential for PET and styrenics, are expected to surpass USD 534 billion by 2034.[136–138] These projections underscore the economic necessity of scaling up catalytic systems that can meet the growing demand while keeping environmental costs in check. From a market perspective, these catalytic solutions are in

alignment with significant growth sectors. These figures reflect not only the economic importance of these products but also the scale at which clean technologies must operate. Table 1-2 illustrates the global demand projections anticipated by the year 2040:

Table 1-2 Projected Market Value and Demand for Key Catalytic Processes in Sustainable Petrochemical Production

Catalytic Process	Market Size (USD B)	Annual Demand (MT)	Key Products	Year
KA Oil to Jet Fuel	131	400-500	Sustainable Aviation Fuel	2040
Ethylene Purification (Pd–Au)	267	>150	Polyethylene	2032
BTX from Olefins (Ru-Catalysed)	534	~150-200	PET, Styrene, High-Octane Fuel Components	2034

In addition to their market relevance, these systems undergo thorough lifecycle assessments (LCA) and techno-economic evaluations to validate their effectiveness. When compared to traditional methods, they offer enhanced environmental and economic performance. For instance, hydrogen-borrowing with Pd/C and related systems has been recognised as a powerful approaches that avoid the direct use of molecular hydrogen, improves atom economy, and minimises waste, offering significant synthetic, economic, and environmental advantages over classical methods.[129] The borrowing hydrogen (BH) principle is

highlighted for its ability to combine dehydrogenation, intermediate reaction, and hydrogenation steps, often with water as the only by-product, thus reducing greenhouse gas emissions and improving process efficiency.[129,139] Furthermore, transition metal-catalysed hydrogen-borrowing systems, including those involving Pd and Ru, are praised for their high selectivity, catalyst stability, and adaptability to both fossil-based and renewable feedstocks, supporting circular carbon strategies and supply chain resilience. The use of earth-abundant and noble metal catalysts in these processes is discussed in the context of both economic and environmental performance, with recent reviews emphasising their role in sustainable chemical synthesis and the potential for broad application across diverse intermediates and feedstocks.[139,140]

The strategic advantage of these systems extends beyond immediate efficiency gains; they also offer long-term resilience through feedstock flexibility. Each platform is capable of processing both fossil-based intermediates and renewable alternatives, such as lignin-derived aromatics, ethanol-based ethylene, and bio-based α-olefins. This compatibility with circular carbon sources encourages diversification and ensures that chemical supply chains are better positioned to withstand raw material volatility and regulatory changes.[141]

Recent advancements in catalyst design are significantly enhancing their capabilities. Innovations like single-atom catalysts, regenerable supports, and intelligent reactor controls are expected to boost scalability and performance.[142,143] This evolution positions noble metal catalysis as a key component of the future of sustainable chemical manufacturing. Moreover, noble metal-based catalysis has transformed into a vital force for industrial change, moving beyond simply refining reactions. Each catalytic system now acts as both a chemical solution and a modular tool that aligns production with sustainability

objectives. By optimising waste streams, improving process selectivity, and promoting the use of renewable resources, these catalytic strategies are leading the charge toward a future characterised by low carbon emissions and high efficiency in petrochemical manufacturing.[144]

Taken together, the convergence of these systems marks a significant shift in petrochemical strategy. The traditional model of centralised, high-temperature processing reliant on fossil fuels is being replaced by a modular, adaptive, and catalyst-driven framework. In this new paradigm, catalytic innovation is not just an enhancement; it acts as a unifying force that promotes decarbonization, operational flexibility, and economic resilience. As industry stakeholders grapple with increasing climate obligations, heightened market competition, and the demand for more sustainable products, the advantages of noble metal catalysis become increasingly apparent. Its adoption will be essential for shaping a petrochemical sector that remains globally competitive while advancing towards carbon neutrality, feedstock circularity, and sustainable growth.

1.2. References

1. Tian C, Liang Y, Lin Q, You D, Liu Z. Environmental pressure exerted by the petrochemical industry and urban environmental resilience: Evidence from Chinese petrochemical port cities. *J Clean Prod*. 2024;471(July):143430. doi:10.1016/j.jclepro.2024.143430

2. Rovira J, Nadal M, Schuhmacher M, Domingo JL. Environmental impact and human health risks of air pollutants near a large chemical/petrochemical complex: Case study in Tarragona, Spain. *Sci Total Environ*. 2021;787:147550. doi:10.1016/j.scitotenv.2021.147550

3. Bauer F;, Kulionis V;, Oberschelp C;, et al. Petrochemicals and Climate Change: Tracing Globally Growing Emissions and Key Blind Spots in a Fossil-Based Industry. *IMES/EESS Rep*. 2022;126. https://lucris.lub.lu.se/ws/portalfiles/portal/117494791/Petrochemicals_climate_change_review_web.pdf

4. EEA. Total greenhouse gas emissions in the chemical industry (Indicator) | European zero pollution dashboards. *Eur Environ Agency*. Published online 2024. https://www.eea.europa.eu/en/european-zero-pollution-dashboards/indicators/total-greenhouse-gas-emissions-in-the-chemical-industry?activeTab=570bee2d-1316-48cf-adde-4b640f92119b

5. World Resources Institute. *Choice Rev Online*. 2010;48(04):48-2101-48-2101. doi:10.5860/choice.48-2101

6. Ahsan M, Tian L, Du R, Alhussan AA, El-kenawy ESM. Enhancing environmental sustainability through code-driven process integration in the petrochemical industry. *Front Environ Sci*. 2024;12(December):1-10. doi:10.3389/fenvs.2024.1389639

7. BASF's Commitment to Sustainability_ Reducing Hydrochloric Acid Disposal –

PEP Mobile.

8. Dow announces targets to conserve water and nature.

9. SABIC - Climate, Energy & Resource Efficiency.

10. Climate Action _ LyondellBasell.

11. Climate _ Shell Global.

12. Johnson A, Fraser A, Elliott N, Hart R. Decarbonize and Defossilize : Transformative Policies to Reduce Chemical Industry Carbon Emissions Acknowledgments. 2024;(April).

13. Abed Yaha AD, Md. Said MA, Lakshmi Devi GS, Azamathulla HM. Assessing the impacts of petrochemical industrial facilities on groundwater in Zubair district. *Water Supply*. 2022;22(10):7713-7731. doi:10.2166/ws.2022.328

14. Jindamanee K, Keawboonchu J, Pinthong N, Meeyai A, Inchai P, Thepanondh S. Environmental impacts and emission profiles of volatile organic compounds from petroleum refineries. *Sci Rep*. 2025;15(1):1-10. doi:10.1038/s41598-025-99932-7

15. Chia-Wei Hsu IS| C. Understanding the power of catalysis. *Am Chem Soc*. Published online 2023. https://www.cas.org/resources/cas-insights/sustainability/understanding-power-catalysis

16. Ertl G, Knozinger H, Weitkamp J. General Principles , Methods and Reaction Engineering. *Handb Heterog Catal*. Published online 1997:1-48.

17. Singh M. Catalysis : Accelerating Chemical Reactions for a Sustainable Future. *Adv Mater Sci*. 2023;6(3):54-56. doi:10.37532/aaasmr.2023.6(3).54-56

18. Kate A, Sahu LK, Pandey J, Mishra M, Sharma PK. Green catalysis for chemical transformation: The need for the sustainable development. *Curr Res Green*

Sustain Chem. 2022;5(December 2021):100248. doi:10.1016/j.crgsc.2021.100248

19. Wu Y. View of Development and Application of Green Catalysts_ Challenges, Optimization, and Future Perspectives.pdf. Published online 2024:308-314. doi:https://doi.org/10.54097/3mn50856

20. Devadasa K LN. View of GREEN CATALYSIS_ INNOVATIONS AND APPLICATIONS IN SUSTAINABLE CHEMISTRY.pdf. :651–658. doi:https://doi.org/10.29121/shodhkosh.v3.i2.2022.2486

21. Anastas PT, Warner JC. *Green Chemistry: Theory and Practice*. Oxford University Press; 1998. https://books.google.es/books?id=SrO8QgAACAAJ

22. Kaur A, Goyal A, Kumari S, et al. Green chemistry and catalysis: An emerging sustainable approach in synthetic chemistry. *BIO Web Conf*. 2024;86. doi:10.1051/bioconf/20248601027

23. Cannon A, Edwards S, Jacobs M, Moir JW, Roy MA, Tickner JA. An actionable definition and criteria for "sustainable chemistry" based on literature review and a global multisectoral stakeholder working group. *RSC Sustain*. 2023;1(8):2092-2106. doi:10.1039/d3su00217a

24. Clark JH, Farmer TJ, Herrero-Davila L, Sherwood J. Circular economy design considerations for research and process development in the chemical sciences. *Green Chem*. 2016;18(14):3914-3934. doi:10.1039/c6gc00501b

25. Mahaffy PG, Matlin SA, Whalen JM, Holme TA. Integrating the Molecular Basis of Sustainability into General Chemistry through Systems Thinking. *J Chem Educ*. 2019;96(12):2730-2741. doi:10.1021/acs.jchemed.9b00390

26. Constable DJC. Green and sustainable chemistry – The case for a systems-based, interdisciplinary approach. *iScience*. 2021;24(12):103489. doi:10.1016/j.isci.2021.103489

27. Guarieiro LLN, Rezende MJC, Barbosa WT, et al. Reaching Circular Economy through Circular Chemistry: The Basis for Sustainable Development. *J Braz Chem Soc*. 2022;33(12):1353-1374. doi:10.21577/0103-5053.20220119

28. Anastas P, Eghbali N. Green Chemistry: Principles and Practice. *Chem Soc Rev*. 2010;39(1):301-312. doi:10.1039/b918763b

29. Sanchez DP, Collina L, Voswinkel F. Chemicals - IEA. *Int Energy Agency*. Published online 2023. https://www.iea.org/energy-system/industry/chemicals

30. Anastas P, Nolasco M, Kerton F, et al. The Power of the United Nations Sustainable Development Goals in Sustainable Chemistry and Engineering Research. *ACS Sustain Chem Eng*. 2021;9(24):8015-8017. doi:10.1021/acssuschemeng.1c03762

31. Roduner E. Understanding catalysis. *Chem Soc Rev*. 2014;43(24):8226-8239. doi:10.1039/c4cs00210e

32. Ertl G. Wilhelm ostwald: Founder of physical chemistry and nobel laureate 1909. *Angew Chemie - Int Ed*. 2009;48(36):6600-6606. doi:10.1002/anie.200901193

33. Matthias Beller, Albert Renken and R van S. Catalysis in perspective : historic review. *Wiley-VCH Verlag GmbH Co KGaA*. Published online 2012:1-17.

34. García-Serna J, Piñero-Hernanz R, Durán-Martín D. Inspirational perspectives and principles on the use of catalysts to create sustainability. *Catal Today*. 2022;387(September 2021):237-243. doi:10.1016/j.cattod.2021.11.021

35. Van Leeuwen PWNM. Introduction. In Homogeneous Catalysis. *Springer*. Published online 2004:1-28.

36. Kakaei K, Esrafili MD, Ehsani A. Introduction to Catalysis. *Interface Sci Technol*. 2019;27:1-21. doi:10.1016/B978-0-12-814523-4.00001-0

37. Ward TR, Copéret C. Introduction: Bridging the Gaps: Learning from Catalysis

across Boundaries. *Chem Rev*. 2023;123(9):5221-5224. doi:10.1021/acs.chemrev.3c00029

38. Parangi T. Heterogeneous catalysis: an alternative approach for energy and environment. *Rev Inorg Chem*. Published online 2025:1-31. doi:10.1515/revic-2024-0047

39. Fadhel AZ, Pollet P, Liotta CL, Eckert CA. Combining the benefits of homogeneous and heterogeneous catalysis with tunable solvents and nearcritical water. *Molecules*. 2010;15(11):8400-8424. doi:10.3390/molecules15118400

40. Unnikrishnan P, Srinivas D. *Heterogeneous Catalysis*. Elsevier Inc.; 2016. doi:10.1016/B978-0-12-801457-8.00003-3

41. Oliver-Meseguer J, Leyva-Pérez A. Single Atom and Metal Cluster Catalysts in Organic Reactions: From the Solvent to the Solid. *ChemCatChem*. 2023;15(10). doi:10.1002/cctc.202201681

42. Heveling J. Heterogeneous Catalytic Chemistry by Example of Industrial Applications. *J Chem Educ*. 2012;89(12):1530-1536.

43. Ma Z, Zaera F. Heterogeneous Catalysis by Metals. *Encycl Inorg Chem*. Published online 2005:1-17. doi:10.1002/0470862106.ia084

44. Hagen J, Santen V. *Catalysis: From Principles to Applications*. Vol 2012.; 2012. doi:10.1016/s1351-4180(12)70467-1

45. Kaewmeesri R, Itthibenchapong V. Advances in nanocatalysts for aviation biofuels. *Handb Nanotechnol Appl*. Published online 2021. doi:10.1016/B978-0-12-821506-7.00011-9

46. Sakata Y, Tamaura Y, Imamura H, Watanabe M. *Preparation of a New Type of CaSiO 3 with High Surface Area and Property as a Catalyst Support*. Vol 162. Elsevier Masson SAS; 2006. doi:10.1016/S0167-2991(06)80924-9

47. Bagheri S, Julkapli NM, Bee S, Hamid A. Titanium Dioxide as a Catalyst Support in Heterogeneous Catalysis. *ScientificWorldJournal*. 2014;2014:727496. doi:10.1155/2014/727496

48. Bahuguna A, Kumar A, Krishnan V. Carbon-Support-Based Heterogeneous Nanocatalysts : Synthesis and Applications in Organic Reactions. Published online 2019:1263-1305. doi:10.1002/ajoc.201900259

49. Valorization B, Production F, Lazzarini A, Colaiezzi R, Gabriele F, Crucianelli M. Support – Activity Relationship in Heterogeneous Catalysis for. *Materials (Basel)*. 2021;14.

50. Bitter JH. Dark material with a bright future : Carbon as support in future heterogeneous catalysis – A short personal perspective. *Catal Today*. 2023;423(February):114015. doi:10.1016/j.cattod.2023.01.022

51. Iwanow M, Gärtner T, Sieber V, König B. Activated carbon as catalyst support : precursors , preparation , modification and characterization. *Beilstein J Org Chem*. Published online 2020:1188-1202. doi:10.3762/bjoc.16.104

52. Ma W, Kugler EL, Dadyburjor DB, Engineering C, Virginia W, Virginia W. Effect of Properties of Various Activated-Carbon Supports and Supported Fe - Mo - Cu - K Catalysts on Metal Precursor Distribution , Metal Reduction , and Fischer - Tropsch Synthesis. *Energy Fuels*. 2010;(5):4099-4110. doi:10.1021/ef1003107

53. Auer E, Freund A, Pietsch J, Tacke T. Carbons as supports for industrial precious metal catalysts. *Appl Catal A Gen*. 1998;173.

54. Weitkamp J. Zeolites and catalysis. *Solid State Ionics*. 2000;131:175-188.

55. Corma A. From Microporous to Mesoporous Molecular Sieve Materials and Their Use in Catalysis. *Chem Rev*. 1997;97(6):2373-2419.

56. Sun Q, Wang N, Yu J. Advances in Catalytic Applications of Zeolite-Supported Metal Catalysts. *Adv Mater*. 2021;2104442:1-37. doi:10.1002/adma.202104442

57. Zhang H, Jaenicke S, Samsudin I. Zeolites in catalysis: sustainable synthesis and its impact on properties and applications. *Catal Sci Technol*. 2022;12:6024-6039. doi:10.1039/d2cy01325h

58. Li J, Sculley J, Zhou H. Metal-Organic Frameworks for Separations. *Chem Rev*. 2012;2:869-932.

59. Yan B. *Metal-Organic Frameworks (MOFs), Rare Earth MOFs , and Rare Earth Functionalized MOF Hybrid Materials*.; 2022. doi:10.1016/B978-0-323-91236-5.00003-7

60. Cavka JH, Jakobsen S, Olsbye U, et al. A New Zirconium Inorganic Building Brick Forming Metal Organic Frameworks with Exceptional Stability. *J Am Chem Soc*. 2008;6:13850-13851.

61. Marsh H, Rodríguez-Reinoso Fr. *Activated Carbon*.; 2006. doi:https://doi.org/10.1016/B978-0-08-044463-5.X5013-4

62. Alvarez-Puebla RA, Ameta RK, Anandan S, et al. *Metal-Organic Frameworks for Chemical Reactions From Organic Transformations to Energy Applications*.; 2021. doi:https://doi.org/10.1016/C2019-0-04610-9

63. Bavykina A, Kolobov N, Khan IS, Bau JA, Ramirez A, Gascon J. Metal − Organic Frameworks in Heterogeneous Catalysis : Recent Progress , New Trends , and Future Perspectives. Published online 2020. doi:10.1021/acs.chemrev.9b00685

64. Alhumaimess MS. Metal – organic frameworks and their catalytic applications. *J Saudi Chem Soc*. 2020;24(6):461-473. doi:10.1016/j.jscs.2020.04.002

65. Haruna A, Uba Z, Tanimu G, Izuagie T. Journal of Environmental Chemical

Engineering A critical review on recent trends in metal-organic framework-based composites as sustainable catalysts for environmental applications. 2024;12(July).

66. Sadakiyo M. Nanoscale Support e ff ects of metal – organic frameworks in. *Nanoscale*. Published online 2022:3398-3406. doi:10.1039/d1nr07659k

67. Pascanu V, González Miera G, Inge AK, Martín-Matute B. Metal-Organic Frameworks as Catalysts for Organic Synthesis: A Critical Perspective. *J Am Chem Soc*. 2019;141(18):7223-7234. doi:10.1021/jacs.9b00733

68. Ballesteros-Soberanas J, Martín N, Bacic M, et al. A MOF-supported Pd1–Au1 dimer catalyses the semihydrogenation reaction of acetylene in ethylene with a nearly barrierless activation energy. *Nat Catal*. 2024;7(4):452-463. doi:10.1038/s41929-024-01130-7

69. Burton PD, Boyle TJ, Datye AK. Facile, surfactant-free synthesis of Pd nanoparticles for heterogeneous catalysts. *J Catal*. 2011;280(2):145-149. doi:10.1016/j.jcat.2011.03.022

70. Aznam I, Muchtar A, Somalu MR, Baharuddin NA, Rosli NAH. Advanced materials for heterogeneous catalysis: A comprehensive review of spinel materials for direct internal reforming of methane in solid oxide fuel cell. *Chem Eng J*. 2023;471(April):144751. doi:10.1016/j.cej.2023.144751

71. Xiong X, Yu J, Huang X, et al. Slightly ruthenium doping enables better alloy nanoparticle exsolution of perovskite anode for high-performance direct-ammonia solid oxide fuel cells. *J Mater Sci Technol*. 2022;125:51-58. doi:10.1016/j.jmst.2022.02.031

72. Zhang L, Liu N, Dai C, et al. Recent advances in shape selectivity of MFI zeolite and its effect on the catalytic performance. *Chem Synth*. 2023;3(1):1-26. doi:10.20517/cs.2022.31

73. Liu M, Miao C, Wu Z. Recent advances in the synthesis, characterization, and catalytic consequence of metal species confined within zeolite for hydrogen-related reactions. *Ind Chem Mater*. 2024;2(1):57-84. doi:10.1039/d3im00074e

74. Liu H, Li J, Liang X, et al. Encapsulation of Pd Single-Atom Sites in Zeolite for Highly Efficient Semihydrogenation of Alkynes. *J Am Chem Soc*. 2024;146(34):24033-24041. doi:10.1021/jacs.4c07674

75. Goel S, Zones SI, Iglesia E. Encapsulation of metal clusters within MFI via interzeolite transformations and direct hydrothermal syntheses and catalytic consequences of their confinement. *J Am Chem Soc*. 2014;136(43):15280-15290. doi:10.1021/ja507956m

76. Zaera F. Designing Sites in Heterogeneous Catalysis: Are We Reaching Selectivities Competitive With Those of Homogeneous Catalysts? *Chem Rev*. 2022;122(9):8594-8757. doi:10.1021/ACS.CHEMREV.1C00905

77. Ping K, Bhadoria R, Starkov P, Kongi N. M–N–C materials as heterogeneous catalysts for organic transformations. *Coord Chem Rev*. 2023;497(August):215412. doi:10.1016/j.ccr.2023.215412

78. Babu, Talal Khaled Al Shamari MS. CN114207092A - Naphtha Catalytic Cracking Process - Google Patents.

79. Karaba A, Dvořáková V, Patera J, Zámostný P. Improving the steam-cracking efficiency of naphtha feedstocks by mixed/separate processing. *J Anal Appl Pyrolysis*. 2020;146(September 2019):104768. doi:10.1016/j.jaap.2019.104768

80. Bhirud VL. WO2006063201A1 - Steam cracking with naphtha dearomatization - Google Patents.

81. ZIMMERMANN H, WALZL R. *Ethylene*. Vol 13.; 2000. doi:10.1016/B978-0-12-824315-2.00101-9

82. Muñoz I, Weidema BP. Ethylene and propylene production from steam cracking in Europe: a consequential perspective. *Int J Life Cycle Assess*. 2024;29(4):745-758. doi:10.1007/s11367-024-02282-1

83. Shin W, Lin B, Lai H, Ibrahim G, Zang G. Decarbonization approaches for ethylene production: Comparative techno-economic and life-cycle analysis. *Green Chem*. 2025;27(April). doi:10.1039/d4gc04538f

84. Tiggeloven JL, Faaij APC, Kramer GJ, Gazzani M. Optimization of Electric Ethylene Production: Exploring the Role of Cracker Flexibility, Batteries, and Renewable Energy Integration. *Ind Eng Chem Res*. 2023;62(40):16360-16382. doi:10.1021/acs.iecr.3c02226

85. Haribal VP, Chen Y, Neal L, Li F. Intensification of Ethylene Production from Naphtha via a Redox Oxy-Cracking Scheme: Process Simulations and Analysis. *Engineering*. 2018;4(5):714-721. doi:10.1016/j.eng.2018.08.001

86. Ren T, Patel M, Blok K. Olefins from conventional and heavy feedstocks: Energy use in steam cracking and alternative processes. *Energy*. 2006;31(4):425-451. doi:10.1016/j.energy.2005.04.001

87. Gary JH, Handwerk GE, Kaiser MJ. Petroleum Refining: Technology and Economics, Fifth Edition. Published online 2007:488. https://books.google.com/books?hl=en&lr=&id=ocbLBQAAQBAJ&pgis=1

88. Xie K, Xu K, Liu M, Song X, Xu S, Si H. Catalysts for selective hydrogenation of acetylene: A review. *Mater Today Catal*. 2023;3(August):100029. doi:10.1016/j.mtcata.2023.100029

89. Zhao X, Chang Y, Chen WJ, et al. Recent Progress in Pd-Based Nanocatalysts for Selective Hydrogenation. *ACS Omega*. 2022;7(1):17-31. doi:10.1021/acsomega.1c06244

90. McCue AJ, Anderson JA. Recent advances in selective acetylene hydrogenation

using palladium containing catalysts. *Front Chem Sci Eng*. 2015;9(2):142-153. doi:10.1007/s11705-015-1516-4

91. Chai S, Gao D, Xia J, Yang Y, Wang X. Facile Synthesis of Palladium-Silver Dilute Alloy Catalyst for Acetylene Hydrogenation. *ChemCatChem*. 2023;15(6):1-10. doi:10.1002/cctc.202300217

92. Ball MR, Rivera-Dones KR, Gilcher EB, et al. AgPd and CuPd Catalysts for Selective Hydrogenation of Acetylene. *ACS Catal*. 2020;10(15):8567-8581. doi:10.1021/acscatal.0c01536

93. Kang L, Cheng B, Zhu M. Pd/MCM-41 catalyst for acetylene hydrogenation to ethylene. *R Soc Open Sci*. 2019;6(11). doi:10.1098/rsos.191155

94. Yurpalova D V., Afonasenko TN, Prosvirin IP, et al. Design of efficient supported Pd-Co catalysts for selective hydrogenation of acetylene. *J Catal*. 2024;432(January):115417. doi:10.1016/j.jcat.2024.115417

95. Zhang W, Uwakwe K, Hu J, et al. Ambient-condition acetylene hydrogenation to ethylene over WS2-confined atomic Pd sites. *Nat Commun*. 2024;15(1):9457. doi:10.1038/s41467-024-53481-1

96. Hosseinzadeh A, Soleimani M, Ravanchi MT. Cost-optimized design of front-end acetylene hydrogenation using artificial neural networks. *Chem Eng Res Des*. 2025;218(September 2024):147-156. doi:10.1016/j.cherd.2025.04.018

97. Sohns D. Consider It To He of General Intmrt To Retiiew. 1980;5.

98. Aeowjaroenlap H, Chotiwiriyakun K, Tiensai N, Tanthapanichakoon W, Spatenka S, Cano A. Model-Based Optimization of an Acetylene Hydrogenation Reactor to Improve Overall Ethylene Plant Economics. *Ind Eng Chem Res*. 2018;57(30):9943-9951. doi:10.1021/acs.iecr.7b05234

99. Yan Z, Xu L, Zhu H. Advances in Electrocatalytic Semi-Hydrogenation of

Acetylene in Aqueous Electrolyte: Progress, Challenges, and Opportunities. *Renewables*. Published online 2023:1-16. doi:10.31635/rnwb.023.202300027

100. C4 Acetylene Hydrogenation Catalysts Market Report _ Global Forecast From 2025 To 2033.

101. Wegelin S, Meier MAR. Bio-based aromatics for chemicals and materials: Advances in renewable drop-in and functional alternatives. *Curr Opin Green Sustain Chem*. 2024;47:100931. doi:10.1016/j.cogsc.2024.100931

102. Straights Research. Benzene-Toluene-Xylene (BTX) Market Report, Manufacturers And Forecast to 2031. Published online 2024. https://straitsresearch.com/report/benzene-toluene-xylene-market

103. Zuiderveen EAR, Caldeira C, Vries T, et al. Evaluating the Environmental Sustainability of Alternative Ways to Produce Benzene, Toluene, and Xylene. *ACS Sustain Chem Eng*. 2024;12(13):5092-5104. doi:10.1021/acssuschemeng.3c06996

104. Zhou T, Baars F. Catalytic reforming options and practices. *Pet Technol Q*. 2010;15(3):21-25.

105. Aromatics BTX Production Cost Analysis, Price Trends 2025 Edition.

106. Brand, Hans Dr. Lansink-Rotgerink RD. EP0601399A1 - Catalytic reforming of naphtha with high yields of BTX-aromatics - Google Patents.

107. Li T, Shoinkhorova T, Gascon J, Ruiz-Martinez J. Aromatics Production via Methanol-Mediated Transformation Routes. *ACS Catal*. 2021;11(13):7780-7819. doi:10.1021/acscatal.1c01422

108. Singh O, Joshi B, Tiwari R, et al. Production of renewable aromatics from tree-borne oils (TBO): Advances and future prospects. *Chem Eng J*. 2025;505(July 2024):159387. doi:10.1016/j.cej.2025.159387

109. Bagnato G, Horgan J, Sanna A. Techno-economic assessment of two-stage hydropyrolysis of lignin for BTX production using iron-based catalysts. *RSC Sustain*. Published online 2025:1448-1460. doi:10.1039/d4su00652f

110. Kulikov L, Dubiniak A, Makeeva D, Egazar'yants S, Maximov A, Karakhanov E. Ruthenium catalysts based on porous aromatic frameworks synthesized by modified impregnation methods for hydrogenation of levulinic acid and its esters. *Mater Today Sustain*. 2024;25(October 2023):100637. doi:10.1016/j.mtsust.2023.100637

111. Akram M, Bhutto SUA, Aftab S, Wang F, Xu X, Xia M. Ruthenium based with carbon supported catalysts for the catalytic transfer hydrogenation of furfural: A review. *Nano Energy*. 2023;117(August):108808. doi:10.1016/j.nanoen.2023.108808

112. Hafeez J, Bilal M, Rasool N, et al. Synthesis of ruthenium complexes and their catalytic applications: A review. *Arab J Chem*. 2022;15(11):104165. doi:10.1016/j.arabjc.2022.104165

113. Bo S, Xiong Z, Wang Y, Wang H, Zhang LB. Progress on ruthenium catalysts for efficiently promoting Z-selective olefin metathesis. *Tetrahedron*. 2025;179(January):134654. doi:10.1016/j.tet.2025.134654

114. Axet MR, Philippot K. Catalysis with Colloidal Ruthenium Nanoparticles. *Chem Rev*. 2020;120(2):1085-1145. doi:10.1021/acs.chemrev.9b00434

115. Engel J, Smit W, Foscato M, Occhipinti G, Törnroos KW, Jensen VR. Loss and Reformation of Ruthenium Alkylidene: Connecting Olefin Metathesis, Catalyst Deactivation, Regeneration, and Isomerization. *J Am Chem Soc*. 2017;139(46):16609-16619. doi:10.1021/jacs.7b07694

116. Colaiezzi R, Saviozzi C, di Nicola N, et al. Ruthenium(ii) arene complexes bearing simple dioxime ligands: effective catalysts for the one-pot transfer

hydrogenation/N-methylation of nitroarenes with methanol. *Catal Sci Technol*. 2023;13(7):2160-2183. doi:10.1039/d3cy00218g

117. Hou L, Gu X, Cui X, et al. Strategies for the design of ruthenium-based electrocatalysts toward acidic oxygen evolution reaction. *EES Catal*. 2023;1(5):619-644. doi:10.1039/d3ey00092c

118. Luo C, Wu C, Wang X, Han Z, Wang Z, Ding K. Ruthenium-Catalyzed Carbocycle-Selective Hydrogenation of Fused Heteroarenes. *J Am Chem Soc*. Published online 2024. doi:10.1021/jacs.4c05365

119. Luo X, Hou P, Shen J, et al. Ligand-enabled ruthenium-catalyzed meta-C−H alkylation of (hetero)aromatic carboxylic acids. *Nat Commun*. 2024;15(1):1-10. doi:10.1038/s41467-024-49362-2

120. Wu Y, Hollmann F, Musa MM. Oxidation of Cyclohexane to Cyclohexanol/Cyclohexanone Using Sol-Gel-Encapsulated Unspecific Peroxygenase from Agrocybe aegerita. *ChemistryOpen*. 2024;202400152. doi:10.1002/open.202400152

121. Abutaleb A, Ali MA. A comprehensive and updated review of studies on the oxidation of cyclohexane to produce ketone-alcohol (KA) oil. *Rev Chem Eng*. 2022;38(7):769-797. doi:10.1515/revce-2020-0059

122. Milas NA, Surgenor DM. Studies in Organic Peroxides. VIII. t-Butyl Hydroperoxide and Di-t-butyl Peroxide1. *J Am Chem Soc*. 1946;68(2):205-208. doi:10.1021/ja01206a017

123. Xu YJ, Landon P, Enache D, Carley AF, Roberts MW, Hutchings GJ. Selective conversion of cyclohexane to cyclohexanol and cyclohexanone using a gold catalyst under mild conditions. *Catal Letters*. 2005;101(3-4):175-179. doi:10.1007/s10562-005-4886-2

124. Reis Conceição N, Mahmoud AG, Guedes da Silva MFC, Mahmudov KT,

Pombeiro AJL. Catalytic cyclohexane oxidation to KA oil using novel hydrosoluble copper(I) complexes bearing aminophosphine ligands: Water as a selectivity promoter. *Mol Catal*. 2023;549(August). doi:10.1016/j.mcat.2023.113512

125. Vomeri A, Stucchi M, Villa A, Evangelisti C, Beck A, Prati L. New insights for the catalytic oxidation of cyclohexane to K-A oil. *J Energy Chem*. 2022;70:45-51. doi:10.1016/j.jechem.2022.02.008

126. EASA publishes report on the European Union Sustainable Aviation Fuels (SAF) market _ EASA.

127. IATA - Disappointingly Slow Growth in SAF Production.

128. Global sustainable aviation fuel industry.

129. Corma A, Navas J, Sabater MJ. Advances in One-Pot Synthesis through Borrowing Hydrogen Catalysis. *Chem Rev*. 2018;118(4):1410-1459. doi:10.1021/acs.chemrev.7b00340

130. Reed-Berendt BG, Latham DE, Dambatta MB, Morrill LC. Borrowing Hydrogen for Organic Synthesis. *ACS Cent Sci*. 2021;7(4):570-585. doi:10.1021/acscentsci.1c00125

131. Geng S, Yang J, Lugovski AA, Liu W. Borrowing hydrogen alkylation of indenes with alcohols by manganese pincer complex. *J Catal*. 2025;445(February):116011. doi:10.1016/j.jcat.2025.116011

132. Arango-Daza JC, Lluna-Galán C, Izquierdo-Aranda L, Cabrero-Antonino JR, Adam R. Heterogeneous Pd-Catalyzed Efficient Synthesis of Imidazolones via Dehydrogenative Condensation between Ureas and 1,2-Diols. *ACS Catal*. 2022;12:6906-6922. doi:10.1021/acscatal.2c01423

133. Kempasiddaiah M, Sree Raj KA, Kandathil V, et al. Waste biomass-derived

carbon-supported palladium-based catalyst for cross-coupling reactions and energy storage applications. *Appl Surf Sci*. 2021;570(September):151156. doi:10.1016/j.apsusc.2021.151156

134. Pham PTH, Pham CQ, Dam TT, Nguyen QA, Nguyen TM. A comprehensive review of catalyst deactivation and regeneration in heavy oil hydroprocessing. *Fuel Process Technol*. 2025;267(December 2024):108170. doi:10.1016/j.fuproc.2024.108170

135. Capelli S, Barlocco I, Scesa FM, et al. Pd–au bimetallic catalysts for the hydrogenation of muconic acid to bio-adipic acid. *Catalysts*. 2021;11(11). doi:10.3390/catal11111313

136. Benzene Toluene Xylene Btx Market Size, Growth Drivers 2034.

137. Sustainable Aviation Fuel Market Size, Share & Outlook - 2032. https://www.gminsights.com/industry-analysis/sustainable-aviation-fuel-market

138. Polyethylene Market Size to Hit USD 266.

139. Nallagangula M, Subaramanian M, Kumar R, Balaraman E. Transition metal-catalysis in interrupted borrowing hydrogen strategy. *Chem Commun*. 2023;59(51):7847-7862. doi:10.1039/d3cc01517c

140. Koy M, Fellert M, Deng C, et al. Bio-Based Surfactants via Borrowing Hydrogen Catalysis. *Chem - A Eur J*. 2025;202500077:6-11. doi:10.1002/chem.202500077

141. Naranov E. Sustainable Production of Chemicals via Hydrotreating of CO2 and Biomass Derived Molecules Using Heterogeneous Noble Metal Oxide Catalysts. *ChemCatChem*. 2024;16(9):1-15. doi:10.1002/cctc.202301268

142. Xiao Y, Zhang J, Liu T, Xu M, Dong Y, Wang CA. Constructing morphologically stable supported noble metal catalysts in heterogeneous catalysis: Mechanisms and strategies. *Nano Energy*. 2024;129(PA):109975.

doi:10.1016/j.nanoen.2024.109975

143. Qiao B, Wang A, Yang X, et al. Single-atom catalysis of CO oxidation using Pt1/FeOx. *Nat Chem*. 2011;3(8):634-641. doi:10.1038/nchem.1095

144. Chu S, Wang E, Feng F, et al. A Review of Noble Metal Catalysts for Catalytic Removal of VOCs. *Catalysts*. 2022;12(12). doi:10.3390/catal12121543

Chapter 2.

Objectives

2.1. Objectives

The principal objective of this thesis is to investigate, develop, and integrate advanced catalytic technologies that enhance the sustainability, efficiency, and decarbonization of the petrochemical industry. This research is focused on three interrelated catalytic processes that facilitate the conversion of hydrocarbon intermediates obtained from naphtha distillation into high-value chemical products. Specifically, the processes examined include:

1. The transformation of KA oil (a mixture of cyclohexanol and cyclohexanone) into precursors for jet fuel.

2. The selective semihydrogenation of acetylene to purify ethylene for polymer applications.

3. The isomerisation and aromatisation of terminal olefins, such as 1-octene, to yield BTX (benzene, toluene, and xylenes) aromatics.

These processes target different downstream markets, sustainable aviation fuel, polymer feedstocks, and aromatic base chemicals, but they are unified by their reliance on naphtha as a common feedstock and noble metal catalysis.

This thesis adopts an integrated perspective, viewing these catalytic systems as interconnected components within a broader framework of hydrocarbon valorisation. This approach highlights the significance of process continuity, mechanistic synergy, and relevance to industrial applications. To achieve this comprehensive objective, the research is organised around the following specific goals:

Chapter 4: To establish a catalytic pathway for the sustainable production of jet fuel from KA oil

This project focuses on the development and optimisation of a palladium on carbon (Pd/C) catalytic system designed to convert cyclohexanol and cyclohexanone into high-density hydrocarbon fuels. This transformation is achieved through mechanisms such as deoxygenation, hydrogen borrowing, and hydrocarbon coupling. The process is intended to operate under mild conditions, specifically, at low temperatures and atmospheric pressure, to minimise energy consumption and eliminate the need for solvents, adhering to green chemistry principles. A key objective is to produce drop-in jet fuels that are fully compatible with existing aviation infrastructure, all while significantly reducing lifecycle greenhouse gas emissions in comparison to fossil-derived jet fuels.

Chapter 5: To design and evaluate Pd- and Pd-Au-based catalysts for the selective semihydrogenation of acetylene

The aim of this research is to selectively convert acetylene, an undesirable impurity in ethylene streams, into ethylene while avoiding overhydrogenation to ethane. This process is designed to yield polymer-grade ethylene that is suitable for polyethylene manufacturing. The study focuses on catalyst composition, particularly bimetallic Pd–Au systems, and explores the role of support materials such as MOFs and zeolites. These aspects are examined to enhance selectivity, improve catalyst stability, and increase resistance to deactivation. This research addresses a crucial industrial need, as acetylene poisoning can impair the efficiency and economic viability of polymerisation catalysts used in polyethylene production.

Chapter 6: To develop a catalytic process for converting terminal olefins into BTX aromatics using Ru-based catalysts

This research explores a one-pot transformation process that efficiently converts 1-octene and related linear olefins into benzene, toluene, and xylenes through a series of tandem steps, including isomerisation, cyclisation, and dehydrogenation. The study emphasises the use of ruthenium-supported catalysts, investigating how factors such as support acidity, pore architecture, and metal dispersion influence catalytic performance. This method offers a more energy-efficient alternative to traditional catalytic reforming of naphtha for aromatic production and represents a promising strategy for valorising olefin-rich streams derived from steam crackers or bio-based sources.

The three catalytic systems are not merely isolated case studies; they form essential components of a broader, interconnected framework for hydrocarbon valorisation. Each process is derived from the naphtha fraction obtained during crude oil distillation, which enhances feedstock continuity and supports the development of modular catalytic platforms. Moreover, the employment of noble metals, specifically palladium, ruthenium, and their alloys with gold, provides a cohesive mechanistic and functional foundation. By merging the principles of catalysis science with process engineering, this thesis contributes to the vision of a circular petrochemical economy. The systems explored in this research facilitate lower carbon footprints through minimised energy inputs, one-pot processing, and the potential adaptation to bio-derived feedstocks. Additionally, this work underscores the significance of catalyst design, especially through alloying and support tailoring, in unlocking new reactivity pathways and improving operational sustainability across diverse industrial sectors. In

conclusion, the objective of this thesis is to present an integrated catalytic framework that demonstrates how targeted innovations in noble metal catalysis and reactor design can transform petrochemical processes to align with the sustainability imperatives of the 21st century.

Chapter 3.

Methodology

Index

3.1. Materials

Unless otherwise noted, all reagents, solvents, and catalysts were used as received from commercial suppliers without any additional purification. These compounds were primarily sourced from Merck Life Science S.L., TCI Europe N.V., and Fluorochem, with typical purities ranging from 95% to 99%. Consumable laboratory materials necessary for the experimental work were procured from suppliers such as ViciLab, Vidra Foc, Agilent Technologies, and Biotage®. A certified gas cylinder containing a custom blend of 1% acetylene in ethylene was provided by Linde and was used as received. Cylinders of deuterium gas (D_2 2.8, 99.8%) and carbon dioxide (CO_2) were also obtained from Abelló Linde and used without further purification.

Compounds that were not commercially available, including starting materials, intermediates, and catalytic systems, were synthesised following established or modified procedures, as detailed in this chapter. The characterisation of these compounds was conducted using standard analytical techniques, including gas chromatography (GC), gas chromatography-mass spectrometry (GC-MS), nuclear magnetic resonance spectroscopy (NMR), ultraviolet–visible spectroscopy (UV-Vis), and X-ray diffraction (XRD), among others.

3.2. Experimental Techniques

A comprehensive set of experimental and physicochemical techniques was employed to characterise the synthesised materials and analyse their properties and catalytic behaviour. The following subsections describe each technique used in this work, detailing instrumentation, experimental conditions, and application purpose:

a) Elemental analysis (E.A.)

The contents of nitrogen, carbon, and hydrogen (N, C, H) were determined using a CNHS EA3000 elemental analyser (Eurovector), calibrated with sulphanilamide standard from Elemental Microanalysis.

b) Inductively coupled plasma spectrometry (ICP-AES)

This technique was utilised to determine the metal content of solid catalysts following complete dissolution via acid digestion. The catalysts were initially treated with *aqua regia* (a combination of hydrochloric acid and nitric acid in a 3:1 ratio) to dissolve the metals. Next, they underwent treatment with a *Piranha solution* (sulfuric acid mixed with a few drops of hydrogen peroxide at 100 °C) to oxidise and remove any organic components. Hydrofluoric acid (HF) was added, as necessary, to ensure the complete dissolution of any remaining residues. After digestion, solutions were diluted with Milli-Q water, centrifuged, and filtered to remove any carbonaceous residues, particularly for carbon-supported noble metal catalysts. Metal quantification was carried out using either a Varian 715-ES or an iCAP PRO XP inductively coupled plasma atomic emission spectrometer.

c) Thermogravimetric Analysis (TGA)

This technique was employed to study the decomposition and desorption of molecules from solid materials as the temperature increased. Measurements were conducted using a Netzsch STA 449F3 Jupiter apparatus, with a heating rate of 25°C per minute, in either an air or pure nitrogen atmosphere, across a temperature range of 25°C to 800°C.

d) Powder X-ray Diffraction (XRD)

X-ray diffraction (XRD) was employed to determine the atomic periodic structure of the solids. Measurements were carried out using a CubiX PRO diffractometer (PANalytical) equipped with a Cu Kα radiation source (λ = 1.5406 Å) and a PANalytical X'Celerator detector. The samples were analysed at room temperature with continuous rotation at 0.5 revolutions per second to ensure uniform exposure. Data were collected in the 2θ range of 2° to 40°, with a step size of 0.020° and an acquisition time of 35 seconds per step. The irradiated sample area was maintained at 5 mm using a variable divergence slit. Experimental diffractograms were compared against the PDF2 database for phase identification.

Crystallite sizes were calculated using the Scherrer equation (1):

$$\textbf{(1)}\quad \boldsymbol{Dp = \frac{K \times \lambda}{\beta \times Cos\,\theta}}$$

where *Dp*= Average cystalite size, *K*=shape factor (0.94), β= FWHM (Full Width at Half Maximum), θ= Bragg angle, λ= X-ray wavelength.

Lattice parameters were determined according to the crystal system (2-3). For cubic systems (a = b = c):

$$\textbf{(2)}\ \ d_{hkl} = \frac{a}{\sqrt{(h^2+k^2+l^2)}}$$

$$\textit{i.e.:}\ d_{111} = \frac{a}{\sqrt{3}}$$

Tetragonal system (a=b≠c):

$$\textbf{(3)}\ \frac{1}{(d_{hkl})^2} = \frac{h^2+k^2}{a^2} + \frac{l^2}{c^2}$$

$$\textit{i.e.:}\ \frac{1}{(d_{110})^2} = \frac{h^2+k^2}{a^2},\ a = b = \sqrt{(\frac{2}{d_{110}})}$$

$$\textit{ie:}\ \frac{1}{(d_{001})^2} = \frac{l^2}{c^2}\ ,\ c = 2 \times d_{002}$$

These equations were used to calculate lattice constants based on measured interplanar spacings.

e) CO chemisorption by the double isotherm method

The dispersion of noble metals (particularly Pd) in the catalyst was evaluated by CO chemisorption using the double isotherm method on a Quantachrome Autosorb-1C instrument. Catalyst samples were mixed with silica in a 60:40 ratio (sample: SiO_2) and pressed into pellets (0.8–1.1 mm, ~300 mg). Prior to CO adsorption, samples were degassed under vacuum. The first isotherm, representing total CO uptake, was recorded by exposing the sample to pure CO. After evacuation at 25 °C to remove reversibly adsorbed CO, a second isotherm was measured. The amount of irreversibly chemisorbed CO was determined by subtracting the second isotherm from the first.

Metal dispersion (D) was calculated using (4):

$$\textbf{(4)}\ \boldsymbol{D}\ (\%) = \frac{\boldsymbol{N_m \times F_s \times M \times 100}}{\boldsymbol{L}} \times\ \mathbf{100}$$

Where: N_m represents the amount of chemisorbed CO ($mol \cdot g^{-1}$), F_s denotes the stoichiometric factor of CO to dispersed metal, M signifies the molar mass of the metal, and L indicates the metal loading (in % wt).

The average metal particle diameter (d) was determined from (5):

$$\textbf{(5)}\ \boldsymbol{d} = \frac{\boldsymbol{L \times 6}}{\boldsymbol{ASA \times Z \times 100}}$$

where: *ASA* is the active surface area ($m^2 \cdot g^{-1}$), calculated as (6):

$$\textbf{(6)}\ ASA = N_m \times F_s \times A_m \times N_A$$

with A_m being the cross-sectional area per surface atom and N_A being Avogadro's number, Z is the density of dispersed metal ($g \cdot m^{-3}$).

f) X-ray absorption spectroscopy (XAS) – CLAESS (BL-22), ALBA Synchrotron

X-ray Absorption Spectroscopy (XAS) at the Ru K-edge was conducted at the CLAESS (BL-22) beamline of the ALBA Synchrotron Light Facility. Samples were diluted in boron nitride and pelletized to optimise absorption. Despite the relatively low Ru content (<1 wt%), measurements were conducted in transmission mode using a multichannel Si detector, enabled by careful sample dilution and optimization of pellet thickness. Monochromatization was achieved with a Si(311) double-crystal monochromator, cryogenically cooled with liquid nitrogen and equipped with piezo-controlled alignment for high stability. Beam collimation and focusing were performed using a silicon mirror and a toroidal

Rh/Pt-coated mirror, respectively, yielding a tunable beam size down to 8 × 1 μm² (H × V). The ex-situ measurements were conducted under ambient conditions, with temperature-controlled environments available when required. Several scans were collected to ensure reproducibility and signal quality.

Data processing was performed using the Athena software package. Energy calibration was done by aligning the first inflexion point of a Ru foil reference to 22117 eV. Background subtraction and normalisation were carried out using standard procedures, and the EXAFS region was isolated using the AUTOBK algorithm with a spline over the k-range of 0–14 Å¹ and Rbkg = 1.1. Resulting k^3-weighted $\chi(k)$ functions were Fourier transformed to R-space, and coordination environments were analysed by fitting the data to single scattering paths generated by FEFF6 based on crystallographic models. Fit quality was assessed by minimising the R-factor and reduced χ^2 using a systematic variable selection strategy. Data treatment was carried out using Athena, with background subtraction and normalisation performed via the AUTOBK algorithm (k = 0–19 Å¹, Rbkg = 1). Scattering paths were generated with FEFF6, and multi-k-weighted fitting was performed in r-space using Larch. Fit quality was evaluated by minimising the R-factor and reduced χ^2.

g) X-ray Absorption Spectroscopy (XAS) – NOTOS (BL-16), ALBA Synchrotron

XANES and EXAFS measurements at the Pd K-edge (24.350 keV) were performed on Pd–Au metal-organic framework (MOF) samples at the NOTOS beamline of the ALBA Synchrotron Light Source (Barcelona, Spain). Synchrotron radiation from a bending magnet was vertically collimated, monochromatized using liquid-nitrogen-cooled Si(111) crystal pairs, and focused

onto the sample area (~500 × 500 μm²). Optical mirrors coated with a Rh stripe were used for higher harmonic suppression.

Samples were prepared as 13 mm pellets diluted in cellulose and measured in transmission mode using a six-element Silicon Drift Detector (Quantum Detectors) in 45° geometry. A 4 μm-thick Pd foil (Goodfellow, 99.99%) served as an internal standard for energy calibration, alignment of consecutive scans, and determination of the amplitude reduction factor (S_0^2). Multiple scans were recorded in continuous mode to ensure reproducibility and a high signal-to-noise ratio.

The extended X-ray absorption fine structure (EXAFS) region was analysed over the k-range of 3–10 $Å^{-1}$. Theoretical scattering paths were generated using the FEFF6 code and fitted to the experimental spectra by adjusting coordination numbers, interatomic distances, and Debye–Waller factors to extract local structural information around the Pd centres.

h) X-ray photoelectron spectroscopy (XPS)

X-ray Photoelectron Spectroscopy (XPS) was employed to investigate the surface composition and chemical states of the samples, taking advantage of the technique's high surface sensitivity (<10 nm) due to the limited escape depth of photoemitted electrons. XPS measurements were conducted using a SPECS system equipped with a Phoibos 150 MCD-9 multichannel analyser and a non-monochromatic Mg Kα X-ray source (1253.6 eV, 50 W). The spectrometer's binding energy (BE) scale was calibrated using core-level signals from Cu and Ag foils to match standard reference values.

Approximately 10 mg of powdered samples were pressed onto stainless-steel sample holders and analysed at 25 °C under ultra-high vacuum (~10^{-9} mbar).

Spectra were acquired using a pass energy of 30 eV over a 7 × 20 mm² analysis area. Recorded intensities were corrected using the instrument's transmission function. Data analysis was performed using CasaXPS software. Core-level spectra were fitted using Gaussian–Lorentzian line shapes, with a fixed reference for the C 1s peak at 284.8 eV (C–C/C–H from sp^3 carbon). Background subtraction was carried out using either Shirley-type or U 2 Tougaard models. A degree of asymmetry was introduced for the C 1s component corresponding to graphitic carbon.

i) UV-Vis Absorption and Emission Spectroscopy.

UV–Vis diffuse reflectance spectroscopy was employed to probe the oxidation state and dispersion of palladium species supported on various zeolites. Absorption spectra were recorded at room temperature using an Agilent Cary spectrophotometer (models 300 and 60) equipped with a xenon lamp and quartz cuvettes of 1.0 and 0.1 cm optical path length. Fluorescence emission spectra were acquired on an FLS1000 photoluminescence spectrometer using a 1 cm quartz cuvette, in the range of 320–650 nm, with excitation at 300 nm.

j) CO adsorption measured by Fourier transform infrared spectroscopy (CO-FTIR).

CO adsorption on metal-organic materials containing isolated Pd atoms and Pd–Au dimers was investigated using Fourier transform infrared spectroscopy (CO-FTIR). Measurements were conducted at room temperature in a sealed, airtight transmission cell. Prior to CO exposure, the samples were subjected to vacuum treatment (10^{-6} mbar) for 1 hour to remove physisorbed species. CO was then introduced at controlled partial pressures ranging from 0.2 to 150 mbar. IR

spectra were collected after equilibration at each pressure to monitor the interaction between CO molecules and the metal centres.

k) Attenuated Total Reflectance Infrared Spectroscopy (IR-ATR)

Attenuated total reflectance infrared spectroscopy (IR-ATR) was employed to record the IR spectra of reaction solutions using a JASCO FT/IR-4000 spectrometer. Spectra were collected in the 400–4000 cm^{-1} range by depositing a small aliquot of the reaction mixture directly onto the instrument's ATR crystal.

l) Pyridine Fourier-Transform Infrared Spectroscopy (Py-FTIR)

This technique was used to examine how the metal composition of materials consisting of Ru nanoparticles supported on HZSM5 affects the density and characteristics of Lewis acid sites. Furthermore, the study quantified both Brønsted and Lewis acid sites across various zeolites.

To achieve this, the adsorption processes of pyridine on acid species were monitored, as infrared spectroscopy allows differentiation between binding to Brønsted acid sites (pyridinium ion formation with a band at $\lambda = 1550\ cm^{-1}$) and Lewis acid sites (band at $\lambda = 1450\ cm^{-1}$). Using the methodology proposed by Emeis[1] and known extinction coefficients, it was possible to calculate the density of Lewis acid sites (LAS, Equation (7)) and Brønsted acid sites (BAS, Equation (8)):

$$\textbf{(7)}\quad [LAS] = 1.42 \cdot A \cdot r^2 \cdot w^{-1}\ (mmol\ g^{-1})$$

$$\textbf{(8)}\quad [BAS] = 1.88 \cdot A \cdot r^2 \cdot w^{-1}\ (mmol\ g^{-1})$$

In both equations, A represents the integrated area of the FTIR signals associated with pyridine, r is the radius of the self-supported pellet, and w is the mass of the sample.

FTIR experiments were conducted using a Nicolet iS10 Thermo FT-IR spectrophotometer. Self-supported pellets containing the sample were degassed at 300 °C for 12 hours under vacuum. After this period, a pyridine stream (at 650 Pa) was introduced into the cell. Once equilibrium was reached, the system was degassed again at the desired temperature and then cooled to room temperature, at which point the FTIR spectrum was recorded. This procedure was repeated at three different temperatures: 150 °C (for weak acid sites), 250 °C (for medium acid sites), and 350 °C (for strong acid sites). In all instances, the spectrum acquired under vacuum prior to pyridine adsorption was used as the background and was subtracted from each measurement. Finally, the absorbance was normalized with respect to the mass employed in each experiment.

m) Gas Chromatography (GC)

Gas chromatography was employed to determine the yield of most reactions discussed in previous chapters and to monitor the concentrations of reactants and products over time during kinetic studies. An external standard method was used, in which a known amount of an inert standard compound is added to the reaction aliquot prior to analysis. This standard does not react with or interfere with components in the sample. The GC instrument provides peak areas for both the analytes and the standard, from which analyte concentrations are calculated using response factors derived from calibration curves. Depending on the analytes under investigation and to avoid signal overlap, either *n*-decane or *n*-dodecane was selected as the external standard. All analyses were performed using a

Shimadzu GC-2025 gas chromatograph equipped with an HP-5MS capillary column (30 m × 0.25 mm × 0.25 µm) featuring a stationary phase composed of 5% phenyl-methylpolysiloxane.

n) Gas Chromatography–Mass Spectrometry (GC–MS).

GC–MS was used to identify and characterise the products and by-products formed during the various reactions. The technique provides mass fragmentation patterns for each compound in the sample after ionisation, which serve as molecular fingerprints. These patterns were compared against a built-in spectral library for preliminary identification and further verified through manual analysis. The measurements were performed using an Agilent 6890N gas chromatograph equipped with an HP-5MS column (30 m × 0.25 mm × 0.25 µm, 5% phenyl methyl silicone stationary phase), coupled to an Agilent 5973N quadrupole mass spectrometer.

o) Nuclear Magnetic Resonance (NMR) Spectroscopy

Liquid-state NMR spectra for ^{1}H, ^{13}C, and DEPT-135 were recorded at room temperature on a Bruker Ascend 400 MHz spectrometer. Solid-state ^{31}P NMR with magic angle spinning (MAS) was performed on the Pd/C sample containing PPh_3 using a Bruker Ascend 400WB. The ^{31}P measurements used a 4 µs 90° pulse, a 20 s recycle delay, and a spinning speed of 20 kHz. Chemical shifts were referenced to H_3PO_4 at 0 ppm.

p) TEM-STEM

Transmission Electron Microscopy (TEM) uses a focused electron beam transmitted through a thin sample to reveal detailed information about its structure, composition, and crystallography. In this work, TEM combined with

Scanning Transmission Electron Microscopy (STEM), Energy-Dispersive X-ray Spectroscopy (EDS), Electron Energy Loss Spectroscopy (EELS), and electron diffraction was essential for analyzing nanoparticle morphology, size distribution, elemental composition, interplanar spacing, and crystalline phases.

Samples for TEM were prepared by depositing a drop of a sonicated suspension of the sample in dichloromethane onto a carbon-coated lacey copper grid (300 mesh). High-resolution TEM (HR-TEM) images were acquired using a JEOL JEM2100F operated at 200 kV, equipped with an EDS X-Max 80 detector. Particle size distributions were determined by measuring at least 100 nanoparticles and fitting size frequency histograms with Gaussian curves using ImageJ software. Interplanar distances were extracted from HR-TEM images using Gatan Digital Micrograph software and matched to known crystalline phases via the X'Pert HighScore Plus database.

The EDS detector (127 eV resolution) provided qualitative elemental mapping, revealing the spatial distribution of elements. Selected Area Electron Diffraction (SAED) patterns were also recorded to support phase identification, with data processed using Gatan Digital Micrograph software.

r) Advanced STEM techniques

Microscopy analyses were carried out using dark-field scanning transmission electron microscopy with a high-angle annular dark-field detector (HAADF-STEM) on a double aberration-corrected, monochromated FEI Titan3 Themis 60–300 microscope operating at 300 kV. To minimise electron beam damage, a fast imaging protocol with a beam current of 30 pA was employed. Chemical mapping was performed at medium magnifications (approximately 100k to 200k)

using the high-efficiency SuperX G2 system, which integrates four windowless detectors surrounding the sample and advanced signal-processing hardware.

Samples were prepared by suspending solid materials in hexane and depositing them directly onto carbon-coated copper grids. Both high-resolution HAADF-STEM and integrated differential phase contrast STEM (STEM-iDPC) images were acquired. STEM-iDPC provided atomic-resolution images with contrast related to atomic number rather than the approximately Z^2-dependent contrast observed in HAADF-STEM. This technique enabled imaging of lighter elements such as oxygen in the presence of heavier elements like silicon, under very low electron dose conditions, critical for the atomic-scale structural analysis of electron beam-sensitive materials like zeolites.

STEM-XEDS elemental mapping was used to visualise the spatial distribution of elements such as Al, Si, Na, Pd, and Ru. For these nanoanalytical experiments, the beam current was increased to 100 pA and the dwell time to 128 μs to improve the signal-to-noise ratio. Elemental maps were processed by background subtraction and smoothed by averaging over 3×3 pixels.

These microscopy and nanoanalytical techniques were applied to study Pd-, Pd–Au-, and Ru-based catalysts. All measurements were performed at the microscopy facility of the University of Cádiz under the supervision of Dr. Hernández-Garrido.

s) Ex-situ and In-situ HAADF-STEM Characterisation of Ru-H-ZSM-5 at the SUperTEM Facility

High-resolution electron-microscopy studies were performed on a double aberration-corrected JEOL ARM 200 F housed at the SUperTEM facility (Université Paris Cité, France). The microscope was operated at 200 kV in STEM mode with a 25 mrad probe-convergence semi-angle, a HAADF detector collecting 68–280 mrad, an information limit better than 0.10 nm, a probe current of 30 pA, and integrated analytical platforms consisting of a 100 mm^2 silicon-drift EDX detector and a Gatan Quantum dual-EELS spectrometer. Catalyst powders were dry-dispersed on lacey-carbon Cu grids and transferred under Ar to minimise oxidation. Ex situ experiments employed a Protochips Fusion Select heating holder under high vacuum (≈10^{-6} mbar); grids were ramped at 10 °C min^{-1} to 150, 200, 250, 300 and 350°C, held 30 min at each plateau, and imaged after thermal equilibration to quantify Ru migration and particle-size evolution. In situ measurements used Protochips E-chips with 30 nm SiN membranes; on-chip microheaters (temperature accuracy ±1.5 °C) enabled a controlled ramp from 280 °C to 300 °C (5 °C min^{-1}) followed by a five-hour isotherm while flowing 5 vol % 1-heptene in Ar at 1 bar. HAADF-STEM images were captured at 15, 45, 90, 150, 210 and 270 min, keeping the cumulative electron dose below 5×10^4 e nm^{-2} s^{-1} to suppress beam damage; EDX spectra confirmed Ru retention throughout. Image datasets were non-rigid-registered, denoised (BM3D-Anscombe), and quantitatively analysed by watershed segmentation (≥200 particles per condition, diameter uncertainty ±0.15 nm). The combined methodology allowed direct comparison of vacuum-induced restructuring, where Ru began migrating from MFI channels to crystal facets at ≈200 °C yet remained <3 nm at 300 °C, with the near-static dispersion observed

under reactive flow, thereby linking nanoparticle dynamics to the catalyst's long-term stability described in Chapter 6.

t) Competitive absorption of acetylene/ethylene

High-resolution isotherms were measured using a Micromeritics ASAP 2010 volumetric instrument. Approximately 50 mg of Pd_1Au_1@MOF in powder form was used for these experiments. The sample was placed in a glass holder and immersed in a thermostatic bath filled with circulating liquid to ensure precise temperature control. Before the adsorption experiments, the sample underwent overnight outgassing at 373 K under high vacuum. This outgassing process is essential for removing any gases or impurities present on the sample's surface, thereby ensuring accurate and reproducible adsorption results. Two distinct gases were used as adsorbates. Isotherms were measured using pure ethylene, while a gas mixture containing 1% acetylene in ethylene was used for the other measurements. The adsorption isotherm was obtained at 298 K, maintaining a constant temperature throughout the experiment. The pressure was gradually increased to a maximum of 100 kPa, and the amount of adsorbate absorbed by the sample was recorded as a function of pressure. This process allowed for the construction of a detailed curve illustrating the relationship between the amount of adsorbate and pressure under the specified conditions.

3.3. General Reaction Setup

This section describes the experimental setups and standard procedures employed for the catalytic reactions discussed in Chapters 4 to 6. Each subsection provides the specific reaction conditions, catalyst preparation, and analytical techniques relevant to the system under study.

3.3.1. Procedures for Chapter 4: KA Oil Coupling Reactions

3.3.1.1. General Reaction Procedure

The catalytic upgrading of KA oil derivatives was carried out in 6 mL round-bottom vials using a typical reaction mixture composed of Pd/C (0.02 mmol), KOH (0.6 mmol), and PPh_3 (0.02–0.32 mmol), to which the ketone (2 mmol) and alcohol (4 mmol) were added under an inert nitrogen atmosphere. The total reaction volume was 0.6 mL. The sealed vials were stirred magnetically and heated in a preheated oil bath at 100 °C for 4 hours. Reaction progress was monitored by periodically sampling aliquots, either directly through a reactor outlet or from the supernatant after stopping the reaction. When solid residues were present, filtration was performed prior to analysis. Conversions and product yields were determined by gas chromatography (GC) using an internal standard method. Product identification was achieved through GC–MS, NMR spectroscopy, and comparison with authentic samples.

3.3.1.2. Catalyst Reuse and Recycling Protocol

After completion, the catalyst was recovered by gravity filtration, rinsed with alcohol, dried, weighed, and reused in subsequent runs. The substrate amounts were adjusted according to the recovered catalyst weight to maintain the same molar ratios.

3.3.1.3. Hot Filtration Test

To assess catalyst leaching, a hot filtration test was conducted by removing the solid catalyst through a 25 μm Teflon™ membrane after 5 minutes of reaction time (12% conversion). The filtrate was transferred to a pre-heated vial and stirred at 100 °C. The reaction progress of the filtrate was monitored by GC.

3.3.1.4. In Situ Hydrogenation after Coupling Reaction

For post-reaction hydrogenation, 9 mol% additional Pd/C was added to the mixture, and the system was sealed, flushed with H_2, and pressurised to 30 bar. The reaction was stirred at 200 °C for 48 hours in a double-walled pressure reactor. Final analysis of the products was performed using the same analytical methods described above.

3.3.2. Procedures for Chapter 5: Semi-Hydrogenation of Acetylene in Ethylene-Rich Streams

3.3.2.1. General Reaction Procedure for Gas-Phase Hydrogenation Reactions

Gas-phase hydrogenation of acetylene (1%) in an ethylene-rich stream (99%) was carried out in a packed-bed reactor loaded with 5–35 mg of catalyst. Reactions were performed at total flow rates ranging from 10 to 150 mL min^{-1}, without the use of an inert carrier gas. Hydrogen was introduced at H_2:C_2H_4 molar ratios between 80:1 and 1:30, with typical conditions ranging from 1:10 to 1:30.

All catalysts, including MOF-based materials as well as Pd- and Pd-Au-supported zeolites, were tested under identical reaction conditions. The reactor effluent was

monitored online by gas chromatography (GC) using a column optimised for the separation of C_1–C_6 hydrocarbons. Prior to each reaction, the reactor was purged with N_2 (20 mL min^{-1} for 30 min) and subsequently heated to the desired temperature (30–150 °C). (Figure 3-1) Calibration of GC signals was performed by flowing the gas mixture through a bypass line. Catalysts were positioned centrally in the tubular reactor, secured between plugs of glass wool. SiO_2 was used as a filler and inert packing material; blank tests confirmed no catalytic activity in its presence.

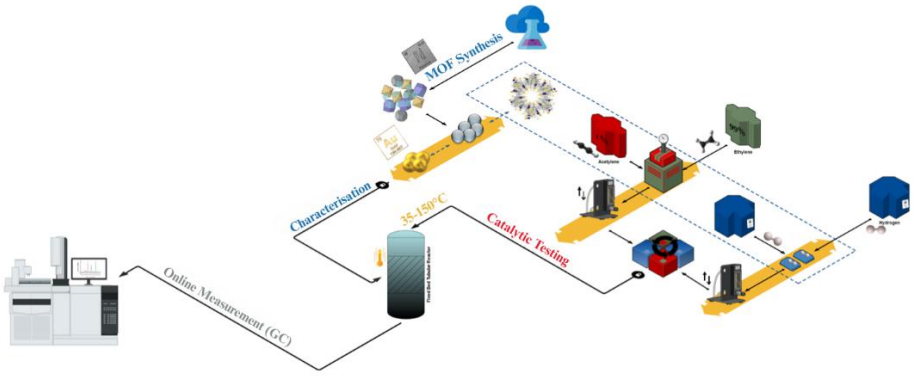

Figure 3-1 Reaction scheme for Semi-Hydrogenation of Acetylene in Ethylene-Rich Streams

3.3.2.2. Catalyst Recovery and Soxhlet Cleaning (Pd_1–Au_1 MOF)

After the flow reaction, the packed bed was disassembled, and the catalyst was recovered by sieving to remove the glass wool. The recovered solid (60–80% yield) was placed in filter paper and subjected to Soxhlet extraction using dichloromethane. The extraction was carried out in a 250 mL round-bottom flask placed on a magnetic stirrer hot plate at 70 °C, running for 1 hour (approximately 10 fill–and–drain cycles). The extract was subsequently analysed by GC–MS.

3.3.2.3. H_2–D_2 Isotope Exchange

Isotope exchange experiments were carried out in a fixed-bed reactor loaded with Pd_1-Au_1@MOF catalyst (2–6 mg). After purging with argon (18 mL min^{-1} for 20 min), a mixture of H_2 (1 mL min^{-1}), D_2 (1 mL min^{-1}), and Ar (18 mL min^{-1}) was passed through the reactor bypass for 15 min to calibrate the mass spectrometry signals. The gas stream was then directed through the catalyst bed for approximately 15 min. The system was maintained at 30 °C and 1 bar throughout. The reactor effluent was analysed by online mass spectrometry to quantify H_2 (m/z = 2), D_2 (m/z = 4), and HD (m/z = 3).

3.3.2.4. Computational Details

Density functional theory (DFT) calculations were performed in collaboration with Prof. Mercedes Boronat from the Instituto de Tecnología Química (ITQ, UPV-CSIC) in Valencia to investigate the structure and reactivity of Au–Pd active sites within a metal-organic framework (MOF) environment.

Periodic DFT calculations were executed using the Vienna Ab-initio Simulation Package (VASP), employing the Perdew–Burke–Ernzerhof (PBE) generalised gradient approximation functional. The valence electron density was expanded in

a plane-wave basis set with a kinetic energy cutoff of 600 eV, while interactions with core electrons were modeled using the projector augmented wave (PAW) method. Brillouin zone integrations were conducted at the Γ-point. Dispersion interactions were accounted for employing Grimme's D3 dispersion corrections. The electronic self-consistent field (SCF) cycles were converged to a precision of 10^{-6} eV, and structural optimisations were performed until the forces acting on all atoms were reduced to below 0.01 $eV \cdot Å^{-1}$. Throughout the geometry optimizations, all atomic positions were fully relaxed. Atomic charges were computed using the Bader theory of atoms in molecules (AIM). The periodic model represented a hexagonal MOF unit cell characterised by lattice parameters a = b = 18.057 Å, c = 12.800 Å. This unit cell contained 2 strontium (Sr), 12 carbon (C), 12 sulfur (S), 12 nitrogen (N), 60 additional carbon (C), 42 oxygen (O), and 80 hydrogen (H) atoms. A single Au–Pd dimer was strategically placed in various configurations within this structure to identify the most stable arrangement.

For the analysis of the reaction mechanism, a discrete cluster model was extracted from the optimised periodic structure. This cluster model consisted of 3 copper (Cu), 3 nitrogen (N), 6 oxygen (O), 3 sulfur (S), 12 carbon (C), 21 hydrogen (H), 1 gold (Au), and 1 palladium (Pd) atom. The model retained the Au–Pd dimer, its three coordinated thioether chains, and the adjacent organic fragment of the MOF. To maintain charge neutrality, nitrogen atoms that originally coordinated with Cu^{2+} cations were capped with hydrogen atoms.

Mechanistic calculations on the cluster model were executed using the Gaussian software package, employing the B3LYP hybrid functional. The 6-311G(d,p) basis set was utilised for light atoms (C, N, O, S, H), while LANL2DZ effective core potentials were utilised for Cu, Au, and Pd. During geometry optimisation,

the positions of the atoms in the organic framework were held fixed, while the Au–Pd dimer, thioether chains, and reactants were fully relaxed.

3.3.3. Procedures for Chapter 6: Catalytic Isomerisation and Aromatisation of 1-Octene over Noble Metal Supported Catalysts

3.3.3.1. General Procedure for Catalytic Conversion of 1-Octene in Batch Reactor

The catalytic transformation of 1-octene was conducted in a 20 mL stainless steel batch reactor, specifically designed to optimize thermal and pressure conditions for catalytic testing. In a typical experiment, the reactor was loaded with 3.5 mmol of the terminal olefin (1-octene) and 50 mg of a catalyst containing between 0.3% and 5% by weight of noble metal supported on various materials (e.g., Ru, Pd, Pt). No solvent was utilised during the process.

To ensure efficient mixing and intimate contact between the catalyst and reactants, the reaction mixture was stirred vigorously at 500 rpm. The temperature was maintained in the range of 290–300 °C, facilitating activation of the catalytic sites and promoting conversion. Reactions were performed for varying durations to monitor the effect of time on conversion and product selectivity. The system pressure could reach up to 5 bar, contributing to the reaction conditions.

Upon completion of the reaction, the reactor was cooled to room temperature before opening. The reaction mixture was subsequently analysed using nuclear magnetic resonance (NMR) spectroscopy and gas chromatography (GC) to

determine substrate conversion and product yield. Gas chromatography-mass spectrometry (GC-MS) was employed for product identification and confirmation.

3.3.3.2. General Procedure for Gas-Phase Isomerisation and Aromatisation of 1-Octene

The gas-phase isomerisation and aromatisation of 1-octene were investigated using a fixed-bed quartz tubular reactor operated under continuous flow. Two catalyst systems were evaluated: Ru/C (5 wt% Ru), used in quantities between 100 and 250 mg, and Ru/HZSM-5 (0.35 wt% Ru), for which 50 mg of catalyst was physically mixed with 50 mg of SiO_2 as an inert diluent to ensure optimal bed packing and heat distribution.

The catalyst bed was placed at the centre of the reactor, supported between plugs of glass wool. Before each reaction, the system was purged with N_2 (20 mL min^{-1} for 30 minutes) to remove air and moisture. The reaction temperature was varied between 250 and 350 °C, depending on the test conditions.

1-Octene was introduced via N_2 carrier gas saturated in a temperature-controlled bubbler (65–90 °C) to generate a controlled vapour-phase feed. The total gas flow rate was adjusted between 3 and 15 mL min^{-1} to modulate the contact time and olefin partial pressure. These conditions ensured a steady 1-octene vapour feed, with the actual molar flow determined by the saturation temperature. (Figure 3-2) Reaction products were collected using a cold trap placed downstream and analysed offline by nuclear magnetic resonance (NMR) spectroscopy and gas chromatography (GC) to quantify conversion and product

selectivity. This setup enabled the investigation of both isomerisation and aromatisation pathways under controlled gas-phase conditions.

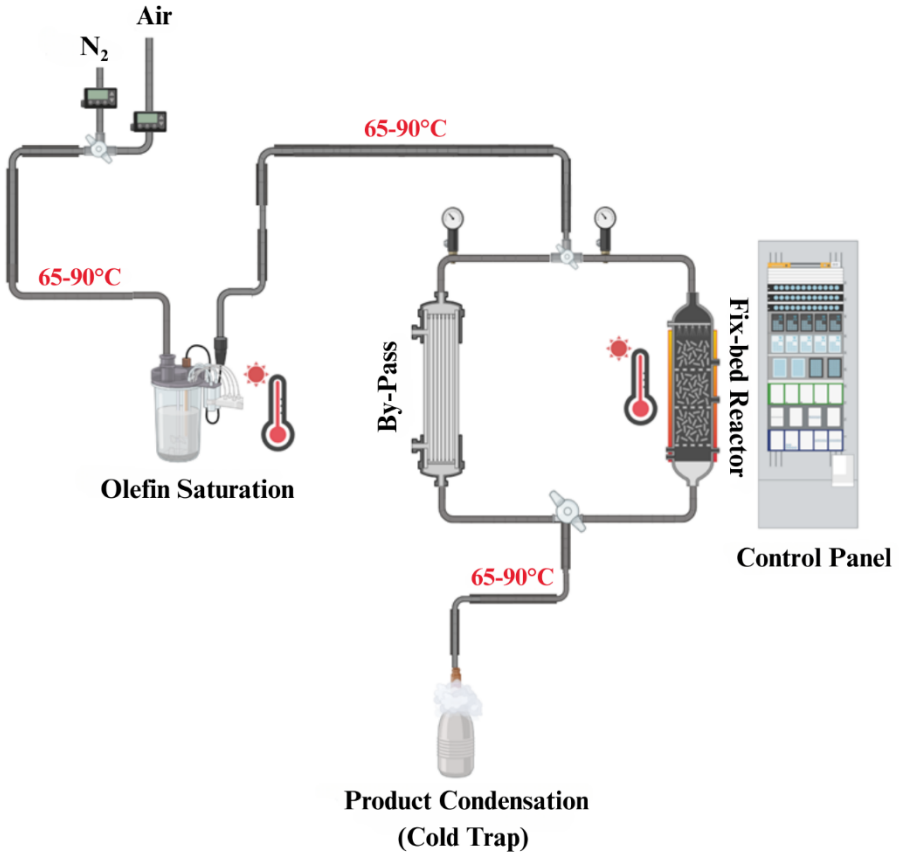

Figure 3-2 Flow reactor configuration used for C_8 terminal olefin isomerisation and aromatisation

3.3.4. Catalysts Preparation

3.3.4.1. Synthesis of Pd_1Au_1@MOF

Well-formed green prisms of Pd_1-Au_1@MOF, suitable for X-ray diffraction, were obtained via a two-step postsynthetic (PS) metal-exchange and reduction procedure. Initially, crystals of the parent compound 1 (ca. 5 mg) were alternately suspended in $AuCl_3$ and $[Pd(NH_3)_4]Cl_2$ solutions (0.2 mmol of metal salt per mmol of 1) prepared in H_2O/CH_3OH (1:2). Each immersion lasted 90 minutes and was repeated five times in alternating sequence. In the second step, the resulting solid was suspended in 5 mL of fresh H_2O/CH_3OH (1:2) and subjected to a slow chemical reduction by incremental addition of $NaBH_4$ (12 aliquots, each with 1 equivalent per mol of 1) over 72 hours. Each addition was followed by a 1.5 h reaction interval. The final product was washed thoroughly with the solvent mixture and filtered. Elemental analysis (calculated/found, %): C, 19.48/19.39; H, 3.49/3.33; S, 10.40/10.49; N, 4.54/4.55. IR (KBr): ν = 3013, 2961, 2914 cm^{-1} (C–H); 1601 cm^{-1} (C=O).

For catalytic testing, the synthesis was successfully scaled up using 5 g of powdered 1 (3 mmol) and proportional amounts of $AuCl_3$, $[Pd(NH_3)_4]Cl_2$, and $NaBH_4$, yielding 4.90 g of Pd_1-Au_1@MOF (93%). Elemental analysis (calculated/found, %): C, 19.48/19.29; H, 3.49/3.29; S, 10.40/10.40; N, 4.54/4.57. IR (KBr): ν = 3011, 2954, 2911 cm^{-1} (C–H); 1606 cm^{-1} (C=O).

3.3.4.2. Preparation of Pd- and PdAu-Zeolite Catalysts

Zeolites (3Å, 5Å, or NaY) were used as support materials for the synthesis of Pd and PdAu catalysts. Molecular sieves 3Å and 5Å (1 g each, Merck Aldrich) or zeolite NaY (Zeolyst) were first activated by heating at 300 °C for 12 h to remove residual moisture and enhance metal uptake. Catalyst preparation involved two sequential metal impregnation steps: one with palladium (Pd), followed by one with gold (Au). For Pd-only catalysts, K_2PdCl_4 was used as the metal precursor, dissolved in bidistilled water. The Pd loading was adjusted to obtain materials with 0.01–1 wt% Pd, using the same salt as for bimetallic PdAu zeolites. The solvent volume (~0.7 mL) was determined based on the water adsorption capacity of the activated support. The Pd^{2+} solution was added dropwise to the zeolite, mixed thoroughly under continuous stirring until a uniform paste formed, indicating successful metal uptake. The resulting material was dried at 100 °C for at least 12 h.

For PdAu catalysts, Pd impregnation was performed first (typically targeting 7 wt% Pd), using the same procedure described above. After drying, the Au impregnation was performed the next day using a solution of $KAuCl_4$ (prepared to reach up to 16 wt% Au loading), and incorporated into the previously Pd-impregnated zeolite. The material was again stirred to form a homogeneous paste, then dried under identical conditions.

The sequence of metal addition (Pd first or Au first) could be inverted, depending on the target composition or experimental design. The final dried solids were used directly for catalytic testing.

3.3.4.3. Preparation of Ru-zeolites (HZSM5) by cation exchange

Ruthenium-containing zeolite catalysts were prepared via incipient wetness impregnation using commercial ammonium-form ZSM-5 supports. Specifically, 500 mg of the selected zeolite, either CBV3024E (SiO_2/Al_2O_3 = 30) or CBV8014/8020 (SiO_2/Al_2O_3 = 80), both obtained in the NH_4^+-form, was added to an aqueous solution of $RuCl_3 \cdot H_2O$ (12 mg in 10 mL of bidistilled water). The mixture was magnetically stirred for 24 hours at ambient temperature to ensure homogeneous dispersion of the metal precursor. Following impregnation, the resulting purple suspension was filtered under vacuum, washed thoroughly with 100 mL of bidistilled water, and then dried at 100 °C for 3 hours. This process yielded greyish solid materials, indicative of partial reduction and precursor interaction with the zeolite framework. The transformation of the ammonium zeolites into their protonated (HZSM-5) forms was achieved via thermal decomposition of the NH_4^+ cations. The dried solids were subjected to calcination in air at 550 °C for 5 hours, employing a controlled heating rate of 1.8 $°C \cdot min^{-1}$, following established procedures in the literature.[2]

3.3.4.4. Preparation of $RuCl_3$-HZSM5 by wetness impregnation

A total of 250 mg of the selected zeolite was weighed and placed into a crucible. An aqueous solution of $RuCl_3 \cdot H_2O$ (6 mg in 0.5 mL of bidistilled water) was carefully added dropwise using a microneedle, allowing for precise and uniform dispersion of the solution across the zeolite surface. This process led to the formation of a purple wet cake, indicative of successful impregnation. The impregnated material was then dried at 100 °C for 3 hours in a static air oven,

yielding a solid precursor suitable for subsequent thermal treatment or catalytic application.

3.3.4.5. Preparation of Hierarchical Ru-Zeolites (HZSM-5) by Cation Exchange

Hierarchical HZSM-5 catalysts were synthesised via desilication of commercial HZSM-5 using aqueous alkaline solutions, followed by cation exchange with Ru^{3+}. The final H-form of both the parent and desilicated zeolites was obtained by calcining the corresponding NH_4-form in air at 823 K for 3 hours. Three types of hierarchical HZSM-5 supports were prepared through alkaline treatment under different conditions: 0.3 M NaOH solution (33 mL per gram of zeolite) and a 1:1 (v/v) mixture of 0.3 M NaOH and 0.25 M TPAOH. Each treatment was conducted under continuous stirring at 343 K for 30 minutes. Upon completion, the reaction mixtures were immediately quenched in an ice bath to halt the desilication process. The solids were then washed repeatedly with deionised water via centrifugation until neutral pH was reached, followed by drying overnight at 110 °C. To reintroduce the protonic form, the desilicated materials were ion-exchanged in 200 mL of 1 M NH_4NO_3 solution at 353 K for 4 hours, then filtered, dried, and calcined at 550 °C for 4 hours. The resulting hierarchical HZSM-5 zeolites were subsequently modified with ruthenium via cation exchange with aqueous $RuCl_3 \cdot H_2O$ solution, following the same procedure described for monometallic Ru-zeolites.[3,4]

3.3.4.6. Preparation of Cation-Exchanged Zeolites (Li^+ to Cs^+ Forms)

Cation-exchanged zeolites were prepared by ion-exchanging NaY or NaX zeolites with alkali metal acetates (Li^+, Na^+, K^+, Rb^+, Cs^+). In a typical procedure, 5.0 g of the parent zeolite was placed in a 500 mL round-bottom flask equipped with a magnetic stirrer. An aqueous solution (0.1–0.5 M) of the corresponding acetate salt was prepared in bi-distilled water and added to the flask. The mixture was heated to 90 °C in a pre-heated oil bath and stirred continuously for 24 hours to ensure complete ion exchange. After the reaction time, the suspension was cooled to room temperature and filtered under vacuum to recover the solid product. The solid was then washed thoroughly with 500 mL of bi-distilled water to remove excess ions and byproducts. Finally, the material was dried in an oven at 100 °C for 24 hours, yielding the desired cation-exchanged zeolite.

3.4. References

1. Ames DEHJ, Chemical D, States U. Styrene. *Ind Org Chem Start Mater Intermed an Ullmann´s Encycl*. 1995;7:4417-4441. doi:10.1002/14356007.a25

2. Serrano DP, García RA, Linares M, Gil B. Influence of the calcination treatment on the catalytic properties of hierarchical ZSM-5. *Catal Today*. 2012;179(1):91-101. doi:https://doi.org/10.1016/j.cattod.2011.06.029

3. Chaihad N, Situmorang YA, Anniwaer A, et al. Preparation of various hierarchical HZSM-5 based catalysts for in-situ fast upgrading of bio-oil. *Renew Energy*. 2021;169:283-292. doi:https://doi.org/10.1016/j.renene.2021.01.013

4. Svelle S, Sommer L, Barbera K, et al. How defects and crystal morphology control the effects of desilication. *Catal Today*. 2011;168(1):38-47. doi:https://doi.org/10.1016/j.cattod.2010.12.013

Chapter 4.

Catalytic Transformation of Biomass-Derived Ketones and Alcohols into Jet Fuel Precursors via Hydrogen-Borrowing Coupling Reactions

Index

4.1. Introduction

The global aviation industry faces growing pressure to decarbonise due to increasing concerns about climate change and environmental harm. Currently, aviation accounts for approximately 2.5% to 3% of global CO_2 emissions, and without significant mitigation strategies, these emissions are projected to rise substantially by 2050.[1] Unlike the road transport sector, which is rapidly advancing toward electrification, aviation continues to rely on high-energy-density liquid fuels, primarily due to the limitations of battery technology in terms of weight, energy storage, and range capability.[2] As a result, there is a heightened urgency to identify viable alternatives to fossil-based jet fuels.[3]

The appeal of zero net emission fuels lies in their ability to mimic the performance characteristics of conventional fossil-based fuels while minimising their climate impact. These fuels are designed to achieve carbon neutrality by capturing an equivalent amount of CO_2 during biomass growth or feedstock production, which is then released during combustion.[4] While renewable energy technologies, such as photovoltaics and hydrogen, have the potential to offer lower overall carbon footprints, the aviation sector's unique energy requirements make it necessary to continue using dense liquid fuels. Thus, the development of zero net emission jet fuels must remain a global priority, especially considering aviation's significant contribution to transport-related CO_2 emissions, which can be as high as 14% in some estimates.[5] However, this balance is only maintained if the conversion processes used are low-emission or emission-free. Therefore, a comprehensive lifecycle analysis is essential to accurately determine the carbon footprint of Sustainable Aviation Fuels (SAFs) production pathways.[6] They offer a groundbreaking solution for lowering aviation emissions, tackling a significant

issue within the industry. According to the International Air Transport Association (IATA), SAFs have the potential to provide up to 65% of the emission reductions required for the aviation sector to achieve net-zero carbon emissions by 2050.[7,8] What makes SAFs particularly noteworthy is their production from renewable resources or waste materials, like agricultural byproducts and used cooking fats. This waste recycling contributes to sustainability and allows these fuels to be integrated easily into the existing aviation fuel supply chain. Furthermore, SAFs are designed to be compatible with current aircraft engines and fueling infrastructure, which means they can be adopted with minimal modifications.[9] The diverse range of feedstocks available for SAF production provides airlines and airports with flexible options to choose from. By incorporating various materials, including biomass, SAFs represent a practical and eco-friendly alternative to traditional jet fuels. This shift is not just technological; it signifies an essential step toward advancing sustainability in aviation and reflects the industry's growing dedication to addressing climate change.[10]

Among the emerging feedstocks for SAF, the intriguing combination of cyclohexanone and cyclohexanol, commonly referred to as KA oil (ketone-alcohol oil), presents a noteworthy and yet underexplored candidate. Traditionally produced at an industrial scale exceeding 8 million metric tons annually[11], KA oil is predominantly employed as an intermediate in the synthesis of adipic acid, a key precursor in the manufacture of nylon-6,6. Given its high-volume availability and existing chemical infrastructure, redirecting even a modest portion of KA oil production toward SAF pathways could substantially benefit aviation sector decarbonization.[12] This dual functionality makes KA oil

an attractive target for alternative valorisation strategies aimed at reducing lifecycle emissions and enhancing feedstock circularity (Figure 4-1)

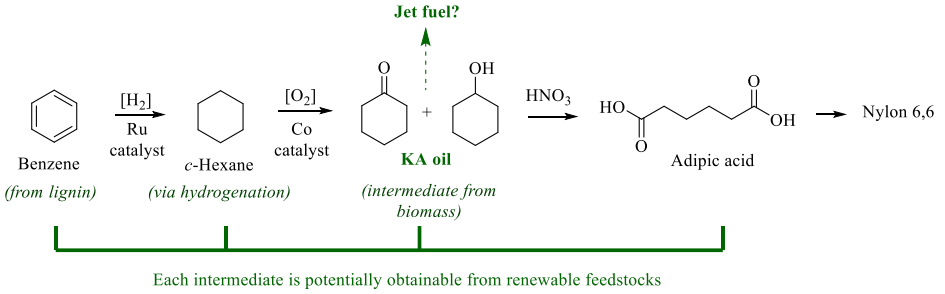

Figure 4-1 Proposed alternative valorisation of KA oil from the conventional adipic acid/nylon 6,6 route to SAF. All feedstocks can be sourced from renewable biomass, with KA oil as the central intermediate for both pathways

Jet fuels consist of hydrocarbon molecules, typically containing between 8 to 16 carbon atoms, with a significant portion being cyclohexane derivatives. KA oil, known for its C_6 cyclic compounds, serves as a structurally compatible and readily accessible precursor for synthesising jet fuel.[13] This indicates its potential role in promoting more sustainable aviation practices while utilising existing industrial resources. Despite its industrial relevance, the application of KA oil in SAF production has not been widely explored in scientific literature. One notable study involved the synthesis of decalin derivatives, a class of thermally stable jet fuel additives, from cycloketones that include five- and six-membered rings.[14,15] This research suggests that cyclohexanone and its derivatives can be effectively converted into high-performance fuel components.

KA oil is produced industrially from benzene in a two-step process. Initially, benzene undergoes hydrogenation to form cyclohexane, which is then subjected

to aerobic oxidation, and this method is well-established in petrochemical operations.[16] Currently, approximately half of the global production of KA oil is allocated to the synthesis of adipic acid using nitric acid. However, this process poses environmental concerns due to nitrous oxide emission, a potent greenhouse gas[17], thus alternative KA oil syntheses are required to meet the SAF standards.

Research has increasingly focused on developing more sustainable methods for producing adipic acid and other intermediates in the nylon production chain in recent years. The synthesis of adipic acid from biomass using heterogeneous catalysts shows promise as an alternative, although it is still under development.[17] Similarly, each step in the production of KA oil, including benzene, cyclohexane, and the KA oil itself, can theoretically be derived from renewable sources. For instance, benzene can be produced from lignin through selective C–O bond cleavage using ruthenium-based catalysts.[18,19] Other renewable pathways include the conversion of fatty acids[20], bioalcohols[21,22] and methane derivatives via CO_2 hydrogenation.[23,24] Moreover, cyclohexane can be obtained from bio-oils[25] or from guaiacol using supported metal catalysts.[26]

Encouragingly, the same KA oil that is currently utilised in petrochemical operations has been successfully synthesised from lignin-derived compounds, underscoring the potential for establishing a fully renewable supply chain in the production of aviation fuel.[15,27] This promising vision entails a renewable-to-renewable transformation, whereby bio-derived benzene is converted into KA oil, which is then further processed into jet fuel. Such a process represents a circular economy model and provides a sustainable alternative to conventional fossil-based aviation fuels.[28] Despite the exciting prospects, economic viability poses a significant challenge, primarily due to the high costs associated with biomass

valorisation and renewable hydrogen production. However, this developmental pathway also benefits from existing infrastructure built for conventional fuels, ensures technical compatibility with current engines, and is supported by an increasingly favourable regulatory environment advocating for deploying SAFs.[12]

Recent studies have quantified the performance characteristics of SAF components derived from KA oil, revealing several key advantages. These include a high energy density ranging from 34 to 35 MJ L^{-1}, a low tendency for sooting, as indicated by a smoke point exceeding 25 mm, and exceptional cold-flow properties, with freeze points reaching as low as −40°C.[29] These properties are critical, as they ensure compatibility with modern turbine engines and optimal performance in extreme atmospheric conditions, such as those encountered at high altitudes or varying temperatures. Moreover, integrating renewable energy sources into the hydrogenation and oxidation processes involved in refining KA oil could lead to a substantial reduction in lifecycle emissions associated with this type of SAF. This enhancement not only improves the overall sustainability profile of KA oil-derived fuels but also aligns with global efforts to reduce aviation's carbon footprint. By marrying advanced technologies with sustainable practices, the aviation industry can move towards a more environmentally friendly future. [29]

As said above, the urgency to address aviation emissions is highlighted by recent estimates indicating that global aviation could triple its current share of greenhouse gas emissions by 2050 if no changes are made.[30] International Civil Aviation Organisation (ICAO) has set a target for net-zero emissions by mid-century, which relies significantly on the development and scaling of SAF

technologies to achieve this goal.[29,31] However, current SAF production methods often face challenges related to feedstock scalability, economic competitiveness, and supply chain resilience. In this context, repurposing well-established chemical intermediates, such as KA oil, offers a practical and potentially scalable approach to bridging the gap between current infrastructure and future sustainability needs.

This chapter explores the catalytic upgrading of KA oil, a commonly produced mixture of cyclohexanone and cyclohexanol, primarily used in the industrial synthesis of adipic acid for nylon-6,6. KA oil represents a promising yet underexplored feedstock for sustainable aviation fuel (SAF) production. Its six-carbon cyclic structure, which contains reactive ketone and alcohol functional groups, provides a unique platform for constructing carbon-carbon (C–C) bonds through catalytic hydrogen-borrowing mechanisms.

4.2. Objectives

The main objective is to develop a solvent-free, heterogeneous catalytic system that transforms KA oil. This transformation can occur either through self-coupling or by cross-coupling with biomass-derived alcohols such as ethanol, butanol, and furfuryl alcohol, resulting in hydrocarbon mixtures that meet Jet A-1 specifications. The catalytic system utilises commercially available palladium supported on activated carbon (Pd/C) and operates under mild basic conditions using potassium hydroxide (KOH). Notably, water is the only stoichiometric by-product, ensuring both environmental and process sustainability.

To fine-tune product selectivity and optimise the fuel range output, we investigate the influence of monodentate and bidentate phosphine ligands on the supported palladium (Pd) active sites. It is hypothesised that electronic and steric effects can modulate the hydrogen-borrowing cycle, potentially shifting product distributions towards favourable linear, branched, or cyclic alkanes. This work encompasses four key goals:

- To assess the reactivity of KA oil under these catalytic conditions;
- To determine how various bio-based alcohols influence product composition and carbon chain length;
- To evaluate catalyst recyclability, reaction robustness, and overall process sustainability; and
- To benchmark the final product mixtures against established jet fuel criteria, such as boiling range, hydrogen-to-carbon ratio, and aromatic content.

Product analysis was conducted using gas chromatography-mass spectrometry (GC-MS), nuclear magnetic resonance (NMR) spectroscopy, and elemental analysis to ensure accurate characterisation and performance alignment. Ultimately, this research aims to demonstrate a technically viable and scalable pathway for converting an industrially abundant intermediate into low-emission, fossil-free aviation fuels using commercially accessible catalytic materials.

4.3. Results and discussion

Following the demonstration of KA oil's catalytic potential for sustainable aviation fuel production, this chapter systematically investigates three strategic pathways for its conversion into jet fuel-range hydrocarbons (Figure 4-2). The study progresses from basic stoichiometric reactions to more advanced catalytic systems, tackling key challenges at each stage of development:

1. **Stoichiometric Aldol Chemistry** (Section 4.3.1) serves as a baseline, confirming C-C coupling feasibility but revealing critical limitations in product suitability and environmental footprint.
2. **Hydrogen-Borrowing Catalysis** (Section 4.3.2) initially pursued with Pd/C, unexpectedly favoured C-O coupling and aromatisation, prompting mechanistic reevaluation.
3. **Integrated Catalytic System** (Sections 4.3.2-4.3.3.) ultimately combines base-catalysed enolate formation with phosphine-modified Pd-mediated hydrogen transfer, achieving:
    - Selective C-C bond formation
    - Tunable product distributions via phosphine design
    - Full utilisation of KA oil components
    - Water as the sole byproduct

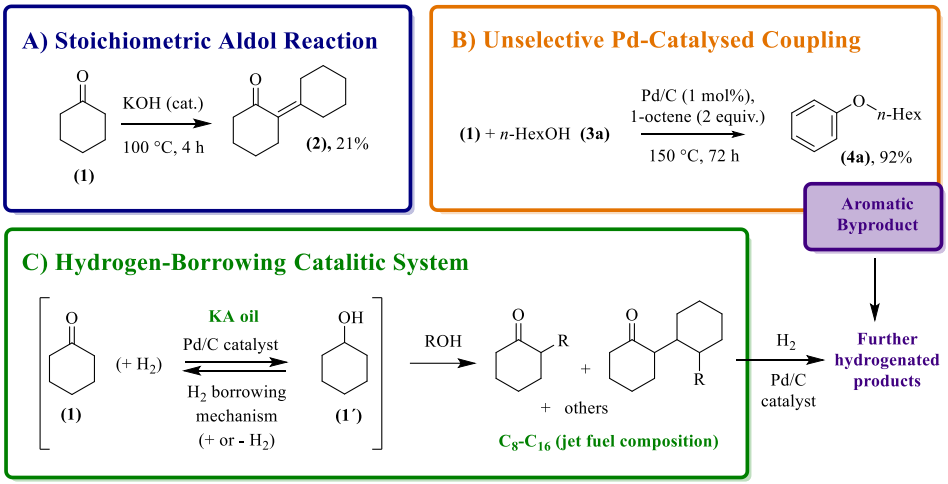

Figure 4-2 Comparative strategies for converting KA oil (cyclohexanone/cyclohexanol) to jet fuel-range hydrocarbons. (A) Stoichiometric aldol condensation yields unsaturated ketone 2 (non-fuel grade). (B) Pd/C-catalyzed hydrogen borrowing with alcohols 3 produces

This progression reflects an iterative optimisation process where each set of results directly informed subsequent experimental design. Kinetic studies, catalyst characterisation (HAADF-STEM, PXRD, ICP-OES), and phosphine ligand tuning based on Tolman electronic parameters provide both mechanistic understanding and practical validation. The final catalytic system achieves conversion metrics and compositional profiles that align with the requirements of

ASTM D7566[32] for sustainable aviation fuels, demonstrating both technical feasibility and potential for scale-up.

4.3.1. Catalytic and Non-Catalytic Strategies for C–C Bond Formation

To initiate the conversion of KA oil into jet fuel-range hydrocarbons, it is crucial to explore direct carbon-carbon (C–C) bond-forming reactions, using cyclohexanone (**1**) as a model substrate. A well-established and straightforward approach is aldol condensation under basic conditions, which facilitates chain elongation by linking two ketone molecules. As depicted in Figure 2a, stoichiometric amounts of potassium hydroxide (KOH) catalyse the self-condensation of cyclohexanone, yielding the α,β-unsaturated ketone product **(2)** with a 21% isolated yield after 4 hours at 100 °C.[33] Although this outcome confirms the inherent reactivity of KA oil toward C–C coupling via enolate chemistry, the resulting product is not suitable for jet fuel applications due to the presence of unsaturated functional groups. These unsaturated groups are undesirable in thermally stable hydrocarbon mixtures intended for aviation use.[34] The reliance on stoichiometric bases poses significant practical and environmental challenges. High base loading can lead to excessive salt formation, which increases waste streams that necessitate neutralisation and limits scalability.[35] These factors are inconsistent with the principles of green chemistry and industrial sustainability. Furthermore, attempts to reduce the base concentration to sub-stoichiometric or catalytic levels have resulted in poor conversion rates, further constraining the applicability of this method.

The Pd/C catalyst utilised for the reaction shown in Figure 2b is a commercially available material containing 5 wt% palladium on carbon. It is characterised by an average nanoparticle size of approximately 1.8 nm, as determined through high-angle annular dark-field scanning transmission electron microscopy (HAADF-STEM) (Figure 4-3).[17] In addition, CO chemisorption experiments indicated a high palladium dispersion of around 78%, reflecting a significant number of accessible active sites on the catalyst surface. The small nanoparticle size and high dispersion contribute to the catalyst's excellent performance by maximizing metal atom efficiency and surface reactivity. Given its wide commercial availability, ease of use, and industrial relevance, Pd/C is a practical and reliable choice for catalytic hydrogenation, dehydrogenation, and coupling reactions. These characteristics support its selection for preliminary screening and scale-up applications.[17]

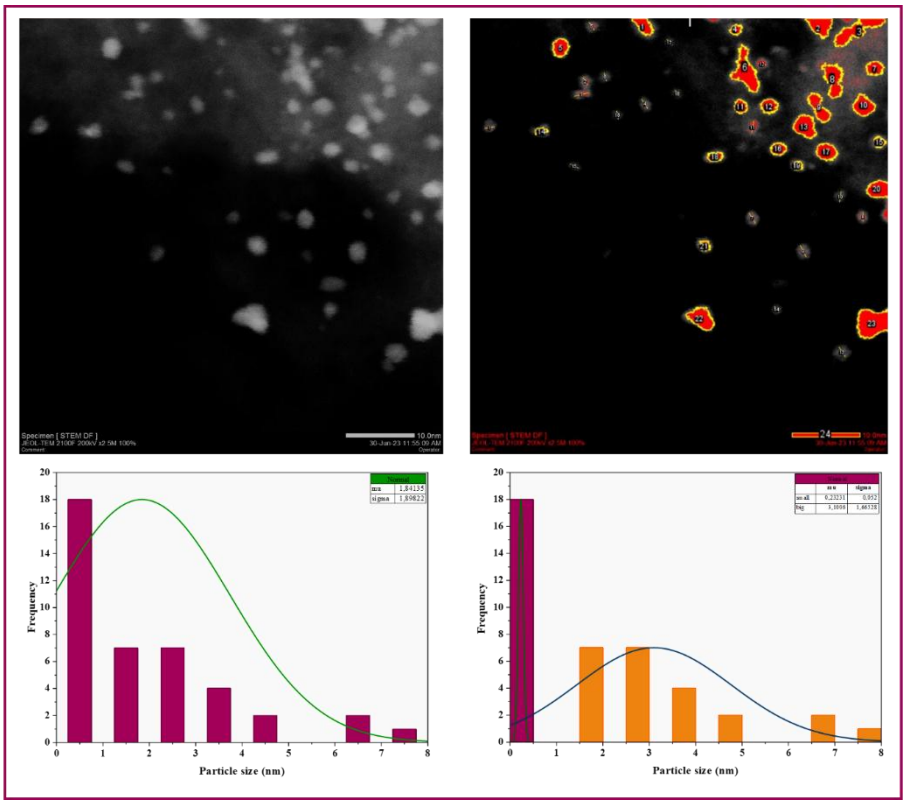

Figure 4-3 A representative high-angle annular dark field scanning transmission electron microscopy (HAADF-STEM) image of the commercial Pd on carbon catalyst (5 wt%) and the corresponding histogram. The average particle size is approximately 1.8 nm (left), with larger particles averaging around 3.1 nm and smaller ones averaging about 0.2 nm (right). The confidence interval can be considered ±0.5 nm (resolution limit of the instrumentation).

These findings are consistent with the literature, where similar Pd/C systems have demonstrated effectiveness in hydrogen-borrowing reactions and alkylation processes.

An alternative method emphasises hydrogen-borrowing (HB) catalysis, which has proven to be an effective strategy for forming carbon-carbon (C–C) bonds between carbonyl compounds and alcohols under redox-neutral conditions.[36–38] Within the framework of KA oil, this approach could facilitate the coupling of cyclohexanone **(1)** with bio-derived alcohols[39] like *n*-hexanol (**3a**), leading to the generation of extended-chain hydrocarbons that satisfy jet fuel specifications. As depicted in Figure 2B, previous studies have reported using palladium on carbon (Pd/C) catalysts along with stoichiometric alkene scavengers (e.g., 1-octene) to capture the hydrogen released during the process[40–42]

According to the conditions adapted from the literature[40–42], the reaction of cyclohexanone with *n*-hexanol predominantly yields aromatic by-products, specifically anisole-type derivatives (**4a**), with yields reaching up to 92%. Notably, this occurred even in the absence of added alkene traps. The prevailing pathways observed were competing C–O coupling and aromatisation, as detailed in Tables 4-1, 4-2 and 4-3 and illustrated in Figure 4A-1 (Appendix). This trend was consistent across a diverse array of alcohol substrates.

Table 4-1 Catalytic results for cyclohexanone (1) alkylation reaction with hexanol (3a)[a].

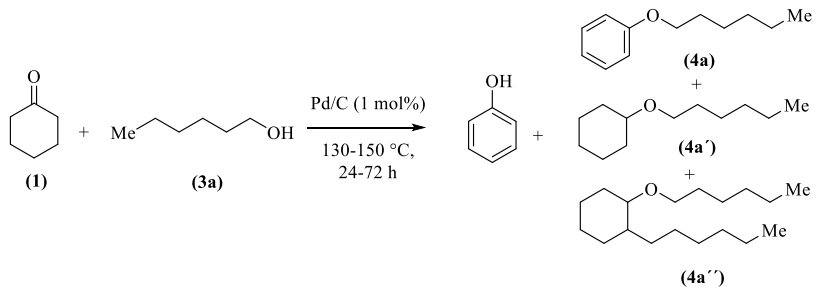

Entry	Atmosphere	T (ºC)	Time (h)	Conversion [%]	Yield [%][b]			
				(1)	Phenol	(4a)	(4a´)	(4a´´)
1	(nitrogen)	130	24	44.8	<1	25.3	14.8	4.7
2	(oxygen)	130	24	29.7	6.3	17.8	1.1	1.0
3[c]	(nitrogen)	150	72	94.0	-	92.0	2.0	-

*[a] GC yields. Exp. conditions: molar ratio **(1)/(3a)** = 1/5, Pd/C (5 wt%) = 1 mol%. [b] The yield of products is calculated by measuring the actual amount of product obtained and dividing it by the theoretical amount that could be obtained from the complete conversion of the starting material, expressed as a percentage. [c] 1-octene as a sacrifical alkene*

Generally, these reactions demonstrated limited selectivity for the desired aliphatic products, instead favouring the formation of oxygenated or unsaturated structures that do not align with hydrocarbon fuel requirements. The undesired aromatisation appeared largely independent of the type of alcohol (Table 4-2) used or the presence of sacrificial alkenes, indicating a mechanistic predisposition of the Pd/C catalyst toward C–O bond formation under thermal hydrogenation (HB) conditions.

Table 4-2 Catalytic Alkylation of Cyclohexanone **(1)** with Primary Alcohols: Influence of Substrate, Atmosphere, and Selectivity Profiles.

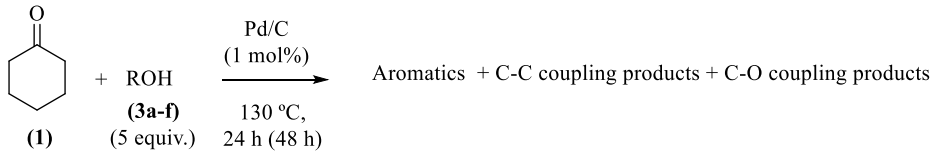

No.	R-OH	Atm.	Conv. [%]	Arom. [%][a]	C-alk, [%][a]	O-alk. [%][a]	Sel. O-alk. [%]	C + O [%]
1	None	N_2	50 (80)	7 (31)	38 (15)	4 (25)	8 (32)	-
2	None	O_2	(60)	(50)	(8)	(11)	2	-
3	MeOH (**3b**)	N_2	35	10	23	-	-	-
4	MeOH (**3b**)	O_2	21	14	6	-	-	-
5	EtOH (**3c**)	O_2	20	8	1	8	40	-
6	*n*-PrOH (**3d**)	N_2	23	5	1	9	39	6
7	*n*-BuOH (**3e**)	N_2	21	4	2	9	43	6
8	*n*-PentOH (**3f**)	N_2	31	<1	4	12	39	14
9	*n*-HexOH (**3a**)	N_2	45	-	0	45	100	-
10	*n*-HexOH (**3a**)	O_2	30	6	1	20	66	-

Abbreviations: Atm. = Atmosphere; Conv. = Conversion; Arom. = Aromatisation; C-alk. = Carbon-linked alkylation; O-alk. = Oxygen-linked alkylation; Sel. O-alk. = Selectivity toward O-alkylation; Reaction conditions: T = 130 °C, Pd/C (5 wt%, 1 mol%), t = 24 h, (1)/R–OH = 1:5 molar ratio. [a]The yield of products is calculated by measuring the actual

amount of product obtained and dividing it by the theoretical amount that could be obtained from complete conversion of the starting material, expressed as a percentage.

The composition of the reaction atmosphere during transformation notably influenced conversion efficiency. Reactions performed under nitrogen consistently showed higher conversion rates compared to those carried out in the presence of oxygen (Table 4-3). However, there was no significant enhancement in selectivity for the target alkanes. These findings underscore the limitations of traditional hydrogen-borrowing (HB) conditions in transforming kerogen-derived (KA) oil and point to the need for a more selective and integrated approach.

Table 4-3 Comparative Catalytic Data for Methanol-Mediated Alkylation of Cyclohexanone (1) (from Entries 3 and 4, Table 4-2)

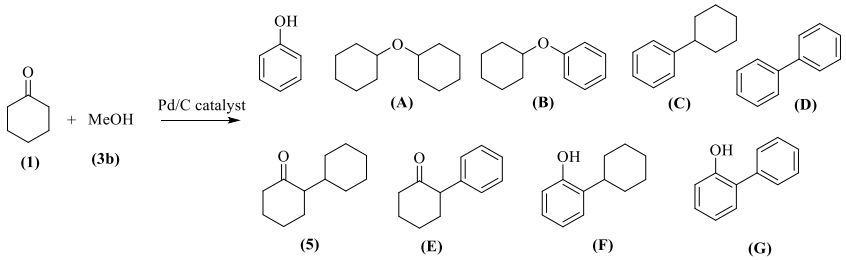

No	Atm	Conv (1) [%]	Yield [%][h]								
			PhOH	(A)	(B)	(C)	(D)	(5)	(E)	(F)	(G)
1[a]	N_2	34.3	9.6	-	-	2.3	<1	13.6	-	4.8	-
2[a]	O_2	20.2	13.8	-	-	0.1	-	3.7	-	2.0	-
3[b]	N_2	80.2	5.5	-	-	3.9	4.7	34.4	-	21.8	-
4[c]	N_2	50.2	7.4	3.3	<1	<1	9.5	17.3	<1	9.5	-
5[d]	N_2	72.7	48.7	0.8	2.6	-	-	5.3	-	-	-
6[e]	O_2	95.3	70.5	0.6	10.9	2.3	<1	-	-	9.5	-
7[f]	N_2	99.4 (47.1)	84.6 (33.2)	1.9 (<1)	9.9 (4.4)	-	<1 (-)	- (1.1)	-	-	2.5 (2.5)
8[g]	N_2	79.9	31.0	10.9	15.8	-	<1	10.8	-	4.1	-
9[c]	O_2	60.3	49.8	-	<1	-		4.2	1.4	2.3	-

Abbreviations: Conv. = Conversion; Atm. = Atmosphere; PhOH = Phenol

[a] *Standard experimental conditions: molar ratio **(1)**/**(3b)**= 1/5, Pd/C (5 wt%) = 1 mol%, 130 °C, 24 h.* [b] *150 °C, 16 h.* [c] ***(1)** = 3 mmol.* [d] *Pd/C (5 wt%) = 5 mol%.* [e] *molar ratio **(1)**/**(3b)**= 1/10, Pd/C (5 wt%) = 5 mol%, 150 °C, 24 h.* [f] ***(1)** = 3 mmol, Pd/C (5 wt%) = 5 mol%, 150 °C, 48 h (sample 24 h).* [g] ***(1)** = 3 mmol, Pd/C (5 wt%) = 1 mol%, 130 °C, 48 h.* [h] *The yield of products is calculated by measuring the actual amount of product obtained and dividing it by the theoretical amount that could be obtained from the complete conversion of the starting material, expressed as a percentage. The mass balance is completed with the non-identified products (minor amounts).*

To tackle these challenges, a novel strategy was devised combining elements of aldol condensation and HB catalysis in a single-pot process. As shown in Figure 2c, this system utilises catalytic amounts of KOH and Pd/C under hydrogen-borrowing conditions, without the need for sacrificial alkenes or excess oxidants.[43,44] In this configuration, the alcohol component of KA oil, cyclohexanol (**1′**), is reversibly dehydrogenated to **(1)** by Pd/C, establishing an equilibrium through the HB mechanism.[45] The subsequent enolate formation and coupling yield C_8–C_{18} hydrocarbon products suitable for jet fuel applications. Critically, the absence of aromatic or C–O bonded by-products enhances the final mixture's compatibility with ASTM standards for sustainable aviation fuels.[46]

In addition to its improved selectivity, this process boasts excellent atom economy, with water being the only stoichiometric by-product.[47] It also allows for post-condensation hydrogenation using the same Pd/C catalyst under mild hydrogen pressure, facilitating the formation of fully saturated hydrocarbons, essential for thermal stability and combustion performance in jet engines.[46, 48] Ongoing optimisation studies (Sections 4.3.2-3) are exploring variations in alcohol structure, base concentration, and catalyst modifications (such as the addition of phosphine ligands), which will provide greater control over the branching and chain length of the resulting hydrocarbon mixtures.[46, 49]

Overall, this integrated approach represents a significant advancement over both stoichiometric aldol and conventional HB systems. It not only enhances selectivity toward jet-fuel-compatible alkanes but also aligns with broader sustainability goals by minimising waste, avoiding the formation of aromatics, and valuing existing industrial intermediates.

4.3.2. Catalytic Alkylation of Cyclohexanone with Alcohols Using Pd/C and KOH Under Phosphine-Free Conditions

The catalytic alkylation of cyclohexanone (**1**) with primary alcohols, specifically *n*-hexanol (**3a**) and *n*-propanol (**3d**), was explored using a heterogeneous palladium on carbon (Pd/C) catalyst at a loading of 1 mol%, alongside potassium hydroxide at 3 mol%. The reactions were performed under an inert atmosphere at 100 °C for 4 hours. This approach seeks to minimise undesirable side reactions, such as aromatisation and C–O coupling, which can adversely affect the production of saturated hydrocarbons suitable for jet fuel applications.

Under the specified reaction conditions (Figure 4-4), the alkylation of cyclohexanone with *n*-hexanol and *n*-propanol was conducted efficiently, yielding the desired saturated alkylated products (**6a** and **6d**) with yields between 45% and 60%. Remarkably, the selectivity for these products exceeded 75%, with minimal formation of undesired by-products, such as unsaturated ketones, aromatic compounds, or C–O coupled species. The remarkable selectivity and yield achieved in this process underscore the successful mitigation of side reactions. This is essential for producing hydrocarbon mixtures that meet rigorous jet fuel specifications. Such effectiveness not only enhances the efficiency of the process but also aligns with the stringent standards required for aviation fuels, thereby contributing to advancements in sustainable fuel production methodologies.

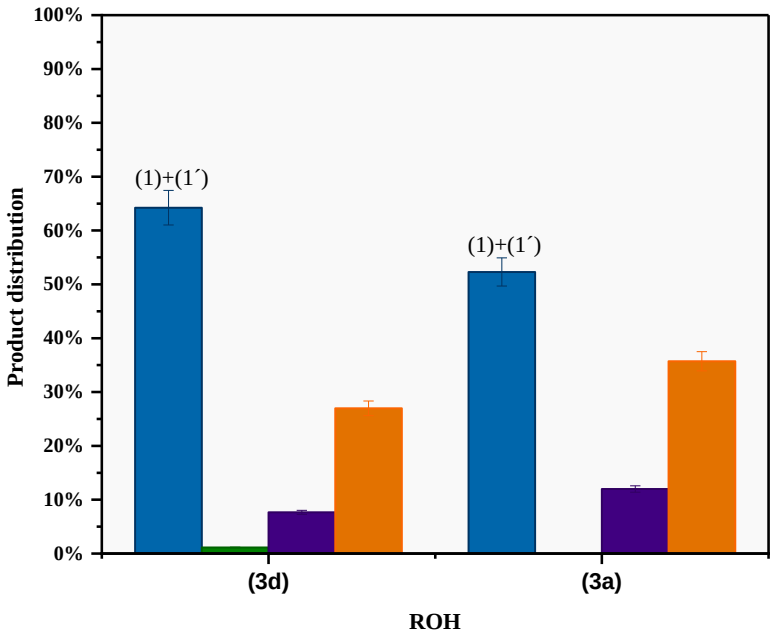

Figure 4-4 Catalytic results for the alkylation of (1) with (3a) or (3d) using Pd/C and KOH as catalysts under the indicated reaction conditions. The remaining % of (1) is

The reaction mixture post-catalysis contained unreacted (**1**) and in situ formed (**1'**), collectively referred to as KA oil. Kinetic studies conducted under identical conditions, as shown in Figure 4-4, using either simulated KA oil or pure cyclohexanol confirmed the reactivity of both substrates towards alkylation, albeit with slightly reduced selectivity compared to cyclohexanone alone (Figures 4-5 and 4-6). The kinetic plot for the KA oil mixture (Figure 4-6) demonstrates that (**1**) reacts more rapidly than (**1´**), which indicates that the alkylation reaction occurs faster than the hydrogen-borrowing reaction between these two

compounds. Additionally, the kinetic plot for pure (**1´**) (Figure 4-6) confirms that both reactants are interconverted throughout the reaction process. These observations suggest that cyclohexanone exhibits greater reactivity than cyclohexanol under the given conditions. This aligns with the mechanistic understanding that an enolisable ketone is more susceptible to base-catalysed deprotonation and subsequent coupling.

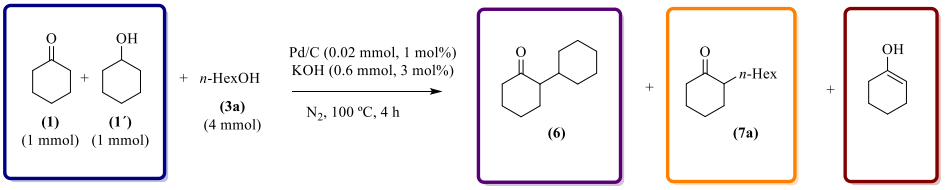

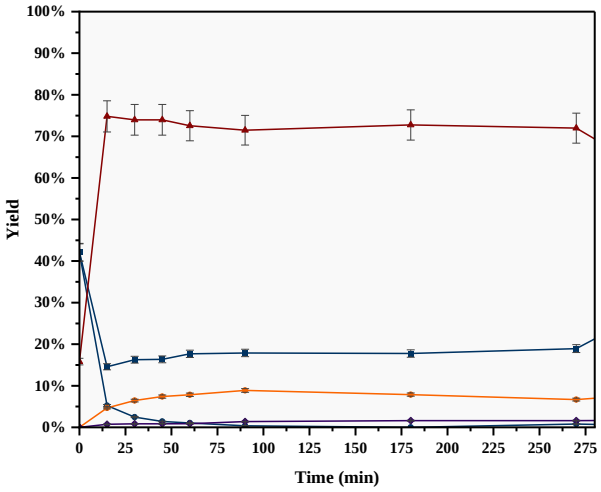

Figure 4-5 Kinetic plot for the reaction between a simulated KA oil mixture (1:1 ratio of (1) and (1´)) and (3a), under the indicated reaction conditions (without phosphine). GC yields. Error bars account for a 5% uncertainty.

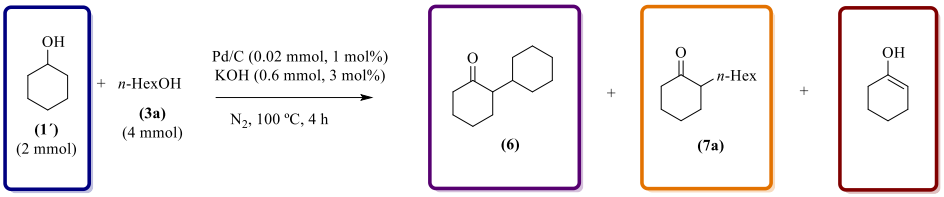

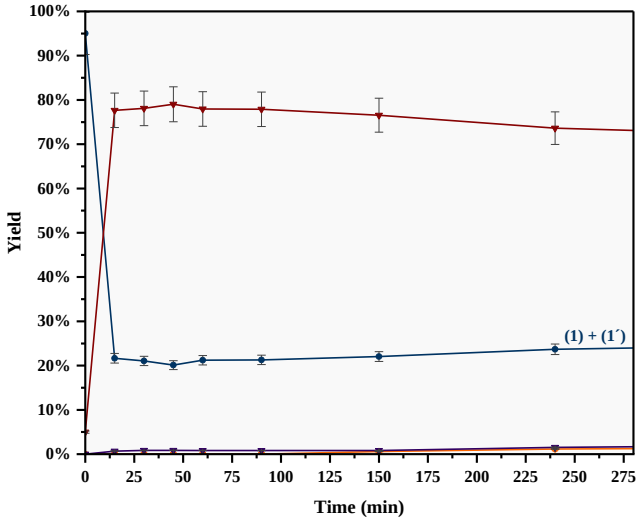

Figure 4-6 Kinetic plot for the reaction between (1´) and (3a), under the indicated reaction conditions (without phosphine). The conversion shows (1´) plus the in-situ formed (1). GC yields. Error bars account for a 5% uncertainty.

The role of KOH as a co-catalyst is pivotal for facilitating the deprotonation of the α-carbon in cyclohexanone, thereby enabling the formation of the enolate intermediate required for C–C bond formation. In the absence of this base catalyst, interconversion between (**1**) and (**1´**) still takes place; however, the

production of coupling products remains minimal, even after an extended reaction time of 6 hours (as shown in Figure 4A-2, Appendix 4A-2). This observation supports the expected functions of each catalyst: Pd/C primarily initiates the hydrogen-borrowing reactions, while KOH activates the alpha carbon atom of the ketone substrate. Further insights are gained by studying the system where equal amounts of (**1**) and (**1'**) are present initially. Notably, no significant transformation of (**1'**) back into (**1**) is observed (Figure 4-7).

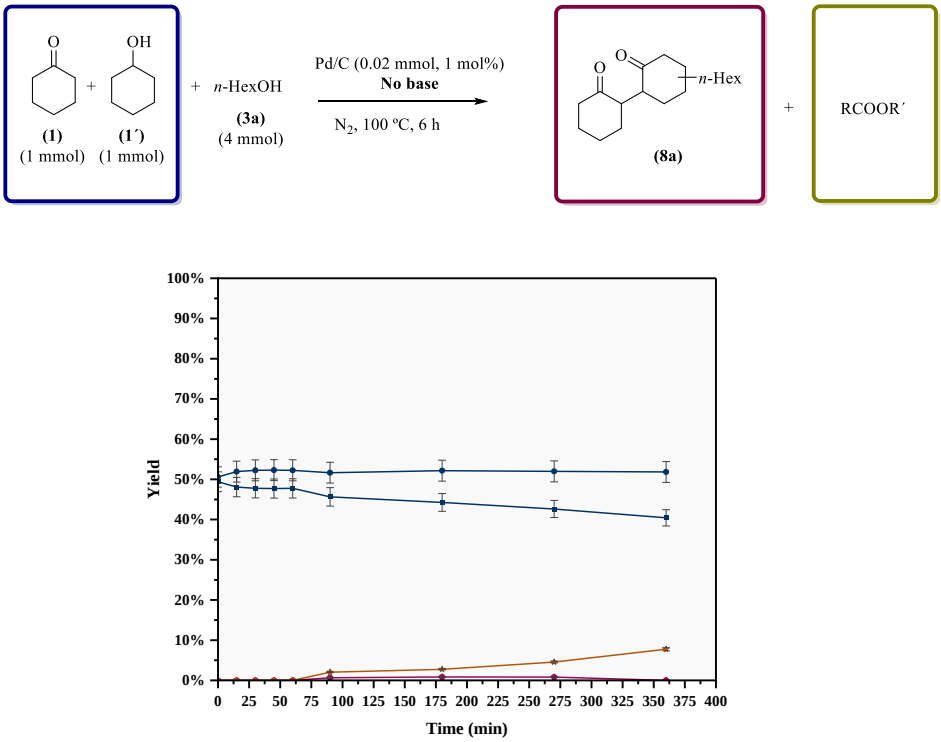

Figure 4-7 Kinetic analysis of the reaction between (1), (1′), and (3a) was performed under conditions lacking both base and phosphine. Yields were measured using gas chromatography (GC), with error bars indicating a 5% uncertainty

This phenomenon is likely due to the initial competitive adsorption of (**1**) onto the Pd/C catalyst surface, which inhibits further reactivity of (**1'**), highlighting a delicate balance between the rates of conversion from (**1'**) to (**1**) and the reverse process. Complementary kinetic experiments with varying initial ratios of (**1**) and (**1'**), conducted both in the absence (Figure 4-8) and presence of base (Figure 4-9), reveal that interconversion between the two species occurs regardless of their initial concentrations when KOH is present.

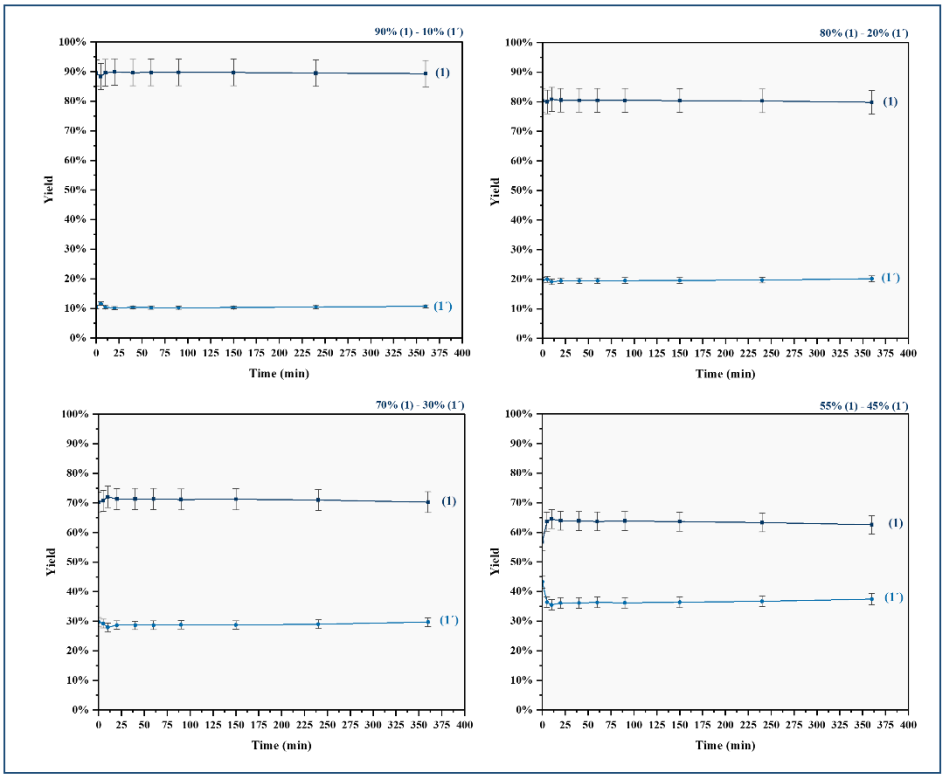

Figure 4-8 Kinetic plots for the reaction between different relative amounts of (1), (1´), and (3a), under standard reaction conditions without base and phosphine. GC yields. Error bars account for a 5% uncertainty.

Interestingly, even in the absence of base, neat (**1'**) can undergo partial transformation into (**1**), which can be tentatively attributed to the spontaneous formation of some active deprotonated species under these conditions.

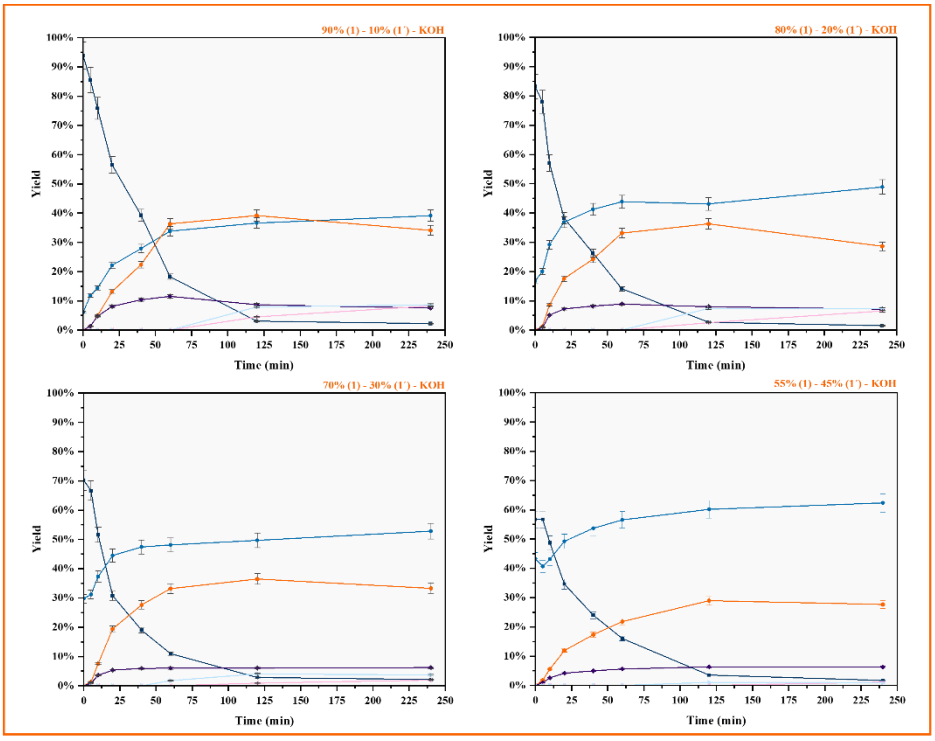

Figure 4-9 Kinetic plots for the reaction between different relative amounts of (1),(1´), and (3a) under the indicated reaction conditions. GC yields. Error bars account for a 5% uncertainty.

Mechanistically, the Pd/C catalyst facilitates the hydrogen-borrowing mechanism, in which the alcohol is oxidised to the corresponding aldehyde or ketone, subsequently undergoing condensation with the enolate. This dual

catalytic system effectively enables the formation of new C–C bonds without needing external hydrogen sources or sacrificial agents, thereby enhancing the atom economy and sustainability of the process.[47]

The recyclability of the catalyst was evaluated through several reaction cycles.[50] The Pd/C catalyst was recovered via filtration, then washed and reused in subsequent reactions.[51] After three cycles, a slight decrease in both catalytic activity and selectivity was noted (see Figure 4A-3, Appendix 4A-3), consistent with literature reports regarding the gradual deactivation of heterogeneous catalysts due to factors such as metal leaching and support degradation.[52]

Hot filtration tests confirmed the heterogeneous nature of the catalysis, indicating that less than 20% (when considering the blank experiment) of the catalytic activity could be attributed to leached palladium species present in the solution (Figure 4-10 A). This aligns with findings that Pd/C catalysts exhibit minimal leaching under optimised conditions, as observed in Suzuki-Miyaura coupling reactions where the support efficiently recaptures dissolved Pd species.[53,54] Notably, the increase in conversion after filtration, represented by the purple line in Figure 4-10, closely resembles the results of the blank experiment, which shows the residual conversion with the base but without the palladium catalyst (green line). This suggests that only a few catalytically active palladium species leach into the solution. To further validate these findings, the hot filtration experiment was repeated, confirming that only slight leaching occurs, which has a negligible impact on the final yield of the reaction (Figure 4-10 B). This result highlights the stability of the Pd/C catalyst under the reaction conditions and demonstrates its suitability for practical applications where catalyst recovery and reuse are essential.

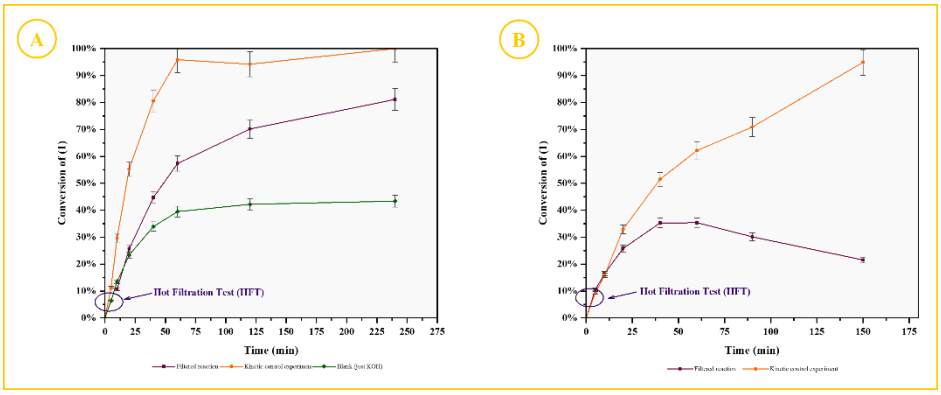

Figure 4-10 A) Hot filtration test for the reaction without phosphine (PPh_3), with just KOH and Pd/C catalysts. Filtration was performed at 12% conversion, after a 5-minute reaction time. The blank experiment without Pd is also shown. GC yields. Error bars account for a 5% uncertainty. B) Repeated experiment. HFT: Hot filtration test.

Inductively coupled plasma optical emission spectroscopy (ICP-OES) analysis of the spent catalyst showed that up to 28% of the original supported Pd might be removed during reaction. While higher than some reports (e.g., 0.1–2.3% Pd leaching in hydrodeoxygenation studies[54], this aligns with the "cocktail" mechanism of Pd/C catalysis, where oxidative addition and redeposition cycles cause gradual metal loss.[53,55] It also indicated that potassium levels reached 5 wt% due to the use of KOH in the reaction. While a portion of the original supported palladium may have been lost, the final Pd/C catalyst still contained significant amounts of potassium, derived from the base. The retained activity despite Pd loss suggests that residual Pd nanoparticles or adsorbed species remain active. While not directly addressed in the provided studies, potassium incorporation is consistent with base-driven reactions and does not inherently deactivate Pd/C.[56] Notably, this loss of Pd and incorporating K (as K^+) on the solid do not compromise catalytic activity. Moreover, palladium recovery after

the reaction, a well-established practice in the industry, can help mitigate the loss of palladium species. Despite these changes, the catalyst demonstrated substantial activity, suggesting that the observed leaching does not significantly impair its catalytic performance.

In conclusion, the phosphine-free catalytic system of palladium on carbon (Pd/C) and potassium hydroxide (KOH) effectively promotes the alkylation of cyclohexanone with primary alcohols. This process produces saturated hydrocarbons with high selectivity and excellent yields. Utilising commercially available catalysts under mild reaction conditions facilitates the potential reuse of the catalyst, aligning with green chemistry principles and offering a promising method for generating jet fuel-range hydrocarbons from renewable feedstocks. This approach resembles advancements in stable Pd/C systems, such as Pd/C ligated with β-hydroxybutyric acid for aerobic oxidations (TON >3000)[52] and hypercrosslinked polymer-supported Pd for carbonylation.[55] These systems focus on commercial catalyst reuse and minimal leaching, essential for the sustainable production of sustainable aviation fuel (SAF).

4.3.3. Catalytic Results with Phosphines as Ligands

The interaction between phosphines and palladium nanoparticles has been the subject of fundamental research for over two decades.[57–63] While early investigations primarily focused on the adsorption modes and binding characteristics of phosphines on metal surfaces, there has been a recent increase in interest regarding their catalytic implications, particularly in heterogeneous systems. Phosphine-ligated Pd catalysts have been extensively studied in the context of hydrogenation reactions[59–64] and cross-coupling processes.[65] However, their application in other catalytic transformations remains relatively underexplored.[66] There are no known reports on using phosphine-ligated Pd nanoparticles for hydrogen-borrowing coupling reactions, highlighting the novelty of the system presented here.

To systematically evaluate the effect of phosphine ligands on the reactivity and selectivity of Pd/C-catalyzed hydrogen-borrowing coupling reactions, a series of transformations involving cyclohexanone (**1**) and primary alcohols (**3a–3f**) was performed under previously optimised reaction conditions (refer to Figure 4-4). The only modification made was the addition of triphenylphosphine (PPh_3, **9a**) as a ligand, employed in a 4 mol% loading relative to the metal. The presence of PPh_3 had a remarkable impact on the outcome of the reaction, notably altering both the product distribution and the nature of the reaction intermediates. As depicted in Figure 4-11, when PPh_3 is employed, the predominant products are alkylated compounds (**8**), which are formed through C–C coupling between the ketone (**1**) and the corresponding alcohol (**3**). Interestingly, the alkyl substituents on these products occupy different positions on the cyclohexane ring, as indicated by undefined bonds in the figure, showcasing the structural diversity of the

alkylated products. The positional variability of alkyl substituents within the cyclohexane moiety aligns with prior observations in ligand-modulated Pd systems, where phosphine ligands influence coordination environments and intermediate stability. For example, phosphine ligands like PPh_3 can stabilise Pd–H species while altering redox states, enabling diverse coupling pathways. This is consistent with studies showing that phosphine oxidation during Pd catalysis generates mixed catalytic species, including nanoparticles, which exhibit distinct reactivity compared to homogeneous counterparts.[67] The increased structural diversity is likely a result of intermediate rearrangements or multiple coupling pathways facilitated by the phosphine-ligated palladium species, as previously reported in similar systems where ligand sterics and electronics modulate the coordination environment and intermediate stability. In addition to these coupling products, a substantial formation of α,β-unsaturated ketone (**5**) was observed, where hydrogen equivalents are preferentially used for reduction. This intermediate, which arises from an initial aldol condensation and subsequent dehydration, was found in much higher concentrations in phosphine-ligated systems than in the reactions lacking phosphines (see Figure 4-4). This shift mirrors findings in hydrogen-borrowing catalysis, where ligand sterics and electronics modulate hydride transfer efficiency. For instance, bulky phosphines like PPh_3 slow hydrogenation steps, favouring condensation intermediates over saturated products.[67, 68] The notable increase in certain intermediates points to a change in the reaction pathway. In this context, hydrogen equivalents, typically released during alcohol dehydrogenation in a hydrogen-borrowing mechanism, seem to be primarily focused on promoting C–C bond formation rather than reducing enone intermediates to create saturated products. This behaviour differs from that observed in the non-ligated Pd/C system, where hydrogen equivalents are more easily available for ketone or alkene hydrogenation. The emergence of

these intermediates indicates that the hydrogen equivalents produced via alcohol dehydrogenation are chiefly utilized in coupling steps instead of reduction pathways, which was noted in phosphine-free reactions (refer to Figure 4-4). To further investigate the mechanism, a control experiment using isolated enone (**5**) and alcohol (**3a**) under standard conditions was performed. The outcome revealed that only trace amounts of the final coupled product (**8a**) were formed (Figure 4A-4, Appendix 4A-4), indicating that enone (**5**) is not a competent intermediate under these conditions unless generated in situ via the complete hydrogen-borrowing sequence. This aligns with the hydrogen-borrowing mechanism's reliance on dynamically formed aldehydes and surface-bound Pd–H species for redox-neutral transformations. Such integrated processes are hallmarks of hydrogen-borrowing systems, where base-mediated aldol condensation and metal-catalysed hydrogenation occur synergistically.[68] This observation strongly supports the hypothesis that the reaction follows a mechanistically integrated process involving three key steps:

(i) hydrogen-borrowing sequence—comprising alcohol dehydrogenation to the corresponding aldehyde,

(ii) base-mediated aldol-type condensation of the aldehyde with the ketone,

(iii) reduction of the α,β-unsaturated intermediate by surface-bound Pd–H species.

The lack of direct involvement of (**5**) in the coupling process suggests that surface-bound hydrogen, rather than molecular H_2, along with intermediates that form dynamically, play a key role in facilitating productive turnover.

Consequently, hydrogenation is essential for the efficient formation of C–C bonds in this system, instead of relying only on base-mediated activation.

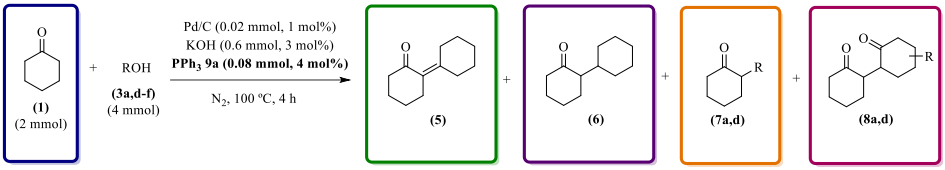

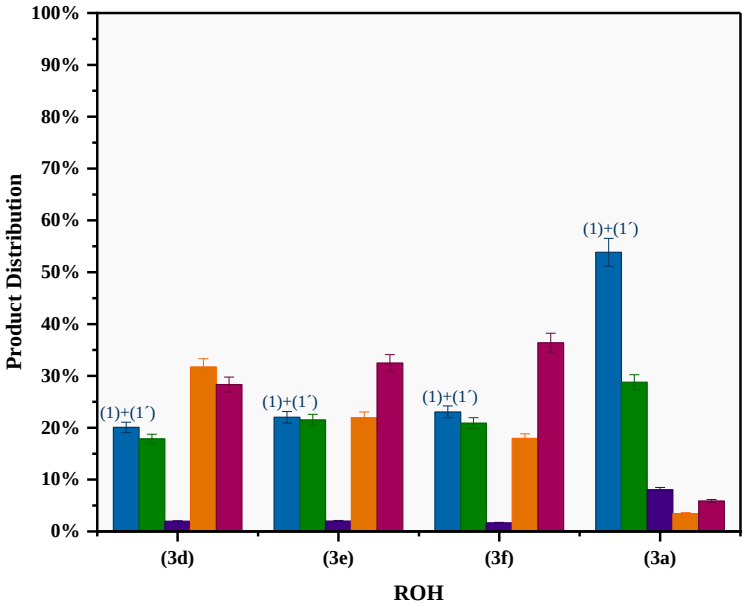

Figure 4-11 Catalytic results for the alkylation of cyclohexanone (1) with different alcohols 3a, 3d–3f using Pd/C and KOH, and PPh_3 (9a, 4 mol%) as ligand. The residual percentage of cyclohexanone includes contributions from in situ formed cyclohexanol (1′, KA oil). Error bars represent ±5% experimental uncertainty.

This mechanistic framework aligns with prior literature on hydrogen-borrowing catalysis, where a cooperative interplay between metal centres and basic co-catalysts enables redox-neutral transformations without external oxidants or reductants.[69] Furthermore, the role of phosphines in tuning the electronic environment of palladium, thus modulating its reactivity towards hydride transfer and substrate coordination, has been documented in various hydrogenation and cross-coupling reactions.[70] Phosphines like PPh_3 alter Pd's electronic environment, reducing its hydrogenation activity and promoting condensation. This contrasts with ligand-free Pd/C, where efficient hydrogen transfer enables full saturation of intermediates. Such ligand-dependent behaviour is well-documented in cross-coupling and hydrogenation reactions, where phosphines modulate metal redox states and intermediate binding.[67] However, their influence in hydrogen-borrowing C–C bond-forming processes remains largely unexplored, making the current study a significant contribution to the expanding field of ligand-modified heterogeneous catalysis.

Kinetic studies have provided valuable insights into how key reaction components influence reaction rates. It was found that increasing the concentration of alcohol (**3a**) significantly accelerated the reaction rate (as illustrated in Figure 4-12), confirming its role as both a coupling partner and a hydrogen donor.[71]

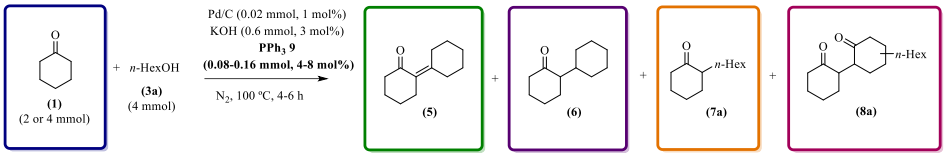

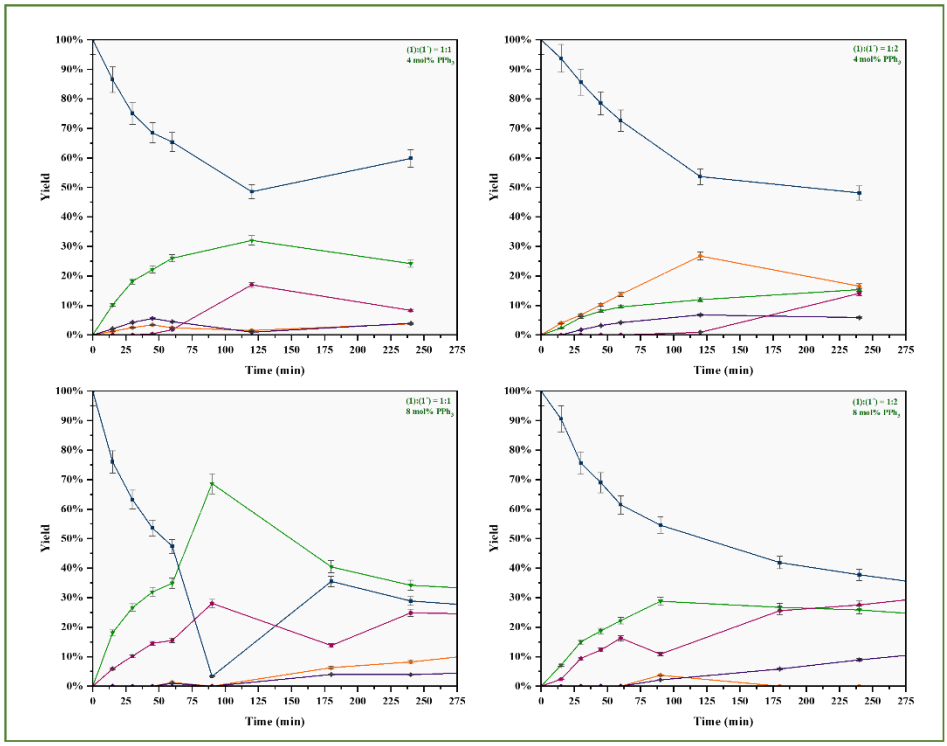

Figure 4-12 Kinetic plots for the reaction between (1) and (3a) in different relative amounts under the indicated reaction conditions (with two different amounts of phosphine). The conversion shows (1) plus the in-situ formed (**1´**). GC yields. Error bars account for a 5% uncertainty

Additionally, the amount of phosphine used had a marked effect; the optimal reaction rate was achieved with 4 mol% of PPh_3 (**9a**), while both lower and higher concentrations of phosphine led to decreased efficiency and slower reaction rates (see Figure 4-13). This indicates the existence of an ideal level of surface coverage of palladium nanoparticles by phosphine ligands, which optimally balances the electronic modification of the active site with substrate accessibility for binding and turnover.[72] From a synthetic perspective, the incorporation of the phosphine ligand (**9a**) facilitated the synthesis of longer hydrocarbon chains, up to C_{17} in length (e.g., product **8f**). This enhancement increases the process's relevance for generating components suitable for sustainable aviation fuels (SAF). These extended alkylated products are particularly desirable for aviation fuels due to their high energy density and favourable volatility profile.[73]

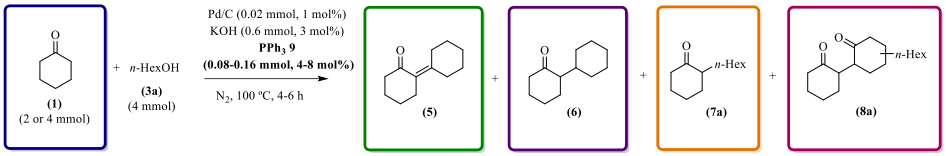

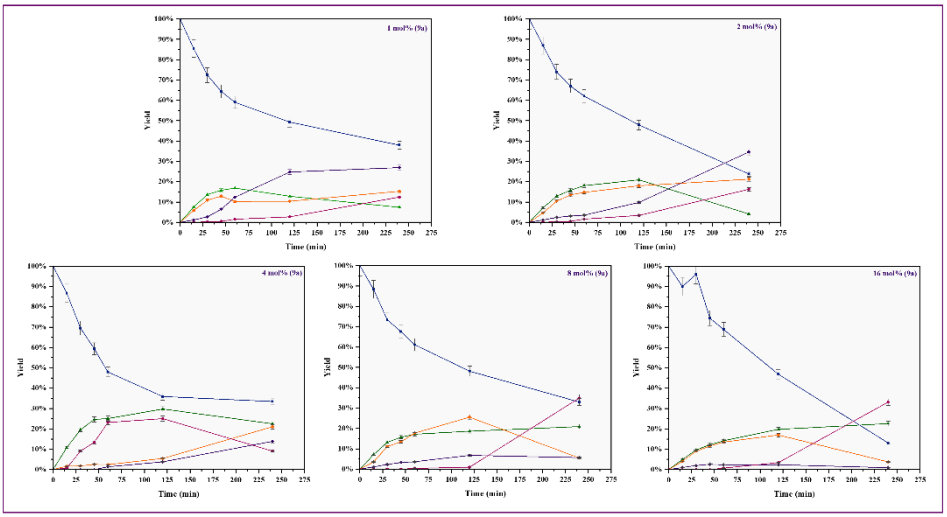

Figure 4-13 Kinetic plots for the reaction between (**1**) and (**3a)** with different amounts of phosphine (**9a**), under the indicated reaction conditions. The conversion shows (**1**) plus the in-situ formed (**1´**). GC yields. Error bars account for a 5% uncertainty.

To further explore the catalyst structure and surface accessibility in the presence of PPh_3, CO chemisorption experiments were attempted. However, these failed to yield reliable data, likely due to several interrelated factors: the volatility of PPh_3, its strong coordination to palladium, potentially blocking active sites, and a potential decrease in CO adsorption equilibrium due to altered Pd electronic

environments.[64] Nonetheless, powder X-ray diffraction (PXRD) analysis (Figure 4-14) confirmed the presence of finely dispersed Pd species with low crystallinity, in agreement with HAADF-STEM measurements of nanoparticle size (~1.8 nm; see Figure 4-3) and consistent with the behaviour of supported nanometals. These findings suggest that phosphine ligation does not lead to significant particle sintering or phase separation, and that catalytic performance is primarily modulated via surface-level interactions rather than gross structural changes.

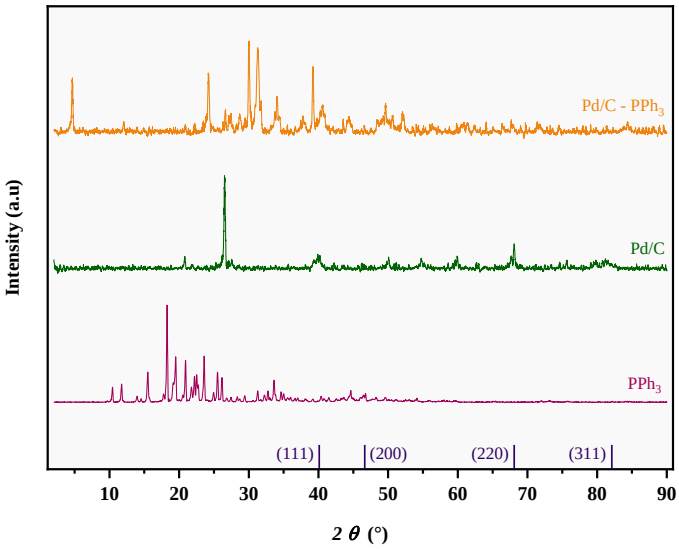

Figure 4-14 Comparison of the PXRD for commercial Pd/C (5 wt% Pd, Sigma Aldrich) and mixed with PPh_3 (Sigma Aldrich) in a mass ratio of 2/1 together with PXRD of Pd on carbon catalyst (5 wt%), indicating the peaks of the different Pd crystallographic planes in the nanoparticles. The prominent peak at 27º corresponds to the carbon support.

Building on these structural insights, the influence of various phosphine ligands on Pd/C-catalyzed hydrogen-borrowing transformations was examined. Ligands **[(9b–9d)]** were evaluated in the alkylation of cyclohexanone **(1)** with *n*-hexanol **(3a)**, a less reactive alcohol identified in prior studies (Figure 4-11), to assess the effect of ligand properties on catalytic performance. The reactions were performed under inert conditions to prevent oxidative degradation of the phosphines. Continuous in situ generation of palladium hydrides during the catalysis indicates the stability of the phosphine ligands. The phosphines were chosen to represent a diverse array of electron-donating capacities and cone angles, providing insight into ligand behaviour in heterogeneous catalysis. Maintaining an inert atmosphere further safeguards against oxidative degradation of the phosphines, a risk alleviated by forming metal hydride species during the alcohol dehydrogenation process.

PXRD analysis confirmed the generation of surface-bound Pd–H species through the appearance of a new signal near 40°, which emerged after catalyst exposure to H_2, regardless of PPh_3 presence (Figure 4-15). This result corresponds with previously reported observations regarding hydride formation on supported Pd catalysts, as well as earlier RAMAN-IR studies.[64] The accompanying decrease in the carbon support peak at 27° may be due to masking or peak convolution from the adsorbed PPh_3, whose diffraction pattern occurs between 25° and 40°, distinctly different from that of the free ligand. The observed shift in diffraction angles compared to free PPh_3 suggests physical adsorption or weak coordination of the ligand to the Pd surface, consistent with previous findings on ligand–support interactions in heterogeneous catalysis.[74]

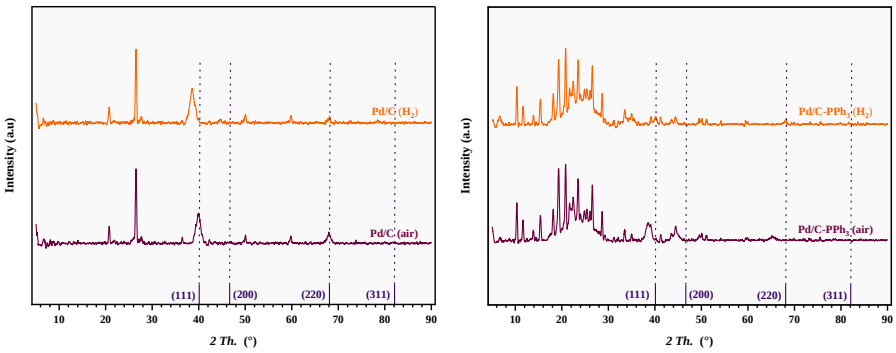

Figure 4-15 *Left. Powder X-ray diffractogram (PXRD) of Pd on carbon catalyst (5 wt%), indicating the peaks of the different Pd crystallographic planes in the nanoparticles under air or H2 atmosphere. Right: PXRD of Pd on carbon catalyst (5 wt%) with* PPh_3*, indicating the peaks of the different Pd crystallographic planes in the nanoparticles under air or* H_2 *atmosphere.*

Most phosphine appears to be retained on the catalyst; however, gas chromatography-mass spectrometry (GC–MS) analysis showed small amounts of oxidised phosphine derivatives, indicating some partial ligand leaching or oxidative decomposition. (Figure 5A-5, Appendix 5A-5) This behaviour aligns with findings from other semi-heterogeneous systems, where interactions with the reaction medium influence ligand stability. Overall, the data suggest efficient ligand retention throughout the catalytic process.[75]

This comparative study allows us to disentangle electronic and steric influences on catalytic activity. As shown in Figure 4-16, a clear inverse correlation was observed between catalytic activity and νCO, indicating that more electron-donating ligands enhance Pd hydride formation and facilitate the hydrogen-

borrowing cycle. On the other hand, activity appeared relatively insensitive to cone angle variation, suggesting that the Pd surface can tolerate substantial ligand bulk without steric hindrance significantly impeding reactivity. Figure 4-16 A illustrates the catalytic outcomes obtained with phosphines **9a**–**9d**, which were selected to span a wide range of electronic and steric properties. Electronic properties were quantified using the carbonyl stretching frequencies (*ν*CO) of their corresponding $Ni(CO)_3$(phosphine) complexes, ranging from 2059 to 2069 cm^{-1}. These values provide a relative scale of electron-donating ability, as lower *ν*CO values are indicative of greater ligand basicity and electron density.[76] Steric bulk was evaluated through the Tolman cone angle, which varied from 127° (1,3-bis(diphenylphosphino)propane, dppp, **9c**) to 205° (2-dicyclohexylphosphino-2′,6′-dimethoxybiphenyl, SPhos, **9d**), offering insight into spatial constraints imposed around the Pd active site.[77, 78]

The catalytic performance exhibited a strong dependence on ligand electronic characteristics. As shown in Figure 4-16 B, a nearly linear inverse correlation was observed between the *ν*CO values and cyclohexanone (1) conversion, suggesting that more electron-rich phosphines enhance catalytic activity. This trend aligns with prior studies demonstrating that phosphine ligands' electronic properties significantly modulate palladium catalysts' reactivity, with electron-rich ligands often facilitating higher activity in redox-neutral transformations.[79,80] The secondary dicyclohexyl phosphine (**9e**) was tested to assess the validity of this correlation, and the results aligned remarkably well (the blue circle, in Figure 4-16 B). These findings integrate seamlessly into the established correlation, further reinforcing the relationship and supporting comparable observations in both aromatic and aliphatic phosphines used in palladium-catalysed systems.[67, 80, 81] In contrast, the steric parameters of the phosphines, summarised in Figure 4-16 C,

appeared to exert minimal influence on the reaction outcome. As shown in Figure 4-16 D, no clear correlation was found between the Tolman cone angle and the conversion of (**1**), suggesting that steric bulk did not significantly hinder substrate access or catalytic turnover within the tested range. This observation is consistent with earlier reports indicating that, although steric factors can affect catalyst lifetime and selectivity, they do not necessarily limit reactivity in hydrogen-borrowing systems.[80] Again, phosphine **9e** further supported this pattern, performing consistently with other ligands irrespective of its steric profile. Overall, these findings highlight the importance of electronic ligand tuning in modulating the reactivity of supported Pd catalysts for hydrogen-borrowing C–C coupling. The use of PPh_3 and related ligands not only enables access to heavier alkylated products with relevance to SAF, but also offers mechanistic insight into surface-mediated hydrogen transfer pathways facilitated by electron-rich palladium hydride species.

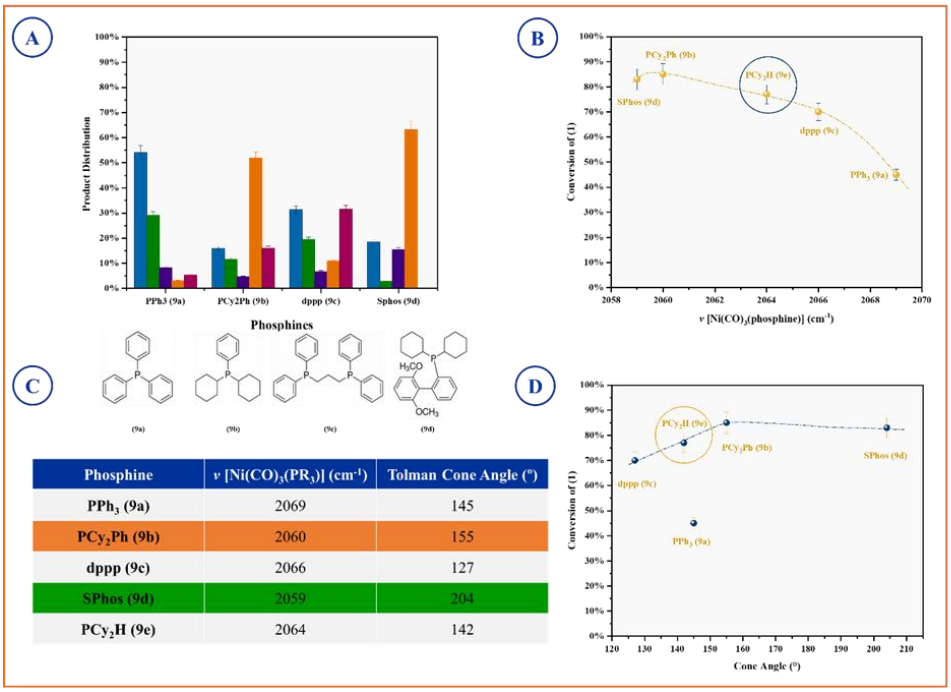

Phosphine	ν [Ni(CO)$_3$(PR$_3$)] (cm^{-1})	Tolman Cone Angle (°)
PPh$_3$ (9a)	2069	145
PCy$_2$Ph (9b)	2060	155
dppp (9c)	2066	127
SPhos (9d)	2059	204
PCy$_2$H (9e)	2064	142

Figure 4-16 A) Catalytic results for different phosphines during the alkylation of cyclohexanone (1) with alcohol 3a under the reaction conditions in Fig. 4-11 above. The remaining % of cyclohexanone (1) is a mixture with in-situ formed cyclohexanol (1´) (KA oil). Error bars account for a 5% uncertainty. B) Correlation between the conversion of **(1)** and the phosphine electronic properties, expressed in terms of ν(CO, cm^{-1}) of the corresponding Ni(CO)$_3$(PR$_3$) complex. C) Electronic and steric values for the different phosphines **(9a-e)**[77, 78] D) Correlation between the conversion of **(1)** and the phosphine Tolman cone angle.

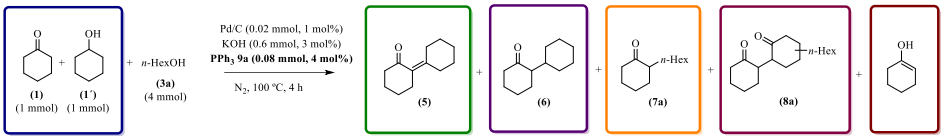

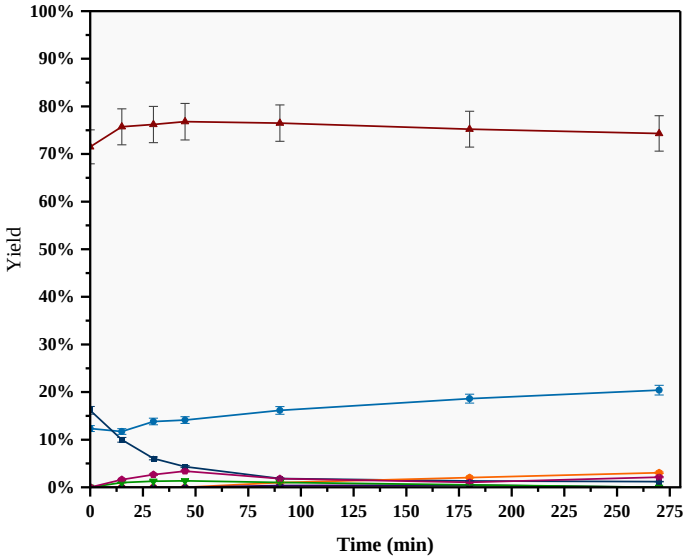

Figure 4-17 Kinetic plot for the reaction between a simulated KA oil mixture (1:1 ratio of (1) and (1´)) and (3a), under the indicated reaction conditions (with phosphine). GC yields. Error bars account for a 5% uncertainty.

Catalytic activity in a simulated KA oil mixture was confirmed under conditions using phosphine (**9a**)-modified Pd/C (Figure 4-17). Similar to reactions without phosphine, a base was essential for facilitating C–C coupling (Figure 4-18).

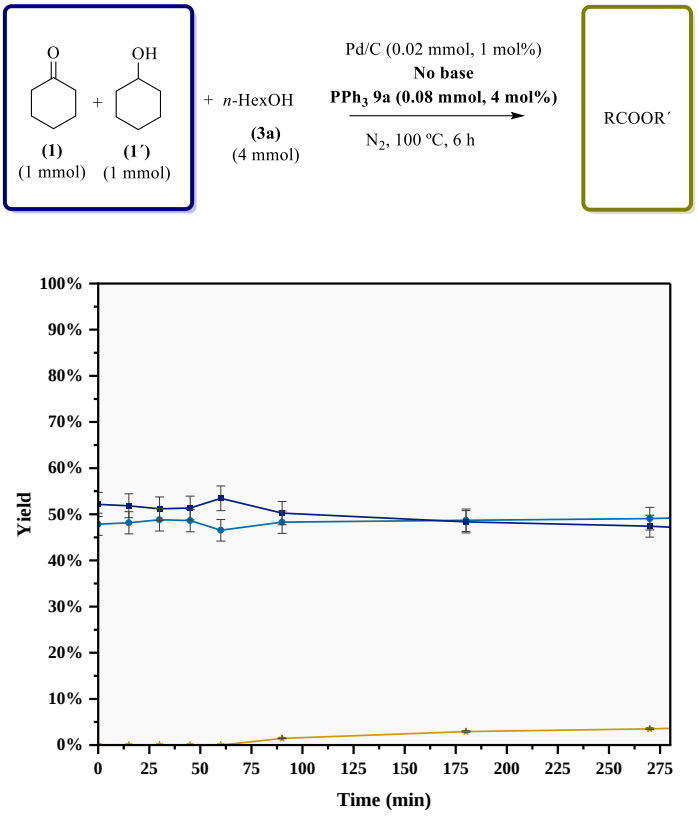

Figure 4-18 Kinetic plot for the reaction between a simulated KA oil mixture (1:1 ratio of (1) and (1´)) and (3a), under the indicated reaction conditions (with phosphine and without base). GC yields. Error bars account for a 5% uncertainty.

The Pd/C-(**9a**) catalyst demonstrated excellent recyclability, maintaining full activity over multiple cycles without requiring additional phosphine supplementation (Figures 4-19 and 4-20). These results indicate that the initially anchored phosphine species remain active throughout recycling. The solvent-free catalytic system, composed of commercially available Pd/C, KOH, and

phosphine (**9a**), offers key advantages for practical application: minimal waste generation (water as the only by-product), catalyst reusability, and straightforward scalability. A reaction conducted at a tenfold gram scale provided similar outcomes to those observed at smaller scales (Figure 4A-6, Appendix 4A-6), confirming the robustness of the methodology. Comparative experiments using $Pd(PPh_3)_4$ resulted in high conversion but a broad product distribution and complete loss of recoverable Pd, highlighting the superior reusability of the Pd/C– (**9a**) system. Although some contribution from leached Pd cannot be ruled out, the ability to recover most of the metal and ligand components (Figure 20) underscores the advantages of the supported catalyst. Solid-state ^{31}P magic angle spinning nuclear magnetic resonance (MAS NMR) spectroscopy confirmed phosphine immobilisation on Pd/C (Figure 4A-7, Appendix 4A-7), with chemical shifts distinct from those of PPh_3 (solid-state)[82], $Pd(PPh_2)Cl_2$ (solid-state)[82], $Pd(PPh_3)_4$ (in $CDCl_3$)[83], and PPh_3O (in $CDCl_3$)[84], suggesting the formation of a unique phosphine–Pd coordination environment.

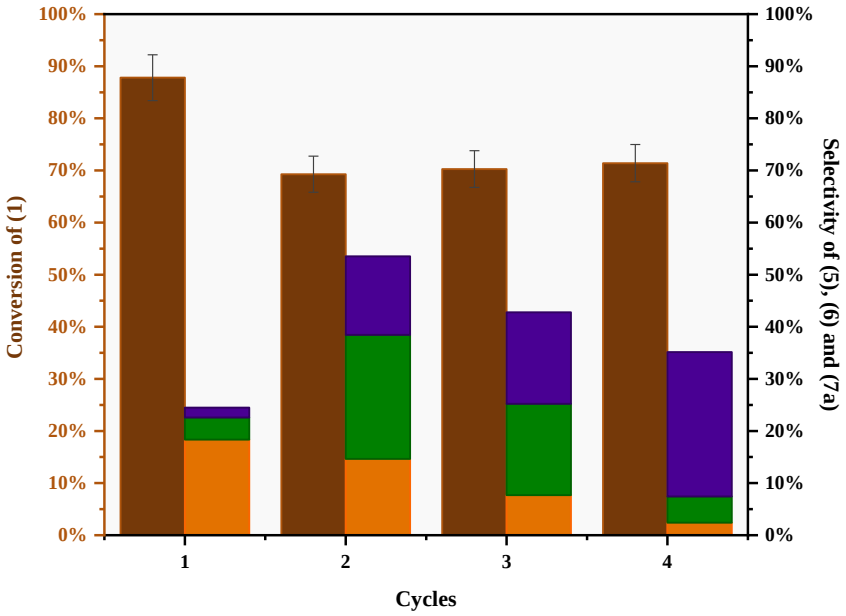

Figure 4-19 Reuse tests for the phosphine-modified Pd/C catalysts; profiles normalised by catalyst mass; PPh_3 (**9a**) (4 mol%) added in each new use of the catalyst. GC yields. Error bars account for a 5% uncertainty.

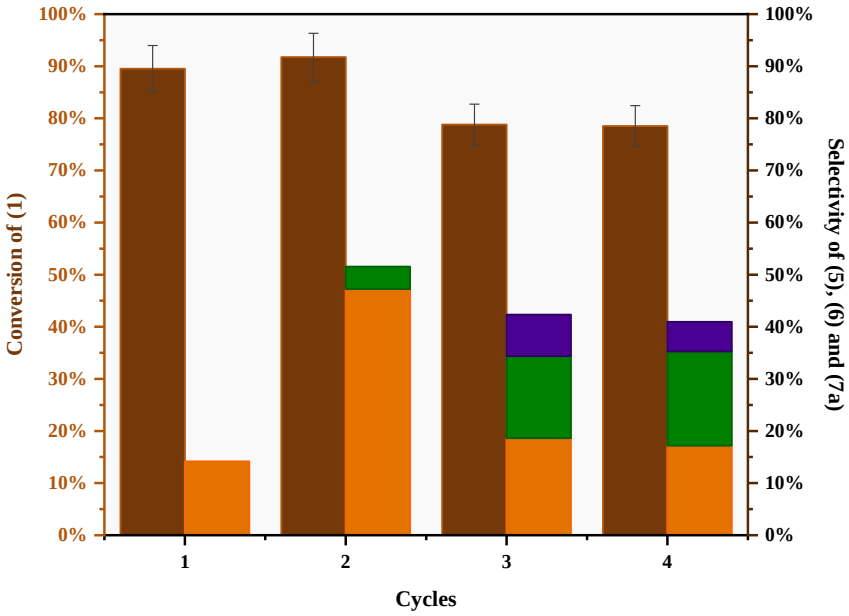

Figure 4-20 Reuse tests for the phosphine-modified Pd/C catalysts; profiles normalised by catalyst mass; PPh_3 (**9a**) (4 mol%) added in the first use of the catalyst, without additional phosphine added in further uses. GC yields. Error bars account for a 5% uncertainty.

4.3.4. Post-Coupling Hydrogenation and Proposed Mechanistic Pathway

Noble metal catalysts supported on carbon, such as palladium on carbon (Pd/C), are renowned for their capacity to facilitate hydrogenation reactions. These reactions encompass not only simple olefins but also carbonyl functional groups. [17, 85] This versatility in hydrogenation allows for a two-step approach: during the hydrogen-borrowing coupling of ketones and alcohols, partially oxygenated intermediates are formed, which can subsequently be selectively reduced to yield fully saturated hydrocarbon products.

The investigation explored a tandem, one-pot process involving a coupling reaction. The reaction mixture consisted of cyclohexanone (**1**), cyclohexanol (**1′**), enone (**5**), condensation products (**6**), hydrogenated intermediates (**7**), and the final alkylated products (**8**). Following the coupling phase, in-situ hydrogenation was conducted by adding more Pd/C catalyst and pressurising the reaction vessel to 30 bar of hydrogen (H_2), which was then heated to 200 °C for 48 hours. This post-treatment step efficiently converted all remaining unsaturated and oxygenated species into a saturated hydrocarbon mixture with carbon chain lengths ranging from C_6 to C_{18}. (Figure 4-21) The absence of aromatic or oxygenated byproducts[86,87] and the high selectivity for bis(cyclohexyl) compounds (53.7%), which dominate the final mixture, are consistent with SAF specifications, as confirmed by GC-MS/FTIR analyses. This ensures that the mixture meets the stringent specifications for synthetic aviation fuel.[88] This streamlined method, which integrates tandem carbon-carbon (C–C) bond formation through hydrogen borrowing with subsequent hydrogenation, offers a promising strategy for converting KA oil and bioalcohols into valuable fuel

components. The lack of oxygen-containing by-products and aromatic compounds further enhances the safety and performance profile of the resulting fuel candidates.

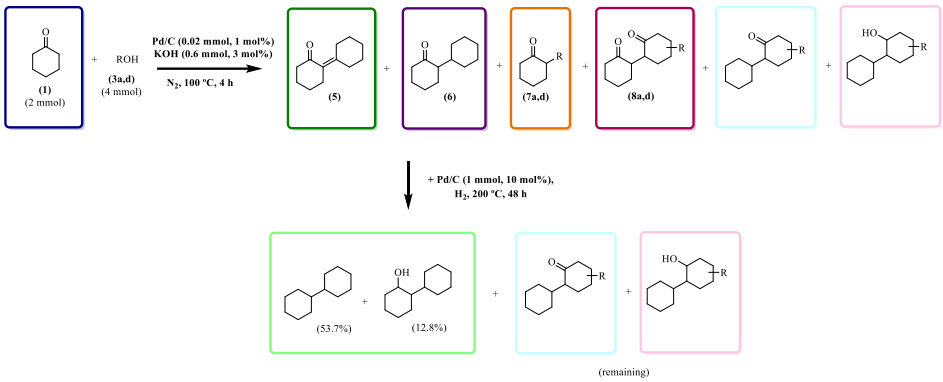

Figure 4-21 The in-situ hydrogenation of the cyclohexanone hydrocarbon mixture was performed utilizing the identical catalytic system under a pressure of 30 bar of hydrogen (H_2) at a temperature of 200 °C for 48 hours

To provide clarity on product distribution and explain the role of phosphine-ligated Pd/C catalysts in the coupling step, a proposed reaction mechanism is presented, illustrated through the transformation of cyclohexanone (**1**) and *n*-hexanol (**3a**), as shown in Figure 4-22. The reaction begins with the dehydrogenation of the alcohol, resulting in the corresponding aldehyde. This process is facilitated by the Pd/C-phosphine complex via a hydrogen-borrowing pathway[68], likely enhanced by the basic environment provided by KOH.[89] Concurrently, the ketone (**1**) undergoes base-promoted deprotonation to form an enolate-like intermediate. This intermediate then nucleophilically adds to the in situ-generated aldehyde, leading to the formation of a β-hydroxyketone intermediate. Subsequently, dehydration and reduction of the resulting α,β-

unsaturated compound occur, producing the saturated product (**7a**). In reactions that involve only cyclohexanone (**1**), this mechanism remains applicable, yielding an unsaturated intermediate (**5**) and a condensation product (**6**). Throughout the reaction, a reversible interconversion between cyclohexanone (**1**) and its corresponding alcohol (**1′**) (i.e., KA oil) is observed, which is expected under hydrogen transfer conditions. The formation of the final alkylated products (**8a**) is proposed to occur through a subsequent sequence of hydrogen-borrowing and deprotonation steps involving either compound (**6**) or intermediate (**7a**). Significantly, both the Pd/C-phosphine catalyst and KOH are engaged in at least five distinct steps of the catalytic cycle, which underscores the complexity and efficiency of this system. Furthermore, water is the only stoichiometric by-product, highlighting the sustainability and atom economy of the overall transformation.[47,68]

The nature of the hydrogen equivalents[86, 87] involved in these transformations' merits further discussion. In the mechanistic scheme, the notation [H_2] refers not to free molecular hydrogen but rather to surface-bound palladium hydride species (Pd–H), which function as transient hydrogen donors. This interpretation is supported by the lack of reactivity observed when compound (**5**) is used as the starting material under standard conditions, indicating that simple thermal hydrogenation, without in-situ hydride formation, fails to drive the reaction forward (see Figure 4A-4, Appendix 4A-4). In contrast, when compound (**6**) was employed as the starting material in the presence of alcohol (**3a**), the formation of alkylated products (**8**) was readily observed (see Figure 4A-8, Appendix 4A-8). This strongly reinforces the proposed hydrogen-borrowing and deprotonation sequence.

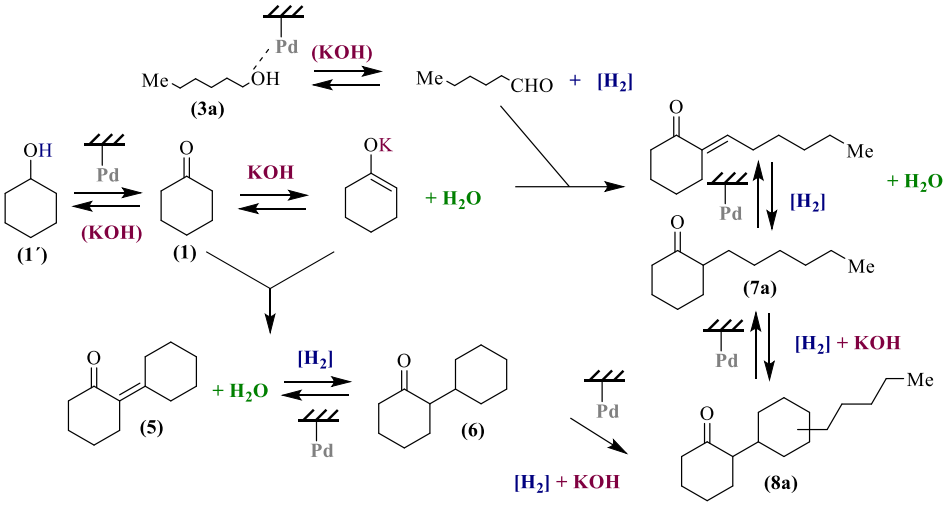

Figure 4-22 Tentative mechanism for the Pd/C–KOH catalysed coupling of KA oil with n-hexanol via hydrogen-borrowing. Pd is ligated by phosphines when applicable (omitted for clarity). [H_2] indicates Pd–H species acting as hydrogen donors.

In summary, the combined mechanistic and reactivity studies presented here provide a comprehensive picture of how phosphine-ligated Pd/C catalysts enable selective C–C bond formation from ketone-alcohol mixtures, and how subsequent in-situ hydrogenation can yield fully saturated hydrocarbon streams compatible with jet fuel applications. This dual-function catalytic strategy offers a scalable and efficient pathway for converting bio-derived feedstocks into renewable aviation fuels.

4.4. Conclusion

This chapter demonstrates the feasibility of producing sustainable aviation fuel (SAF) precursors through a solvent-free hydrogen-borrowing coupling of cyclohexanone (or KA oil) with bio-based alcohols, catalysed by Pd/C in the presence of KOH. The process is noted for its operational simplicity, high atom economy, and environmental compatibility, yielding only water as a by-product while utilising easily accessible catalytic materials.

A critical aspect of this study is the utilisation of phosphine ligands to influence the electronic environment of the Pd/C catalyst. A systematic examination of phosphines with varying electronic and steric properties revealed that the electronic characteristics of the ligands significantly impact catalytic activity. A pronounced inverse correlation was observed between the phosphines' νCO values and cyclohexanone's conversion rates, indicating that electron-rich phosphines enhance hydrogen-borrowing efficiency. This observation is consistent with established literature on phosphine-ligated palladium systems and was further corroborated by the performance of secondary dicyclohexyl phosphine (**9e**), which aligned well with the observed trend. In contrast, no notable correlation between catalytic performance and the steric properties of the phosphines was identified, suggesting that steric bulk within the examined range does not obstruct access to the active sites under the specified reaction conditions.

The mechanistic profile of the transformation indicates that hydrogen-borrowing reactivity predominates over base-mediated aldol pathways, as supported by control experiments involving isolated enones. The generation of highly alkylated products, relevant for SAF applications, is facilitated by surface-mediated

dehydrogenation and rehydrogenation steps, likely involving transient Pd–H species. Furthermore, solid-state ^{31}P MAS-NMR and PXRD analyses confirmed effective ligand coordination to the catalyst surface, with minimal phosphine degradation observed under the inert conditions employed.

The robustness and scalability of the catalytic system were also demonstrated. The combination of Pd/C and PPh_3 exhibited recyclability over multiple reaction cycles without significant loss of activity or selectivity.

These findings collectively highlight a viable catalytic strategy for converting biomass-derived ketones and alcohols into hydrocarbon-rich mixtures suitable for SAF formulations. The process adheres to key principles of green chemistry, such as waste reduction, catalyst reuse, and the utilisation of renewable feedstocks. By harnessing the tunability of phosphine ligands and the reusability of Pd/C, this catalytic system presents a promising pathway for developing scalable, low-aromatic, net-zero carbon aviation fuels.

4.5. Appendix

a) 4A-1

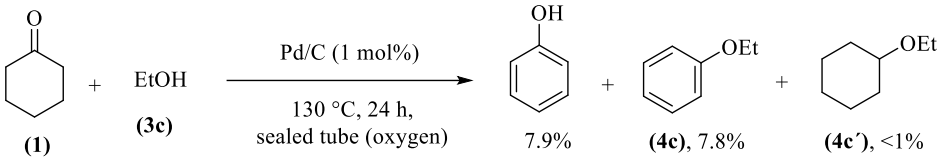

Figure 4A-1 Detailed catalytic results for the reaction between cyclohexanone 1 and ethanol 3c (entry 5 in Table 4-2). Exp. conditions: molar ratio (1)/(3c)= 1/5, Pd/C (5 wt%) = 1 mol%, 130 °C, 24 h. GC yields.

b) 4A-2

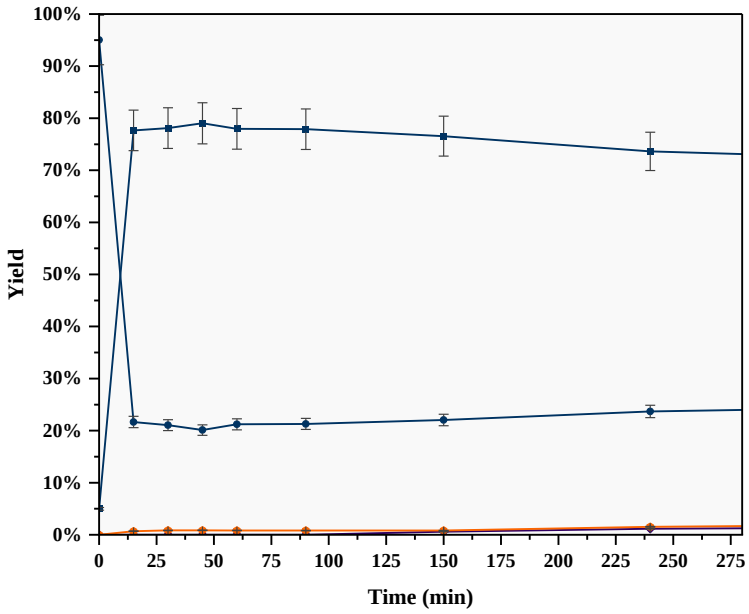

Figure 4A-2 Kinetic plot for the reaction between (1´) and (3a), under the indicated reaction conditions (without base and without phosphine). GC yields. Error bars account for a 5% uncertainty.

c) 4A-3

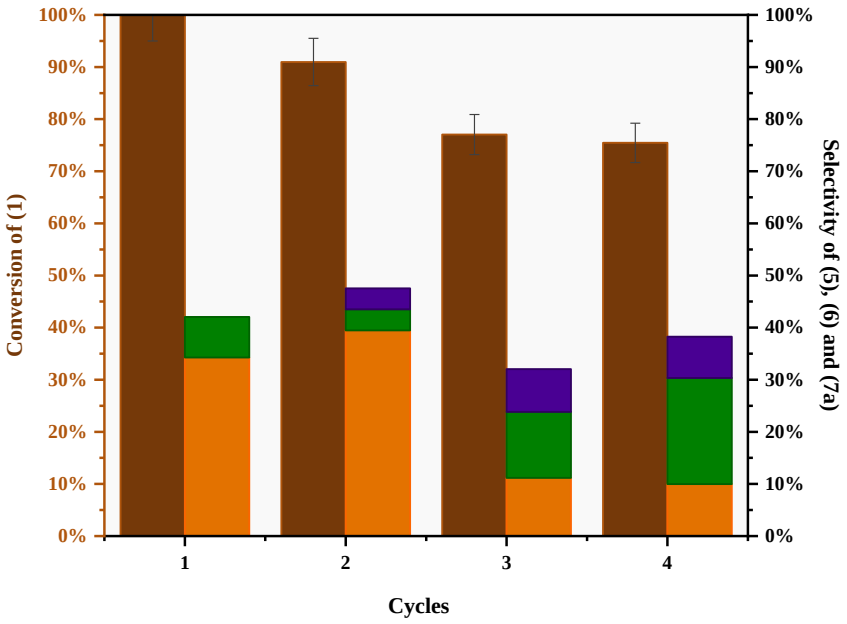

Figure 4A-3 Reuse tests for the reaction without phosphine (PPh_3), utilising just KOH and Pd/C catalysts; profiles normalised by catalyst mass. Top: conversion; bottom: selectivity. GC yields. Error bars account for a 5% uncertainty.

d) 4A-4

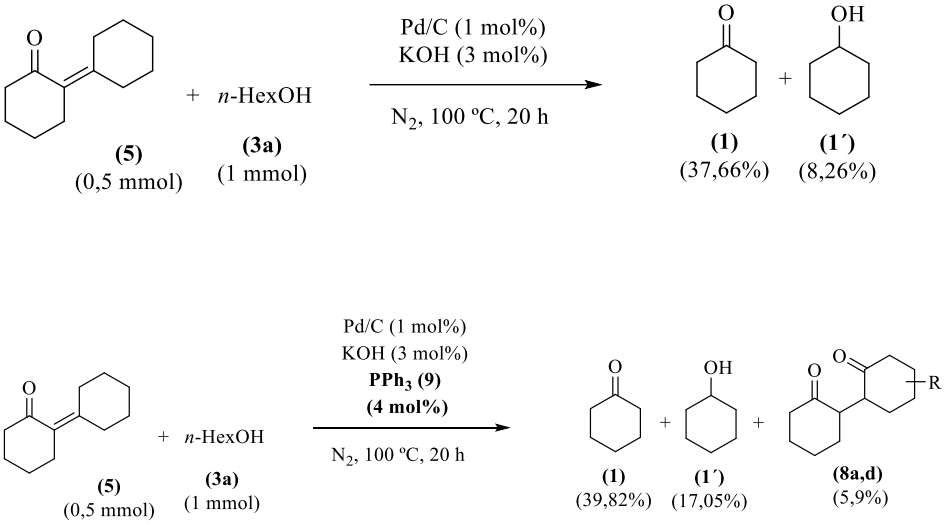

Figure 4A-4 Reactivity tests with unsaturated ketone (5) and alcohol 3a under Pd/C-catalyzed reaction conditions, either with (top) or without phosphine (bottom).

e) 4A-5

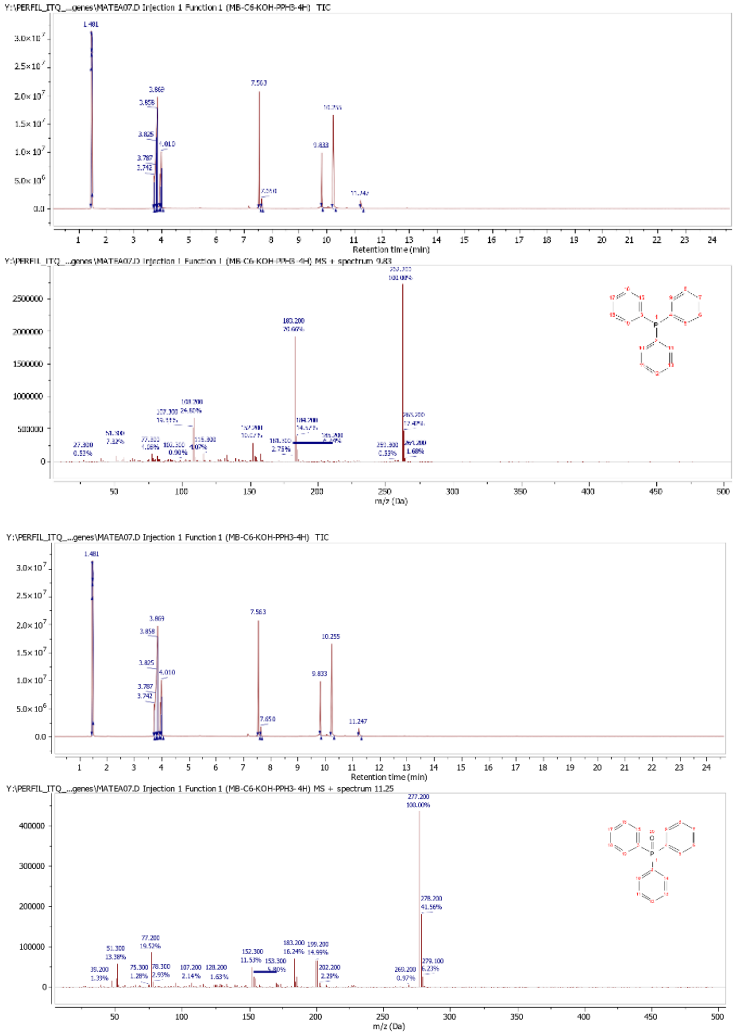

Figure 4A-5 Representative GC and GC-MS chromatograms of a reaction mixture, where the minor amounts of oxidised PPh_3 can be observed: PPh_3 oxidised (11.25 min retention time in the GC analysis of the reaction) and PPh_3 (9.83 min retention time in the GC analysis of the response).

f) 4A-6

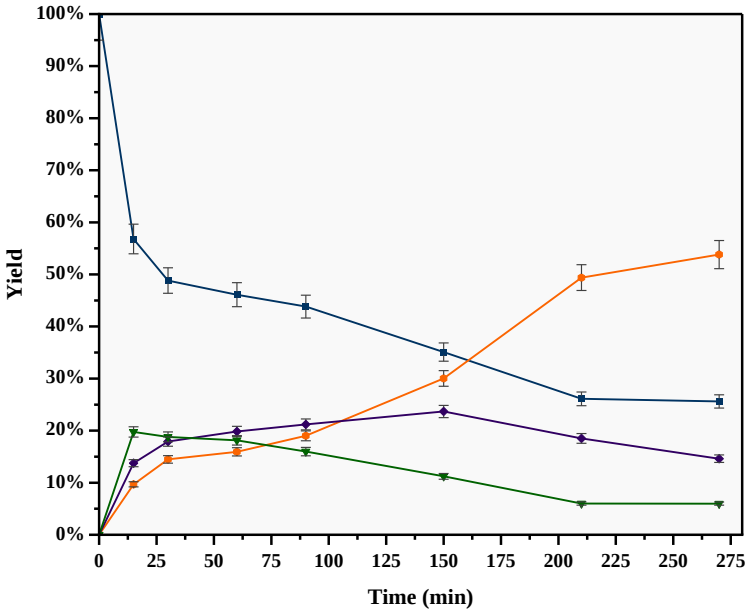

Figure 4A-6 Reaction at 10 times the gram scale, performed under optimised reaction conditions (see Figure 4-11 in the main text for reaction conditions and colour code). GC yields. Error bars account for a 5% uncertainty

g) 4A-7

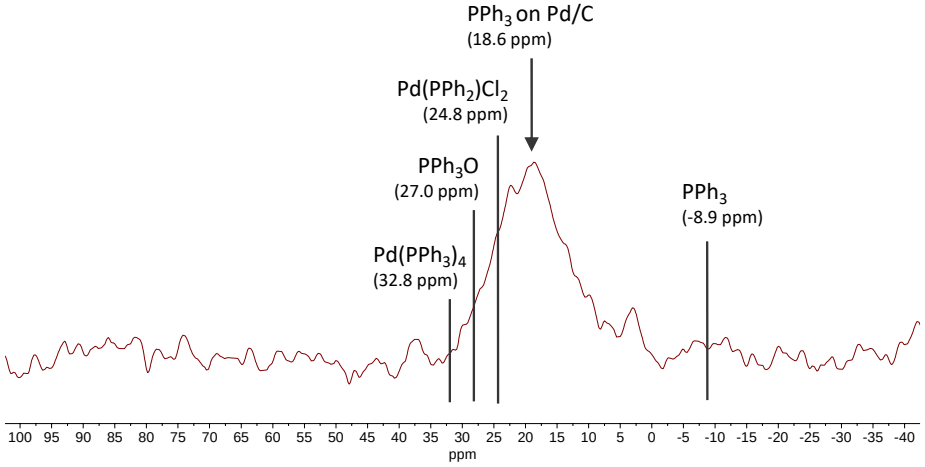

Figure 4A-7 ^{31}P solid state magic angle spinning nuclear magnetic resonance (MAS NMR) of the Pd/C catalyst mixed with one equivalent of triphenylphosphine (PPh_3). The catalyst and the phosphine were stirred together for one hour in ethanol, and the catalyst was centrifuged and separated and rinsed with cold ethanol. A new peak was observed in the spectrum at 18.6 ppm. The values for the ^{31}P chemical shifts of PPh_3 (solid-state NMR), $Pd(PPh_2)Cl_2$ (solid-state NMR), $Pd(PPh_3)_4$ (in $CDCl_3$) and PPh_3O (in $CDCl_3$) have been included for comparison.[65,66,76,90]

h) 4A-8

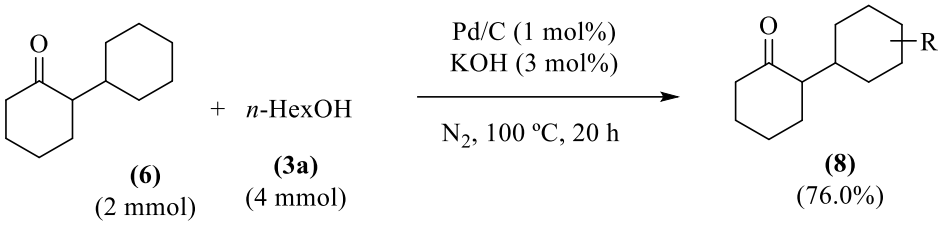

(6) (2 mmol)

(3a) (4 mmol)

(8) (76.0%)

Figure 4A-8 Reactivity test with the obtained product (6) and alcohol (3a) to confirm the formation of products (8); reaction was performed under optimized reaction conditions (see Figure 4-11 in the main text)

i) Product characterisation – Product 4a

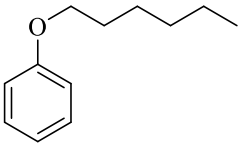

4a

(hexyloxy)benzene

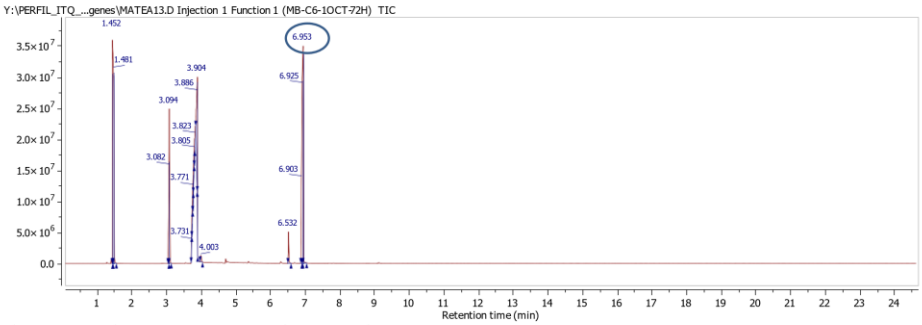

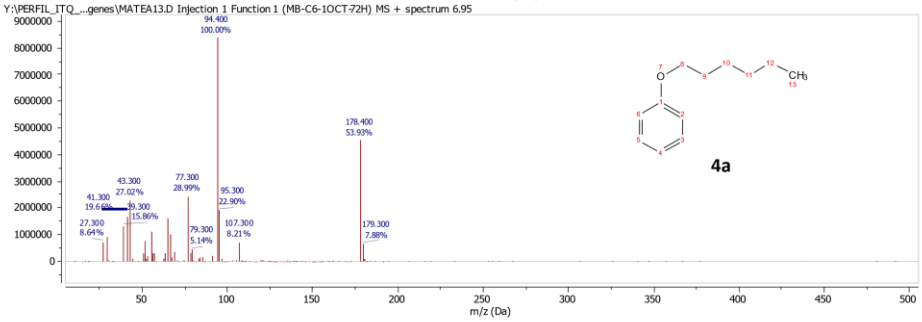

j) Product characterisation – Product 5

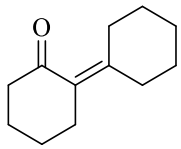

5

[1,1'-bi(cyclohexylidene)]-2-one

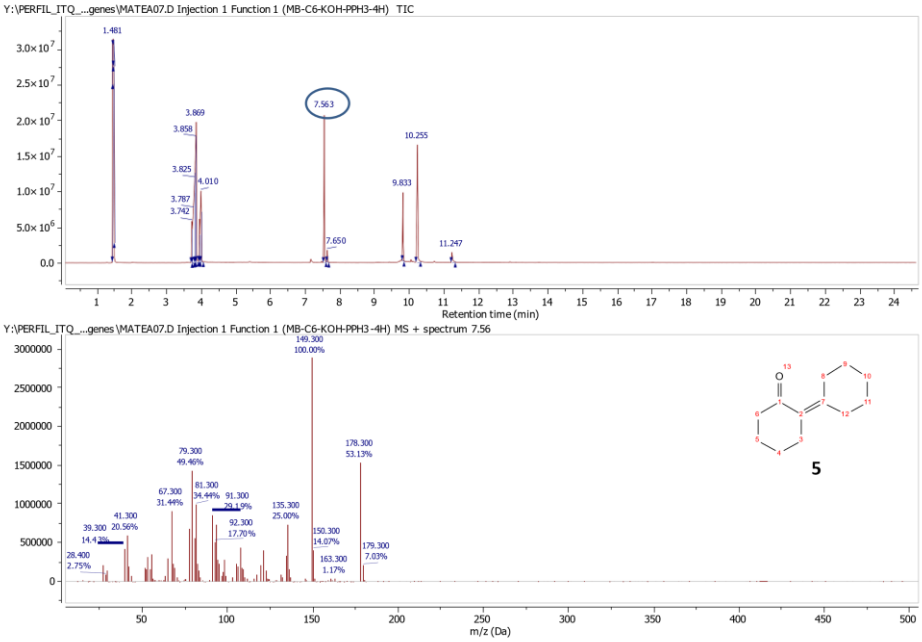

k) Product characterisation – Product 6

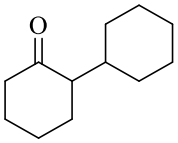

6

[1,1'-bi(cyclohexan)]-2-one

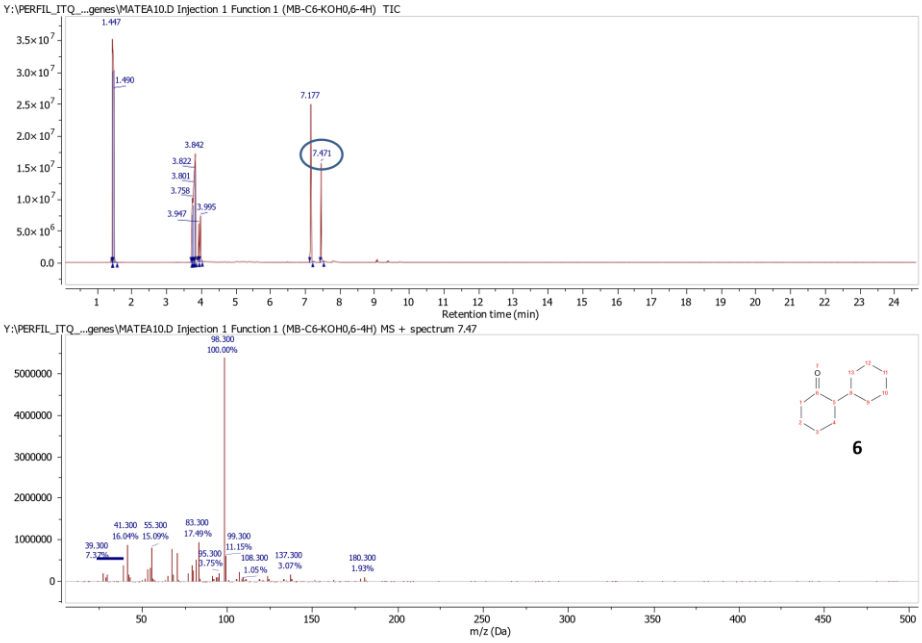

l) Product characterisation – Product 7a

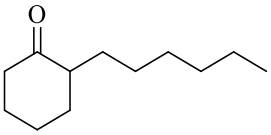

7a

2-hexylcyclohexan-1-one

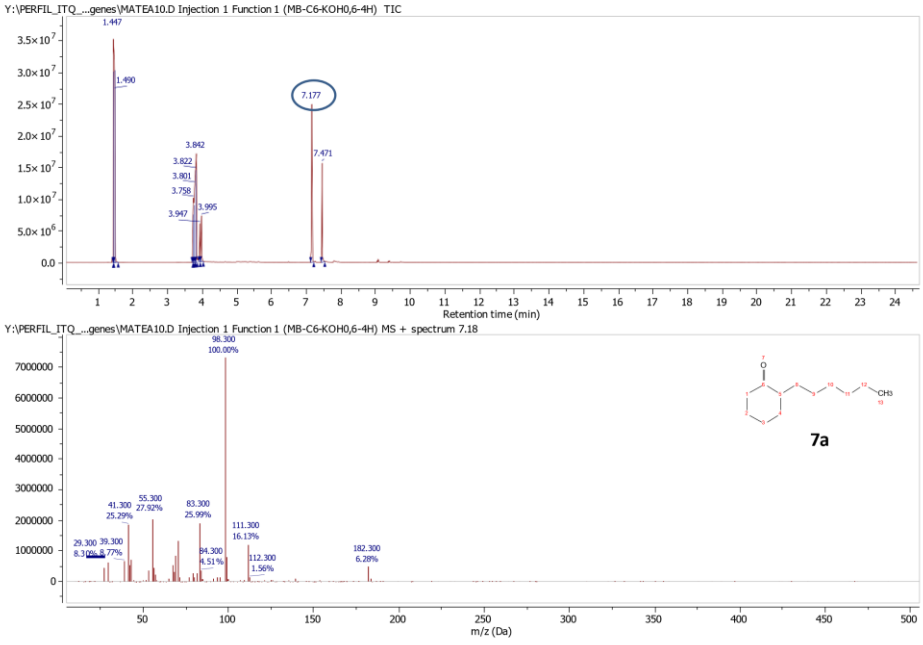

m) Product characterisation – Product 8a

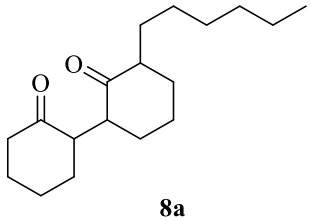

8a

3-hexyl-[1,1'-bi(cyclohexane)]-2,2'-dione

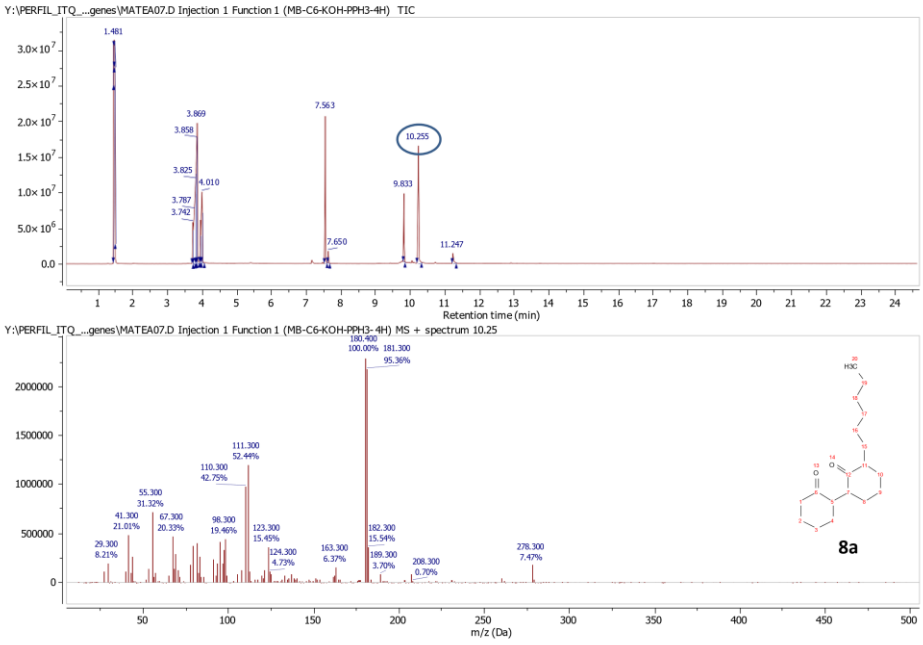

4.6. References

1. Climate Change 2022 - Mitigation of Climate Change. *Clim Chang 2022 - Mitig Clim Chang*. Published online 2023. doi:10.1017/9781009157926

2. Hizarci H, Arifoğlu U. Challenges with the electrification of aircraft for a sustainable and greener aviation. *Int J Sustain Aviat*. 2023;9(1):58-72. doi:10.1504/IJSA.2023.127484

3. Agreement P. Pathways towards 90% decarbonization of aviation by 2050. *Nat Clim Chang*. 2022;12(10):895-896. doi:10.1038/s41558-022-01486-3

4. Szyc R, Lenort R. Sustainable Aviation Fuels as the Path to Carbon Neutrality in Air Transport. *Rocz Ochr Sr*. 2024;26(December):707-715. doi:10.54740/ros.2024.062

5. European Commission. Reducing emissions from aviation - European Commission. *EcEuropaEu*. Published online 2015. https://ec.europa.eu/clima/policies/transport/aviation_en

6. Bergero C, Gosnell G, Gielen D, Kang S, Bazilian M, Davis SJ. Pathways to net-zero emissions from aviation. *Nat Sustain*. 2023;6(4):404-414. doi:10.1038/s41893-022-01046-9

7. International Air Transport Association. Net zero 2050: Sustainable Aviation Fuels. *IATA Fact sheet*. 2023;(December):1-3. chrome-extension://efaidnbmnnnibpcajpcglclefindmkaj/https://www.iata.org/en/iata-repository/pressroom/fact-sheets/fact-sheet---alternative-fuels/

8. IATA. IATA - Sustainable Aviation Fuel (SAF). *Int Air Transp Assoc*. Published online 2023. https://www.iata.org/en/programs/environment/sustainable-aviation-fuels/

9. Esqué A, Franz F, Mulder G, Riedel R, Riefer D. Decarbonizing aviation: Executing on net-zero goals. 2023;(June).

10. Zahid I, Nazir MH, Chiang K, Christo F, Ameen M. Current outlook on sustainable feedstocks and processes for sustainable aviation fuel production. *Curr Opin Green Sustain Chem*. 2024;49:100959. doi:10.1016/j.cogsc.2024.100959

11. Commission E. CASE M . 8674 – BASF / Solvay ' s Polyamide Business MERGER PROCEDURE REGULATION (EC) 139 / 2004. 2019;8(2).

12. Chang CF, Paragian K, Sadula S, Rangarajan S, Vlachos DG. Sustainable Aviation Fuel Molecules from (Hemi)Cellulose: Computational Insights into Synthesis Routes, Fuel Properties, and Process Chemistry Metrics. *ACS Sustain Chem Eng*. 2024;12(34):12927-12937. doi:10.1021/acssuschemeng.4c04199

13. Wang H, Wang H, Kuhn E, Tucker MP, Yang B. Production of Jet Fuel-Range Hydrocarbons from Hydrodeoxygenation of Lignin over Super Lewis Acid Combined with Metal Catalysts. *ChemSusChem*. 2018;11(1):285-291. doi:10.1002/cssc.201701567

14. Wang W, Li N, Li G, et al. Synthesis of renewable high-density fuel with cyclopentanone derived from hemicellulose. *ACS Sustain Chem Eng*. 2017;5(2):1812-1817. doi:10.1021/acssuschemeng.6b02554

15. Wang R, Li G, Tang H, et al. Synthesis of Decaline-Type Thermal-Stable Jet Fuel Additives with Cycloketones. *ACS Sustain Chem Eng*. 2019;7(20):17354-17361. doi:10.1021/acssuschemeng.9b04288

16. Zhou WJ, Wischert R, Xue K, et al. Erratum: Highly selective liquid-phase oxidation of cyclohexane to KA oil over Ti-MWW catalyst: Evidence of formation of oxyl radicals (ACS Catalysis (2014) 4:1 (53-62)). *ACS Catal*. 2014;4(5):1616. doi:10.1021/cs500400v

17. Rubio-Marqués P, Hernández-Garrido JC, Leyva-Pérez A, Corma A. One pot synthesis of cyclohexanone oxime from nitrobenzene using a bifunctional catalyst. *Chem Commun*. 2014;50(14):1645-1647. doi:10.1039/c3cc47693f

18. Wu D, Wang Q, Safonova O V., et al. Lignin Compounds to Monoaromatics: Selective Cleavage of C−O Bonds over a Brominated Ruthenium Catalyst. *Angew Chemie - Int Ed*. 2021;60(22):12513-12523. doi:10.1002/anie.202101325

19. Meng Q, Yan J, Wu R, et al. Sustainable production of benzene from lignin. *Nat Commun*. 2021;12(1):1-12. doi:10.1038/s41467-021-24780-8

20. He S, Klein FGH, Kramer TS, et al. Catalytic Conversion of Free Fatty Acids to Bio-Based Aromatics: A Model Investigation Using Oleic Acid and an H-ZSM-5/Al2O3Catalyst. *ACS Sustain Chem Eng*. 2021;9(3):1128-1141. doi:10.1021/acssuschemeng.0c06181

21. Palla VCS, Shee D, Maity SK. Production of Aromatics from n-Butanol over HZSM-5, H-β, and γ-Al2O3: Role of Silica/Alumina Mole Ratio and Effect of Pressure. *ACS Sustain Chem Eng*. 2020;8(40):15230-15242. doi:10.1021/acssuschemeng.0c04888

22. Gong Q, Fang T, Xie Y, et al. High-Efficiency Conversion of Methanol to BTX Aromatics over a Zn-Modified Nanosheet-HZSM-5 Zeolite. *Ind Eng Chem Res*. 2021;60(4):1633-1641. doi:10.1021/acs.iecr.0c06342

23. Natesakhawat S, Means NC, Howard BH, et al. Improved benzene production from methane dehydroaromatization over Mo/HZSM-5 catalysts via hydrogen-permselective palladium membrane reactors. *Catal Sci Technol*. 2015;5(11):5023-5036. doi:10.1039/c5cy00934k

24. Fang X, Liu H, Chen Z, et al. Highly Enhanced Aromatics Selectivity by Coupling of Chloromethane and Carbon Monoxide over H-ZSM-5. *Angew Chemie - Int Ed*. 2022;61(13):1-6. doi:10.1002/anie.202114953

25. Zhao C, Kou Y, Lemonidou AA, Li X, Lercher JA. Highly selective catalytic conversion of phenolic bio-oil to alkanes. *Angew Chemie - Int Ed*. 2009;48(22):3987-3990. doi:10.1002/anie.200900404

26. Chang J, Danuthai T, Dewiyanti S, Wang C, Borgna A. Hydrodeoxygenation of

guaiacol over carbon-supported metal catalysts. *ChemCatChem*. 2013;5(10):3041-3049. doi:10.1002/cctc.201300096

27. Gui C, Wang L, Liu G, Ogunbiyi AT, Li W. The Catalytic Valorization of Lignin from Biomass for the Production of Liquid Fuels. *Energies*. 2025;18(6). doi:10.3390/en18061478

28. Zhang J, Webber MS, Pu Y, et al. Sustainable aviation fuels from biomass and biowaste via bio- and chemo-catalytic conversion: Catalysis, process challenges, and opportunities. *Green Energy Environ*. 2025;(xxxx). doi:10.1016/j.gee.2024.09.003

29. Chen X, Orton KA, Mukarakate C, et al. Cycloalkane-rich sustainable aviation fuel production via hydrotreating lignocellulosic biomass-derived catalytic fast pyrolysis oils. *Sustain Energy Fuels*. Published online 2024:5504-5513. doi:10.1039/d4se01151a

30. Ahire JP, Bergman R, Runge T, et al. Techno-economic and environmental impacts assessments of sustainable aviation fuel production from forest residues. *Sustain Energy Fuels*. Published online 2024:4602-4616. doi:10.1039/d4se00749b

31. Griffin MB, Iisa K, Dutta A, et al. Opening pathways for the conversion of woody biomass into sustainable aviation fuel via catalytic fast pyrolysis and hydrotreating. *Green Chem*. Published online 2024:9768-9781. doi:10.1039/d4gc03333g

32. ASTM. Standard Specification for Aviation Turbine Fuel Containing Synthesized Hydrocarbons. *Annu B ASTM Stand*. Published online 2017:1-16. doi:10.1520/D7566-22.operated

33. Martín A, Arribas-Yuste E, Paniagua M, Morales G, Melero JA. Efficient Self-Condensation of Cyclohexanone into Biojet Fuel Precursors over Sulfonic Acid-Modified Silicas: Insights on the Effect of Pore Size and Structure. *ACS Sustain*

Chem Eng. 2024;12(27):10175-10185. doi:10.1021/acssuschemeng.4c01956

34. Jessop PG, Ikariya T, Noyori R. Homogeneous Hydrogenation of Carbon Dioxide. *Chem Rev*. 1995;95(2):259-272. doi:10.1021/cr00034a001

35. Gabriëls D, Hernández WY, Sels BF, Van Der Voort P, Verberckmoes A. Review of catalytic systems and thermodynamics for the Guerbet condensation reaction and challenges for biomass valorization. *Catal Sci Technol*. 2015;5(8):3876-3902. doi:10.1039/c5cy00359h

36. Gao H, Han F, Li G, et al. Synthesis of jet fuel range high-density polycycloalkanes with vanillin and cyclohexanone†. *Sustain Energy Fuels*. 2022;6(6):1616-1624. doi:10.1039/d1se01732b

37. Taguchi K, Nakagawa H, Hirabayashi T, Sakaguchi S, Ishii Y. An Efficient Direct α-Alkylation of Ketones with Primary Alcohols Catalyzed by [Ir(cod)CI]2/PPh3/KOH System without Solvent. *J Am Chem Soc*. 2004;126(1):72-73. doi:10.1021/ja037552c

38. Corma A, Ródenas T, Sabater MJ. A bifunctional PdVMgO solid catalyst for the one-pot selective N-monoalkylation of amines with alcohols. *Chem - A Eur J*. 2010;16(1):254-260. doi:10.1002/chem.200901501

39. Breitkreuz K; Menne A; Kraft A. New process for sustainable fuels and chemicals from bio-based alcohols and acetone Klaas. *Biofuels, Bioprod Biorefining*. 2014;8(6):743. doi:10.1002/BBB

40. Sutter M, Sotto N, Raoul Y, Métay E, Lemaire M. Straightforward heterogeneous palladium catalyzed synthesis of aryl ethers and aryl amines via a solvent free aerobic and non-aerobic dehydrogenative arylation. *Green Chem*. 2013;15(2):347-352. doi:10.1039/c2gc36776a

41. Sutter M, Lafon R, Raoul Y, Métay E, Lemaire M. Heterogeneous palladium-catalyzed synthesis of aromatic ethers by solvent-free dehydrogenative aromatization: Mechanism, scope, and limitations under aerobic and non-aerobic

conditions. *European J Org Chem*. 2013;(26):5902-5916. doi:10.1002/ejoc.201300485

42. Simon MO, Girard SA, Li CJ. Catalytic aerobic synthesis of aromatic ethers from non-aromatic precursors. *Angew Chemie - Int Ed*. 2012;51(30):7537-7540. doi:10.1002/anie.201200698

43. Nimmanwudipong T, Runnebaum RC, Tay K, Block DE, Gates BC. Cyclohexanone conversion catalyzed by Pt/γ-Al2O 3: Evidence of oxygen removal and coupling reactions. *Catal Letters*. 2011;141(8):1072-1078. doi:10.1007/s10562-011-0659-2

44. Zhao C, Camaioni DM, Lercher JA. Selective catalytic hydroalkylation and deoxygenation of substituted phenols to bicycloalkanes. *J Catal*. 2012;288:92-103. doi:10.1016/j.jcat.2012.01.005

45. Rubio-Marqués P, Leyva-Pérez A, Corma A. A bifunctional palladium/acid solid catalyst performs the direct synthesis of cyclohexylanilines and dicyclohexylamines from nitrobenzenes. *Chem Commun*. 2013;49(74):8160-8162. doi:10.1039/c3cc44064h

46. Dunås P, Paterson AJ, Lewis SE, Kann N. Carbon-carbon bond formation using aromatics from biomass. *Chem Commun*. Published online 2024:14885-14895. doi:10.1039/d4cc05664g

47. Corma A, Navas J, Sabater MJ. Advances in One-Pot Synthesis through Borrowing Hydrogen Catalysis. *Chem Rev*. 2018;118(4):1410-1459. doi:10.1021/acs.chemrev.7b00340

48. Climent MJ, Corma A, Iborra S, Sabater MJ. Heterogeneous catalysis for tandem reactions. *ACS Catal*. 2014;4(3):870-891. doi:10.1021/cs401052k

49. Kumar A, Daw P, Milstein D. Homogeneous Catalysis for Sustainable Energy: Hydrogen and Methanol Economies, Fuels from Biomass, and Related Topics. *Chem Rev*. 2022;122(1):385-441. doi:10.1021/acs.chemrev.1c00412

50. Nuri A, Vucetic N, Smått JH, Mansoori Y, Mikkola JP, Murzin DY. Pd Supported IRMOF-3: Heterogeneous, Efficient and Reusable Catalyst for Heck Reaction. *Catal Letters*. 2019;149(7):1941-1951. doi:10.1007/s10562-019-02756-0

51. Rasina D, Kahler-Quesada A, Ziarelli S, et al. Heterogeneous palladium-catalysed Catellani reaction in biomass-derived γ-valerolactone. *Green Chem*. 2016;18(18):5025-5030. doi:10.1039/c6gc01393g

52. Xue T, Lin Z, Chiu CY, et al. Molecular ligand modulation of palladium nanocatalysts for highly efficient and robust heterogeneous oxidation of cyclohexenone to phenol. *Sci Adv*. 2017;3(1):1-6. doi:10.1126/sciadv.1600615

53. Uno K, Itoh T, Sato H, Lloyd-Jones GC, Orito Y. Direct Observation of Palladium Leaching from Pd/C by a Simple Method: X-ray Absorption Spectroscopy of Heterogeneous Mixtures. *ACS Omega*. 2023;8(24):21787-21792. doi:10.1021/acsomega.3c01343

54. Espinosa JC, Contreras RC, Navalón S, et al. Influence of Carbon Supports on Palladium Nanoparticle Activity toward Hydrodeoxygenation and Aerobic Oxidation in Biomass Transformations. *Eur J Inorg Chem*. 2019;2019(14):1979-1987. doi:10.1002/ejic.201900190

55. Yue C, Xing Q, Sun P, Zhao Z, Lv H, Li F. Enhancing stability by trapping palladium inside N-heterocyclic carbene-functionalized hypercrosslinked polymers for heterogeneous C-C bond formations. *Nat Commun*. 2021;12(1):1-14. doi:10.1038/s41467-021-22084-5

56. Li MB, Bäckvall JE. Efficient Heterogeneous Palladium Catalysts in Oxidative Cascade Reactions. *Acc Chem Res*. 2021;54(9):2275-2286. doi:10.1021/acs.accounts.1c00122

57. Son SU, Jang Y, Yoon KY, Kang E, Hyeon T. Facile synthesis of various phosphine-stabilized monodisperse palladium nanoparticles through the understanding of coordination chemistry of the nanoparticles. *Nano Lett*.

2004;4(6):1147-1151. doi:10.1021/nl049519+

58. Ramirez E, Jansat S, Philippot K, et al. Influence of organic ligands on the stabilization of palladium nanoparticles. *J Organomet Chem*. 2004;689(24 SPEC. ISS.):4601-4610. doi:10.1016/j.jorganchem.2004.09.006

59. McCue AJ, McKenna FM, Anderson JA. Triphenylphosphine: A ligand for heterogeneous catalysis too? Selectivity enhancement in acetylene hydrogenation over modified Pd/TiO2 catalyst. *Catal Sci Technol*. 2015;5(4):2449-2459. doi:10.1039/c5cy00065c

60. Guo M, Li H, Ren Y, Ren X, Yang Q, Li C. Improving Catalytic Hydrogenation Performance of Pd Nanoparticles by Electronic Modulation Using Phosphine Ligands. *ACS Catal*. 2018;8(7):6476-6485. doi:10.1021/acscatal.8b00872

61. Sánchez-Resa D, Delgado JA, Fernández-Martínez MD, et al. Pd, Cu and Bimetallic PdCu NPs Supported on CNTs and Phosphine-Functionalized Silica: One-Pot Preparation, Characterization and Testing in the Semi-Hydrogenation of Alkynes. *Eur J Inorg Chem*. 2021;2021(47):4970-4978. doi:10.1002/ejic.202100806

62. Staiger L, Kratky T, Günther S, et al. Steric and Electronic Effects of Phosphane Additives on the Catalytic Performance of Colloidal Palladium Nanoparticles in the Semi-Hydrogenation of Alkynes. *ChemCatChem*. 2021;13(1):227-234. doi:10.1002/cctc.202001121

63. Fernández-Martínez MD, Godard C. Hydrogenation of CO2 into Formates by Ligand-Capped Palladium Heterogeneous Catalysts. *ChemCatChem*. 2023;15(6):2-8. doi:10.1002/cctc.202201408

64. Ballesteros-Soberanas J, Leyva-Pérez A. Electron-Poor Phosphines Enable the Selective Semihydrogenation Reaction of Alkynes with Pd on Carbon Catalysts. *J Phys Chem Lett*. 2023;14(4):965-970. doi:10.1021/acs.jpclett.2c03428

65. Wu L, Li BL, Huang YY, Zhou HF, He YM, Fan QH. Phosphine dendrimer-

stabilized palladium nanoparticles, a highly active and recyclable catalyst for the Suzuki-Miyaura reaction and hydrogenation. *Org Lett*. 2006;8(16):3605-3608. doi:10.1021/ol0614424

66. Ortuño MA, López N. Creating Cavities at Palladium-Phosphine Interfaces for Enhanced Selectivity in Heterogeneous Biomass Conversion. *ACS Catal*. 2018;8(7):6138-6145. doi:10.1021/acscatal.8b01302

67. Fantoni T, Palladino C, Grigolato R, et al. Mastering palladium-catalyzed cross-coupling reactions: the critical role of in situ pre-catalyst reduction design. *Org Chem Front*. 2025;(0):1982-1991. doi:10.1039/d4qo02335h

68. Reed-Berendt BG, Latham DE, Dambatta MB, Morrill LC. Borrowing Hydrogen for Organic Synthesis. *ACS Cent Sci*. 2021;7(4):570-585. doi:10.1021/acscentsci.1c00125

69. Balanta A, Godard C, Claver C. Pd nanoparticles for C-C coupling reactions. *Chem Soc Rev*. 2011;40(10):4973-4985. doi:10.1039/c1cs15195a

70. Liu J, Yang J, Ferretti F, Jackstell R, Beller M. Pd-Catalyzed Selective Carbonylation of gem-Difluoroalkenes: A Practical Synthesis of Difluoromethylated Esters. *Angew Chemie - Int Ed*. 2019;58(14):4690-4694. doi:10.1002/anie.201813801

71. Dobereiner GE, Crabtree RH. Dehydrogenation as a substrate-activating strategy in homogeneous transition-metal catalysis. *Chem Rev*. 2010;110(2):681-703. doi:10.1021/cr900202j

72. Biffis A, Centomo P, Del Zotto A, Zecca M. Pd Metal Catalysts for Cross-Couplings and Related Reactions in the 21st Century: A Critical Review. *Chem Rev*. 2018;118(4):2249-2295. doi:10.1021/acs.chemrev.7b00443

73. Wang H, Male J, Wang Y. Recent advances in hydrotreating of pyrolysis bio-oil and its oxygen-containing model compounds. *ACS Catal*. 2013;3(5):1047-1070. doi:10.1021/cs400069z

74. Liu L, Corma A. Metal Catalysts for Heterogeneous Catalysis: From Single Atoms to Nanoclusters and Nanoparticles. *Chem Rev*. 2018;118(10):4981-5079. doi:10.1021/acs.chemrev.7b00776

75. Richardson JM, Jones CW. Poly(4-vinylpyridine) and Quadrapure TU as selective poisons for soluble catalytic species in palladium-catalyzed coupling reactions - Application to leaching from polymer-entrapped palladium. *Adv Synth Catal*. 2006;348(10-11):1207-1216. doi:10.1002/adsc.200606021

76. Suresh CH, Koga N. Quantifying the electronic effect of substituted phosphine ligands via molecular electrostatic potential. *Inorg Chem*. 2002;41(6):1573-1578. doi:10.1021/ic0109400

77. Tolman CA. Steric Effects of Phosphorus Ligands in Organometallic Chemistry and Homogeneous Catalysis. *Chem Rev*. 1977;77(3):313-348. doi:10.1021/cr60307a002

78. Jover J, Cirera J. Computational assessment on the Tolman cone angles for P-ligands. *Dalt Trans*. 2019;48(40):15036-15048. doi:10.1039/c9dt02876e

79. Garnes-Portolés F, Sanz-Navarro S, Ballesteros-Soberanas J, et al. Indomuscone-Based Sterically Encumbered Phosphines as Ligands for Palladium-Catalyzed Reactions. *J Org Chem*. 2023;88(9):5962-5971. doi:10.1021/acs.joc.3c00314

80. Shabalin AY, Adonin NY, Bardin V V., Parmon VN. The influence of the nature of phosphine ligand on palladium catalysts for cross-coupling of weakly nucleophilic potassium pentafluorophenyltrifluoroborate with ArHal and PhCH2Hal (Hal=Br, Cl). *Tetrahedron*. 2014;70(23):3720-3725. doi:10.1016/j.tet.2014.04.019

81. Zhao K, Wang H, Li T, et al. Identification of a potent palladium-aryldiphosphine catalytic system for high-performance carbonylation of alkenes. *Nat Commun*. 2024;15(1):1-11. doi:10.1038/s41467-024-46286-9

82. Maheut G, Hervieu M, Fernandez C, Montouillout V, Villemin D, Jaffrès PA.

Palladium complex immobilised on zirconium-phosphite: Characterisation by 31P MAS NMR and TEM and behaviour towards reducing agents. *J Mol Struct*. 2003;659(1-3):135-142. doi:10.1016/S0022-2860(03)00409-5

83. Ye E, Tan H, Li S, Fan WY. Self-organization of spherical, core-shell palladium aggregates by laser-induced and thermal decomposition of [Pd(PPh3)4]. *Angew Chemie - Int Ed*. 2006;45(7):1120-1123. doi:10.1002/anie.200503408

84. Moedritzer K, Maier L, Groenweghe LCD. Phosphorus-31 Nuclear Magnetic Resonance Spectra of Phosphorus Compounds. *J Chem Eng Data*. 1962;7(2):307-310. doi:10.1021/je60013a043

85. Rivero-Crespo MA, Rubio-Marqués P, Hernández-Garrido JC, Mon M, Oliver-Meseguer J, Leyva-Pérez A. Intimate ruthenium-platinum nanoalloys supported on carbon catalyze the hydrogenation and one-pot hydrogenation-coupling reaction of oxidized amino derivatives. *Catal Sci Technol*. 2023;13(8):2508-2516. doi:10.1039/d2cy01846b

86. Polidano K, Allen BDW, Williams JMJ, Morrill LC. Iron-Catalyzed Methylation Using the Borrowing Hydrogen Approach. *ACS Catal*. 2018;8(7):6440-6445. doi:10.1021/acscatal.8b02158

87. Fridrich B, Stuart MCA, Barta K. Selective Coupling of Bioderived Aliphatic Alcohols with Acetone Using Hydrotalcite Derived Mg-Al Porous Metal Oxide and Raney Nickel. *ACS Sustain Chem Eng*. 2018;6(7):8468-8475. doi:10.1021/acssuschemeng.8b00733

88. Chau HK, Resasco DE, Do P, Crossley SP. Acylation of m-cresol with acetic acid supported by in-situ ester formation on H-ZSM-5 zeolites. *J Catal*. 2022;406:48-55. doi:10.1016/j.jcat.2021.12.020

89. Chen W, Sohail M, Veeranna Y, et al. N-Alkylation through the Borrowing Hydrogen Pathway Catalyzed by the Metal-Organic Framework-Supported Iridium-Monophosphine Complex. *ACS Appl Mater Interfaces*. Published online

2024. doi:10.1021/acsami.4c02143

90. Mastalir Á, Rác B, Király Z, Molnár Á. In situ generation of Pd nanoparticles in MCM-41 and catalytic applications in liquid-phase alkyne hydrogenations. *J Mol Catal A Chem*. 2007;264(1-2):170-178. doi:10.1016/j.molcata.2006.09.021

Chapter 5.

Pd and Pd–Au Catalysts on MOF and Zeolite Supports for Selective Acetylene Semi-Hydrogenation in Ethylene-Rich Feedstocks

Index

5.1. Introduction

The production of ethylene (C_2H_4) is a pivotal aspect of the global petrochemical industry. Ethylene serves as a primary feedstock for a diverse array of materials, most prominently polyethylene, which is the most extensively produced plastic worldwide, with annual production surpassing 100 million tons.[1]

The predominant industrial method for generating ethylene is steam cracking of hydrocarbons, such as ethane, propane and naphtha. However, this high-temperature process inherently produces a complex mixture of by-products, most notably acetylene (C_2H_2) and hydrogen (H_2), with typical output streams containing over 1% acetylene and more than 20% hydrogen. [2]

Although acetylene shares a similar structure with ethylene, it is highly undesirable in downstream applications, particularly in polymerisation processes. Its significant reactivity and toxicity pose challenges, notably in deactivating key catalysts such as Ziegler–Natta and metallocenes. Therefore, it is imperative to selectively remove or convert acetylene prior to the production of polymerisation-grade ethylene.[3]

As a result, the selective semi-hydrogenation of acetylene to ethylene has emerged as one of the most crucial and large-scale catalytic processes within the petrochemical sector.[4,5]

In industrial plants, the conversion of acetylene plays a crucial role in the front end of the separation train, where the raw cracked gas mixture, containing high concentrations of ethylene and hydrogen, is treated directly. The selective hydrogenation of acetylene to ethylene is thermodynamically favourable, with a standard enthalpy change ($\Delta H°298$) of –172 $kJ \cdot mol^{-1}$. However, this process

faces competition from unwanted side reactions, including the hydrogenation of ethylene to ethane (–136 kJ·mol^{-1}) and the direct hydrogenation of acetylene to ethane (–308 kJ·mol^{-1}).[6, 7]

To ensure high product quality, it is crucial to minimise acetylene levels before the gas enters the polymerisation units. Even trace amounts, as low as 1 ppm, can poison polymerisation catalysts and adversely affect their performance. Furthermore, the polymerisation process may generate oligomers and coke, collectively known as green oil, which can further deactivate the catalysts. For effective acetylene conversion, hydrogenation catalysts must meet several strict criteria: they should achieve a minimum of 99.99% acetylene conversion, ideally reducing C_2H_2 levels to below 1 ppm; maintain ethylene selectivity above 98%; and limit ethane formation to less than 2% to preserve ethylene yield. Additionally, the formation of green oil must be avoided. The preferred hydrogenation process occurs during the treatment of cracked gas streams prior to cryogenic separation, when significant amounts of hydrogen and ethylene are present. Catalysts must function at low temperatures, typically below 60 °C, to prevent undesirable side reactions, and they must be able to tolerate high space velocities that exceed 50,000 mL·g^{-1}·h^{-1} to ensure adequate throughput. Furthermore, robust thermal and chemical stability over time is essential.[8]

To meet these rigorous demands, current catalysts primarily comprise palladium (Pd) nanoparticles supported on alumina, often modified with silver (Ag) to enhance electronic properties. Furthermore, alkali additives such as sodium (Na) or calcium (Ca) are used to boost selectivity. Even with established constraints, achieving the required selectivity in industrial catalysis remains a major challenge. The effectiveness of the separation process heavily relies on the careful

selection and design of catalysts, highlighting the importance of developing and comprehending these systems in research.

In contrast, tail-end configurations operate after the majority of ethylene has been separated, typically employing different operational parameters. These parameters often include slightly elevated reaction temperatures and modest excesses of hydrogen to ensure the complete conversion of any residual acetylene.[9]

While the tail-end approach alleviates some of the safety and selectivity issues associated with the front-end process, it still necessitates careful adjustment of operational conditions to prevent the undesired hydrogenation of ethylene and to maintain high product purity.[9, 10]

The significance of removing acetylene extends beyond catalyst protection. As a highly flammable and reactive compound, acetylene poses considerable safety risks in processing environments. Its presence not only jeopardises equipment integrity and personnel safety but also complicates downstream purification stages, thereby increasing operational complexity and costs. Furthermore, even trace amounts of acetylene in polymerisation-grade ethylene can significantly influence polymer properties, leading to off-specification products and a reduction in market value.[11]

Despite the maturity of this industrial process, the scientific community continues to devote substantial effort toward developing improved materials and understanding the underlying reaction mechanisms that govern acetylene hydrogenation. This interest is driven by the complex interplay of kinetics, thermodynamics, and catalyst surface chemistry, which collectively determine the performance of the catalytic system. Particular attention has been given to the

exploration of novel catalyst supports and active phases that can achieve superior selectivity and resistance to deactivation under industrially relevant conditions. A recent review of over 100 catalytic systems [2, 12] indicates that while many achieve acetylene conversions exceeding 99%, they often do so at the expense of ethylene selectivity or under impractical laboratory conditions. These conditions include the use of inert gas diluents to suppress reactivity, operation in tail-end scenarios with a low H_2/C_2H_2 ratio, the removal of ethylene from the feed to simplify the reaction, and temperatures exceeding 100 °C, which diverge significantly from typical industrial practices.

This research identifies a critical need for a comprehensive redesign of catalysts, centred around two key mechanistic strategies. A promising approach is the isolation of active sites, which involves separating palladium (Pd) atoms to prevent multi-site hydrogenation. This ensures that each active centre can convert acetylene to ethylene selectively, minimising the risk of over-hydrogenation and polymerisation. The ultimate aim is to utilise single-atom palladium (Pd_1) sites that efficiently dissociate hydrogen while maintaining high selectivity. Another key strategy for enhancing selectivity is electronic tuning through alloying. By alloying palladium with noble metals such as silver (Ag) or gold (Au), the adsorption strength of ethylene is reduced. This modification aids in the desorption of ethylene, thereby improving overall selectivity in the process. Recent research has led to the development of single-atom catalysts (SACs) and single-atom alloys (SAAs) that show improved performance in model studies. Notably, the Pd_1–Au_1 dimer has been identified as a promising configuration due to its unique combination of site isolation and electronic tuning, as revealed through machine learning and density functional theory (DFT) calculations. Despite the potential of Pd_1–Au_1 dimers, realising these systems in experimental

settings, particularly under industrially relevant conditions, remains uncommon and technically challenging. However, their ability to combine the reactivity of palladium with the electronic modulation properties of gold highlights their significance in the development of more efficient catalysts for hydrogenation processes.[13]

While Pd–Ag systems are already utilised in industrial applications and take advantage of established principles, model studies indicate that isolating Pd_1 atoms on Au clusters or forming Pd_1–Au_1 dimers can provide enhanced control over selectivity. However, to date, there has yet to be an experimental demonstration of single-atom Pd alloy dimers (especially Pd_1–Au_1) in solid-state catalysts under authentic industrial conditions. The stabilisation of single-atom species and bimetallic dimers is contingent upon the precise control of the local environment around the metal centres. Porous materials, such as metal-organic frameworks (MOFs) and zeolites, are exemplary candidates for site-controlled heterogeneous catalysis owing to their distinctive structural properties.[14]

MOFs are distinguished by their exceptionally high surface areas and adaptable pore environments, which allow for the anchoring of isolated metal atoms or clusters via functionalized linkers. The formation of single-atom species of palladium (Pd) and gold (Au) has been successfully demonstrated, with these atoms being intricately supported within advanced MOFs. These highly porous structures provide an ideal environment for the stabilisation of the noble metal atoms, opening up potential applications in catalysis and materials science.[15, 16, 17, 18, 19, 20]

Additionally, dimers of platinum (Pt) and silver (Ag) have been synthesised, achieving metal loadings of up to 13 wt%. These structures can be precisely

tailored using linker chemistry. For example, incorporating thioether groups allows for effective trapping and stabilisation of Pd_1–Au_1 dimers in pores as small as 0.5 nm, resulting in the creation of nanoconfined reaction environments.

In contrast to MOFs, zeolites and molecular sieves are crystalline inorganic materials celebrated for their remarkable thermal and hydrothermal stability, making them highly suitable for catalytic applications in demanding industrial settings.[21] Their rigid microporous structures create topologically defined environments that can stabilise isolated metal atoms or small clusters, thereby enhancing site uniformity and resistance to sintering, both of which are essential features in the realm of single-atom catalysis.[22]

Among these materials, Zeolite Y, defined by its faujasite (FAU) topology, offers tunable acidity through the silicon-to-aluminium (Si/Al) ratio, making it an ideal platform for hosting catalytically active species. In this study, molecular sieves and Zeolite Y served as supports for palladium and palladium–gold species to assess their performance in the selective hydrogenation of acetylene. The incorporation of gold alongside palladium was investigated to explore potential synergistic effects on the electronic and geometric properties of the active sites.[23]

The systems provided a basis for comparing monometallic and bimetallic configurations, with a focus on how the support's structural properties, the arrangement of metal centres, and the surrounding environment impact catalytic activity, selectivity, and stability.[24] The analysis of Pd_1–Au_1 dimers and single-atom Pd species supported on metal-organic frameworks (MOFs) and zeolites utilised a dual approach, demonstrating their effectiveness in industrially relevant conditions.

5.2. Objectives

This study is centred on the development and evaluation of innovative palladium-based catalytic systems for the selective hydrogenation of acetylene under conditions relevant to industrial applications. The research entails the incorporation of bimetallic Pd_1–Au_1 sites into MOFs-and a comparative analysis with monometallic and bimetallic catalysts supported on molecular sieves and Zeolite Y. Through a comprehensive approach that includes synthesis, characterization, catalytic testing, and mechanistic investigation, the objective is to reveal key structure-function relationships and optimize the catalytic process to achieve high efficiency and selectivity.

The specific objectives of the research are as follows:

- To synthesise and structurally characterise Pd_1–Au_1 dimer catalysts within MOF matrices, as well as Pd and Pd–Au catalysts supported on molecular sieves and Zeolite Y.
- To perform comprehensive physicochemical characterisation of the prepared materials using techniques such as X-ray diffraction, infrared spectroscopy, and inductively coupled plasma atomic emission spectroscopy (ICP-AES).
- To evaluate the catalytic activity, selectivity, and stability of these systems in the semi-hydrogenation of acetylene under front-end conditions, where ethylene and hydrogen are present in excess.
- To investigate the roles of palladium and gold species in the hydrogenation mechanism, with attention to site isolation, metal–support interactions, and electronic effects.

- To compare the performance of MOF-based and zeolite-supported catalysts in order to determine the influence of pore architecture, metal nuclearity, and support composition on catalytic behavior.
- To analyse kinetic parameters, including apparent activation energies and by-product formation, in order to establish structure–activity relationships relevant to the rational design of single-site and bimetallic catalysts.

5.3. Results and Discussion

The development of advanced catalysts based on MOFs with atomically dispersed metals presents a promising approach to address the challenges of selective acetylene hydrogenation in industrial ethylene purification processes.

The initial phase of this study concentrated on the synthesis and thorough characterization of MOFs specifically designed to accommodate atomically dispersed palladium and gold species. Collaborators (see Chapter 3; Section 3.3.4.1.) successfully synthesised a MOF with the formula $\{Cu_6Sr[(S,S)\text{-}Mecysmox]_3(OH)_2(H_2O)\}\cdot 15H_2O$, which possesses well-defined channels suitable for the incorporation of metal precursors. In these channels, the palladium precursor $[Pd(NH3)_4]Cl_2$ was introduced, resulting in a MOF containing isolated palladium atoms, referred to as Pd_1-MOF. Similarly, impregnation with $AuCl_3$ yielded the Au_1-MOF, containing isolated gold atoms. A bimetallic analogue, incorporating equimolar amounts of both Pd and Au precursors, was also synthesised, leading to the formation of Pd_1–Au_1 MOFs with heteronuclear Pd–Au dimeric sites.

Single-crystal X-ray diffraction of the Pd_1–Au_1 MOF revealed a framework topology that closely resembles the previously reported Pd_1-MOF, suggesting that the incorporation of gold does not significantly perturb the host structure but enables the spatial proximity necessary for controlled Pd–Au bimetallic interactions. (Figure 5-1) This finding is consistent with earlier structural analyses, which demonstrated the chemical robustness of this MOF scaffold upon integration of transition-metal ions [20]

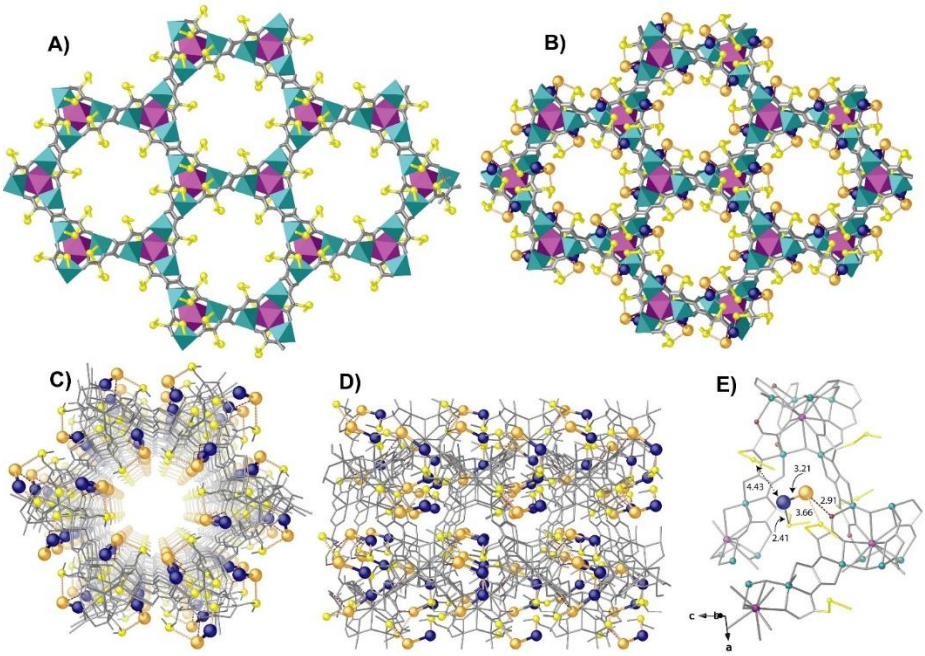

Figure 5-1 X-ray crystal structure of Pd_1Au_1@MOF. a,b, Formation of Pd_1–Au_1 dimers showing the structures of MOF (a) and Pd_1Au_1@MOF (b) determined by SCXRD. c,d, A single channel of Pd_1Au_1@MOF in the *ab* (c) and *bc* (d) plane. Copper and strontium atoms from the network are represented by cyan and purple polyedra, respectively, in a,b, whereas they are represented by grey sticks in c,d. Organic ligands are depicted as grey sticks and thioether groups as yellow sticks in all cases. Orange and blue spheres represent gold and palladium atoms, respectively, in Pd_1–Au_1 dimers. Blue, orange and red dotted lines represent the Pd···S, Au···S and Au···O interactions, respectively. e, Details of X-ray crystal structure showing the main host–guest interactions and related structural parameters of Pd_1–Au_1 dimers.

Quantitative analysis using inductively coupled plasma atomic emission spectroscopy (ICP-AES) confirmed that the targeted metal loadings were achieved. The Pd_1–Au_1 MOF contained 7.1 wt% Pd and 16.0 wt% Au, corresponding to an approximate Pd:Au molar ratio of 1:1.2 (Appendix 5A-1;

Table 5A-1), supporting the efficacy of the synthetic strategy in establishing controlled bimetallic dispersion within the porous matrix.

To further probe the electronic and geometric properties of the incorporated metal sites, CO adsorption infrared spectroscopy was conducted. The spectrum of the Pd_1@MOF displayed a sharp vibrational band at 2110 cm^{-1}, characteristic of CO linearly bound to isolated metal atoms, in agreement with literature reports for single-atom Pd sites [20] The corresponding spectrum of the Pd_1–Au_1@MOF exhibited the same 2110 cm^{-1} band, albeit at significantly lower intensity, consistent with ICP-AES results indicating a minor fraction of isolated Au atoms. Additional bands at lower wavenumbers provide further insight into the metal–metal interactions within the bimetallic system. A prominent band at 1975 cm^{-1} was attributed to CO molecules bridging between adjacent Pd and Au atoms, indicative of dimer formation[25, 26] A broader band at 1872 cm^{-1} is consistent with more complex coordination environments, potentially involving Pd_2Au or $PdAu_2$ trimers or interactions with neighbouring framework elements such as thioether ligands[27, 28] These vibrational features highlight the nuanced electronic environment within the MOF and provide spectroscopic evidence of metal–metal cooperation in the bimetallic Pd_1–Au_1 sites. (Appendix 5A-2; Figure 5A-2)

Taken together, these preliminary results highlight the successful synthesis MOF materials that feature atomically precise palladium (Pd) and palladium-gold (Pd–Au) active sites, thereby establishing a solid foundation for further catalytic evaluation. The ability to precisely control the speciation and distribution of metals within the MOF channels is vital for elucidating the structure-activity relationships that are pertinent to the selective hydrogenation of acetylene and other related industrial processes.

5.3.1. Catalytic Performance of Pd_1Au_1-MOF in Acetylene Semi-Hydrogenation

To evaluate the catalytic performance of the bimetallic catalyst Pd_1-Au_1@MOF under conditions pertinent to industrial applications, 30 mg of the MOF catalyst was thoroughly combined with 300 mg of inert SiO_2 and then packed into a fixed-bed tubular reactor. A series of semi-hydrogenation experiments were conducted using a feed composed of 1.12 vol% acetylene in ethylene, which simulates front-end purification processes. During these experiments, various operational parameters were adjusted, including flow rates, H_2:hydrocarbon (C_2) ratios, and reaction temperatures (see Table 5-1).

Table 5-1 Numerical values for the acetylene conversion and selectivity experiments; Effect of Flowrate and Temperature Variations with Pd_1 – Au_1@MOF

	Flow Conditions	Acetylene left (%)	Acetylene (ppm)	Ethane/Ethene Ratio (%)
	Initial feed	100.00	11220	0.03
Flow rate variation	80 H_2 to 1 acetylene (100 ºC) (8 mL/min H_2 + 8 mL/min C_2)	0.00	< 1	207.30
	3.75 H_2 to 1 acetylene (100 ºC) (3 mL/min H_2 + 80 mL/min C_2)	30.51	3410	1.23
	10 H_2 to 1 acetylene[a] (100 ºC) (3 mL/min H_2 + 30 mL/min C_2)	0.00	< 1	59.80
	6 H_2 to 1 acetylene (100ºC) (3 mL/min H_2 + 50 mL/min C_2)	0.56	60	.26
Temperature variation	8 H_2 to 1 acetylene (50 ºC) (3 mL/min H_2 + 37.5 mL/min C_2)	1.58	170	5.72
	8 H2 to 1 acetylene (75 ºC) (3 mL/min H_2 + 37.5 mL/min C_2)	0.46	50	5.55
	8 H_2 to 1 acetylene (100 ºC) (3 mL/min H_2 + 37.5 mL/min C_2)	0.47	50	5.85
	8 H_2 to 1 acetylene (125 ºC) (3 mL/min H_2 + 37.5 mL/min C_2)	0.64	70	4.18
	8 H_2 to 1 acetylene (150 ºC) (3 mL/min H_2 + 37.5 mL/min C_2)	-	-	-

[a] *The throughput at optimal conditions (3 mL/min H_2 + 30 mL/min C_2) has a 10:1 H_2:acetylene stoichiometry, the same one as the ethane cracking outlet fractions (the so-called front-end conditions). Detection limit = 1 ppm acetylene.*

The reaction temperature exhibited minimal impact on acetylene conversion across a broad range (50–150 °C), indicating a remarkably low apparent activation energy. This suggests that the kinetics associated with the Pd_1-Au_1@MOF catalyst are near-barrierless (see Figure 5-2). Notably, even at higher

temperatures, there were no detections of byproducts associated with dimerisation or polymerisation, such as C_4 hydrocarbons, green oils, or coke. Post-reaction extractions and elemental analyses confirmed the absence of these byproducts, highlighting the selectivity and stability of the catalytic process.

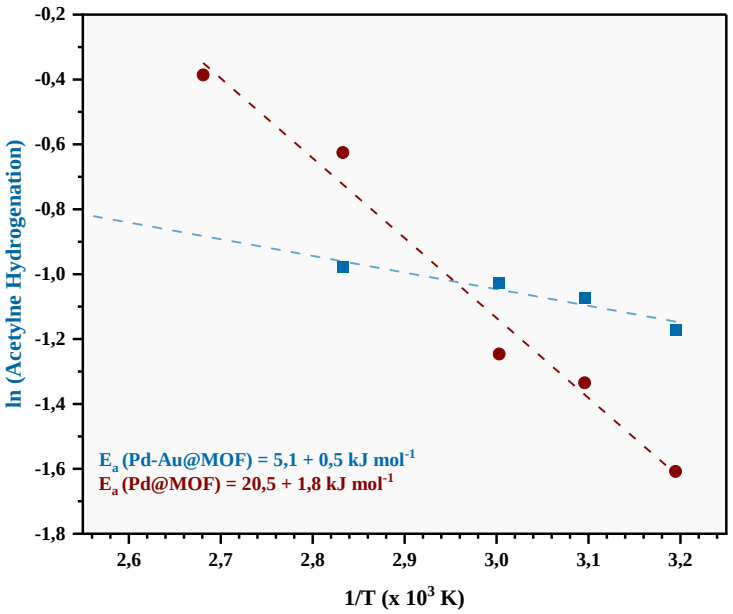

Figure 5-2 Apparent activation energy profiles for the overall acetylene hydrogenation reaction over Pd_1–Au_1@MOF (blue) and Pd@MOF (red)

Through parameter optimisation, an optimal hydrogen to acetylene ratio of 10:1 was determined, aligning with industry-standard front-end hydrogenation protocols. Under these conditions, acetylene conversion reached an impressive ≥99.99%, with residual levels falling below the 1 ppm detection limit of the gas

chromatograph. Furthermore, ethylene selectivity was consistently maintained above 90%, and the space velocity attained was 66000 $mL \cdot h^{-1} \cdot g_{cat}^{-1}$, reflecting exceptional productivity. Although efforts to quantify trace acetylene in the parts per billion (ppb) range were constrained by the gas chromatograph's detection capabilities, the performance metrics clearly met or exceeded industrial benchmarks.

The long-term catalytic stability of the Pd_1-Au_1@MOF catalyst was demonstrated through continuous flow operation, achieving a sustained conversion rate exceeding 99.99% and selectivity of approximately 90% after a brief stabilisation period (Appendix 5A-3; Figure 5A-3). Additionally, post-reaction analyses utilising X-ray Photoelectron Spectroscopy (XPS) and Powder X-ray Diffraction (PXRD) (Appendix 5A-4-5; Figures 5A-4-5) confirmed the structural and chemical integrity of the material, highlighting its robustness under operational conditions.

ICP-AES measurements indicated metal loadings of 2.9 wt% Pd and 5.2 wt% Au (Appendix 5A-6; Table 5A-6), which ensure a high density of active sites, thereby contributing to the catalyst's exceptional productivity. To provide a performance benchmark, monometallic analogues, Pd_1@MOF and Au@MOF, were synthesised with comparable noble metal contents and evaluated under similar conditions.

The Pd_1@MOF material exhibited catalytic activity but required significantly stricter conditions to match the performance of the bimetallic system. Specifically, it demanded a threefold increase in residence time and higher levels of H_2 excess. Even under these optimised conditions, Pd_1@MOF achieved a lower weight hourly space velocity (WHSV) of 20282 $mL \cdot h^{-1} \cdot g_{cat}^{-1}$ and left 40

ppm of unreacted acetylene remaining (Appendix 5A-7; Figure 5A-7). In contrast, Au@MOF displayed no catalytic activity under any of the tested conditions and did not enhance the performance of Pd_1@MOF when physically mixed. This underscores the synergistic effect of the bimetallic Pd–Au interface in the Pd_1-Au_1@MOF system.

5.3.2. Effect of Pore Size and Support Architecture

The selective semi-hydrogenation of acetylene in ethylene-rich gas streams poses a significant challenge in industrial catalysis. The goal is to entirely convert trace amounts of acetylene, an undesirable impurity, without over-hydrogenating ethylene, the primary product. This process requires catalysts that can effectively differentiate between molecules with similar sizes and reactivities, making both the nature of the active metal sites and the support material critical for optimal performance. While much focus has traditionally been on the intrinsic activity of metal centres like palladium and gold, increasing evidence highlights the significant role of support architecture. Specifically, the physical and chemical properties of the catalytic support, such as pore size, confinement geometry, and surface coordination, have a crucial impact on reaction kinetics and product distribution. In microporous catalysts, particularly those using zeolitic supports, the molecular dimensions of the reactants and products can critically govern diffusion, site accessibility, and reaction selectivity.

Acetylene (C_2H_2) is a linear molecule with a relatively small kinetic diameter of approximately 3.3 Å, allowing it to navigate narrow pore channels. Ethylene (C_2H_4), the desired product of selective hydrogenation, is slightly bulkier, with a kinetic diameter around 4.2 Å and molecular dimensions of 4.84 × 4.18 × 3.28

Å. In contrast, the over-hydrogenation product ethane (C_2H_6) is larger still, at approximately 4.82 × 4.08 × 3.81 Å. These sizes become critical when matched against the pore apertures of common molecular sieve materials.[29]

To evaluate the role of pore size, framework architecture, and metal identity in the semi-hydrogenation of acetylene, a comparative study was conducted using both Pd-only and Pd_1Au_1 bimetallic catalysts supported on a series of crystalline microporous materials. Specifically, molecular sieves MS 3Å (~3 Å), MS 5Å (~5 Å), and NaY zeolite (~7.4 Å) were selected to systematically explore the impact of pore diameter on mass transport and catalytic performance. These materials offer a rigid, crystalline framework ideal for evaluating steric and diffusional limitations.[30, 31, 32, 33]

MS 3Å, the narrowest of the sieves, features pore openings that are close to the size threshold for acetylene and are smaller than the minimum cross-section for ethylene or ethane. Consequently, this material significantly restricts molecular transport, hindering the access of both C_2H_2 and H_2 to the catalytic sites. Catalysts incorporating MS 3Å exhibited poor acetylene conversion, underscoring the diffusion-limited conditions imposed by the tight confinement. This observation aligns with studies suggesting that micropore bottlenecks can considerably reduce turnover frequencies due to entropic and enthalpic penalties during molecular ingress.[34]

MS 5Å, with an intermediate pore size of approximately 5 Å, provides enhanced channels for reactant accessibility. Catalysts supported on MS 5Å demonstrated significantly higher conversion rates for acetylene, suggesting that a larger pore diameter fosters improved mass transport. However, this increased accessibility comes with a trade-off in selectivity; the formation of ethane was notably higher

in this system. This is likely due to less restricted diffusion of intermediate products and a greater tendency for over-hydrogenation, a phenomenon frequently observed in semi-hydrogenation studies employing mesoporous supports. NaY zeolite, characterised by its large pore openings (~7.4 Å) and spacious supercages, facilitates the unrestricted diffusion of both reactants and products.[35]

Catalysts based on this support achieve complete conversion of acetylene, even at high space velocities. However, the expansive internal cavities also promote undesirable secondary reactions, such as the further hydrogenation of ethylene into ethane and potential C–C coupling events. This results in the formation of oligomeric side products and a reduction in ethylene selectivity. The increased residence time and spatial freedom within NaY contribute to these challenges, consistent with previous findings that excessive pore volume can compromise product purity.[36]

This size-selective behaviour is graphically illustrated in Figure 5-3, which shows the relationship between molecule size and pore accessibility. The fusiform channel depicted has an aperture in the range of 3.47–3.69 Å. Ethylene, with a cross-section of 3.28 Å, is shown entering the channel, while ethane, slightly larger at 3.81 Å, is sterically hindered. This visual model emphasises the principle that molecular sieving effects, based not just on average pore diameter but also on precise shape and dimensional compatibility, are key to optimising both activity and selectivity in catalytic systems.[37]

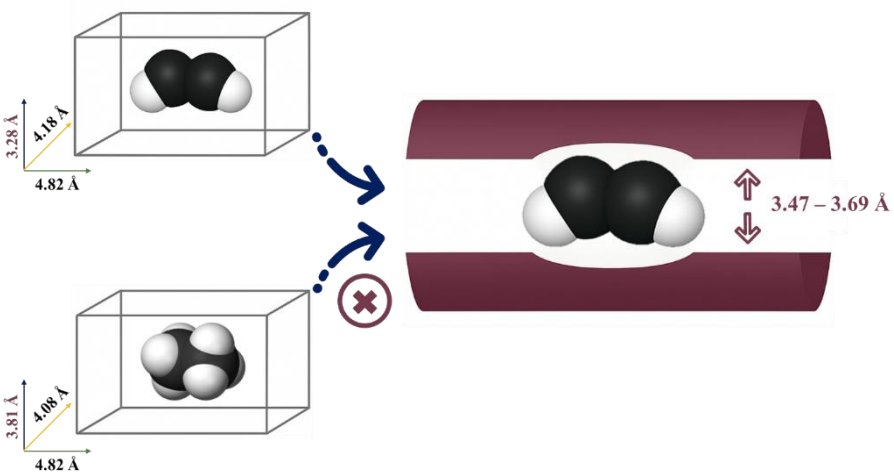

Figure 5-3 Illustration of size-selective molecular transport through a fusiform channel.

In summary, pore size and molecular geometry are key factors that influence the catalytic behaviour of Pd- and Pd-Au-supported materials. Small pores, such as those in MS 3Å, limit activity due to transport challenges, while larger pores, like those in NaY, compromise selectivity by allowing undesirable side reactions. Supports with intermediate pore diameters, seen in MS 5Å and certain MOFs, strike a balance by providing adequate access for reactants while minimising over-hydrogenation.

To elucidate the structural preservation and modes of metal incorporation across various porous supports, we compared the XRD profiles of monometalic Pd-catalysts supported on zeolitic MS 5Å with those confined within a crystalline MOF. Figure 5-4 presents the experimental XRD patterns for pristine MS 5Å and its metal-loaded derivatives, while Figure C includes both calculated and experimental PXRD profiles for pristine MOF and its bimetallic analogue, Pd_1-Au_1@MOF, across the 2θ range of 2.0–60.0°. In the zeolite-based systems (Appendix 5A-8 Figure 5A-8), the XRD patterns confirmed the support's high crystallinity and the successful incorporation of Pd without the formation of large crystalline nanoparticles. Notably, the absence of distinct reflections for Pd or Au, as compared to JCPDS standards, indicates a high level of dispersion or atomic-scale confinement of the metals within the MS 5Å pore network.

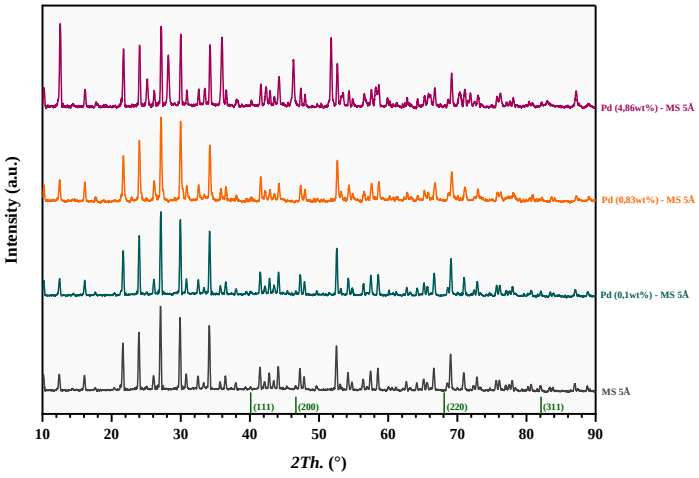

Figure 5-4 X-ray diffractograms (XRD) comparing Pd-zeolite with a 5 Å pore size to its zeolite supports (MS 5Å), Pd@MS. Below, reference patterns for palladium (Pd, JCPDS 06–1043) confirm the absence of large metal nanoparticles, indicating a finer distribution of the metals within the zeolite.

The PXRD patterns of MOF and Pd_1-Au_1@MOF (Figure 5-5) reveal that the crystalline framework is well-preserved after metal incorporation. The experimental profiles for both materials align closely with their respective calculated patterns, confirming that the framework maintains its periodicity and long-range order following the introduction of metal species. The lack of additional peaks or significant peak broadening upon the formation of Pd_1-Au_1@MOF strongly suggests that the bimetallic species are accommodated within the intrinsic pore environment of the MOF instead of forming segregated metallic clusters.

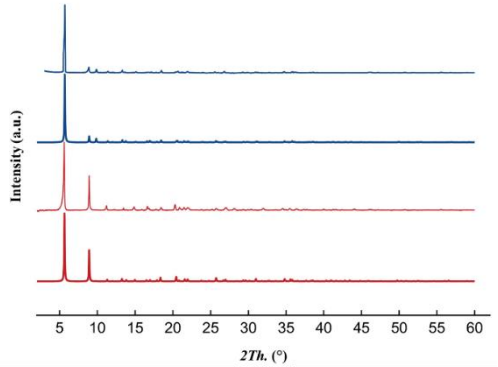

Figure 5-5 Calculated (bold lines) and experimental (solid lines) PXRD pattern profiles of MOF and Pd_1-Au_1@MOF in the 2θ range 2.0–60.0°.

Compared to the zeolite-based catalysts, the MOF-supported system exhibits lower peak intensities and broader reflections, particularly in the higher 2θ region (30–60°), which may stem from reduced crystallite size or intrinsic framework flexibility typical of many MOFs.[38]

Additionally, the lower symmetry and complex coordination environment in the MOF may contribute to more diffuse scattering, in contrast to the sharper

diffraction observed in the highly crystalline aluminosilicate lattice of MS 5Å. Despite the structural differences among the supports, a common theme emerges: the PXRD data indicate that the incorporation of Pd and/or Pd and Au does not disrupt the parent framework or lead to the formation of bulk metal phases.[39, 40]

This structural stability during metalation, confirmed by the alignment with theoretical patterns observed in the MOF case, underscores the effectiveness of both microporous architectures in immobilising metal species at the atomic or sub-nanometric scale.

These findings are pivotal for catalytic performance, as high metal dispersion and confinement within a robust crystalline framework are often associated with enhanced activity and selectivity in size-sensitive hydrogenation reactions.[38, 40, 41]

The consistency between simulated and experimental PXRD patterns for the MOF further establishes its suitability as a model system for mechanistic investigations, allowing for a direct correlation between structure and reactivity.[40, 42]

This principle highlights the significance of aligning the support architecture with the molecular dimensions of the reactive species to optimise catalytic performance.[39, 41]

Both monometallic (Pd-only) and bimetallic (Pd_1Au_1) systems exhibited these pore-dependent effects, with bimetallic catalysts typically providing improved selectivity in larger-pore supports.[39] Nonetheless, their performance remained influenced by the transport and confinement properties of the supporting framework.[38, 40]

Transmission electron microscopy (TEM) and high-angle annular dark-field scanning transmission electron microscopy (HAADF-STEM) were employed to assess the dispersion, particle size distribution, and spatial arrangement of Pd species in the monometallic Pd@MS 5Å catalyst. Low-magnification TEM images of the fresh Pd@MS 5Å sample indicated the presence of large Pd aggregates**,** some of which exceeded 50 nm in diameter. These large domains suggest a degree of Pd sintering or uncontrolled growth during synthesis or thermal treatment, which may negatively influence catalytic performance. Such large metallic ensembles are known to facilitate non-selective hydrogenation pathways due to the abundance of contiguous Pd atoms that promote deep hydrogenation, leading to excessive ethane formation. (Figure 5-6)

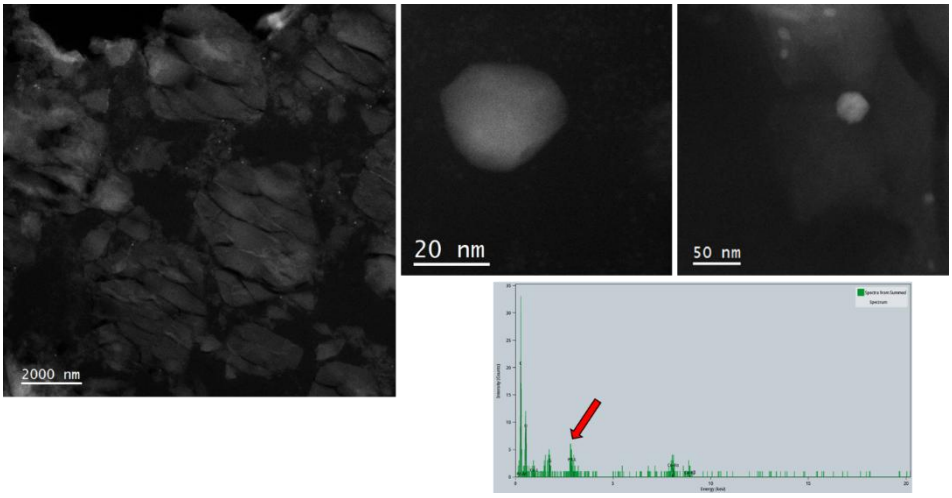

Figure 5-6 Low-magnification TEM analysis of the fresh Pd@MS 5Åcatalyst.

To achieve a deeper understanding of the population of finely dispersed palladium (Pd) species, HAADF-STEM was employed in conjunction with advanced image processing and segmentation techniques. The initial step involved enhancing the contrast of HAADF images through filtering, followed by converting these images into colour scale maps to facilitate clearer visualisation of atomic features. Next, a segmentation algorithm was utilised to identify individual Pd species based on intensity thresholds and spatial characteristics. This approach enabled a quantitative analysis of over 1,000 individual Pd features, allowing for a rigorous statistical assessment of particle size distribution. The resulting data revealed a bimodal distribution of Pd species. A significant portion of the population consisted of highly dispersed Pd entities with sizes below 1 nm, likely corresponding to isolated atoms, sub-nanometric clusters, or very small nanoparticles. These ultrasmall Pd species are particularly advantageous in selective hydrogenation reactions, as they minimise the risk of over-hydrogenation and promote monoselective activity due to their limited surface ensemble size and altered electronic structure. Additionally, a secondary population of larger Pd species was identified, with sizes reaching approximately 3 nm. While still classified as nanoscale, these particles may begin to exhibit multi-atom surface ensembles, thereby increasing the likelihood of side reactions, such as ethane formation. (Figure 5-7)

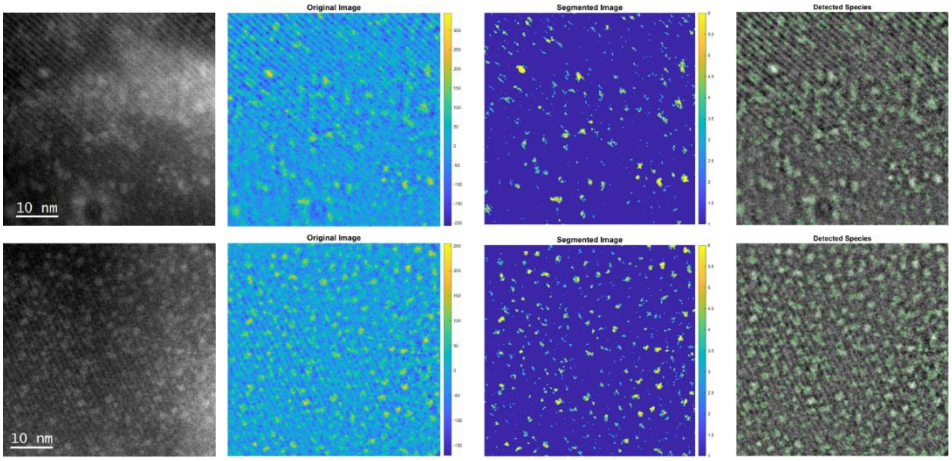

Figure 5-7 HAADF-STEM imaging and quantitative analysis of Pd species dispersion in the Pd@MS 5Å catalyst.

The combination of HAADF imaging and statistical segmentation offers compelling evidence of a heterogeneous distribution of Pd on the MS 5Å support.(Figure 5-8) While the presence of large Pd aggregates (greater than 50 nm) raises concerns, the detection of a significant proportion of sub-nanometric Pd species suggests that a portion of the Pd remains catalytically active, particularly in selective reactions. This dual population of Pd is consistent with the catalytic behaviour observed in the Pd@MS 5Å system, which exhibited moderate activity and limited selectivity. The larger Pd clusters likely contribute to unselective hydrogenation, whereas the finely dispersed Pd species account for the observed ethylene production. To enhance selectivity and reduce over-hydrogenation, improving the uniformity of Pd dispersion could prove beneficial. This may be achieved through optimised synthesis methods or by incorporating a second metal, such as Au, to provide electronic dilution and stabilisation. In

summary, the analyses of Pd@MS 5Å performed using TEM and HAADF-STEM underscore the crucial role of metal dispersion in catalyst performance. The coexistence of both highly dispersed Pd species and large metallic aggregates emphasises the need for precise control over metal nucleation and growth, especially when designing catalysts for monoselective hydrogenation. Future strategies should focus on eliminating oversized Pd domains while maximising the density of sub-nanometric, electronically tailored Pd sites, preferably within structurally confining and stabilising supports such as zeolites.

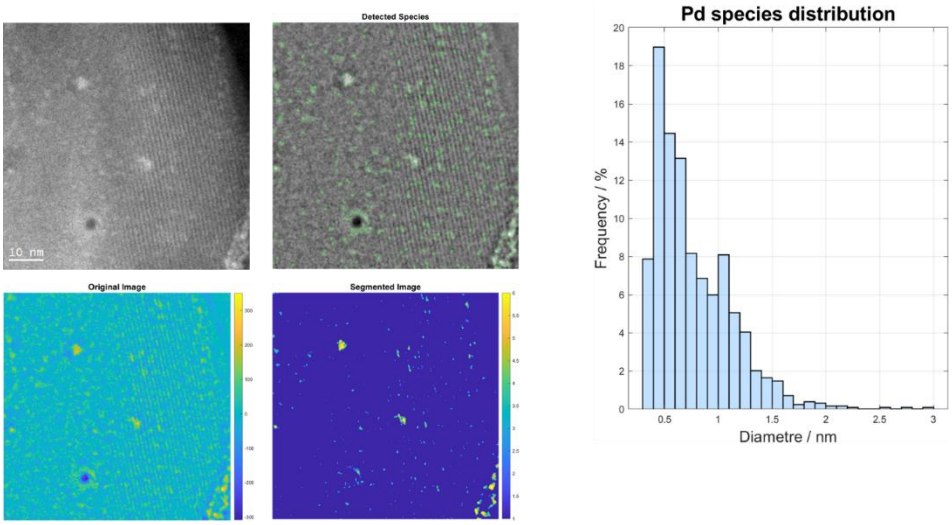

Figure 5-8 Comprehensive TEM and HAADF-STEM characterisation of Pd dispersion in the Pd@MS 5Å catalyst.

The structural and electronic characteristics of palladium species supported on various zeolitic substrates were further elucidated through UV–Vis diffuse reflectance spectroscopy, thereby complementing insights obtained from XRD

analysis. As depicted in Figure 5-9, all Pd-supported materials, Pd@MS 3Å, Pd@MS 5Å, and Pd@NaY, exhibit a pronounced absorption band in the ultraviolet region (~220–250 nm). This band is indicative of ligand-to-metal charge transfer (LMCT) transitions in oxidised Pd species, particularly in the form of Pd^{2+} complexes such as $[PdCl_4]^{2-}$ or PdO clusters. [43]

The absence of broad, featureless absorption bands extending into the visible range (400–600 nm) in all samples further suggests that metallic Pd^0 nanoparticles, which typically exhibit localised surface plasmon resonance (LSPR) in this wavelength range, are not present. This observation is consistent with the XRD results presented in Figure 5-4, which show no discernible reflections associated with bulk Pd phases, in accordance with reference patterns (JCPDS 46-1043 for Pd). The lack of metallic diffraction peaks implies mark that the metal species are either highly dispersed or exist as small clusters that fall below the detection limit of XRD, a conclusion corroborated by the electronic absorption spectra.

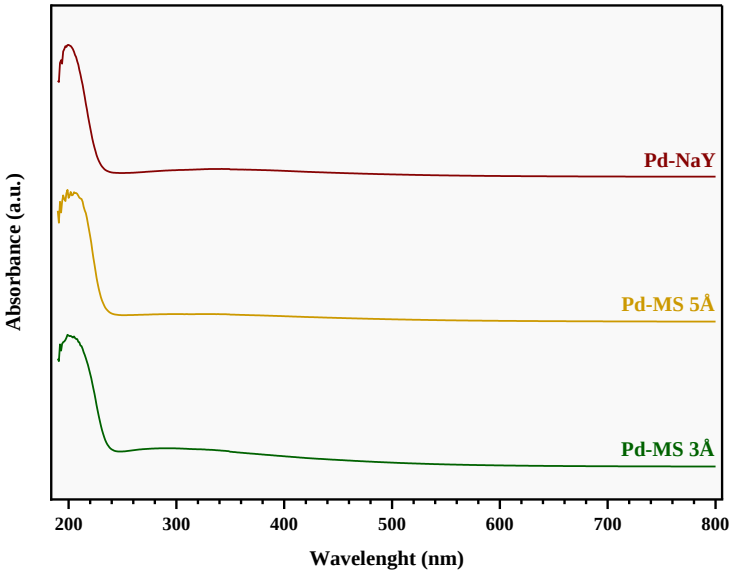

Figure 5-9 UV–Vis diffuse reflectance spectra of Pd-supported zeolitic materials: Pd@MS 3Å, Pd@MS 5Å, and Pd@NaY.

Notably, the intensity of the LMCT band varies with the type of support, reflecting disparities in Pd dispersion and support–metal interactions. Pd@NaYexhibits the most intense absorption, likely due to its larger supercage volume, which facilitates greater Pd incorporation or stronger metal–framework interactions. Conversely, Pd@MS 5Å demonstrates moderate absorption intensity, suggesting a balanced interplay between accessible pore space and uniform dispersion of Pd^{2+} species. Pd@MS 3Å, characterised by the narrowest pore openings (~3 Å), displays the weakest absorption, which may be attributed to steric constraints that hinder effective Pd loading or limit its homogeneous

distribution within the framework. These trends are further paralleled in the XRD profiles, where all catalysts maintain the crystalline integrity of the parent zeolite but differ in the degree of peak broadening and relative intensity. This variation may reflect localised strain or defect formation due to metal incorporation.

X-ray Photoelectron Spectroscopy (XPS) was employed to probe the electronic states and surface composition of palladium species across the different catalyst systems (Figure 5-10). The high-resolution Pd 3d spectra for the zeolite-supported catalysts (Pd@MS 3Å, Pd@MS 5Å, and Pd@NaY) all exhibited characteristic doublets corresponding to Pd $3d_{5/2}$ and Pd $3d_{3/2}$ core-level transitions. For all samples, the Pd $3d_{5/2}$ peak was located in the range of 337.7–338.1 eV, which is consistent with the presence of oxidised Pd^{2+} species, such as PdO or framework-bound Pd^{2+} cations. These binding energies are significantly higher than those typically associated with metallic Pd^0 (~335.0 eV), confirming the predominant oxidation state of palladium in these materials. This finding aligns with both the UV–Vis DRS data, where no LSPR features were detected, and the PXRD results, which showed no peaks attributable to bulk metallic phases.

Saliently, subtle shifts in the Pd 3d binding energies were observed depending on the zeolite support. Pd@NaYexhibited the highest binding energy (~338.1 eV), suggesting stronger Pd–support interactions, likely due to the more polar and spacious supercage environment in the NaY framework. In contrast, Pd@MS 3Å displayed slightly lower binding energy (~337.7 eV), consistent with weaker interactions due to the more restrictive pore dimensions. The intermediate binding energy observed for Pd@MS 5Å (~337.9 eV) reflects a moderate interaction, correlating well with its balanced Pd dispersion and accessibility.

The full-width at half maximum (FWHM) of the Pd 3d peaks was also analysed as an indirect indicator of electronic heterogeneity and particle size distribution. Broader peaks in Pd@MS 5Å and Pd@NaY samples suggest the coexistence of multiple Pd^{2+} environments or coordination states, possibly including highly dispersed Pd^{2+} ions and small oxidic clusters. This observation supports the HAADF-STEM findings, which identified a bimodal size distribution in Pd@MS 5Å and sub-nanometric dispersion in Pd-NaY. In contrast, narrower peaks in Pd@MS 3Å suggest fewer distinct environments, likely due to restricted Pd incorporation.

Collectively, the XPS data reinforce the conclusion that Pd is predominantly present in oxidised, highly dispersed states within all zeolite supports, with no detectable Pd^0 on the surface. These oxidised Pd species are known to be catalytically active in selective hydrogenation reactions, particularly when stabilised within microporous environments. Furthermore, the observed support-dependent shifts in binding energy and peak width highlight the critical role of framework structure in tuning metal–support interactions, electronic properties, and, by extension, catalytic behaviour.

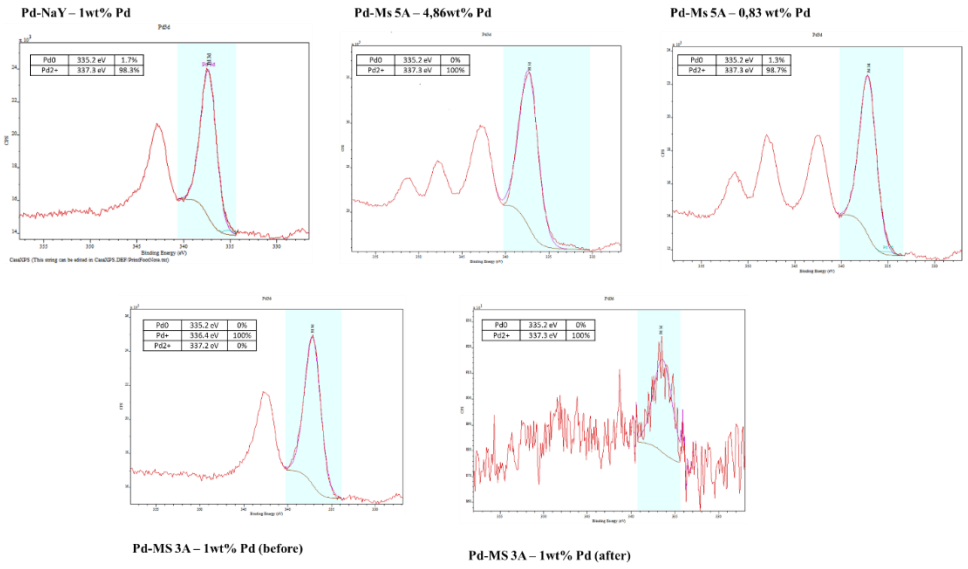

Figure 5-10 High-resolution XPS spectra of Pd 3d regions for Pd-supported zeolitic catalysts (Pd@MS 3Å, Pd@MS 5Å, and Pd@NaY).

The combined XRD, HAADF-STEM, XPS and UV–Vis analyses confirm that Pd is primarily incorporated in an oxidised, highly dispersed state across all zeolitic supports. The architecture of the pores plays a pivotal role in determining metal uptake, distribution, and the associated electronic environment, factors that are expected to directly influence catalytic performance.

5.3.3. Catalytic Results

The catalytic performance of the prepared materials was systematically evaluated under the optimal reaction conditions previously established for the Pd_1-Au_1@MOF system. These conditions were selected to maximise acetylene conversion while maintaining high ethylene selectivity, providing a benchmark for comparative analysis. The results presented here focus on the semi-hydrogenation of acetylene, a reaction that is highly sensitive to both mass transport limitations and the configuration of active sites.

Activity and selectivity profiles of Pd and Pd–Au catalysts supported on molecular sieves with varying pore sizes (MS 3Å, MS 5Å, and NaY) were examined to elucidate the interplay between support architecture, metal composition, and reaction performance. Differences in molecular diffusion, product confinement, and the extent of over-hydrogenation were critically assessed to determine how the support structure influences catalytic efficiency and selectivity under industrially relevant conditions. To gain a better understanding of how palladium loading and support pore structure influence catalytic behaviour, a series of catalysts composed solely of palladium on zeolite supports was initially synthesised. Three types of supports were utilised: MS 3Å, MS 5Å, and NaY, each with three distinct palladium loadings: approximately 0.025 wt%, 0.1 wt%, and 1 wt% (exact values are provided in Appendix 5A-1; Table 5A-1). Importantly, H^+-form zeolites were excluded to avoid Brønsted acid-catalysed side reactions.

The semi-hydrogenation of acetylene was conducted under identical conditions using a 10:1 hydrogen-to-acetylene ratio (3 sccm H_2 + 30 sccm C_2H_2 mixture), ensuring a consistent basis for comparison. (see Figure 5-11) This systematic

variation enabled the exploration of the effects of metal dispersion and the density of active sites on the semi-hydrogenation performance of acetylene across supports with differing pore sizes and diffusion characteristics. These Pd-only systems served as a baseline for assessing metal-support interactions and provided crucial insights into optimal metal loading ranges prior to the introduction of bimetallic functionality through the incorporation of gold.

In addition to the optimal conditions previously established for MOF-based catalysts, an extended investigation was carried out involving a range of flow rate conditions tailored to each catalyst system studied. These experiments were designed to evaluate performance sensitivity and stability under varied hydrogen-to-acetylene ratios, and the resulting data are provided in Appendix 5A-9.

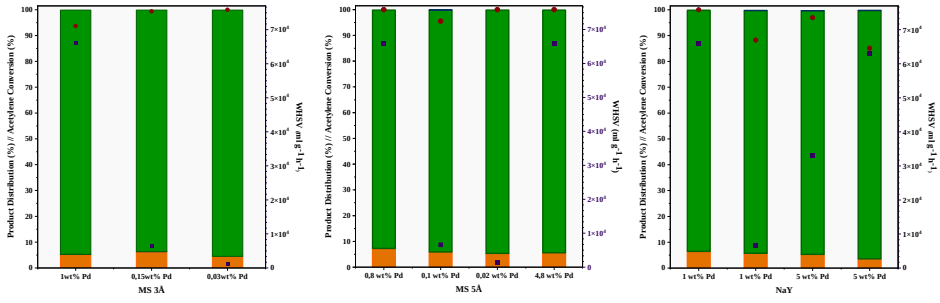

Figure 5-11 Comparison of Pd-supported zeolites with varying pore sizes under optimised semi-hydrogenation conditions (H_2:C_2H_2 = 10:1). Catalytic performance of Pd@MS 3Å (left), Pd@MS 5Å (middle), and Pd@NaY (right) is evaluated in terms of product selectivity and acetylene conversion. Bar plots represent product distribution: acetylene (blue), ethylene (green), and ethane (orange). Superimposed markers indicate acetylene conversion (red dots) and WHSV (purple dots).

Despite the lowest Pd content, the 0.03 wt% Pd@MS 3Å catalyst exhibited the highest acetylene conversion (100%) and ethylene selectivity (95.36%), with only minor ethane formation (4.47%). This suggests that at low Pd loading, the metal is highly dispersed within the microporous structure of the 3Å support, facilitating isolated Pd active sites or small clusters that preferentially promote selective hydrogenation of acetylene to ethylene while effectively suppressing over-hydrogenation to ethane. Furthermore, the low WHSV (1320 mL g^{-1} h^{-1}) associated with this sample implies longer residence time, which likely contributed to the complete acetylene conversion.

As Pd loading increased to 0.15 wt%, acetylene conversion remained high (99.33%), though a slight decline in ethylene selectivity was observed (93.51%), accompanied by a corresponding increase in ethane formation (6.35%). This trend continued with the 1 wt% Pd sample, which exhibited the lowest acetylene conversion (93.67%) and a further reduction in selectivity (94.54%), alongside elevated ethane production (5.23%). The decrease in performance at higher loadings can be attributed to the formation of larger Pd ensembles due to metal particle agglomeration. These larger clusters present a broader range of active sites, including those capable of facilitating full hydrogenation of ethylene to ethane. Additionally, excessive Pd may block micropores, reducing diffusion efficiency and active site accessibility. This is further evidenced by the increasing ethane/ethylene (single-bond to double-bond) product ratio with Pd loading, highlighting a progressive loss of control over selectivity. These findings underscore the critical importance of tuning Pd dispersion within molecular sieves to balance catalytic activity and selectivity. The MS 3Å support, with its narrow pore architecture, inherently limits metal diffusion and favours atomic dispersion at low loading, making it particularly well-suited for selective

hydrogenation applications. Optimal performance was achieved at 0.03 wt% Pd, offering a promising route toward minimising precious metal usage while maintaining high catalytic efficiency under industrially relevant conditions.

The catalytic efficiency of Pd-supported MS 5Å (Figure 5-11, in the middle) materials was examined under optimised semi-hydrogenation conditions (H_2:C_2H_2 = 10:1; 3 sccm H_2 + 30 sccm acetylene mixture) across a range of Pd loadings, specifically 0.02 wt%, 0.1 wt%, 0.8 wt%, and 4.8 wt%. The 5 Å pore size offers a balance between molecular access and confinement, allowing effective diffusion of both acetylene and hydrogen while moderating the formation of over-hydrogenated products.

In all samples tested, complete conversion of acetylene (100%) was achieved, confirming the adequate accessibility of active sites throughout the series. However, the selectivity for ethylene compared to ethane varied with the metal loading, illustrating the sensitivity of catalytic outcomes to the size and nature of the palladium (Pd) ensembles. At the lowest Pd loading of 0.02 wt%, ethylene selectivity reached a maximum of 94.46%, with no detectable acetylene present. This result underscores the effectiveness of highly dispersed Pd species in enabling selective semi-hydrogenation. Additionally, the high ethane-to-ethylene ratio of 0.103 suggests minimal over-hydrogenation, a highly desirable characteristic in industrial processes where the purity of ethylene is crucial. Upon increasing the Pd content to 0.1 wt%, a modest decrease in ethylene selectivity was noted (93.90%), with 5.9% ethane detected. This reflects a growing contribution of larger Pd ensembles, where adjacent active sites may promote full hydrogenation to ethane.

The distinction between the 0.8 wt% and 4.8 wt% Pd-loaded catalysts is more pronounced. While both catalysts achieved complete conversion of acetylene, ethylene selectivity exhibited a slight decrease, with values of 92.53% for the 0.8 wt% catalyst and 94.19% for the 4.8 wt% catalyst. Importantly, ethane formation was recorded at 7.3% for the 0.8 wt% sample and 5.6% for the 4.8 wt% sample. These findings suggest that increasing the Pd content does not lead to a proportional enhancement in selectivity; rather, it can enhance tendencies for over-hydrogenation. This phenomenon is likely due to the greater likelihood of multiple hydrogenation events occurring on larger metallic domains.

From an industrial standpoint, selecting the appropriate Pd loading requires a careful balance between two critical priorities: achieving high selectivity toward ethylene and ensuring long-term durability of the catalyst under demanding operational conditions. In this context, Pd catalysts with lower metal loadings (0.02–0.1 wt%) exhibit exceptional selectivity by effectively suppressing over-hydrogenation and minimising ethane formation. However, despite their favourable selectivity profile, these low-loading catalysts may encounter significant limitations in terms of mechanical integrity, resistance to deactivation, and performance at WHSV, which are typical in industrial reactors. On the other hand, catalysts with higher Pd loadings, specifically 0.8 wt% and 4.8 wt%, tend to generate greater quantities of ethane, thereby compromising the purity of ethylene. Consequently, they are less suitable for applications requiring ultra-high selectivity, such as polymer-grade ethylene production. Nevertheless, these higher-loading catalysts present advantages that merit further consideration. In particular, the increased Pd content may enhance the catalyst's robustness, thermal stability, and lifespan, making them more appropriate for processes where selectivity can be moderately sacrificed in favour of improved operational

resilience, regeneration capacity, or throughput. Striking a balance between these competing factors, the ~4.8 wt% Pd@MS 5Å catalyst stands out as an appealing compromise. It achieves complete acetylene conversion with a high ethylene selectivity of 94.1%, all while managing ethane formation effectively. This higher Pd loading supports strong long-term performance, positioning it as an attractive option for industrial applications. While low Pd loadings are optimal for maximising selectivity, and high loadings introduce certain trade-offs, both the ~1 wt% and 4.8 wt% Pd catalysts warrant further investigation. Each may fulfil distinct industrial roles: the former offering a balanced, high-performance solution for general use, while the latter may serve as a viable option in systems prioritising catalyst longevity, operational flexibility, or ease of regeneration.

Following the promising results obtained with MS 5 Å supports, particularly at Pd loadings of approximately 1 wt% and 5 wt%, the investigation was extended to Pd-loaded NaY zeolites to assess the influence of a more open pore system (~7.4 Å) on catalytic performance. Unlike the more restrictive MS 3 Å and moderately confining MS 5 Å, NaY offers a spacious pore network and large supercages, which facilitate unobstructed diffusion of both acetylene and hydrogen, as well as the intermediate and product molecules.[30, 44]

Catalysts comprising 1 wt% Pd on NaY (see Figure 5-11, right) exhibited full acetylene conversion under high WHSV conditions (66000 mL g^{-1} h^{-1}), with no detectable acetylene in the product stream and relatively low levels of ethane (6.5%), suggesting efficient semi-hydrogenation activity and moderate selectivity. However, under reduced WHSV (6600 mL g^{-1} h^{-1}), the same catalyst displayed a decrease in selectivity, with ethane formation increasing and ethylene selectivity dropping to ~88%. This decline can be attributed to the prolonged residence time within the large-pore system, which facilitates secondary

hydrogenation of ethylene to ethane, especially under excess hydrogen conditions. Furthermore, the introduction of a higher Pd loading (5 wt%) maintained full conversion, but similarly revealed selectivity losses under specific conditions. Notably, reducing the H_2:C_2H_2 ratio to 5.5:1 while using the 5 wt% Pd@NaY catalyst led to a marked increase in ethane formation (~14.9%) and a further decline in ethylene selectivity (~85%), underscoring the sensitivity of the system to hydrogen partial pressure in large-pore environments. These observations affirm that while NaY enables excellent activity through enhanced mass transport and reactant accessibility, it does so at the cost of reduced control over over-hydrogenation reactions. The lack of steric hindrance in NaY, unlike in MS 3 Å or 5 Å, eliminates diffusion constraints that might otherwise suppress unwanted secondary reactions.[30] Thus, although NaY-supported Pd catalysts perform effectively in terms of conversion, their selectivity is more susceptible to reaction conditions, particularly at elevated metal loadings and under suboptimal hydrogen flow regimes.[45, 46, 47]

The data suggest that for industrially relevant semi-hydrogenation processes, the structural openness of NaY must be carefully balanced with reaction engineering strategies to mitigate ethylene loss and suppress ethane formation.

5.3.4. Catalytic Performance and Structural Effects in Acetylene Semi-Hydrogenation

Catalytic testing demonstrated that pore size and support architecture significantly impact acetylene conversion and ethylene selectivity. This relationship is especially evident when comparing Pd–Au metal-organic frameworks (MOFs) with Pd-loaded zeolites under identical weight hourly space

velocity (WHSV) conditions. (Figure 5-12) The variations in product distribution and catalytic efficiency observed can be attributed to differences in textural properties, molecular diffusion, and the accessibility of active sites. As shown in Figure 5-3, the kinetic diameters of acetylene (C_2H_2, ~3.3 Å), hydrogen (H_2, ~2.9 Å), ethylene (C_2H_4, ~4.2 Å), and ethane (C_2H_6, ~4.4 Å) suggest that the diffusion and transformation of these species are strongly influenced by the pore architecture of the catalyst supports. Materials with pore diameters below or close to these values may impose steric constraints, impacting both reaction kinetics and product selectivity.

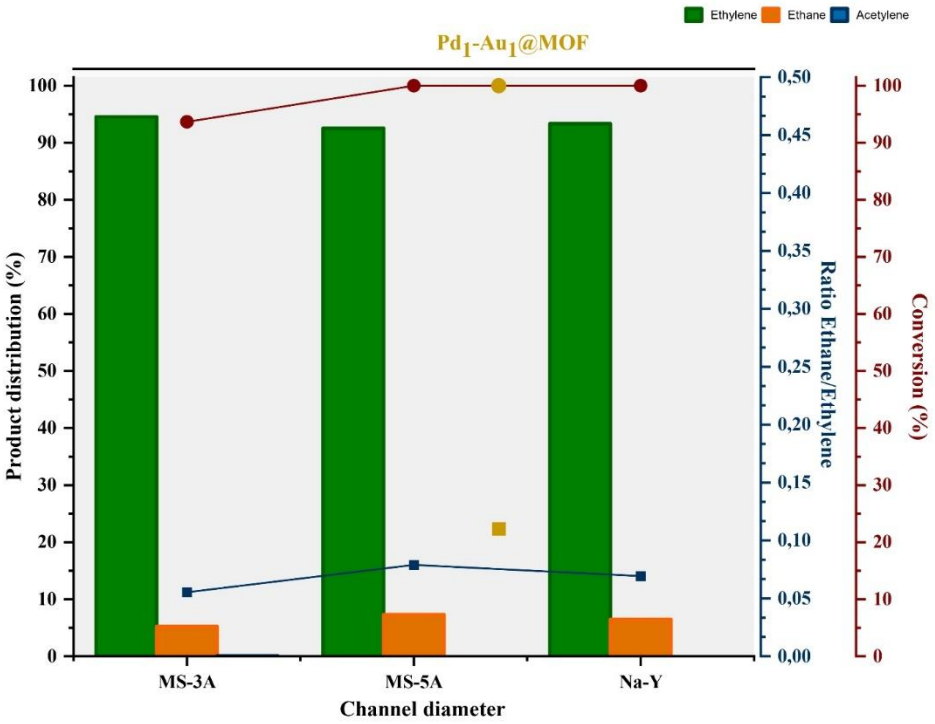

Figure 5-12 Effect of support pore size and architecture on acetylene conversion and ethylene selectivity.

Among the zeolites examined, MS 5 Å emerges as the most balanced and promising candidate for industrial applications. Its pore openings of approximately 5 Å provide ample accessibility for reactants while simultaneously offering a molecular sieving effect that mitigates the risk of over-hydrogenation. This dual functionality is demonstrated by the complete conversion of acetylene and a relatively low ethane yield of 7.30%, highlighting its high selectivity for ethylene. Additionally, a high-loading MS 5 Å catalyst (approximately 5 wt% Pd) exhibited enhanced performance, achieving full acetylene conversion with reduced ethane formation, resulting in only 5.61% ethane and an improved ethane-to-ethylene ratio. This improvement is likely attributed to a higher density of accessible active sites, which closely resembles the palladium content of the MOF system (approximately 7.1 wt%). These findings highlight the impact of metal loading on catalytic performance and indicate that selecting the right precursors can optimise the catalyst. Moreover, this improvement may stem from better palladium dispersion or altered electronic properties at the active sites.

This catalytic performance is strongly supported by post-reaction HAADF-STEM analysis. Low-magnification images revealed the formation of Pd agglomerates, particularly on the external surfaces of the zeolite, as indicated by red arrows in Figure 5-13.

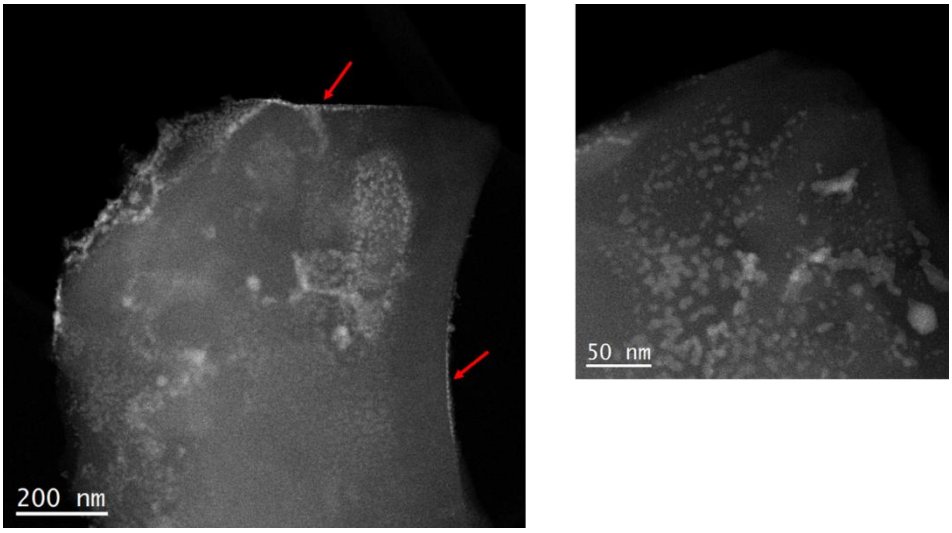

Figure 5-13 Post-reaction HAADF-STEM analysis of Pd distribution on zeolite catalysts.

Compared to the fresh catalyst, a reduction in the overall number of metal species was observed, along with a clear increase in the population of particles larger than 2 nm, suggesting the occurrence of sintering of surface-bound Pd species. (Figure 5-14)

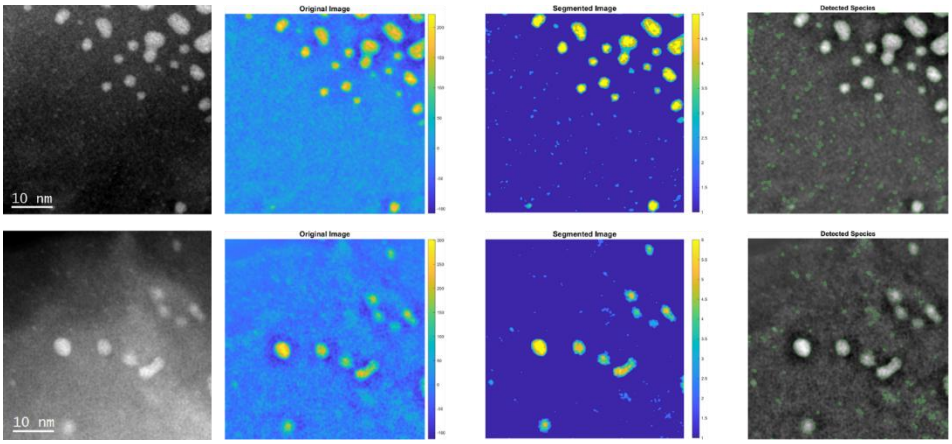

Figure 5-14 Filtered HAADF-STEM images and Pd particle detection following catalytic testing

Despite this, a significant fraction of sub-nanometric Pd clusters (<1 nm) was retained, most likely residing within the internal zeolite framework where sintering is suppressed due to spatial confinement. Size distribution analysis confirmed a post-reaction shift toward larger particles, as indicated by increases in both the mean particle size and standard deviation. This broader distribution was primarily associated with particles exceeding 2.5 nm, while a concurrent decrease was observed in the 1.0–1.5 nm range. In contrast, clusters in the 0.3–0.5 nm range shifted slightly toward 0.6–0.8 nm, suggesting moderate structural evolution without complete loss of high dispersion. (Figure 5-15) These findings indicate that while external Pd sites are susceptible to aggregation, internal sites remain relatively protected and catalytically relevant.

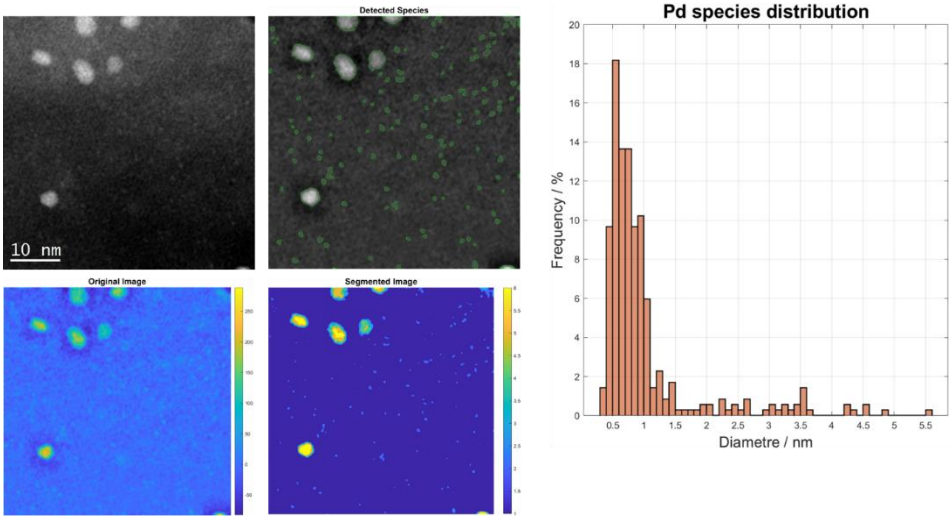

Figure 5-15 Post-reaction Pd particle size distribution and spatial retention on zeolite catalysts.

This coexistence of stabilised, highly dispersed clusters with partially sintered external domains aligns with the catalytic behaviour observed for Pd@MS 5Å. The internal sub-nanometric species are likely responsible for maintaining high selectivity and activity, as their electronic isolation and spatial restriction limit the ensemble size required for over-hydrogenation pathways. Meanwhile, the external Pd sites, prone to agglomeration, contribute less to selective transformation and may be passivated during reaction. (Figure 5-16) These observations reinforce the critical role of support morphology, not only in initial dispersion but also in preserving catalytic function under reaction conditions.

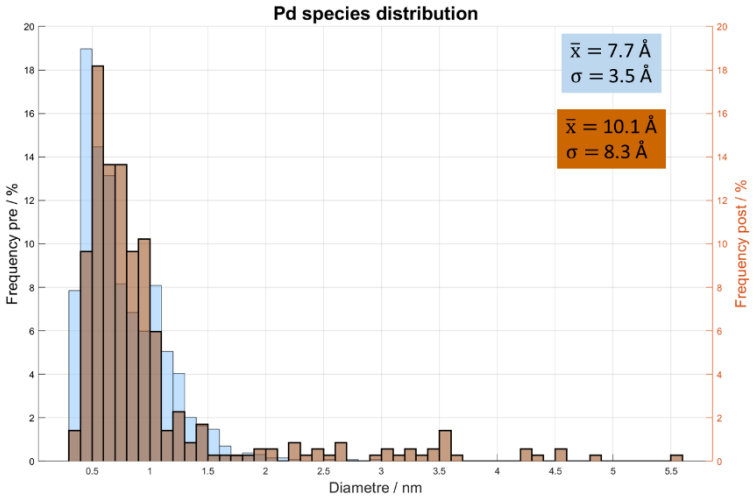

Figure 5-16 Comparison of Pd particle size distributions before and after the reaction.

The comparison with other supports underscores this finding. The narrower-pore MS 3Å zeolite, while providing limited diffusion access that reduces ethane production to 5.23%, nonetheless experiences incomplete conversion of acetylene, achieving only about 94% conversion. The restricted pore size hampers the diffusion of acetylene molecules to the active sites, leading to a decreased effective turnover frequency and overall activity. On the other hand, NaY zeolites, which feature larger pore diameters of approximately 7.4 Å, enable excellent reactant diffusion and achieve complete acetylene conversion. However, this benefit comes with the drawback of increased over-hydrogenation, resulting in a higher ethane yield of 6.47%. These findings underscore a significant trade-off: while smaller pores limit conversion efficiency, larger pores can promote undesirable side reactions. This highlights the need to identify an optimal intermediate pore size for maximising catalytic performance.

The Pd_1Au_1@MOF, characterised by one-dimensional channels measuring approximately 5.6 Å, serves as a performance benchmark. Under standard conditions, it achieves conversion and selectivity levels comparable to MS 5Å. (Figure 5-17) However, when exposed to intensified conditions, such as elevated WHSV or increased gas flow rates, the MOF exhibits superior performance. This enhancement is primarily due to the high density of atomically dispersed Pd–Au dimeric sites, which are effectively stabilised within its well-ordered framework. The architecture of the MOF enables a controlled spatial distribution of active sites, effectively minimising site aggregation and facilitating more consistent molecular transport. Significantly, the structural distinctions between the three-dimensional microporous networks of zeolites and the one-dimensional channel system in MOFs have important implications. While zeolites are robust and economically viable, they often face challenges related to non-uniform diffusion paths and limited flexibility in the positioning of active sites. In contrast, the linear, modular design of the MOF provides predictable channel geometry, enhanced site accessibility, and improved catalytic longevity, particularly under conditions that replicate industrial stress.

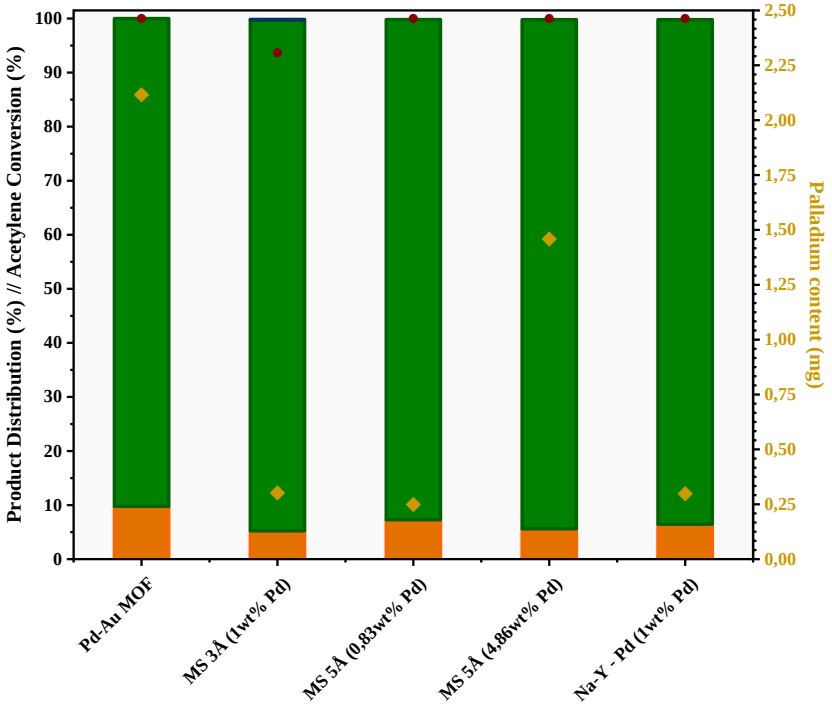

Figure 5-17 Catalytic results for the different Pd-zeolites with different pore size (3,5and 7 Å) and loading of ~ 1wt% Pd compared to Pd_1-Au_1@MOF, with channels of 5.6 Å and loading 7,1wt% Pd; Legend: Ethane (orange); Ethylene(green); Acetylene (blue); Conversion of Acetylene (red dots); Palladium content (Yellow dots)

In addition to the optimal conditions previously established for MOF-based catalysts, a comprehensive investigation was conducted to assess various flow rate conditions tailored to each specific catalyst system. The experiments were designed to evaluate performance sensitivity and stability under different

hydrogen-to-acetylene ratios. The resulting data are presented in Appendix 5A-10.

While the Pd_1–Au_1@MOF exhibits exceptional catalytic performance, its large-scale application is constrained by economic and practical factors, particularly the high cost of gold and the complexity of its synthesis. In contrast, Pd@MS 5Å presents a more viable industrial alternative. It achieves high conversion rates and selectivity with lower metal loading, utilising cost-effective and abundant supports along with simpler preparation methods. Moreover, its advantageous ethane-to-ethylene ratio and reduced ethane production further enhance its suitability for ethylene purification processes.

The structural, kinetic, and catalytic data collectively suggest that MS 5Å is an ideal platform for the selective hydrogenation of acetylene. Its intermediate pore size is well-aligned with the kinetic diameters of both reactants and products, facilitating efficient conversion while minimising the likelihood of over-hydrogenation. Building on this premise, Pd–Au catalysts supported on MS 5Å were developed as a strategic design approach to replicate the high activity observed in Pd–Au metal-organic frameworks (MOFs), while also capitalising on the economic and structural benefits of zeolitic materials. This hybrid strategy offers a pathway for the creation of scalable, efficient, and cost-effective catalysts for the purification of industrial ethylene streams.

In addition to the Pd-only systems, a monometallic Au@MS 5Å zeolite catalyst was synthesised and evaluated under the same optimal reaction conditions as the Pd-based materials. However, akin to the previously studied Au@MOF system, no measurable conversion of acetylene was achieved. This absence of catalytic activity suggests that, under the conditions examined, gold alone, whether

contained within a zeolite or a MOF framework, is not effective for the semi-hydrogenation of acetylene. These findings further highlight the crucial role of palladium in facilitating hydrogen activation and enabling selective hydrocarbon transformation within the tested catalytic systems.

5.3.5. Pd-Au-zeolite

Based on a comparative catalytic evaluation of various zeolite supports, MS 5Å has emerged as the most effective material for achieving an optimal balance between activity and selectivity in the semi-hydrogenation of acetylene. Its intermediate pore size of approximately 5 Å provides a favourable compromise, mitigating the diffusion limitations associated with the narrower-pore MS 3Å while avoiding the excessive openness of the wider-pore NaY. Catalysts utilising MS 5Å consistently reached full acetylene conversion at both low and high palladium loadings, simultaneously reducing ethane formation and enhancing selectivity for ethylene. These findings emphasise the significance of the steric effects generated by the pore framework, where moderate spatial confinement can restrict the diffusion of bulky intermediates and over-hydrogenated products, while still allowing reactants to access the active sites effectively.[48]

Given its favourable performance, MS 5Å was selected as a structural template for the development of a new series of bimetallic Pd–Au catalysts. The aim was to replicate the outstanding performance characteristics of Pd_1-Au_1@MOF materials, particularly their high selectivity and atomically dispersed dimeric active sites, while leveraging the structural robustness, ease of synthesis, and cost-effectiveness of zeolitic supports.[45] To investigate how different metal

incorporation strategies affect the catalytic properties of these systems, three distinct Pd–Au@MS 5Å catalysts were synthesised using various protocols.

In the first approach, palladium and gold precursors were co-impregnated simultaneously onto the MS 5Å support. The second approach involved impregnating and drying Pd before introducing Au, while the third approach reversed this order by impregnating Au first, followed by Pd. These variations were designed to explore the effects of simultaneous versus sequential metal deposition on metal dispersion, bimetallic site formation, and interactions with the zeolite framework.[49, 50]

This investigation stems from the well-established sensitivity of bimetallic catalysts to factors such as metal distribution, support coordination, and electronic modification, all of which can significantly impact both their activity and selectivity.

It is particularly intriguing to investigate how the sequence of metal incorporation influences the accessibility and distribution of active sites, potentially impacting catalytic performance through mechanisms such as site competition, preferential anchoring, or metal–metal synergy. Studies have indicated that the spatial arrangement and proximity of Pd and Au atoms can either facilitate or obstruct the formation of catalytically active bimetallic ensembles. Moreover, Au can electronically stabilise Pd and modify hydrogen activation pathways.[51]

Additionally, the occupation of microporous environments within zeolites by either metal can lead to variations in accessibility and turnover frequency, depending on whether the metal particles are confined within the pores or deposited on external surfaces.[45]

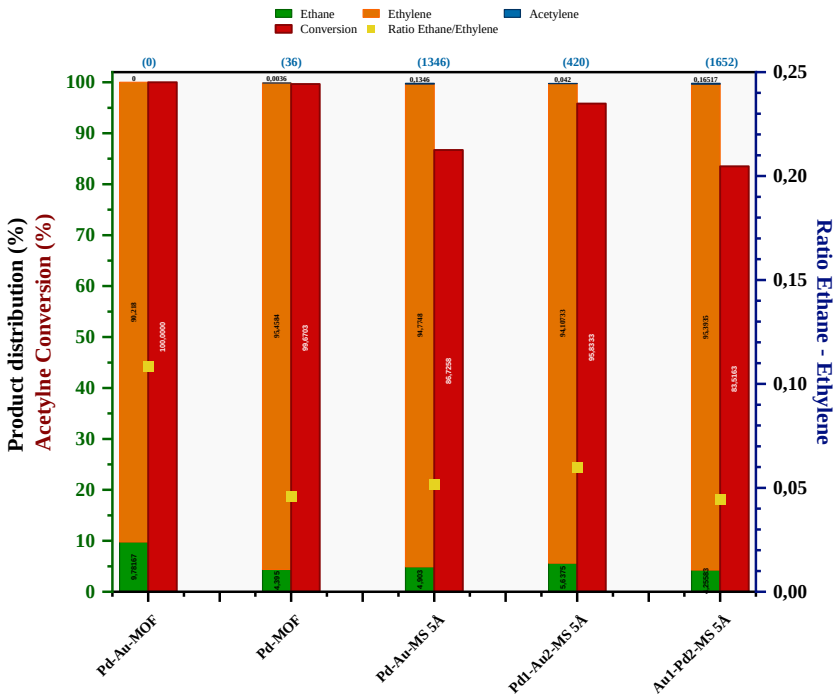

Figure 5-18 Product yield distribution (%) for the semi-hydrogenation of acetylene over Pd–Au catalysts supported on MS 5Å and MOF under identical reaction conditions; Legend: Ethane (orange); Ethylene (green); Conversion of acetylene (red); Ratio ethane-to-ethylene (yellow dots)

The catalytic performance of the Pd–Au@MS 5Å systems was evaluated under identical reaction conditions for a direct comparison with monometallic analogues and the Pd_1-Au_1@MOF benchmark (see Figure 5-18). This study examined acetylene conversion, ethylene selectivity, ethane suppression, and the ratio of single bonds to double bonds (ethane/ethylene) in the products. The aim

was to explore how various synthetic strategies impact the structure–function relationships in these bimetallic systems. The effectiveness of the Pd–Au systems in the selective hydrogenation of acetylene is strongly influenced by support architecture, metal dispersion, and deposition methods. A comparison of the Pd_1–Au_1@MOF with the MS 5Å-supported catalysts highlights how spatial confinement and bimetallic site structure can affect catalytic activity and selectivity.

The Pd_1–Au_1 @MOF features one-dimensional channels approximately 5.6 Å in diameter, hosting atomically dispersed Pd–Au dimeric sites. Owing to its high surface area and open pore architecture, this system enables complete acetylene conversion with a product distribution of 90.22% ethylene and 9.78% ethane. While the extensive pore accessibility facilitates efficient reactant diffusion and interaction with active sites, it simultaneously allows for re-adsorption of the ethylene product, promoting secondary hydrogenation and leading to undesired ethane formation. Moreover, the absence of spatial constraints limits the suppression of over-hydrogenation pathways. In contrast, the MS 5Å zeolite, with its narrower pore size (~5 Å), introduces a size-selective diffusion barrier that effectively moderates access to active sites. This confinement aligns with the kinetic diameters of acetylene (3.3 Å) and ethylene (4.2 Å), restricting the entry of larger species and hindering product re-adsorption.[52] As a result, the MS 5Å-supported Pd–Au catalysts demonstrated markedly improved selectivity while maintaining high levels of activity. Notably, the manner in which Pd and Au were introduced into the zeolite support had a profound impact on catalytic behaviour.

Among the MS 5Å-based systems, catalysts synthesised using different metal deposition sequences exhibited distinct product distributions. These variations can be attributed to differences in metal dispersion, alloying, and electronic

interactions. In all cases, Pd and Au were sequentially introduced using wet impregnation to replicate the optimised configuration observed in Pd_1–Au_1 @MOF, with total metal loadings adjusted as necessary to align with those of the MOF (7.1 wt% Pd). To examine structural preservation and metal incorporation methods in various porous supports, the XRD profiles of bimetallic catalysts (Pd_1Au_1) on zeolitic MS 5Å were compared to those in a crystalline MOF. Figure 5-19 displays the XRD patterns of pristine MS 5Å and its metal-loaded variants, while Figure 5-4 shows the calculated and experimental PXRD profiles for the pristine MOF and its bimetallic analogue, Pd_1-Au_1@MOF, in the 2θ range of 2.0–60.0°. In the zeolite-based system, the XRD patterns confirmed the high crystallinity of the support and the successful incorporation of Pd and Au without the formation of large crystalline nanoparticles. Notably, the absence of distinct reflections for Pd or Au, compared to JCPDS standards, indicates a high level of dispersion or atomic-scale confinement of the metals within the MS 5Å pore network.

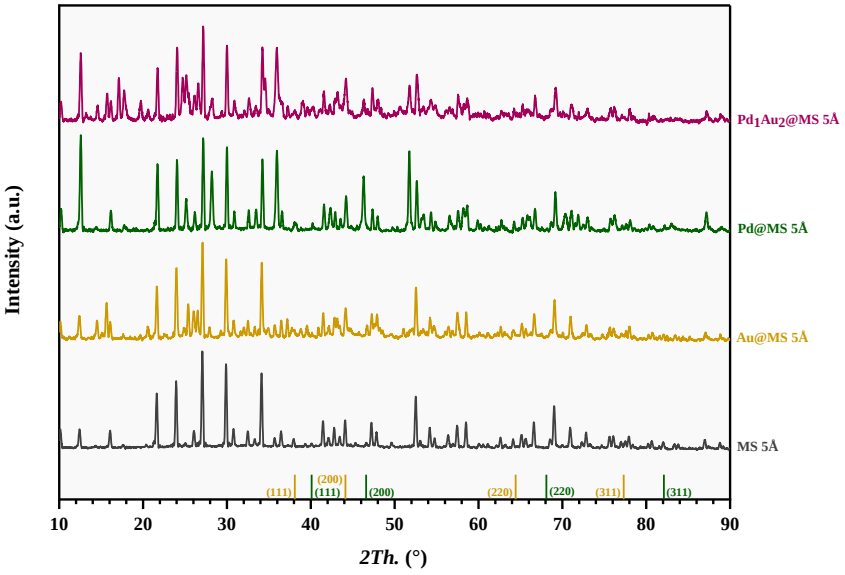

Figure 5-19 X-ray diffractograms (XRD) comparing PdAu-zeolite with a 5 Å pore size to its zeolite supports (MS 5Å), Pd@MS 5Å and Au-MS 5Å. Below, reference patterns for palladium (Pd, JCPDS 46–1043) and gold (Au, JCPDS 04-0784) confirm the absence of large metal nanoparticles, indicating a finer distribution of the metals within the zeolite.

The co-impregnated Pd–Au@MS 5Å catalyst, synthesised by simultaneous addition of both metal precursors, achieved complete acetylene conversion with an ethylene yield of 94.77% and ethane formation of only 4.90%. (Figure 5-18) This performance is attributed to the formation of homogeneously alloyed Pd–Au sites during the drying and activation stages, which likely facilitated optimal metal–metal interactions and electronic tuning. As a result, the configuration likely generated electronically tuned active sites that facilitated semi-

hydrogenation while minimising hydrogen spillover and excessive reduction. Sequential deposition strategies produced notably different results. In the Pd_1–Au_2@MS 5Å catalyst, where palladium was deposited before gold, the ethylene yield reached 94.11%, accompanied by a slight increase in ethane production to 5.64% and nearly complete conversion of acetylene, with only 420 ppm of residual acetylene. When Pd is deposited prior to Au, the resulting catalyst structure is often characterised by Pd nanoparticles that are subsequently modified by the introduced Au species. This configuration typically leads to partial alloying or surface decoration, where Au atoms interact with pre-formed Pd domains to create bimetallic interfaces. These interactions can alter the electronic environment of Pd, weakening Pd–H bonding and favouring the adsorption of π-bound acetylene species over strongly held ethylene intermediates. However, the extent of alloying may be limited, leaving portions of extended Pd ensembles exposed. This incomplete modification can reduce the catalyst's selectivity, as the exposed Pd sites are more prone to facilitating over-hydrogenation pathways. Although such catalysts retain high activity, the increased formation of ethane reflects the challenge of fully suppressing multi-step hydrogenation in the absence of complete site isolation or homogeneous alloy formation.[53]

In contrast, the Au_1–Pd_2@MS 5Å catalyst, where gold (Au) was introduced before palladium (Pd), exhibited the lowest ethane formation at 4.26% and the highest ethylene yield at 95.39%. This occurred despite a slightly less complete conversion of acetylene, with 1652 ppm of acetylene remaining. This suggests that the pre-deposition of Au modifies the zeolite surface, improving Pd dispersion and promoting the formation of electronically isolated Pd sites. It is known that Au functions as both an electronic and geometric modulator,

weakening Pd–H binding and disrupting extended Pd ensembles that favour deeper hydrogenation.[53] These variations confirm that the bimetallic performance is sensitive to the deposition sequence. This finding aligns with studies of Au-modified oxides and nanoparticle catalysts, where the order of metal addition significantly alters particle size, alloy composition, and surface reactivity.[54]

The overall performance trends observed in the MS 5Å-based catalysts underscore the importance of not only the support's pore structure but also the bimetallic configuration and preparation techniques employed. The confinement effect of MS 5Å plays a pivotal role in limiting over-hydrogenation, while the interaction between Pd and Au, shaped by their spatial arrangement and the degree of alloying, modulates hydrogenation pathways at the molecular level.[55]

As reported in various studies, Pd–Au alloy catalysts typically demonstrate reduced hydrogen adsorption strength and enhanced selectivity in alkyne hydrogenation due to electronic charge transfer from Au to Pd. This transfer alters the d-band centre of Pd, thereby suppressing the formation of excessively strong intermediate adsorbates.[53]

The atomic ratio and absolute loading of Pd and Au are crucial factors that shape the structural and electronic environment of bimetallic active sites. These parameters significantly influence alloy formation, hydrogen binding energy, and ultimately, the catalytic behaviour in the semi-hydrogenation of acetylene.

5.3.6. Selectivity and Structure–Function Relationships in Pd–Au Catalysts

The ethane/ethylene ratio, which reflects the relative formation of ethane (single bond) compared to ethylene (double bond), is a crucial selectivity metric in acetylene hydrogenation. Lower values of this ratio indicate a greater selectivity for ethylene, which is vital for industrial applications.[56] Among catalysts with comparable Pd:Au weight ratios (approximately 1:2), the Pd_1–Au_2@MS 5Å and the Pd_1–Au_1@MOF exhibit markedly differing performances. Both catalysts achieve similar acetylene conversion rates, yet Pd_1–Au_2@MS 5Å shows significantly enhanced selectivity, as demonstrated by its lower ethane/ethylene ratio. This disparity emphasises the importance of support architecture, metal dispersion, and synthetic methods, in addition to mere compositional control. [44,57] MOFs provide atomically dispersed Pd–Au sites with excellent catalytic activity. However, their practical applications are hindered by several challenges, including sensitivity to moisture, complex synthesis processes, and limited thermal stability.[58] In contrast, MS 5Å zeolite offers a thermally stable and scalable platform that is ideal for industrial applications. Its shape-selective microporosity effectively reduces the risk of over-hydrogenation by limiting the re-adsorption of ethylene. The enhanced performance of the Pd_1–Au_2@MS 5Å system results from the synergy between structural confinement and electronic modulation. The intermediate pore size of the zeolite restricts the diffusion of reactive intermediates, thereby minimising secondary hydrogenation reactions. Additionally, employing a Pd-first deposition strategy creates isolated or weakly interacting Pd sites that are electronically influenced by adjacent Au atoms. These features replicate the principles of site isolation and metal synergy typical of

MOF catalyst design, while providing a more stable and scalable support framework.

The excess gold present in the Pd:Au = 1:2 composition serves two main functions. Firstly, it dilutes the palladium ensembles, thereby inhibiting the formation of multi-atom Pd sites.[59] Secondly, it modifies the electronic structure of Pd by lowering the d-band centre. This alteration weakens the interactions between Pd and hydrogen, stabilising π-bound acetylene intermediates, promoting ethylene formation, and reducing the likelihood of over-hydrogenation. Structural analysis using X-ray diffraction reveals an observable shift of Pd reflections toward lower 2θ values when Pd@MS 5Å is exposed to hydrogen, compared to air. This shift signifies lattice expansion associated with the formation of palladium hydride (PdHx), a phenomenon where interstitial hydrogen atoms are incorporated into the Pd lattice.[56] This transformation alters the electronic environment of Pd, weakening Pd–H interactions and thereby enhancing selectivity by stabilising π-bound intermediates. The observed lattice flexibility under hydrogen aligns with the bimetallic system's ability to promote ethylene formation while suppressing over-hydrogenation. (Figure 5-20)

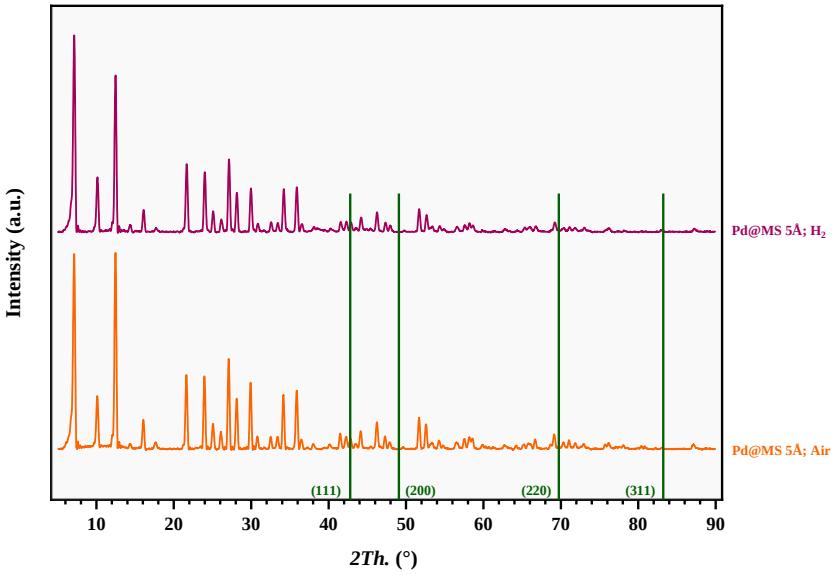

Figure 5-20 Powder X-ray diffractogram (PXRD) of Pd@MS 5A (4.86 wt% Pd), indicating the peaks of the different Pd crystallographic planes in the nanoparticles under air or H_2 atmosphere with reference patterns for Pd (JCPDS 46–1043)

Both Pd_1–Au_2@MS 5Å and Au_1–Pd_2@MS 5Å exhibit enhanced selectivity, with Au_1–Pd_2@MS 5Å achieving the most favourable selectivity-to-dispersion balance (ethane/ethylene ratio), though this comes with a slight compromise in conversion. This trade-off indicates that the initial deposition of gold may restrict the accessibility of Pd sites or impede hydrogen activation, a well-established phenomenon in bimetallic systems where increased selectivity often corresponds to a lower turnover frequency.[56,60] Additionally, the order of deposition significantly impacts both the morphology and functionality of the catalysts. In Pd_1–Au_2@MS 5Å, gold likely decorates pre-existing Pd particles, resulting in the

formation of alloyed or partially alloyed domains. In contrast, Au_1–Pd_2@MS 5Å encourages the nucleation of Pd on gold-modified surfaces, leading to more dispersed, electronically fine-tuned Pd sites that are less prone to over-hydrogenation.[61] The MOF catalyst, characterised by the highest Au content, achieves strong conversion rates but falls short in selectivity due to the unrestricted access of molecules to its active sites. In contrast, the MS 5Å-supported catalysts employ pore confinement to modulate reactivity and enhance selectivity.[56] Particularly, the Au_1–Pd_2@MS 5Å catalyst, with minimal Au and a moderately high palladium (Pd) loading, demonstrates the most selective profile for ethylene production. In conclusion, Au_1–Pd_2@MS 5Å emerges as the most selective catalyst in this series, whereas Pd_1–Au_2@MS 5Å strikes a robust balance between activity and selectivity. This comparative study underscores the necessity of integrating support morphology, controlled metal dispersion, and a strategic deposition approach in the design of effective catalysts.[56,61]

Ultimately, the combination of geometric confinement and bimetallic site engineering plays a vital role in steering hydrogenation pathways toward desirable industrial outcomes.[56, 62]

While the Pd_1–Au_1@MOF achieves perfect acetylene conversion, it exhibits a drawback in selectivity, due to enhanced ethane formation. The Pd_1–Au_2@MS 5Å zeolite-based system demonstrates an ideal compromise, combining high conversion efficiency with superior selectivity, facilitated by its confining pore geometry and precisely engineered Pd–Au interfaces.[56,61] These findings establish Pd_1–Au_2@MS 5Å as a more industrially viable alternative, capable of mimicking the advantages of MOFs without their inherent limitations.[56]

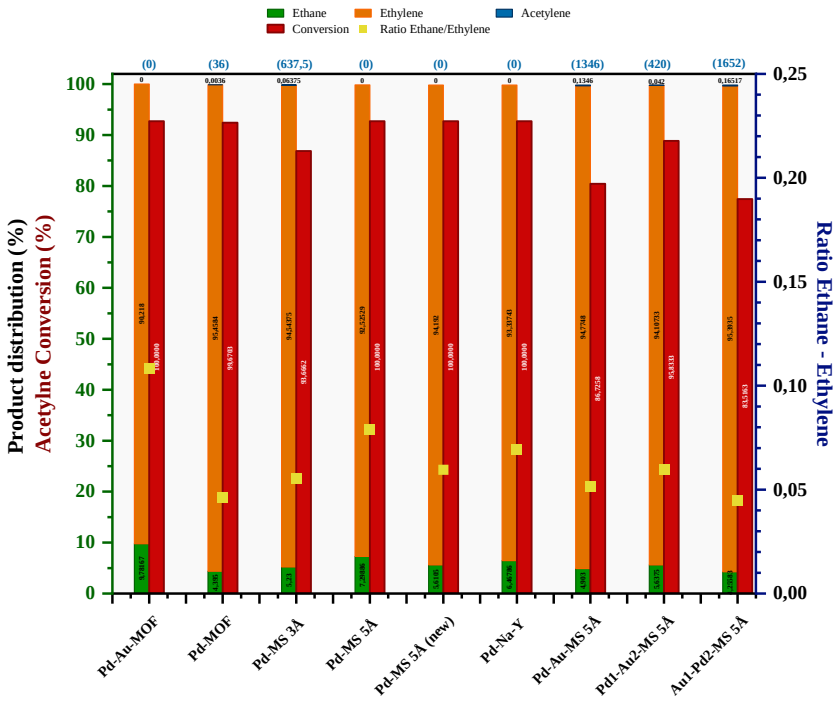

Figure 5-21 Comparative catalytic performance of MOF- and zeolite-supported systems in acetylene semi-hydrogenation. Legend: Ethane (orange); Ethylene (green); Conversion of acetylene (red); Ratio ethane-to-ethylene (yellow dots)

To comprehensively assess the catalysts developed in this study, we present a comparative analysis of MOFs and zeolite-supported systems, as illustrated in Figure 5-21. All formulations achieved acetylene conversions exceeding 90%, yet their selectivity profiles varied significantly, underscoring the critical influence of support architecture and metal configuration.

The MOF-based catalysts, including Pd@MOF and Pd_1Au_1@MOF, accomplished complete conversion but exhibited lower selectivity toward

ethylene. This phenomenon can be attributed to the open pore structure of MOFs, which facilitates the re-adsorption of ethylene and promotes its over-hydrogenation to ethane. Despite these selectivity challenges, MOFs fulfil a dual role: they stabilise atomically dispersed metal sites and regulate the diffusion of reactants and intermediates, thereby enhancing catalytic efficiency. The performance of Pd_1-Au_1@MOF illustrates how cooperative interactions between metal sites and the support framework can be leveraged in gas-phase transformations, where the chemistries of products and reactants are closely intertwined.

To further elucidate the role of support topology, we evaluated materials with varying pore sizes and geometries. It was observed that increasing pore size improved site accessibility and conversion, yet also correlated with a higher ethane-to-ethylene ratio, indicating a trade-off between activity and selectivity.

In contrast, zeolite-supported catalysts, particularly those based on MS5Å, achieved a more favourable balance between conversion and selectivity. The microporous structure of MS 5Å offers spatial confinement that restricts over-hydrogenation, thereby maintaining high selectivity for ethylene. Among the formulations tested, Pd_1Au_2@MS 5Å and Pd@MS 5Å (4.8 wt% Pd) demonstrated the best overall performance, characterised by very low residual acetylene and minimised ethane formation. These enhancements result from both geometric effects, limiting the formation of large palladium ensembles, and electronic modifications induced by gold, which weaken the Pd–H interactions and promote ethylene desorption. While Au_1Pd_2@MS 5Å exhibited the highest ethylene selectivity, Pd_1Au_2@MS 5Å presented a more advantageous compromise between conversion and selectivity, rendering it particularly attractive for industrial-scale applications. Additionally, the thermal stability,

scalability, and established use of MS5Å in conventional catalytic systems further bolster its practical deployment.

The catalytic performance of these systems is governed by the interplay between metal dispersion and pore confinement. Optimal activity and selectivity are achieved when pore dimensions closely match the kinetic diameters of the involved species, facilitating efficient transport while controlling the lifetimes of intermediates. Among all the catalysts studied, Pd_1Au_2@MS 5Å emerges as the most promising candidate for selective acetylene hydrogenation under realistic process conditions, offering a durable and industrially relevant solution.

5.3.7. Theoretical Mechanistic Insights via DFT Calculations

To gain molecular-level insight into the reaction mechanism, periodic DFT calculations were performed on Pd_1–Au_1 dimers embedded within the MOF framework. Six possible configurations were evaluated, with structure F identified as the most stable. (Figure 5-22). In this configuration, Pd is coordinated to two sulfur atoms and Au to one, with an optimised Pd–Au bond length of ~2.6 Å and Pd–S / Au–S distances of ~2.3 Å. Bader charge analysis revealed that Pd remained slightly positively charged, while Au was nearly neutral, suggesting a polarisation of electron density favourable for catalytic activity.

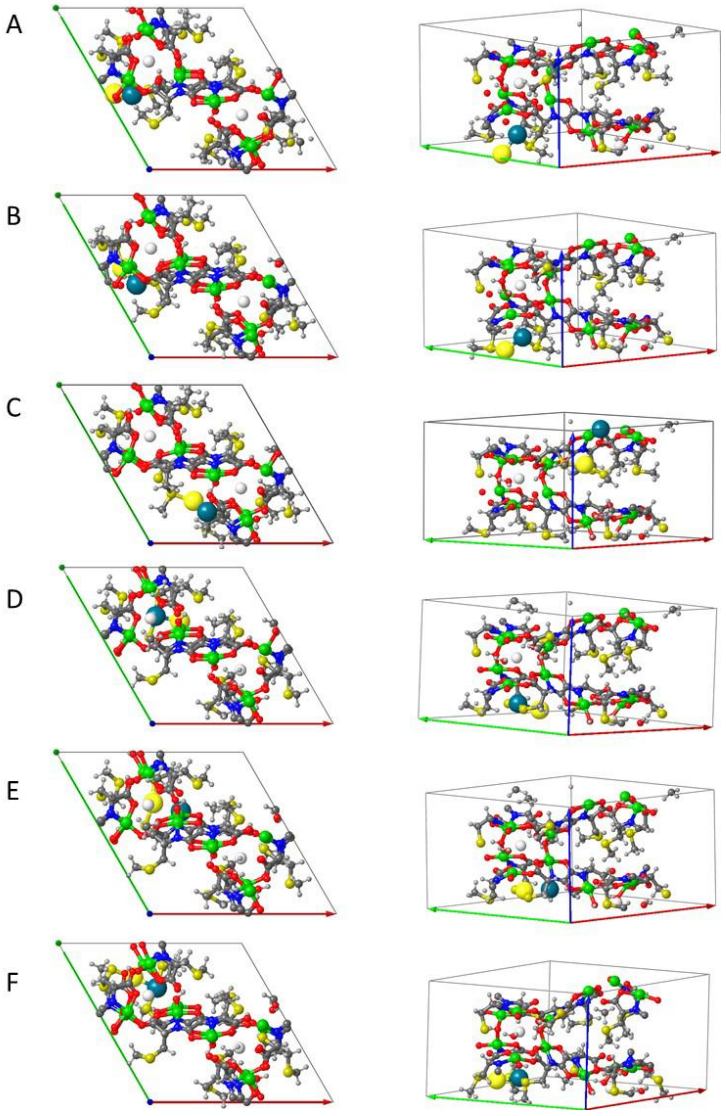

Figure 5-22 Optimised geometries of Pd1Au1 dimers within the MOF. Au, Pd, Cu, S, O, N, C and H atoms are depicted as gold, cyan, green, yellow, red, blue, grey and white balls, respectively.

Using a fragment of structure F, the semi-hydrogenation mechanism of acetylene was investigated. Hydrogen activation was initially considered. Although molecular H_2 could bind on Pd opposite to the Au atom, the calculated activation energy for H–H bond dissociation was too high (208 $kJ \cdot mol^{-1}$) to align with experimental observations. An alternative pathway involving displacement of a thioether ligand allowed H_2 activation with a much lower barrier (42 $kJ \cdot mol^{-1}$), especially in the presence of additional H_2 molecules. In all viable pathways, the first hydrogenation step yielded intermediates where one H atom bridged Pd and Au, and the other remained on Pd. The Au atom played a key role as an electronic modifier, enhancing both activity and selectivity, and stabilising transition states during H_2 dissociation.

Acetylene adsorption on these intermediates required partial ligand detachment and proceeded through a transition state, with activation energies ranging from 17 to 34 $kJ \cdot mol^{-1}$, depending on the pathway. Subsequent steps, involving the addition of another H_2 molecule and hydrogen transfer, led to the formation of ethylene. The most favourable pathway (from 2–B) showed low barriers (17 and 29 $kJ \cdot mol^{-1}$), and ethylene desorption regenerated the active intermediate without requiring further H_2 dissociation, highlighting an efficient catalytic cycle (Figure 5-23).

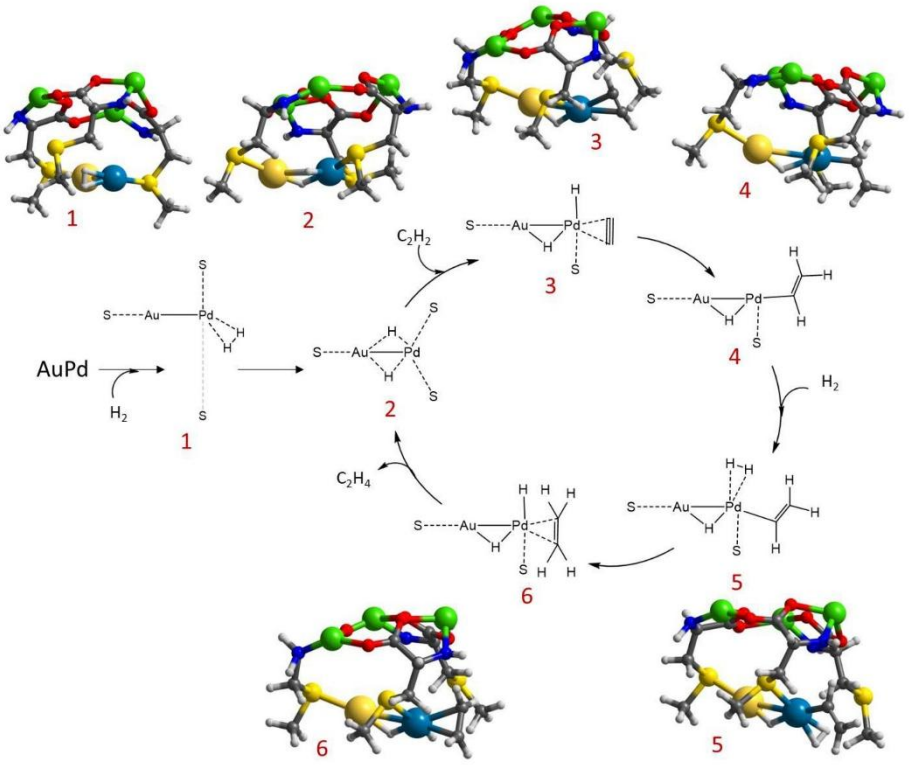

Figure 5-23 DFT-derived reaction mechanism for acetylene semi-hydrogenation on Pd_1Au_1@MOF. Au, Pd, S, O, N, C, and H atoms are represented as gold, cyan, yellow, red, blue, grey, and white spheres, respectively.

Overhydrogenation to ethane was also studied. Although the first hydrogen transfer to ethylene required only 11 $kJ \cdot mol^{-1}$, subsequent H_2 adsorption and activation steps were less favorable and endothermic. Thus, ethylene formation was both kinetically and thermodynamically preferred, consistent with experimental selectivity trends.

5.4. Conclusion

This chapter presents a detailed assessment of metal-organic framework (MOF) and zeolite-supported catalysts for the selective semi-hydrogenation of acetylene under conditions that mimic front-end industrial processes. All evaluated systems recorded high acetylene conversion rates exceeding 90%. However, their selectivity for ethylene varied considerably, shaped by the support's topology and the electronic and geometric configurations of the active metal sites.

Among these catalysts, the MOF-based catalyst Pd_1-Au_1@MOF demonstrated remarkable performance, achieving nearly complete removal of acetylene with remarkably low activation energy of approximately 1 kcal mol^{-1}, an unprecedented feature for this type of reaction. The synergistic interaction between palladium (Pd) and gold (Au), integrated within thioether-functionalized MOF channels, enabled effective hydrogen (H_2) activation and selective ethylene production. The MOF structure not only stabilised isolated active sites but also modulated the local reaction environment, yielding valuable insights into the interplay between structure and function. Nevertheless, the open and highly porous framework of the MOF can lead to the re-adsorption of ethylene, resulting in its over-hydrogenation to ethane, which in turn limits product selectivity. Additionally, the sensitivity of MOFs to moisture and the complexities of their synthesis present challenges for practical implementation, despite the significant mechanistic insights they offer.

Zeolite-supported systems, particularly those employing MS 5Å, offer an advantageous balance of conversion, selectivity, and durability. Palladium-only catalysts, such as Pd@MS 5Å (4.8 wt% Pd), achieved complete conversion with minimal ethane formation, demonstrating that the spatial confinement provided

by the zeolite is sufficient to suppress over-hydrogenation even in the absence of gold (Au). This is accomplished by isolating palladium (Pd) sites and controlling the lifetimes of intermediates. The bimetallic catalyst Pd_1Au_2@MS 5Å further enhances performance by diluting Pd ensembles and optimising metal-hydrogen interactions, resulting in near-complete conversion with low ethane-to-ethylene ratios. While Au_1Pd_2@MS 5Å exhibited slightly higher selectivity, Pd_1Au_2@MS 5Å proves to be the most effective compromise between activity and selectivity, making it the most promising candidate for industrial applications.

The catalytic behaviour observed across both types of support reveals a clear relationship between structure and performance, influenced by pore size. Systems with excessively large pores, such as MOFs, enable rapid mass transport and high activity but may also facilitate unwanted side reactions. In contrast, microporous frameworks like MS 5Å impose spatial constraints that limit the extent of hydrogenation, thereby enhancing selectivity without sacrificing conversion when combined with properly engineered metal sites. This balance is essential in gas-phase reactions involving chemically similar species, such as acetylene and ethylene.

In conclusion, Pd_1Au_2@MS 5Å emerges as the most viable formulation for industrial use, combining high conversion, exceptional selectivity, and material robustness. Although Pd_1-Au_1@MOF is less stable, it offers important atomic-level insights into the catalytic mechanism. Together, these systems underscore the significance of tailoring both the architecture of metal sites and the pore environment to achieve efficient, selective, and scalable catalytic performance.

5.5. Appendix

a) 5A-1

Table 5A-1. Metal content of the used catalysts measured by inductively coupled plasma atomic emission spectroscopy (ICP-AES).

Name	Metal Species	ICP Metal Content (wt%)
MOF Pd_1 - Au_1; CuMecys PdAu	Pd, Au	7.1 Pd; 16.0 Au
MOF Pd_1; CuMecys Pd	Pd	5.9 Pd; 0.07 Au
MOF Au_1; CuMecys Au	Au	0.05 Pd; 22.1 Au
Pd@MS 3Å	Pd	1.01 Pd 0.15 Pd 0.03 Pd
Pd@MS 5Å	Pd	4.86 Pd 0.83 Pd 0.12 Pd 0.02 Pd
Au@MS 5Å	Au	3.11 Au
Pd-Au@MS 5Å	Pd; Au	3.18 Pd; 5.83 Au
Pd_1-Au_2@MS 5Å	Pd; Au	3.89 Pd; 6.25 Au
Au_1-Pd_2@MS 5Å	Pd; Au	4.22 Pd; 1.73 Au
Pd@NaY	Pd	5.00 Pd 0.99 Pd

b) 5A-2

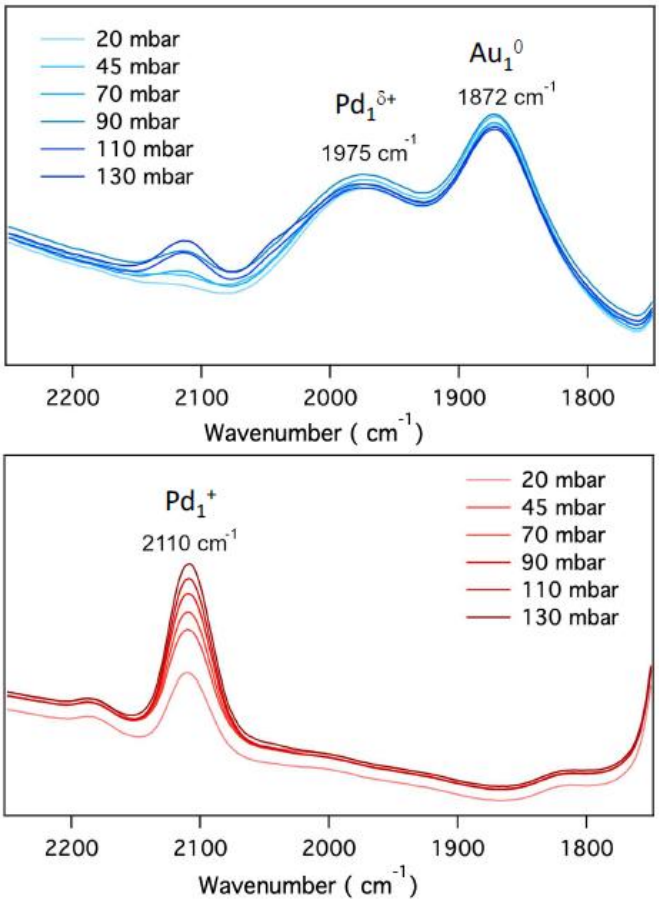

Figure 5A-2 Diffuse reflectance infrared Fourier transform spectroscopy with CO probe (DRIFTS) of Pd_1Au_1@MOF (top) and Pd_1@MOF (bottom), recorded at 77 K with increasing pressure of CO and subsequent evacuation at 10^{-6} mbar desorption cycles. The samples were activated at 80 °C under reduced pressure for 16 h prior to carrying out the sorption measurements.

c) 5A-3

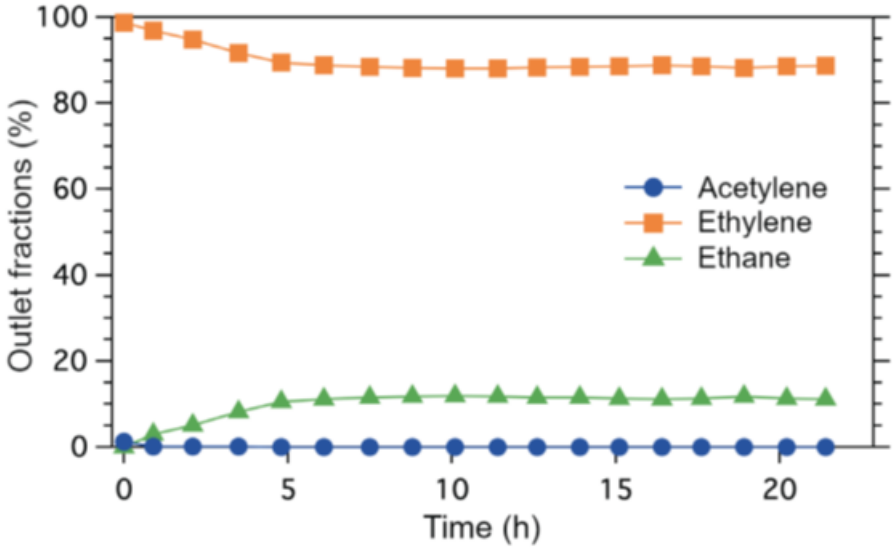

Figure 5A-3 Results of the continuous-flow semi-hydrogenation of acetylene using the Pd_1–Au_1@MOF catalyst over one full day of uninterrupted operation. Conditions: 100 °C, 10:1 H_2 to hydrocarbons ratio, 33 mL min^{-1} total feed flow.

d) 5A-4

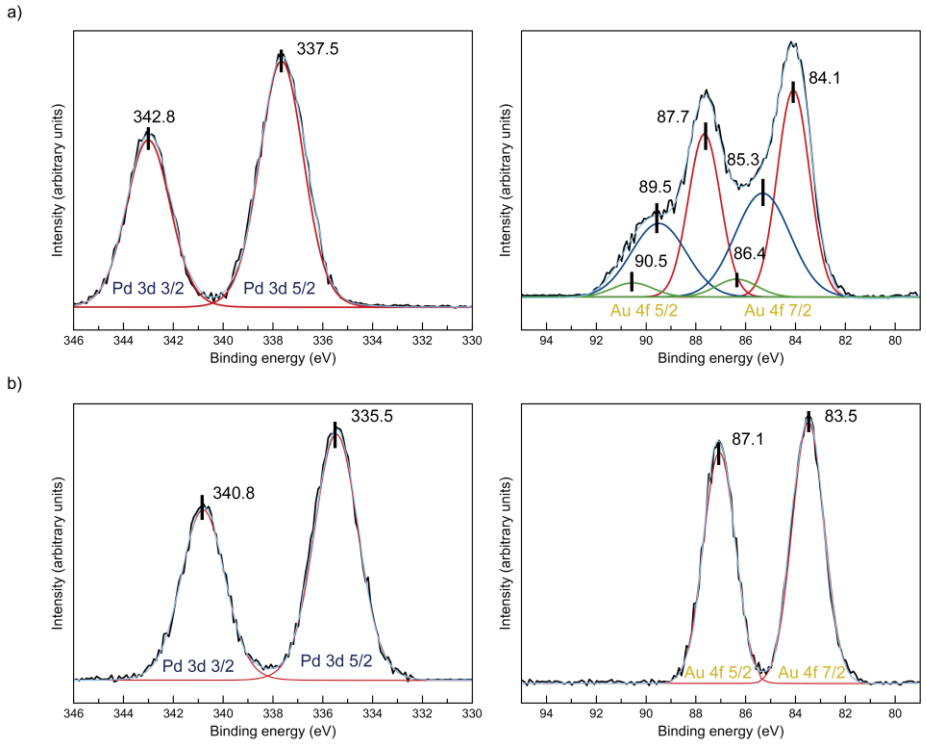

Figure 5A-4 X–ray photoelectron spectroscopy (XPS) of Pd_1Au_1@MOF before (a) and after reduction with $NaBH_4$ (Pd_1Au_1@MOF, b) showing the deconvoluted signals of $Au4f_{7/2}$ and $Au4f_{5/2}$ (left) and $Pd3d_{5/2}$ and $Pd3d_{3/2}$.

e) 5A-5

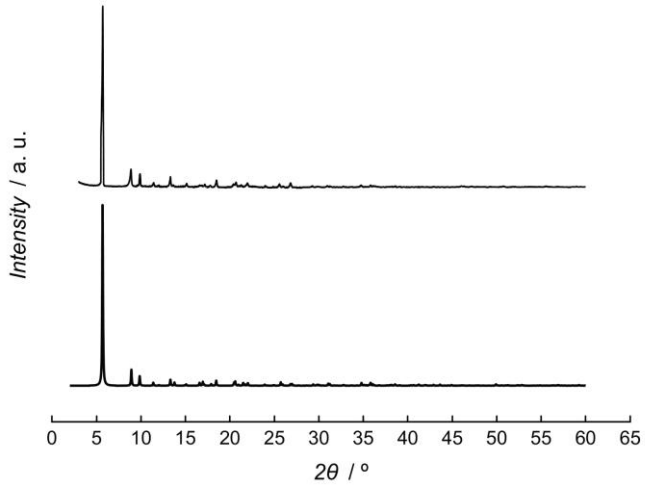

Figure 5A-5 Theoretical (bold) and experimental (solid line) PXRD pattern profile of Pd_1-Au_1@MOF, in the 2θ range 2–60°, after the catalytic experiments.

f) 5A-6

Table 5A-6 Selected data from the ICP–MS[a] and SEM/EDX[b].

Metal	% mass[a]	Metal stoichiometry[a]	% mass[b]	Metal stoichiometry
Cu	20.68	6.02	20.23	5.89
Sr	4.69	0.99	4.41	0.93
Au	5.25	0.49	5.37	0.50
Pd	2.93	0.51	2.83	0.49

[a] Solid samples were digested with 0.5 mL of 69% HNO_3 at 60 °C for 4 hours, followed by the addition of 0.5 mL of 37% HCl and digestion at 80 °C for 1 hour.

g) 5A-7

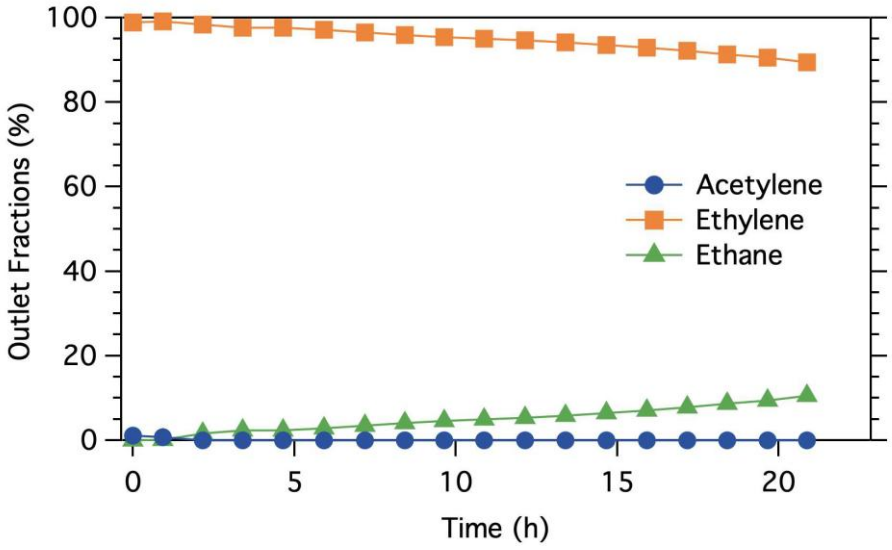

Figure 5A-7 Catalytic activity and stability over time for the Pd_1@MOF catalyst. Reaction conditions: 30:1 H_2:acetylene ratio, 12 mL/min, 24 h reaction time and 100 ºC reaction temperature. Blue circles correspond to acetylene, orange squares correspond to ethylene and green triangles correspond to ethane

h) 5A-8

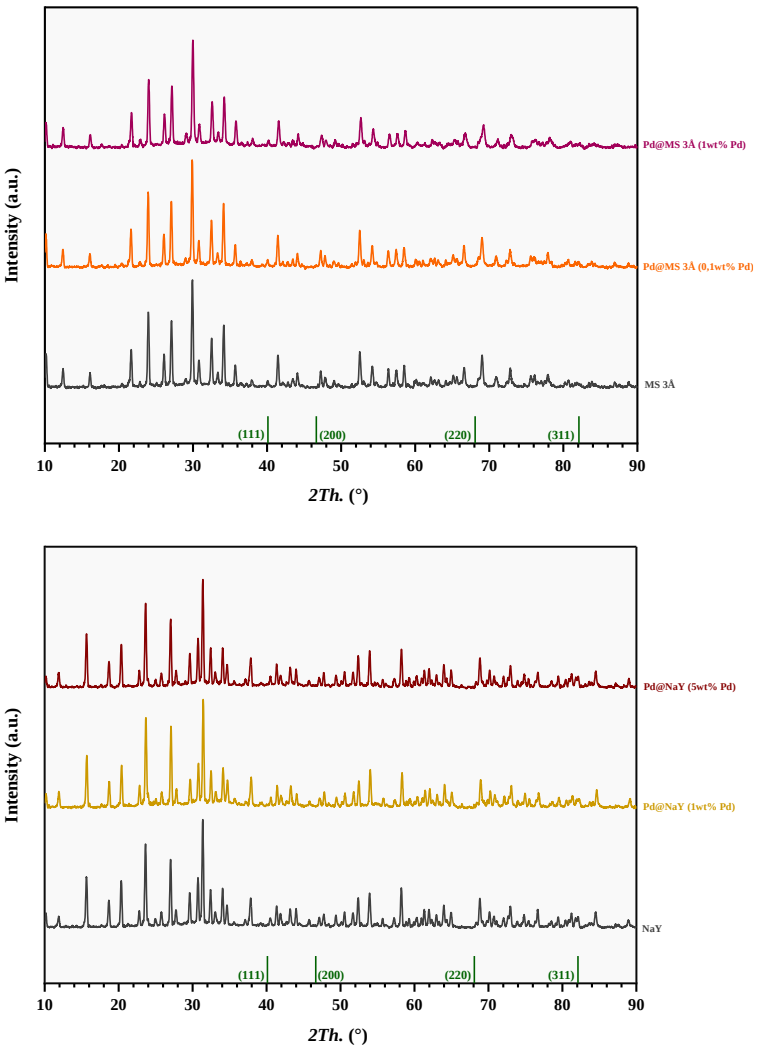

Figure 5A-8 X-ray diffractograms (XRD) comparing Pd-zeolite with a 3 Å pore size to its zeolite supports (MS 3Å), Pd@MS. (top), and XRD comparing Pd-zeolite with a 7,4 Å pore size to its zeolite supports (NaY), Pd@MS. (bottom)

i) 5A-9

Pd@MS 3Å (1wt% Pd)

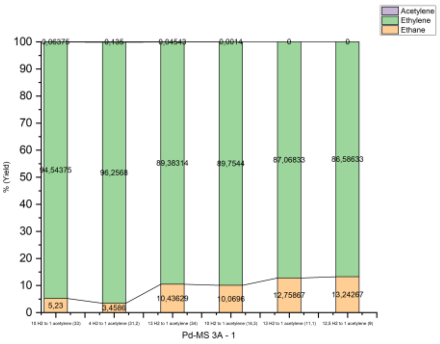

Pd@MS 3Å (0,1wt% Pd)

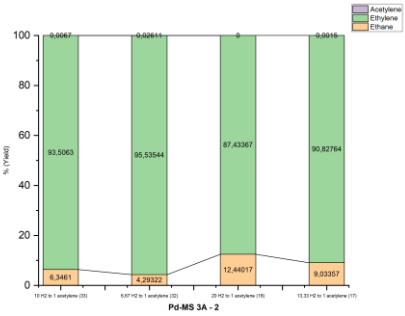

Pd@MS 3Å (0,03wt% Pd)

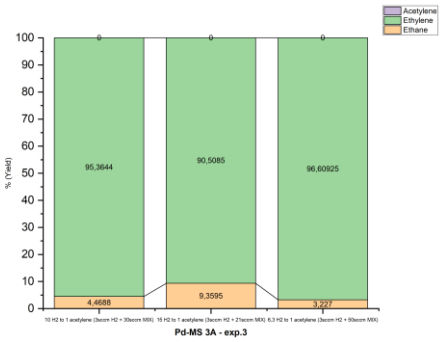

Pd@MS 5Å (0,83% Pd)

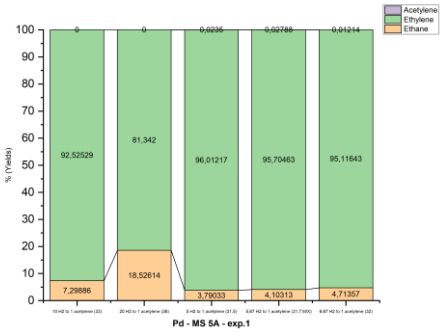

Pd@MS 5Å (0,12% Pd)

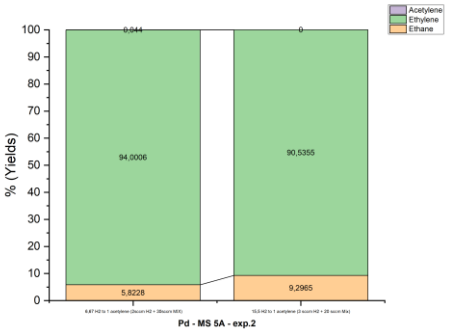

Pd@MS 5Å (0,02% Pd)

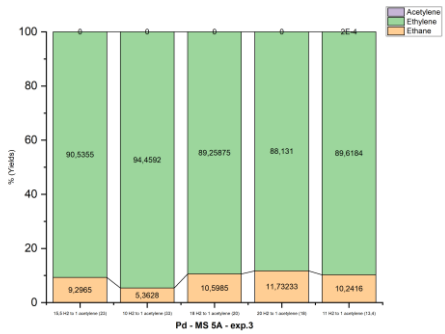

Pd@MS 5Å (4,86% Pd)

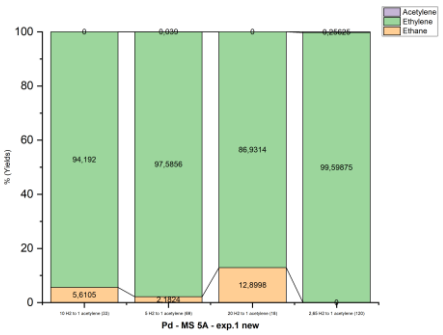

Pd@NaY(5wt% Pd) **Pd@NaY(1wt% Pd)**

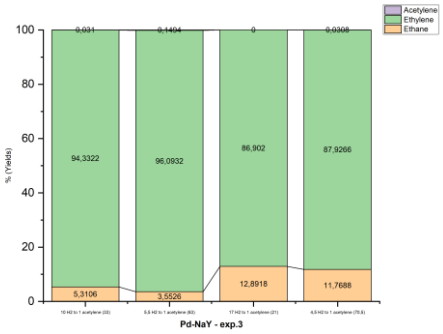

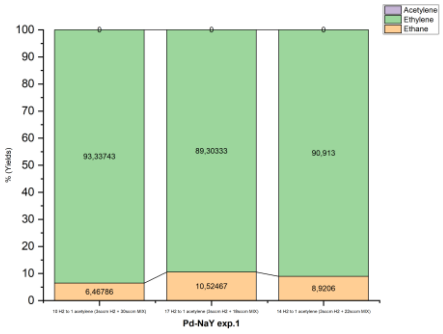

Figure 5A-9 Catalytic performance of Pd@MS 3Å, Pd@MS 5Å, and Pd@NaY under varying flow rates and catalyst loadings.

j) 5A-10

Pd-Au@MS 5Å

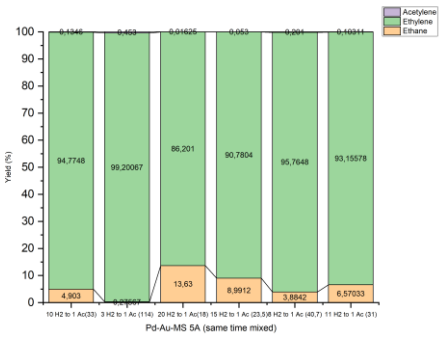

Pd1-Au2@MS 5Å

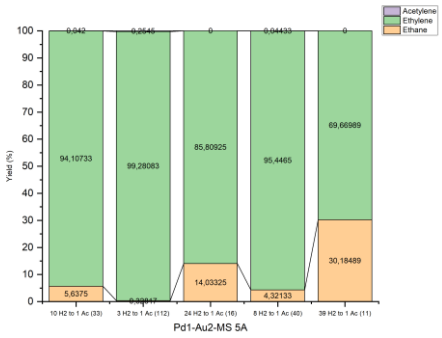

Au1-Pd2@MS 5Å

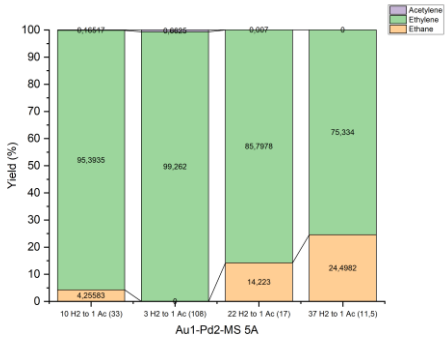

Figure 5A-10 Catalytic performance of Pd-Au@MS 5Å, Pd_1-Au_2@MS 5Å, and Au_1-Pd_2@MS 5Å under varying flow rates and catalyst loadings.

5.6. References

1. Martín, A. J., Mondelli, C., Jaydev, S. D. & Pérez-Ramírez, J. Catalytic processing of plastic waste on the rise. *Chem* 7, 1487–1533 (2021).

2. Shittu, T. D. & Ayodele, O. B. Catalysis of semihydrogenation of acetylene to ethylene: current trends, challenges, and outlook. *Front Chem Sci Eng* 16, 1031–1059 (2022).

3. Szukiewicz, M. & Petrus, R. Selective Hydrogenation of an Acetylene Process: An Example of Modeling an Industrial Reactor Process. *Chem Eng Technol* 22, 1059–1061 (1999).

4. Rijo, B., Lemos, F., Fonseca, I. & Vilelas, A. Development of a model for an industrial acetylene hydrogenation reactor using plant data – Part I. *Chemical Engineering Journal* 379, 122390 (2020).

5. Hock, S., Iser, L., Lucas, M. & Rose, M. Reaction Kinetics of an Industrial Front-End Acetylene Hydrogenation Catalyst Using the Advanced TEMKIN Reactor. *Chem Ing Tech* 94, 1704–1710 (2022).

6. Schbib, N. S., García, M. A., Gígola, C. E. & Errazu, A. F. Kinetics of front-end acetylene hydrogenation in ethylene production. *Ind Eng Chem Res* 35, 1496–1505 (1996).

7. Dehghani, O., Rahimpour, M. R. & Shariati, A. An Experimental Approach on Industrial Pd-Ag Supported α-Al2O3 Catalyst Used in Acetylene Hydrogenation Process: Mechanism, Kinetic and Catalyst Decay. *Processes 2019, Vol. 7, Page 136* 7, 136 (2019).

8. Catalyst composition for selective hydrogenation with improved characteristics. (2019).

9. Xie, K. *et al.* Catalysts for selective hydrogenation of acetylene: A review. *Materials Today Catalysis* 3, 100029 (2023).

10. Kley, K. S., De Bellis, J. & Schüth, F. Selective hydrogenation of highly concentrated acetylene streams over mechanochemically synthesized PdAg supported catalysts. *Catal Sci Technol* 13, 119–131 (2023).

11. Yuk, S. F. *et al.* Selective acetylene hydrogenation over single metal atoms supported on Fe3O4(001): A first-principle study. *Journal of Chemical Physics* 152, 154703 (2020).

12. Zou, S. *et al.* Grafting nanometer metal/oxide interface towards enhanced low-temperature acetylene semi-hydrogenation. *Nature Communications 2021 12:1* 12, 1–11 (2021).

13. Feng, H. *et al.* Machine-Learning-Assisted Catalytic Performance Predictions of Single-Atom Alloys for Acetylene Semihydrogenation. *ACS Appl Mater Interfaces* 14, 25288–25296 (2022).

14. Li, Q., Wang, Y., Skoptsov, G. & Hu, J. Selective Hydrogenation of Acetylene to Ethylene over Bimetallic Catalysts. *Ind Eng Chem Res* 58, 20620–20629 (2019).

15. Viciano-Chumillas, M. *et al.* Metal-Organic Frameworks as Chemical Nanoreactors: Synthesis and Stabilization of Catalytically Active Metal Species in Confined Spaces. *Acc Chem Res* 53, 520–531 (2020).

16. Mon, M. *et al.* Selective Gold Recovery and Catalysis in a Highly Flexible Methionine-Decorated Metal-Organic Framework. *J Am Chem Soc* 138, 7864–7867 (2016).

17. Mon, M. *et al.* Synthesis of Densely Packaged, Ultrasmall Pt02 Clusters within a Thioether-Functionalized MOF: Catalytic Activity in Industrial Reactions at Low Temperature. *Angewandte Chemie - International Edition* 57, 6186–6191 (2018).

18. Tiburcio, E. *et al.* Highly Efficient MOF-Driven Silver Subnanometer Clusters for the Catalytic Buchner Ring Expansion Reaction. *Inorg Chem* 61, 11796–11802 (2022).

19. Mon, M. *et al.* Hydrolase–like catalysis and structural resolution of natural products by a metal–organic framework. *Nature Communications 2020 11:1* 11, 1–9 (2020).

20. Tiburcio, E. *et al.* Soluble/MOF-Supported Palladium Single Atoms Catalyze the Ligand-, Additive-, and Solvent-Free Aerobic Oxidation of Benzyl Alcohols to Benzoic Acids. *J Am Chem Soc* 143, 2581–2592 (2021).

21. Corma, A. From microporous to mesoporous molecular sieve materials and their use in catalysis. *Chem Rev* 97, 2373–2419 (1997).

22. Liu, L. & Corma, A. Metal Catalysts for Heterogeneous Catalysis: From Single Atoms to Nanoclusters and Nanoparticles. *Chem Rev* 118, 4981–5079 (2018).

23. Thorum, M. S., Yadav, J. & Gewirth, A. A. Oxygen reduction activity of a copper complex of 3,5-diamino-1,2,4-triazole supported on carbon black. *Angewandte Chemie - International Edition* 48, 165–167 (2009).

24. Yang, X. F. *et al.* Single-atom catalysts: A new frontier in heterogeneous catalysis. *Acc Chem Res* 46, 1740–1748 (2013).

25. Ward, T. *et al.* Effects of Pd on catalysis by Au: CO adsorption, CO oxidation, and cyclohexene hydrogenation by supported Au and Pd-Au catalysts. *ACS Catal* 3, 2644–2653 (2013).

26. Elgayyar, T., Atwi, R., Tuel, A. & Meunier, F. C. Contributions and limitations of IR spectroscopy of CO adsorption to the characterization of bimetallic and nanoalloy catalysts. *Catal Today* 373, 59–68 (2021).

27. Zeinalipour-Yazdi, C. D., Willock, D. J., Thomas, L., Wilson, K. & Lee, A. F. CO adsorption over Pd nanoparticles: A general framework for IR simulations on nanoparticles. *Surf Sci* 646, 210–220 (2016).

28. (PDF) A photoelectron diffraction study of the Pd{111}(root 3x root 3)R30 degrees-CO chemisorption phase. https://www.researchgate.net/publication/259214292_A_photoelectron_diffraction_study_of_the_Pd111root_3x_root_3R30_degrees-CO_chemisorption_phase.

29. Bao, Z. *et al.* Molecular Sieving of Ethane from Ethylene through the Molecular Cross-Section Size Differentiation in Gallate-based Metal–Organic Frameworks. *Angew Chem Int Ed Engl* 57, 16020 (2018).

30. Pérez-Botella, E., Valencia, S. & Rey, F. Zeolites in Adsorption Processes: State of the Art and Future Prospects. *Chem Rev* 122, 17647–17695 (2022).

31. What's the difference molecular sieve 3a 4a 5a 13x - Jalon. *https://www.jalonzeolite.com/*.

32. Veerapandian, S. K. P., De Geyter, N., Giraudon, J. M., Lamonier, J. F. & Morent, R. The Use of Zeolites for VOCs Abatement by Combining Non-Thermal Plasma, Adsorption, and/or Catalysis: A Review. *Catalysts 2019, Vol. 9, Page 98* 9, 98 (2019).

33. Zeolite Molecular Sieves: Structure, Chemistry, and Use D. W. Breck (Union Carbide Corporation, Tarrytown, New York) John Wiley and Sons, New York, London, Sydney, and Toronto. 1974. 771 pp. $11.95. *J Chromatogr Sci* 13, 18A-18A (1975).

34. What's the difference molecular sieve 3a 4a 5a 13x - Jalon. *https://www.jalonzeolite.com/*.

35. Zhang, Q. *et al.* Facile synthesis of regenerable NaY zeolite adsorbent relying on alcohol-terminated compounds for efficient trace sulfur dioxide capture. *Chemical Engineering Journal* 475, 146265 (2023).

36. Pérez-Botella, E., Valencia, S. & Rey, F. Zeolites in Adsorption Processes: State of the Art and Future Prospects. *Chem Rev* 122, 17647–17695 (2022).

37. Li, J. R., Sculley, J. & Zhou, H. C. Metal-organic frameworks for separations. *Chem Rev* 112, 869–932 (2012).

38. Opanasenko, M. Catalytic behavior of metal-organic frameworks and zeolites: Rationalization and comparative analysis. *Catal Today* 243, 2–9 (2015).

39. Peralta, D. *et al.* Comparison of the behavior of metal-organic frameworks and zeolites for hydrocarbon separations. *J Am Chem Soc* 134, 8115–8126 (2012).

40. Derbe, T., Sani, T., Amare, E. & Girma, T. Mini Review on Synthesis, Characterization, and Application of Zeolite@MOF Composite. *Advances in Materials Science and Engineering* 2023, 8760967 (2023).

41. Ogawa, T., Iyoki, K., Fukushima, T. & Kajikawa, Y. Landscape of Research Areas for Zeolites and Metal-Organic Frameworks Using Computational Classification Based on Citation Networks. *Materials* 10, 1428 (2017).

42. Peralta, D. *et al.* Comparison of the behavior of metal-organic frameworks and zeolites for hydrocarbon separations. *J Am Chem Soc* 134, 8115–8126 (2012).

43. Bols, M. L. *et al.* In Situ UV-VIS-NIR Absorption Spectroscopy and Catalysis. *Chem Rev* 124, 2352 (2024).

44. Vito, J. & Shetty, M. Challenges and Opportunities for Exploiting the Role of Zeolite Confinements for the Selective Hydrogenation of Acetylene. *ACS Appl Mater Interfaces* 16, 67010 (2023).

45. Liu, H. *et al.* Encapsulation of Pd Single-Atom Sites in Zeolite for Highly Efficient Semihydrogenation of Alkynes. *J Am Chem Soc* 146, 24033–24041 (2024).

46. Luo, Q., Wang, H., Wang, L. & Xiao, F. S. Alloyed PdCu Nanoparticles within Siliceous Zeolite Crystals for Catalytic Semihydrogenation. *ACS Materials Au* 2, 313–320 (2022).

47. Choudary, B. M. *et al.* Hydrogenation of acetylenics by Pd-exchanged mesoporous materials. *Appl Catal A Gen* 181, 139–144 (1999).

48. Liu, M., Miao, C. & Wu, Z. Recent advances in the synthesis, characterization, and catalytic consequence of metal species confined within zeolite for hydrogen-related reactions. *Industrial Chemistry & Materials* 2, 57–84 (2024).

49. Patent, U. S. Palladium-gold catalyst synthesis. (2009).

50. Patent, U. S. Palladium-gold catalyst synthesis. (2010).

51. Hutchings, G. J. Catalysis using gold containing materials. *J Catal* 432, 115392 (2024).

52. Li, R. *et al.* Selective hydrogenation of acetylene over Pd-Sn catalyst: Identification of Pd2Sn intermetallic alloy and crystal plane-dependent performance. *Appl Catal B* 279, 119348 (2020).

53. Joudeh, N., Saragliadis, A., Koster, G., Mikheenko, P. & Linke, D. Synthesis methods and applications of palladium nanoparticles: A review. *Frontiers in Nanotechnology* 4, 1062608 (2022).

54. Sagar, T. V., Zavašnik, J., Finšgar, M., Novak Tušar, N. & Pintar, A. Evaluation of Au/ZrO2 Catalysts Prepared via Postsynthesis Methods in CO2 Hydrogenation to Methanol. *Catalysts* 12, 218 (2022).

55. Takahashi, T. *et al.* Chemoselective hydrogenation using molecular sieves-supported Pd catalysts: Pd/MS3A and Pd/MS5A. *Tetrahedron* 68, 8293–8299 (2012).

56. McCue, A. J. & Anderson, J. A. Recent advances in selective acetylene hydrogenation using palladium containing catalysts. *Front Chem Sci Eng* 9, 142–153 (2015).

57. Navlani-García, M. *et al.* Pd/zeolite-based catalysts for the preferential CO oxidation reaction: ion-exchange, Si/Al and structure effect. *Catal Sci Technol* 6, 2623–2632 (2016).

58. Furukawa, H., Cordova, K. E., O'Keeffe, M. & Yaghi, O. M. The chemistry and applications of metal-organic frameworks. *Science (1979)* 341, (2013).

59. McCue, A. J., Baker, R. T. & Anderson, J. A. Acetylene hydrogenation over structured Au–Pd catalysts. *Faraday Discuss* 188, 499–523 (2016).

60. Lee, G., Jeong, W.-J. & Ahn, H.-G. Selective Hydrogenation of Acetylene to Ethylene Over Nanosized Gold and Palladium Supported Catalysts. *J Nanosci Nanotechnol* 20, 5800–5803 (2020).

61. Zhang, R. *et al.* Insight into the Effects of Cu Component and the Promoter on the Selectivity and Activity for Efficient Removal of Acetylene from Ethylene on Cu-Based Catalyst. *Journal of Physical Chemistry C* 121, 27936–27949 (2017).

62. Ding, L. *et al.* Activating Edge Sites on Pd Catalysts for Selective Hydrogenation of Acetylene via Selective Ga2O3 Decoration. *ACS Catal* 6, 3700–3707 (2016).

Chapter 6.

Aromatisation of Linear Alkenes over Few-Atom Ruthenium Oxide Clusters at 300 °C: Mechanistic Insights and Catalytic Performance

Index

6.1. Introduction

Alkylated aromatic hydrocarbons, especially ethylbenzene and the three isomers of xylene (*para*-, *meta*-, *and ortho*-), are among the most significant chemical intermediates in the global petrochemical industry.[1] These mono-alkylated benzenes are crucial building blocks in synthesising high-value materials and consumer products across various industrial sectors.[2] *Ortho*-xylene and ethylbenzene are fundamental building blocks in polymer chemistry, and, for instance, the latter is predominantly used (over 99%) for the production of styrene monomer, which is subsequently polymerised into polystyrene, ABS plastics, and other styrenic copolymers. These polymers are used in various products, such as electronics casings, insulation materials, automobile parts, and disposable consumer goods. According to recent industrial data, global ethylbenzene production capacity exceeds 47 million metric tonnes annually, primarily within large-scale steam cracking and reforming complexes. Both ethylbenzene and mixed xylenes (encompassing all three isomers) are integral to high-octane gasoline blends, enhancing fuel quality and engine performance. Their dual role, as chemical feedstocks and fuel additives, highlights their strategic value across multiple industrial sectors.[3]

The synthesis of xylenes and ethylbenzene is a cornerstone of modern petrochemical manufacturing, owing to their widespread industrial applications and high global demand.[4] Traditionally, these aromatic compounds are produced via two principal industrial pathways: catalytic reforming of Naphtha and Friedel–Crafts alkylation of benzene (only for ethylbenzene)[5] with light olefins, as shown in Figure 6-1. Among these, Naphtha cracking remains the more established route for bulk production. This process converts straight-chain

alkanes and cycloalkanes found in light petroleum fractions into aromatic hydrocarbons through a series of reactions including dehydrogenation, isomerisation, cyclisation, and aromatisation. Naphtha cracking typically operates at high temperatures (480–520 °C) and moderate pressures, employing Pt-based catalysts supported on chlorinated alumina.[6] While effective, the process is energy-intensive and poses sustainability and toxicity concerns due to using chlorinated supports. Furthermore, coke formation during operation necessitates periodic catalyst regeneration, which involves the oxidative removal of carbonaceous deposits and reduction and re-chlorination. This cyclic regeneration can progressively degrade catalyst performance and reduce operational efficiency over time.[7]

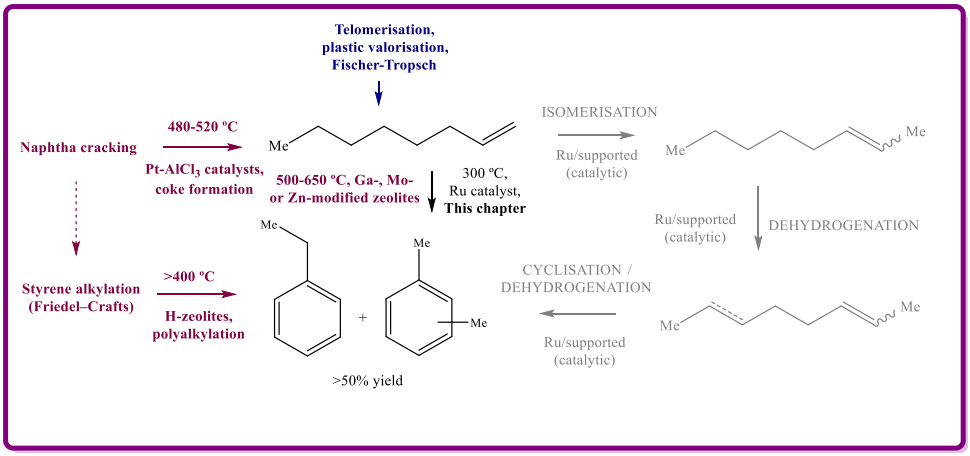

Figure 6-1 Current industrial routes and the proposed reaction scheme for the Ru-catalysed aromatisation of long-chain alkenes.

The second major route (for producing ethylbenzene) is the Friedel–Crafts alkylation, which involves the alkylation of benzene with ethylene or light olefins, often derived from methanol. This reaction is typically catalysed by zeolite-based solid Brønsted acids such as H-ZSM-5, Beta, and Mordenite, which are prized for their high activity and shape selectivity, particularly in maximising *para*-xylene yield due to their well-defined microporous structures.[8,9] However, the process is not without drawbacks. Neat Brønsted acid zeolite efficiently catalyses polyalkylation reactions at >400 ºC, which leads to undesired heavy byproducts, and suffers from rapid deactivation due to coke accumulation within its narrow pore networks.[10] Furthermore, these neat Brønsted acid zeolites show limited effectiveness in processing longer-chain alkenes, which tend to undergo fragmentation and oligomerisation under the strongly acidic conditions typically employed at these high reaction temperatures.[11] In conclusion, while both catalytic reforming and zeolite-based alkylation technologies exhibit a high degree of technical maturity, they nevertheless confront considerable environmental, economic, and operational limitations.[12]

Alternative catalytic strategies are gaining momentum in response to decarbonisation goals and the shift away from fossil-based feedstocks. These include low-temperature transformations, non-acidic catalytic pathways, and the valorisation of olefinic feedstocks from both fossil and renewable origins.[13] A growing consensus among industry and academic circles identifies several key priorities for developing next-generation catalytic systems. These priorities include reducing operating temperatures to below 400 °C,[14] minimising undesirable side reactions such as over-alkylation and cracking, enhancing the longevity of catalysts, and ensuring compatibility with olefinic and bio-derived feedstocks.[14] These demands shift research focus away from conventional neat

Brønsted acid zeolite systems toward neutral or mildly reducing catalytic environments. A promising direction would involve converting terminal long-chain alkenes into aromatic compounds, potentially offering improved selectivity and reduced process complexity.[13] Alkenes can be regarded as a pre-activated form of alkanes, which enhances their suitability for the aromatisation reaction.[11,15,16]

In this context, ruthenium (Ru) has emerged as a promising catalyst for the low-temperature aromatisation of long-chain alkenes, providing a versatile and selective alternative to traditional systems.[17] Unlike traditional noble metals such as Pt or Pd, Ru supported on charcoal and amorphous oxides (including SiO_2, Al_2O_3 and perhaps also zeolites) might efficiently catalyse a range of key steps relevant to alkene aromatisation. These would include the isomerisation of long-chain terminal alkenes to internal isomers under relatively mild conditions (<300 °C),[18] as well as the dehydrogenation, cyclisation, and aromatisation steps required to produce mono-alkylated aromatic compounds, as shown in Figure 6-1. These transformations could be achieved in a single reactor step, eliminating the need for external ligands, solvents, or strong acidic or basic promoters.[19] This Ru-based catalytic system would represent a notable advantage over multi-step reforming or alkylation processes, which often require separate reactor beds, co-feeds, or subsequent separation procedures.

Ru possesses several advantages for treating long-chain terminal alkenes at higher reaction temperatures than Pt or Pd. For instance, Ru exhibits redox flexibility and low propensity for coking at moderate reaction temperatures, allowing for straightforward reactivation through hydrogen or air flushing and simplifying regeneration.[20] Typically, catalyst regeneration for Ru-supported catalysts can be accomplished through mild oxidation treatments (using air or O_2

at 350–400 °C) without the necessity for acid/base neutralisation or solvent washes. This method effectively reduces energy costs and the complexity of maintenance operations.[21] Indeed, the integration of Ru-based aromatisation represents a departure from traditional petrochemical pathways, with the comparative advantages shown in Table 6-1.

Table 6-1 Comparative analysis of conventional aromatisation methods and the Ru-based catalytic system reported here.

Entry	Feature	Conventional methods	Ru-based aromatisation
1	Temperature	500–650°C	~300°C
2	Catalyst	Zeolites (acidic), Pt, Ga, Mo	Ru-supported catalysts
3	Feedstocks/origin	Naphtha, ethylene, n-alkanes / petrochemistry	1-Octene, terminal alkenes Telomerisation, plastic or lignin valorisation / Fischer-Tropsch
4	Aromatics	<30% for long chains	>50%
5	Regeneration	Frequent, aggressive (air burns, re-chlorination)	Mild, oxidative or reductive
6	Byproducts	Coke, Light gases, polyalkylates	Minimal low coke formation

Furthermore, 1-octene is increasingly available from the industrial-scale telomerisation of butadiene, a process that can be coupled with renewable carbon sources.[22] Alternatively, the valorisation of used plastics[23,24] and lignin[20], or Fischer-Tropsch processes, can also circumvent the naphtha cracking process (see Figure 6-1). Therefore, the direct aromatisation of 1-octene with Ru-supported catalysts would combine the positive catalytic features of Ru for the

aromatisation of long-chain terminal alkenes with the availability of 1-octene from alternative routes, also avoiding the Friedel-Crafts alkylation of benzene. These advances with a low-temperature, single-step, Ru-catalysed process hold considerable promise for the modular, decentralised and sustainable production of aromatic hydrocarbons, offering both environmental and economic benefits in the medium to long term.

6.2. Objectives

The primary aim of this research is to develop an efficient, selective, and sustainable catalytic process for the direct synthesis of alkylated aromatic hydrocarbons, namely xylenes and ethylbenzene, from terminal long-chain alkenes like 1-octene. In accordance with the growing industrial demand for greener alternatives to traditional petrochemical methods, this study concentrates on a catalytic system that utilises ruthenium species supported on non-acidic, amorphous solids.

The specific objectives of the research are as follows:

- To evaluate the influence of the catalyst support (e.g., carbon, zeolites, SiO_2, Al_2O_3) on the activity, selectivity, and stability of the Ru catalytic species, aiming to identify optimal physicochemical characteristics for enhanced aromatic yield.
- To investigate the catalytic performance of ruthenium-supported materials for the isomerisation, cyclisation, and dehydrogenation of 1-octene under mild reaction conditions ($T \approx 300$ °C) and in the absence of strong acidic or basic promoters.
- To establish structure–activity relationships (SAR) for Ru-supported catalysts by correlating catalyst morphology, dispersion, and surface properties with aromatic product selectivity and conversion efficiency.
- To optimise the reaction parameters (temperature, gas-phase flow, contact time, and pressure) to maximise conversion and selectivity toward the desired C_8 aromatic compounds, while minimising undesired side reactions such as cracking, oligomerisation, or over-alkylation, under both batch and flow conditions.

- To elucidate the reaction mechanism by identifying key intermediates and transformation pathways involved in the sequential isomerisation–cyclisation–aromatisation process.
- To identify and characterise secondary alkene products and assess their formation pathways, with the aim of understanding side reactions and improving overall selectivity.

6.3. Results and Discussion

6.3.1. Batch Reactor Studies for Catalyst Screening and Mechanistic Insights

Before initiating the experimental investigation, it is essential to establish a controlled and reproducible environment that allows for accurate assessment of catalytic performance under static conditions. Batch reactors represent a closed system ideal for studying time-resolved reaction profiles, catalyst stability, and mechanistic pathways without the influence of continuous flow dynamics. This approach enables precise control over variables such as temperature, pressure, reactant concentrations, and reaction time, making it particularly suitable for screening catalyst formulations, evaluating conversion and selectivity trends, and collecting samples for offline analysis such as NMR, GC-MS, or elemental characterisation. The following section outlines the materials, procedures, and operating conditions employed in the batch experiments conducted in this study.

A series of metal-on-carbon (metal/C) catalysts was initially tested for the isomerisation and aromatisation of 1-octene (1). These catalysts, either commercially sourced or synthesised in-house (see Chapter 3, Section 3.3.4 for experimental details), were characterised using powder X-ray diffraction (PXRD), X-ray photoelectron spectroscopy (XPS), transmission electron microscopy (TEM), and aberration-corrected high-angle annular dark-field scanning transmission electron microscopy (AC-HAADF-STEM). Particular attention was given to the most active catalysts.

The Ru/C catalyst (referred to as oxRu-C to distinguish it from the in situ reduced form, redRu-C, discussed later) was extensively characterised to elucidate its structural and electronic features.[18] Aberration-corrected HAADF-STEM

imaging revealed the presence of ultrasmall Ru nanoparticles, with an average size of approximately 1.5 nm. X-ray photoelectron spectroscopy (XPS) indicated that Ru predominantly exists in the +2 oxidation state, while PXRD patterns were consistent with the formation of Ru oxide species. (Figure 6-2) These results confirm the dispersion of oxidised Ru clusters on the carbon support, offering a well-defined system for evaluating catalytic performance. For comparison, other metal/C catalysts such as Fe, Au, Pd, and Pt were also examined under identical conditions, but their structural details are not discussed here.

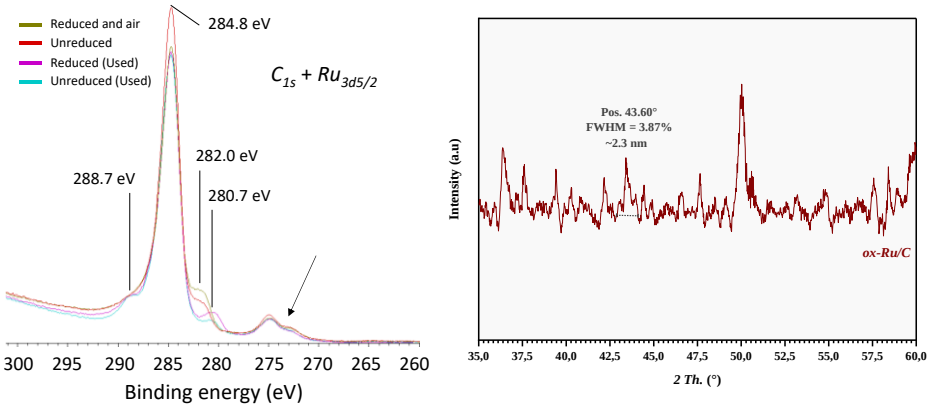

Figure 6-2 Left: X-ray photoelectron spectroscopy (XPS) spectrum showing the predominant Ru(II) oxidation state in oxRu-C. Right: Powder X-ray diffraction (PXRD) pattern confirming the presence of Ru oxide species supported on carbon.

Table 6-2 shows the catalytic results, and the key parameters analysed included conversion of **1**, selectivity for internal alkenes (including the primary *trans*- and *cis*-2-octene products **2**), the yield to cyclic alkenes **3** and the formation of aromatic compounds **4**. The reactions were performed in batch reactors, which enable precise control over variables such as temperature, pressure, reactant

concentration and reaction time, particularly suitable for screening catalyst formulations. Samples were collected for offline ^{1}H and ^{13}C nuclear magnetic resonance (^{1}H and ^{13}C NMR) and gas chromatography-mass spectrometry (GC-MS) analysis. The amount of solid catalyst was fixed (50 mg) to have a similar diffusion rate in all cases; the mol% amount for each metal is also indicated in Table 6-2.

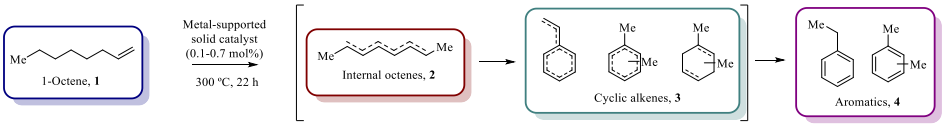

Table 6-2 Catalytic performance of different metal-supported catalysts for the isomerisation and aromatisation reaction of 1-octene **1** (conversion, selectivity and yields). The results are an average of ^{1}H NMR and GC results (after two reproductions).

No.	Catalyst	Conv. 1 (%)	Yield [%]				
			2 (isom.)*	Internal Olefin 2		3 (cycl.)*	4 (arom)*
				Trans-2-octene	*Cis*-2-octene		
1	**oxRu-C (5 wt%, 0.7 mol%)**	**88.12**	**86.22**	**56.93**	**29.30**	**0**	**1.90**
2	Fe-C (1 wt%, 0.1 mol%)	16.32	16.32	6.67	9.65	0	0
3	Au-C (1.7 wt%, 0.5 mol%)	22.18	22.18	12.81	9.36	0	0
4	Pd-C (5 wt%, 0.7 mol%)	61.54	60.77	23.24	37.52	0	0.07
5	**Pt-C (5 wt%, 0.3 mol%)**	95.37	89.65	58.49	31.61	1.77	3.98

No.	Catalyst	Conv. 1 (%)	Yield [%]				
			2 (isom.)*	Internal Olefin 2		3 (cycl.)*	4 (arom)*
				Trans-2-octene	*Cis*-2-octene		
6	Pd (0,7wt%)-Au(0,8wt%)-C	57,36	54,37	33,90	20,47	0	2,99
7	Pd (5wt%)-Au(2,5wt%)-C	92,92	85,86	50,09	35,77	0	7,06
8	Pd (2,5wt%)-Au(5wt%)-C	89,67	87,85	52,77	35,08	0	1,82
9	oxRu-C[b] (5wt%, 0.7 mol%,)	75,36	75,27	51,03	24,24	0	0,08
10	oxRu-C[c] (5wt%. 0.7 mol%)	69,43	65,27	37,47	27,80	0	4,16
11	Ru-SiO_2 (5 wt%, 0.7 mol%)	80.49	80.10	56.41	23.69	0	1.82
12	Ru-Al_2O_3 (5 wt%, 0.7 mol%)	53.81	53.81	32.07	21.75	0	0
13	**Ru-NaY (1 wt%, 0.2 mol%)**	**93.11**	**69.48**	**42.02**	**27.46**	**23.63**	**0**

**Abbreviation: isom.=Isomerisation; cycl.=Cyclisation; arom.=Aromatisation Reaction conditions (unless otherwise stated): 1-octene (0.55 mL, 3.5 mmol), catalyst (50 mg, metal wt% supported on the solid, as indicated), temperature = 290–300 °C, time = 1320 min (22 h), no additives or solvents. Reactions were carried out in a sealed batch*

reactor under an inert atmosphere. [b] *Starting reagent 1-hexene.* [c] *Starting reagent 1-heptene.*

oxRu-C demonstrated a very good conversion of 88.12% alongside a selectivity for trans-2-octene of 56.93% (entry 1). Indeed, the alkene isomerisation of 1-octene can occur even at a lower reaction temperature (150 °C), fully forming the internal olefin products. The solid oxRu-C catalyst can be reused up to four times with minimal loss of activity, as confirmed by both the final yield of internal alkenes and the initial rate determined from kinetic experiments.

This catalytic behaviour is not limited to 1-octene; the isomerisation also proceeds efficiently for smaller linear alkenes such as 1-hexene (entry 9) and 1-heptene (entry 10), yielding their respective internal olefin mixtures in high yields. Notably, when 1-heptene was used as the substrate, the Ru-C catalyst displayed a slightly lower conversion along with an increased tendency for aromatisation, reaching 4.16%, compared to the reaction with 1-octene.

These findings support the conclusion that Ru(II) species initially present in oxRu-C are the catalytically active phase for isomerisation. The observed high trans-selectivity is attributed to strong π-backdonation from Ru(II) to the alkene, stabilising π-complexes and favouring the thermodynamically preferred trans-isomer. To confirm the oxidation state and local environment of Ru in oxRu-C, X-ray absorption spectroscopy (XAS), including XANES and EXAFS, was conducted. The XANES spectra (Figure 6-3, left) revealed an absorption edge consistent with Ru oxide species, distinct from a Ru^0 metallic reference. This was corroborated by EXAFS, which showed a first coordination shell at 1–2 Å, corresponding to Ru–O/N/C bonds, confirming the presence of oxidised Ru species as the active catalytic sites.

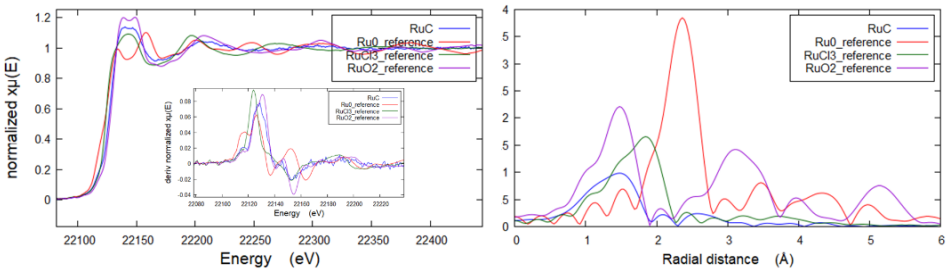

Figure 6-3 Normalised X-ray absorption near-edge structure (XANES, left) at the Ru K-edge and Fourier-transformed extended X-ray absorption fine structure (EXAFS, right) spectra for the fresh Ru-C catalyst, compared to RuO_2 and metallic Ru as references.

In comparison to Ru-C, the Fe-C, Au-C, and Pd-C catalysts exhibited lower conversion rates (entries 2-4). Notably, only Pd-C demonstrated moderate activity, achieving a conversion rate of 61.54%. Unlike Ru, Pd-C favoured the formation of cis-2-octene (37.52%), a trend that can be attributed to the typical π-allyl formation, Pd–H insertion followed by β-H elimination, and nucleometallation along with β-elimination of alkenes occurring on Pd sites.[25] This change in the isomerisation mechanism, hence of selectivity, is associated with the relatively weak π-backdonation of Pd(0) compared to Ru(II), which restricts its ability to stabilise π-complexes and allyl intermediates, leading to a lower *trans*-selectivity. Additionally, the lack of any aromatisation product **4** indicates that, under our reaction conditions, Pd does not effectively facilitate the cyclisation or dehydrogenation process.[26] The low conversion of Au-C (entry 3) can be ascribed to their limited efficacy to activate alkenes, indeed, Au is characterised by a fully filled closed-shell electronic configuration that results in a weak adsorption of alkenes, requiring sizes below 5 nm on reducible metal oxides such as titanium dioxide (TiO_2) to exhibit any appreciable catalytic activity (here the size of the Au nanoparticles is, in average, just above 5 nm).[27,28]

Gold alone exhibits minimal activity in isomerisation and hydrogenation, but when alloyed with palladium, its role becomes crucial in tuning catalytic performance. The Pd: Au ratio significantly affects both activity and selectivity in alkene upgrading. A catalyst with 5 wt% Pd and 2.5 wt% Au (entry 7) showed the best performance, with 92.92% conversion and a notable 7.06% aromatisation yield**,** indicating effective facilitation of both isomerisation and more profound transformations. In contrast, higher Au content (2.5 wt% Pd, 5 wt% Au) yielded high conversion. Still, it suppressed aromatisation **(**1.82%**),** highlighting gold's tendency to isolate active Pd sites, which are essential for multi-step reactions like C–C rearrangement and dehydrogenation. This inverse correlation between gold content and aromatisation is linked to electronic effects: Au alters Pd's d-band centre, weakening its ability to activate hydrogen and bind unsaturated intermediates.[27] Nonetheless, gold enhances catalyst stability and selectivity by mitigating over-adsorption. Thus, by fine-tuning the Pd:Au ratio, one can achieve a balanced synergy that maximises conversion while controlling product distribution, making Pd–Au/C alloys highly effective for selective linear alkene upgrading.

Fe-C (entry 2) shows significantly low catalytic activity, despite being used in a lower mol% amount, achieving only a 16.32% conversion without any observed aromatisation products. This limited activity can be attributed to the susceptibility of Fe to oxidation, exacerbated at higher temperatures and where the carbon support can contribute to a decline in catalytic efficiency.[29] Besides, in the absence of ligands, iron is prone to a fast agglomeration and deactivation.[30,31,32]

Pt-C does catalyse the isomerisation of 1-octene **1** (entry 5), delivering a conversion of 95.37% and an isomerisation yield of 89.65%. The product distribution shows a marked preference for *trans*-2-octene (58.49%) over *cis*-2-

octene (31.61%), as in the case of Ru-C, with some aromatisation products (3.98%). This high *trans/cis* ratio reflects thermodynamic control, where the more stable *trans* isomer is favoured. Mechanistically, it has been reported that Pt facilitates isomerisation through the formation of π-complexes with the alkene, which stabilises key intermediates and reduces the activation energy.[33] The Pt(111) surface is especially effective in promoting alkene adsorption and bond rearrangement, while the strong capacity of Pt to activate molecular hydrogen is essential for the hydride transfer mechanism.[34–37] These combined features, common to Ru(II)[17,38,39], account for the high activity, selectivity, and stability of Pt in hydrocarbon isomerisation processes.

Since both Ru-C and Pt-C exhibit noteworthy catalytic activity, presumably due to a similar reaction mechanism[40,41], the selection of the solid catalyst must now extend beyond catalytic efficiency to incorporate considerations such as cost, elemental abundance, environmental impact, and long-term supply sustainability. All these factors favour the selection of Ru-C over Pt-C. Pt is one of the rarest and most expensive precious metals, typically priced 3 to 10 times higher than Ru[42], moreover, Pt mining is geographically concentrated, primarily in South Africa and Russia, raising concerns over geopolitical supply risks and market volatility, while Ru can be produced as a by-product of nickel mining, resulting in a more diversified extraction profile that enhances supply stability. In terms of environmental sustainability, the combination of lower costs and greater availability makes Ru, arguably, a more suitable candidate for large-scale applications or catalyst formulations that require higher loadings or frequent regeneration. Furthermore, Ru-based catalysts demonstrate enhanced tunability, exhibiting a broader range of oxidation states and compatibility with various support materials, including carbon, alumina, and silica.[43–45] Indeed, Ru-SiO_2

achieves an 80.49% conversion and a *trans*-selectivity of 56.41% (entry 11), while Ru-Al_2O_3 gives a 53.81% conversion and a 32.07% *trans* product (entry 12). These results showcase that the support material significantly influences the catalytic performance. Carbon supports enhance electron donation while stabilising Ru nanoparticles,[46,47] but, in contrast, SiO_2 offers enhanced thermal stability and better dispersion of the catalyst, albeit with a somewhat reduction in catalytic activity for some processes attributable to a weakened metal-support interaction.[46] Nevertheless, this property helps to prevent unwanted acid-catalysed pathways, making it advantageous for a clean isomerisation reaction.[48,49] Alumina (Al_2O_3), in contrast, introduces Lewis acidity that can prompt parallel reactions such as hydride shifts, cyclisation, or even aromatisation reactions,[50,51] but a strong interaction between the metal and the support often results in the over-stabilisation of Ru, which diminishes its catalytic activity and increases the likelihood of side reactions.[52] Moreover, the electron-withdrawing characteristics of alumina inhibit the π-backdonation capability of Ru, and literature reports confirm that the acidity of alumina can bind reaction intermediates too tightly, altering product distribution and potentially deactivating metal sites.[50,51] These effects collectively explain the observed lower performance of Ru-Al_2O_3 compared to the other supports.

In view that both Ru-SiO_2 and Ru-Al_2O_3 were anyway catalytically active for the reaction but with notable differences, not only in conversion but also in selectivity, the micro-structured Ru-supported aluminosilicate zeolite NaY was prepared and tested as a catalyst. In this case, only 1 wt% of Ru was incorporated in order to avoid further agglomeration of the Ru catalyst.[53] The PXRD measurements (Figure 6A-1, Appendix 6A-1) confirm the absence of big (>3 nm) Ru nanoparticles, and since the zeolite support is white and transparent to visible

and infrared light, in contrast to the carbon support, diffuse reflectance ultraviolet visible (UV-Vis) and Fourier transformed infrared (FT-IR) measurements of the Ru supported zeolite could be carried out, indicating the formation of Ru(II)-oxide species. HR-TEM images of Ru-NaY confirm the presence of tiny Ru clusters (Figure 6-4), a Brunauer-Emmett-Teller surface area (BET) measurement shows that the surface area and micropore volume of Ru-NaY are practically the same as that of the pristine NaY zeolite (668 $m^2 \cdot g^{-1}$, 0.323 $cm^3 \cdot g^{-1}$),[54] and a Ru *3p* XPS analysis shows that Ru is completely in the form of Ru(II) or Ru(III) oxidation state (binding energy at 463.0 eV, Figure 6-5, left).

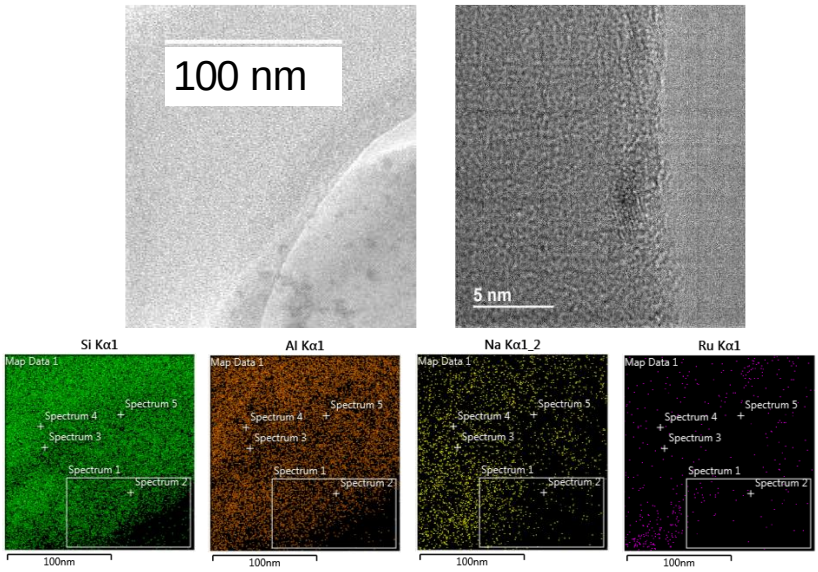

Figure 6-4 High-resolution transmission electron microscopy (HR-TEM) images of the Ru-NaY zeolite (top) with the corresponding energy-dispersive X-ray spectroscopic elemental mappings (Si, Al, Na or K, and Ru, bottom).

An in-situ diffuse reflectance infrared Fourier transform spectrum (DRIFTS) of the Ru–NaY zeolite with carbon monoxide as a probe shows three peaks associated to linearly bonded CO–Ru^{2-3+} species (Figure 6-5, right): two bands at 2075 and 2125 cm^{-1} corresponding to the symmetric and asymmetric stretches of two CO molecules in gem–dicarbonyl Ru compounds, respectively[55], and a third band at 2170 cm^{-1} which can be assigned to Ru^{3+} stabilized by MO_x oxides [MO_x–Ru^{3+}–CO].[56] The absence of any band at <2040 cm^{-1} confirms that any reduced Ru species, agglomerated or not, are present in significant amounts in the zeolite. These results strongly indicate that the Ru-NaY zeolite is composed of very small Ru(II-III) oxide species, as will be confirmed by XAS experiments (see ahead).

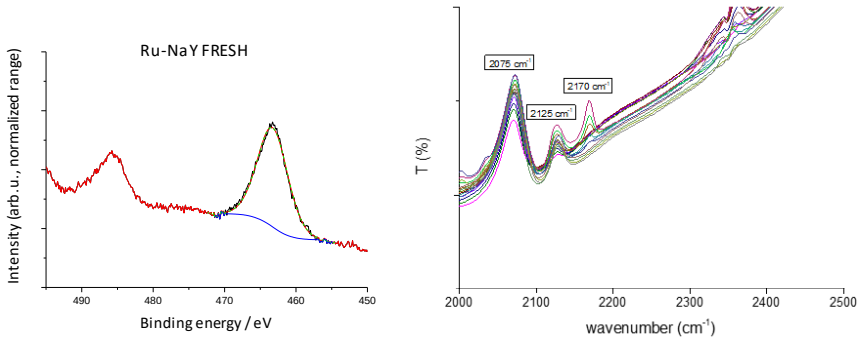

Figure 6-5 Electronic and surface coordination features of Ru species in Ru–NaY. (Left) XPS spectrum of Ru 3p confirming the presence of Ru(II/III) oxidation states. (Right) In situ DRIFTS spectrum using CO as a probe, indicating the formation of gem-dicarbonyl Ru species and MO_x–Ru^{3+}–CO complexes.

6.3.2. Different Ru-zeolites as catalysts: Ru-ZSM-5 as the optimum material

It has been reported that the structural conformation of zeolite Y facilitates the formation of stable, monodisperse Ru species under reaction conditions, thereby enhancing overall catalytic selectivity.[57–60] The spatial confinement provided by the zeolite's channels and cages has been shown to inhibit sintering and promote a more uniform distribution of Ru atoms, contributing to improved longevity and selectivity of the catalyst.[59,60] Furthermore, recent studies have highlighted the critical role of aligning metal dispersion with the acid/base functionality of zeolite-based bifunctional catalysts to enable cooperative reaction mechanisms.[61] Given these attributes, and recognising that zeolites can be synthesised from abundant and low-cost raw materials such as kaolinite or volcanic ash, offering scalability and high purity comparable to carbon supports,[62,63] but with superior thermal stability[57,64] various Ru-loaded, ion-exchanged forms of zeolite Y were prepared in the present study. For comparative purposes, analogous Ru-supported systems based on zeolite MFI (ZSM-5) were also synthesised. The inclusion of ZSM-5 was justified by its known capacity to stabilise aromatic species, attributed to the closer match between the size of its 5.5 Å channels and the kinetic radii of aromatics, relative to the larger 7.7 Å pores of zeolite Y (Table 6A-2, Appendix 6A-2 and Figure 6-6).

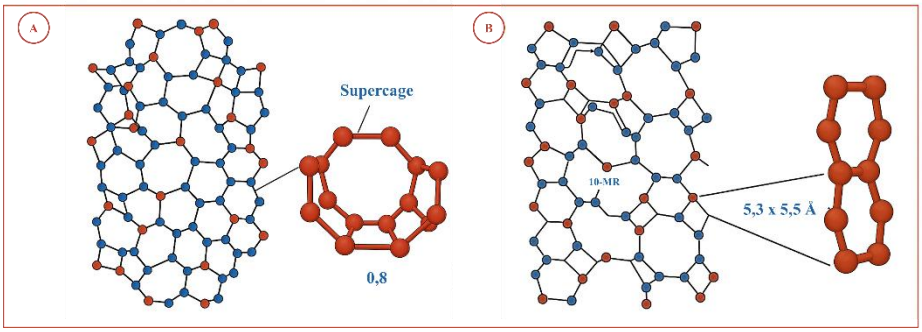

Figure 6-6 Comparison of Structural Properties of HY (a) and HZSM-5 (b) Zeolites

The parent zeolite-NaY was cationically exchanged by a known procedure to achieve LiY, KY and CsY with the framework Y structure untouched.[65] Besides, the commercially available protic ultra-stabilised Y zeolite (H-USY) was also tested as a support for Ru.[66,67] The alkaline and Ru content for each zeolite was determined by inductively coupled plasma-optical emission spectrometry (ICP-OES), and the catalytic results are shown in Table 6-3.

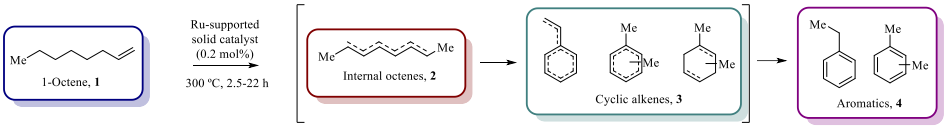

Table 6-3 Influence of metal identity and zeolite structure on the isomerisation and aromatisation reaction of 1-octene **1**.

No.	Catalyst	Time (h)	Conv. 1 [%]	Yield [%]		
				2 (isom.)*	3 (cycl.)*	4 (arom.)*
1	Ru-HUSY	2.5	65.93	52.30	11.93	1.70
2	RuLiY	2.5	58.68	48.76	9.92	0
3	RuNaY	2.5	69.45	53.59	18.86	0
4	**Ru-KY**	**2.5**	**81.27**	**68.16**	**13.11**	**0**
5	Ru-CsY	2.5	15.25	15.25	0	0
6	Ru-HZSM-5	2.5	36.51	20.00	16.51	0
7	Ru-HUSY	8.5	77.77	54.25	21.12	2.40
8	Ru-HZSM-5	8.5	57.62	27.97	27.54	2.12
9	**Ru-HUSY**	**22**	**90.71**	**58.32**	**27.58**	**4.81**
10	**Ru-HUSYimp**	**22**	**88.36**	**57.69**	**20.91**	**7.15**
11	**Ru-HZSM-5**	**22**	**97.67**	**27.59**	**68.20**	**1.88**
12	Ru-HZSM-5 imp	22	86.76	65.71	21.05	0

**Abbreviation: isom.=Isomerisation; cycl.=Cyclisation; arom.=Aromatisation Reaction conditions (unless otherwise stated): 1-octene (0.55 mL, 3.5 mmol), catalyst (50 mg, metal wt% as indicated by ICP (Appendix 6A-1)), temperature = 290–300 °C, time*

= 150 min, no additives or solvents. Reactions were carried out in a sealed batch reactor under an inert atmosphere.

It can be observed that the catalytic activity for the isomerisation reaction under the optimised reaction conditions after 2.5 h reaction time follows the order Ru-KY > Ru-NaY ≈ Ru-HUSY > RuLiY > Ru-CsY (entries 1-5 in Table 6-3), and the selectivity to *trans*- or *cis*-2-octene was proportional to the isomerisation yield (Table 6-3). However, in contrast, the order for the cyclisation/aromatisation reaction is Ru-NaY > Ru-KY ≈ Ru-HUSY > Ru-LiY > Ru-CsY. In other words, Ru-KY exhibited the highest conversion of **1** (81.27%) and isomerisation yield to **2** (69.48%), but Ru-NaY and Ru-HUSY showed the highest yields to cyclised and aromatic products **3** and **4**, despite having a lower conversion of **1**. The fact that the catalytic activity and selectivity peaks at intermediate cation sizes, thus an intermediate basicity in the zeolite, can be attributed to two primary factors: (i) a balance between the electronics of the zeolite and the size of the extra-framework cation, generating some steric hindrance (enhanced for Cs), and (ii) the Ru species formed in the exchanged Y zeolites are different. For the former, Li^+ and Na^+ have the smallest ionic radii (76 and 108 pm, respectively) among the alkali metals used, and a relatively high charge density, which helps in stabilising the Ru species within the zeolite matrix without significantly blocking the pore entrances.[57,68] Moreover, Li^+ and Na^+ maintain the openness of the supercages of the faujasite structure, allowing for efficient substrate diffusion and interaction with the Ru active sites. Literature reports have consistently shown that smaller alkali metal cations are less prone to inducing pore blockage and thus better preserve the catalytic accessibility of zeolite frameworks,[69,70] which explains why the best selectivity to products **3** and **4** occurs in the Ru-NaY, Ru-HUSY and Ru-LiY zeolites. In contrast, Ru-KY shows the highest conversion,

but the cyclisation decreases significantly (13.11%), suggesting that larger K^+ cations begin to partially hinder reactant accessibility. As the ionic radius of the alkali metal cation further increases (i.e. K^+: 138 pm, Cs^+: 167 pm), the catalytic performance of the corresponding Ru-zeolite Y system declines,[71,72] to give just a mere 15.25% with Ru-CsY. The large Cs^+ ions likely occupy critical positions at pore mouths or within supercage windows, a phenomenon referred to as "pore mouth poisoning".[73] Spatial hindrance restricts the diffusion of 1-octene **1** molecules and the movement of intermediates, leading to significantly limited catalytic turnover. This type of inhibitory mechanism has been extensively documented in similar systems, such as alkane cracking and olefin metathesis.[74] A comparative study was also carried out on other Ru-exchanged zeolites, such as Ru-KY, to assess their similarity to Ru-NaY. These materials were found to contain similarly small (<2 nm) Ru(II,III) oxide clusters, consistent with those observed in Ru-NaY. However, since these catalysts are not central to the scope of this thesis, the full characterisation data are not included.

In contrast to alkali-exchanged zeolites, which lack Brønsted acid functionality, the protonic forms of zeolites, H-USY and HZSM-5, reintroduce Si–OH–Al bridging groups that are capable of stabilising carbocation intermediates and promoting skeletal rearrangement, cyclisation, and aromatisation pathways.[75,76] These Brønsted acid sites might be crucial for initiating β-scission, hydride shift, and ring closure events, which occur in synergy with the hydrogenation–dehydrogenation steps catalysed by Ru. Indeed, the conversion, cyclisation and aromatisation with the Ru-HUSY catalyst can reach 90.71%, 27.58% and 4.81%, respectively, after 22 h of reaction (entry 9 in Table 6-3). Ru–HZSM-5, in contrast, demonstrates a lower initial conversion (36.51% at 2.5 h, entry 6 in Table 6-3), likely due to mass transport constraints imposed by its narrow pore

openings (~0.55 nm), but, however, its higher acid strength and increased density of Brønsted acid sites results in a markedly higher selectivity for cyclised products (27.54% at just 2.5 h) and comparable aromatisation yields (2.12%). A cooperation between metal and acid sites underpins the potential bifunctional catalytic behaviour observed in both Ru–HUSY and Ru–HZSM-5,[77–79] where more cyclised and aromatic products **3** and **4** are found, particularly at longer reaction time (entries compare entries 6-12 in Table 6-3). These results are consistent with literature findings on MFI zeolites, which highlight their shape-selective catalytic potential for aromatisation,[77,80,81] since the MFI topology, with its intersecting sinusoidal and straight channels, imposes strong spatial constraints that stabilise compact carbocation intermediates and drive the reaction toward selective cyclisation and monoaromatic formation. In other words, the large-pore FAU topology of HUSY enables a wider distribution of products and strikes a balance between metal-catalysed and acid-catalysed reactions, while, in contrast, the medium-pore MFI framework of HZSM-5 promotes shape-selective transformations that favour the formation of monoaromatic compounds. Thus, it can be concluded that the interplay between Ru, silanols, and the zeolite framework is crucial for the transformation of linear alkenes into more valuable cyclic and aromatic products.

To further explore the influence of zeolite structure and acidity, both protonated forms of HUSY and HZSM-5 were used as supports for Ru, not only after ion exchange but also by impregnation (imp). Impregnation is the more common method in industry to prepare metal-supported catalysts since no metal is lost during the catalyst preparation. The catalytic results for the impregnated Ru-zeolites were similar to those exchanged (entries 10 and 12 in Table 6-3), which assures a more efficient employment of the metal when supported. XPS analyses

of the exchanged and impregnated Ru-HZSM-5 samples show that Ru predominantly exists in Ru(II) and Ru(III) in both, and that only calcination at 500 ºC achieves significant amounts of Ru(0) in the zeolite (binding energy= 461.5 eV, Figure 6-7).[82–85]

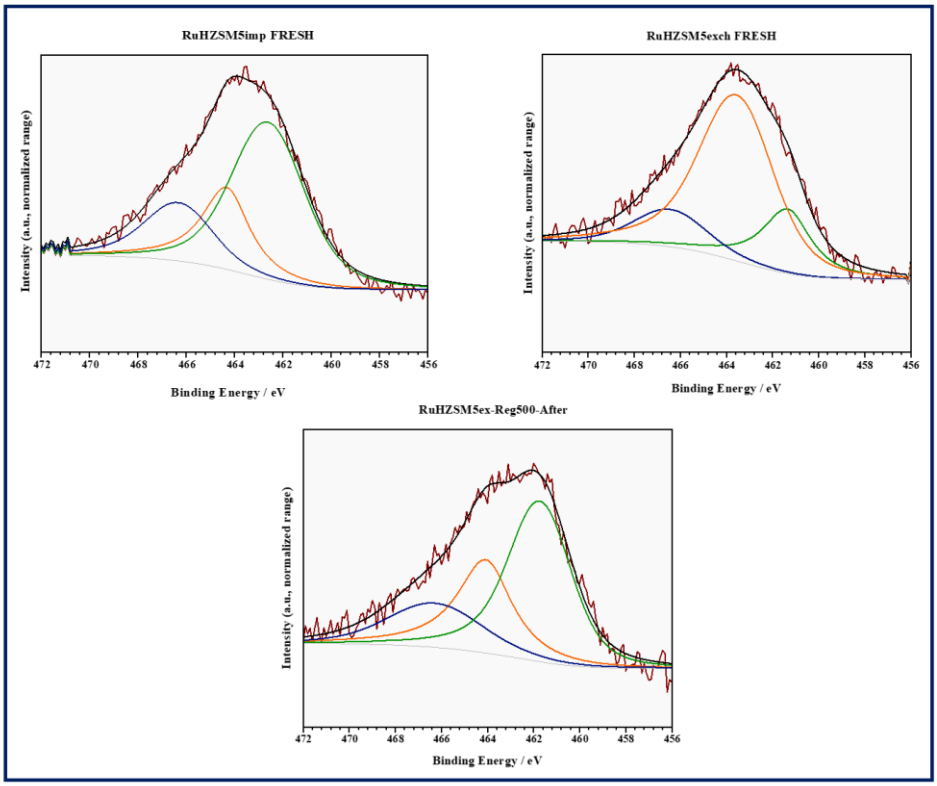

Figure 6-7 X–ray photoelectron spectroscopy (XPS) spectra of the Ru $3p_{3/2}$ region for the impregnated (top left), exchanged (top right), and calcined Ru-HZSM-5 catalyst (bottom).

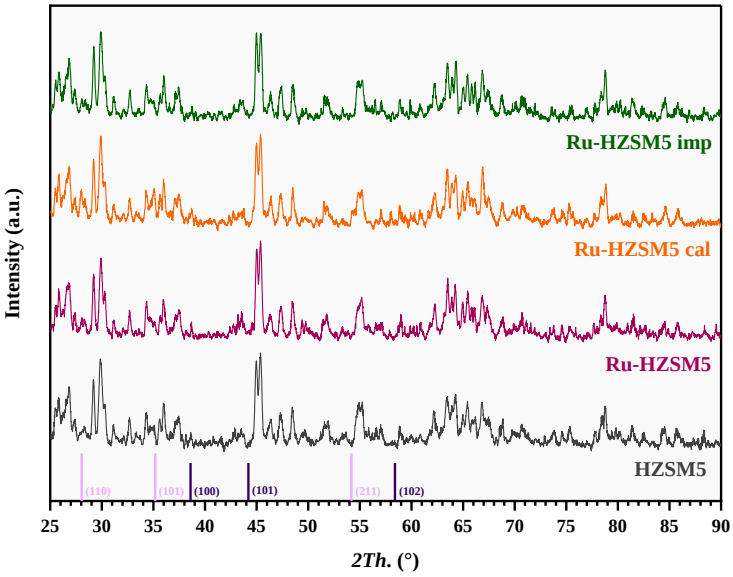

Figure 6-8 Comparison of the PXRD patterns for the parent zeolite (grey), the ion-exchanged sample without subsequent calcination (pink), the ion-exchanged and then calcined sample (orange), and the impregnated sample (green). The samples were compared with reference diffraction patterns from the PDF database, specifically MFI-type zeolite (PDF# 44-0003), metallic Ru (PDF# 06-0663), and tetragonal RuO_2 (PDF# 65-2824).

Complementary, PXRD analysis was employed to probe the structural integrity of the zeolite and the phase composition of Ru species (Figure 6-8), and all samples retained the typical MFI-type diffraction peaks (2θ ≈ 7–10°, 22–35°, 45°), confirming the preservation of the zeolite framework regardless of the treatment for the Ru incorporation,[86] and only the calcination at 500 ºC of the

sample begins to reveal faint peaks of RuO_2 in the PXRD pattern.[87,88] HAADF-STEM and energy-dispersive X-ray spectroscopy (EDX) measurements further confirmed the similarity between both samples, revealing a homogeneous Ru distribution across the zeolite particles without any bright, high-intensity feature characteristic of large Ru crystals (Figures 6-9; Figures 6A-3-4; Appendix 6A-3-4). These results confirm the absence of substantial Ru aggregates, aligning with the PXRD results, strongly suggesting that the Ru species are highly dispersed within the zeolite channels as ultrasmall Ru oxide clusters.

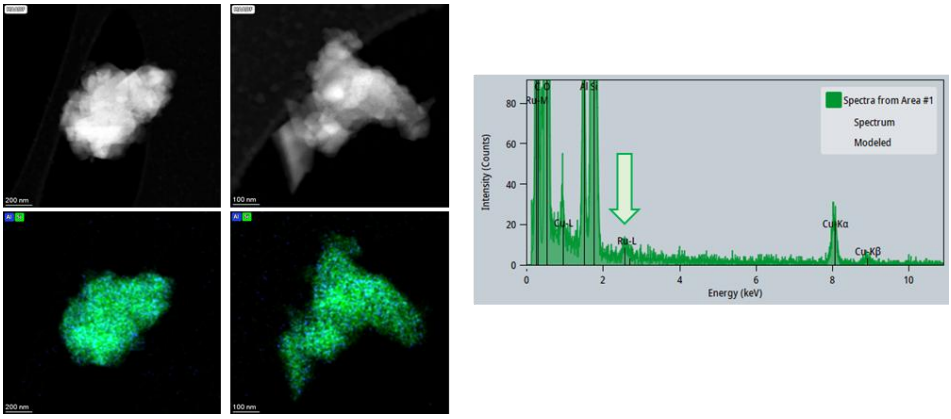

Figure 6-9 Two representative high angle annular dark field scanning transmission electron microscopy (HAADF-STEM) images, at low-magnification, of the Ru-HZSM-5 catalyst, showing the overall morphology and contrast features across the support, together with energy-dispersive X-ray (EDX) elemental maps and the corresponding spectrum, showing the spatial distribution of elements and confirming the presence of Ru.

To further assess the presence of the Ru oxide clusters in the zeolite, AC-HR-TEM and high-resolution HAADF-STEM (AC-HR-HAADF-STEM) measurements of the Ru-HZSM-5 zeolite combined with an integrated differential phase contrast (iDPC) analysis were performed. The results in Figure 6-10 (see Figures 6A-5-6; Appendix 6A-5-6 for more images) show that the Ru species are homogeneously distributed across the zeolite´s channels, with an estimated average size of 1 nm.

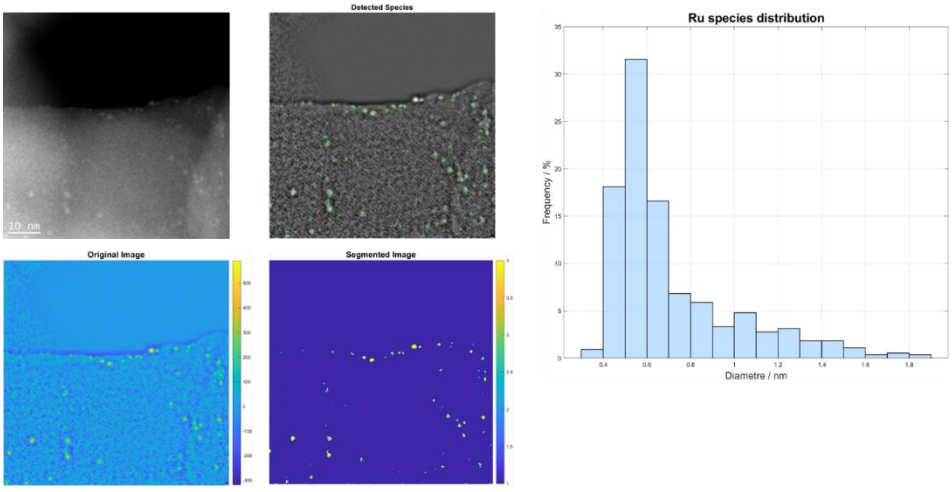

Figure 6-10 A representative aberration-corrected high-resolution HAADF-STEM (AC-HR-HAADF-STEM) image of the Ru-HZSM-5 zeolite, with the corresponding integrated differential phase contrast (iDPC) analysis (left), and the corresponding histogram (taking into account more images). The observed Ru particles show sizes between 0.5 and 1.5 nm, approximately.

The Ru-HZSM-5 catalyst retained its catalytic activity upon reuse following regeneration by calcination.[89] This treatment restores access to the microporous network while maintaining the structural integrity of the HZSM-5 framework.[72,90] For Ru-HZSM-5, effective calcination typically involves a temperature ramp of 1–5 °C per minute up to 450–500 °C, with airflow rates of 30–50 mL min^{-1} g^{-1}, using either air or a 10–20% O_2/N_2 mixture.[91,92] Although similar treatment may be beneficial for oxRu-C,[68,91–95] it was not required in this case, as heavier aromatic compounds were not formed.[96]

All these results, together, indicate that small (≈1 nm) Ru oxide clusters in zeolites are active catalysts for the tandem dehydrogenation/cyclisation/aromatisation reaction of linear chain terminal alkenes, although still in low yields for the aromatic products at <1 mol% Ru catalytic loadings.

6.3.3. Transition from batch to flow reaction conditions for a higher aromatisation reaction

6.3.3.1. The oxRu-C catalyst

After conducting comprehensive initial investigations under batch conditions, which provided key insights into the reactivity of 1-octene **1** and other alkenes, the study advanced to continuous-flow operations. This transition aimed at replicating more realistic process conditions, assessing catalyst performance under steady-state operation, and ultimately enhancing catalytic productivity and robustness for the synthesis of aromatics **4**. In the first set of flow experiments, the oxRu/C catalyst was utilised due to its established functionality in

hydrogenation and dehydrogenation, as well as its widespread application in industrial processes.[97]

First, an optimisation study was carried out to identify the most effective combination of reaction parameters for the aromatisation reaction. This study systematically examined the influence of catalyst mass (100–250 mg), total flow rate (1–15 mL min^{-1}), reactor temperature (250–350 °C), and bubbler temperature (60–90 °C) on the conversion of **1** and product selectivity. The multi-variable plots (Figure 6-11) reveal the synergistic effects of flow and thermal parameters on catalytic performance, and, notably, the flow rate significantly affected the aromatisation process.

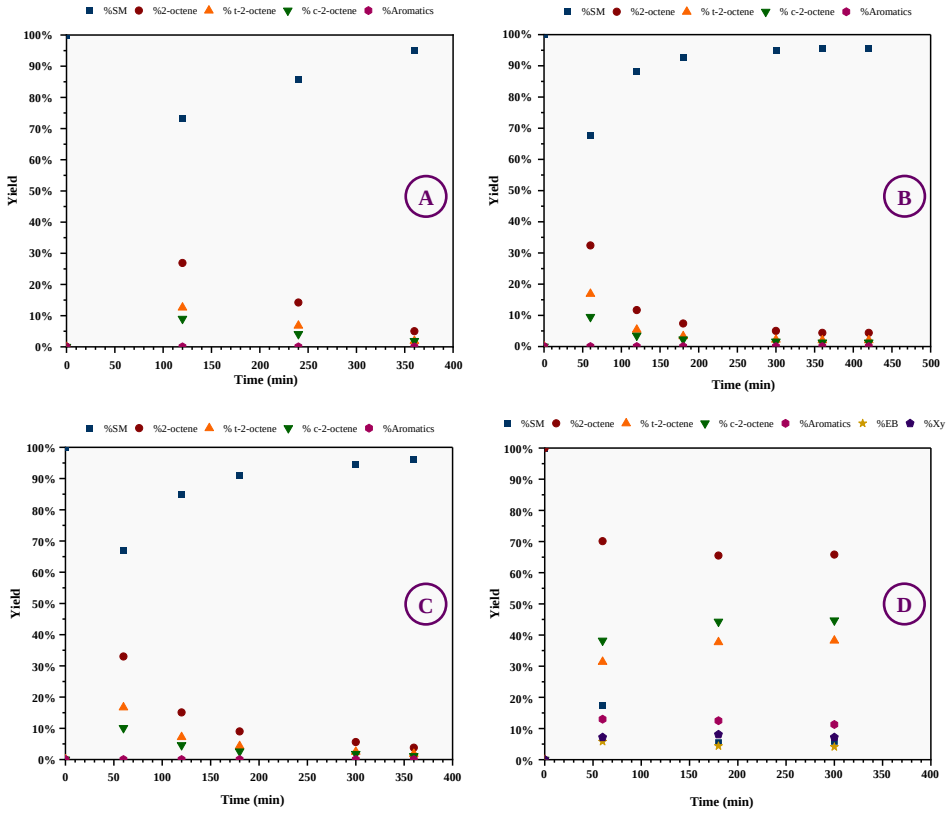

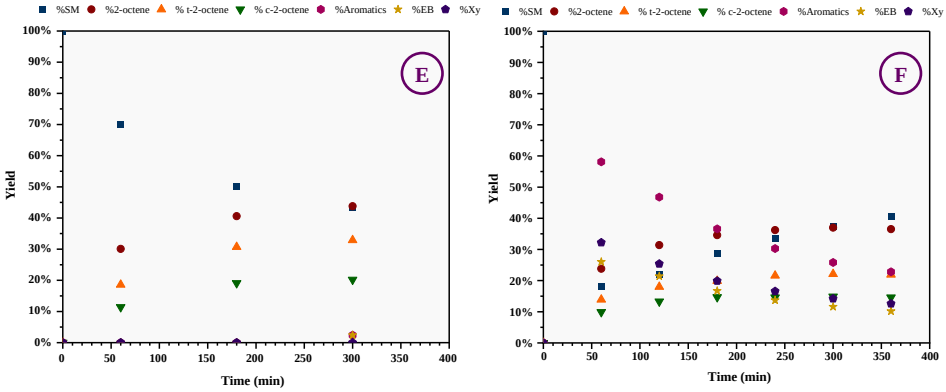

Figure 6-11 Catalytic performance of Ru-supported catalysts for 1-octene conversion under varying conditions. (A–F) Product distribution (isomerisation, cyclisation, aromatisation) and conversion under different operational parameters. Reaction Conditions: 1-Octene (5 vol% in N_2), atmospheric pressure; (A) 250 °C, Sat. Temp. 65 °C, 5 mL min^{-1}, 100 mg; (B) 250 °C, Sat. Temp. 65 °C, 15 mL min^{-1}, 100 mg; (C) 250 °C, Sat. Temp. 95 °C, 15 mL min^{-1}, 100 mg; (D) 300 °C, Sat. Temp. 65 °C, 5 mL min^{-1}, 250 mg; (E) 320 °C, Sat. Temp. 65 °C, 5 mL min^{-1}, 250 mg; (F) 300 °C, Sat. Temp. 65 °C, 5 mL min^{-1}, 100 mg

A flow rate of 5 mL min^{-1} produced higher overall conversion and significantly improved aromatic selectivity compared to the higher flow rate of 15 mL min^{-1} (compare Figures 6-11 A and B), and the enhanced performance at lower flow can be attributed to the longer residence time, which promotes the sequential isomerisation, dehydrogenation, and cyclisation steps required for aromatic formation. The temperature of the bubbler, which influences feed vaporisation and the partial pressure of the reactant, can also be a critical factor for optimal performance. Indeed, a bubbler temperature of 65 °C yielded the best vapour-

phase delivery of 1-octene **1**, resulting in a steady-state concentration in the gas phase without condensation or flooding, since lower bubbler temperatures (50 °C) impeded feed transport, leading to reduced space-time yield and unstable operation, and higher temperatures (90 °C) did not offer any additional benefits, since it increased the risk of condensation at the reactor inlets[98] and the formation of undesired poly-condensated aromatic by-products (Figure 6-12).[99,100]

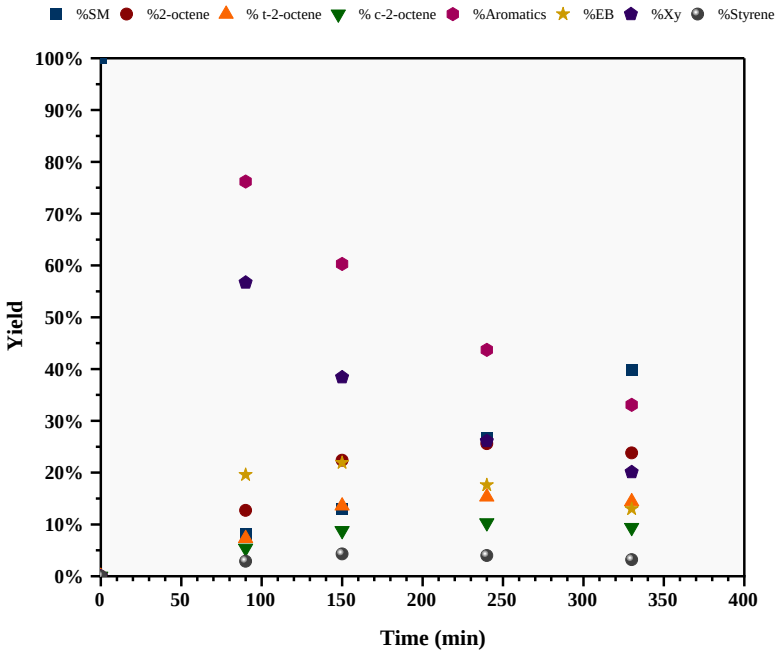

Figure 6-12 The distribution of undesired heavy aromatics

Furthermore, variations in catalyst mass (from 100 mg to 250 mg) and reaction temperature (300 to 320 ºC) indicated that 100 mg and 300 ºC are the optimal parameters for achieving a balance between surface activity and residence time

(compare Figures 6-11 A, E, F), since increasing the catalyst mass to 250 mg or increasing the reactor temperature to 320 ºC did not enhance aromatics formation; rather, it promoted over-hydrogenation and minor coking, likely due to prolonged exposure of intermediates to active Ru sites. In these instances, the metallic Ru sites are vulnerable to the irreversible adsorption of these large aromatic species. Over time, this accumulation results in a considerable decline in conversion, selectivity, and overall catalyst stability.[68,101] Finally, the optimised reaction conditions were set, and the catalytic results in flow with oxRu-C are shown in Figure 6-13.

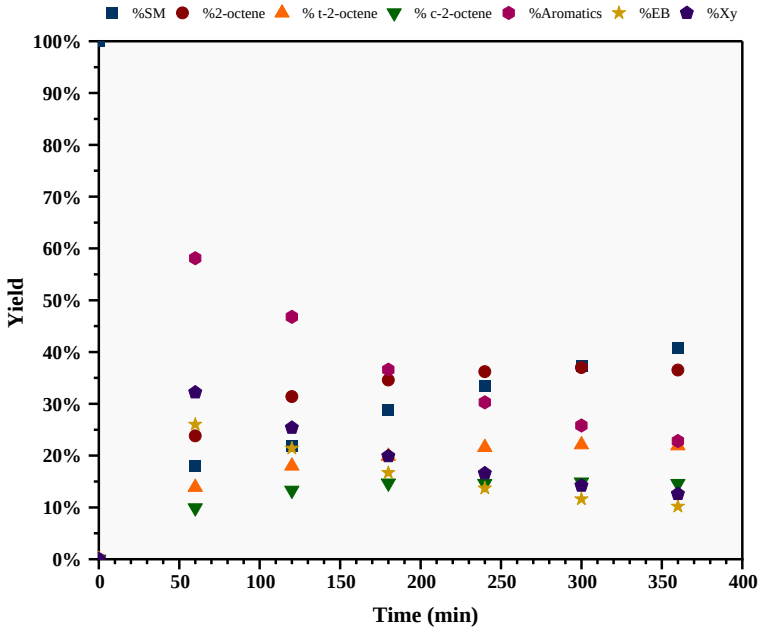

Figure 6-13 Catalytic results in flow for the conversion of 1-octene **1** with the oxRu-C under the indicated optimised reaction conditions.

The optimal conditions for maximising aromatics yield using oxRu-C in a continuous flow system were identified as follows: a flow rate of 5 mL min^{-1}, a bubbler temperature of 65 °C, a reactor temperature of 300 °C, and a catalyst mass of 100 mg. Under these parameters, the system demonstrated the highest yield for the desirable mono-aromatic products (68%), such as ethylbenzene (26%) and *o*-xylene (34%), after 50 min reaction time, while effectively minimising side reactions like over-cracking and oligomerisation reactions. The conversion at this point was 82%, thus the selectivity to the desired aromatics was higher >70%. However, a rapid deactivation was found with time. Given this, the catalytic behaviour of oxRu-C was examined at lower reaction temperatures (Figure 6A-7; Appendix 6A-7). At 160 °C, the reaction exclusively proceeded via double bond migration, resulting in a mixture of *trans*- and *cis*-2-octene. The initial *trans/cis* ratio was notably high (~4.5), indicating a thermodynamic preference for the formation of the more stable *trans*-isomer. Over a duration of 3 h, this *trans/cis* ratio gradually decreased to approximately 3.0, suggesting a slow progression towards thermodynamic equilibrium. The conversion rate was moderate, at around 38%, without any aromatic products **4** not observed. These findings are consistent with previous studies that indicate that the Ru(II) complexes on carbon supports promote double bond isomerisation at low temperatures through π-allyl-type intermediates or surface hydride mechanisms, without causing C–C bond reorganisation.[102,103] The isomerisation of 1-decene, 1-hexene, and 1-butene proceeded efficiently under the specified reaction conditions, even at 120 °C (refer to Figures 6A-8-10; Appendix 6A-8-10). At 200 °C, isomerisation remained the primary reaction pathway, not only for 1-octene but also for all other alkenes examined (refer to Figures 6A-8-11; Appendix 6A-8-11). The *trans* to *cis*-2-octene ratio decreased from approximately 2.9 to around 1.9 over time, while the conversion rate increased to about 68% after 5 h. Any

significant amount of aromatic compounds **4** was not detected yet, suggesting that the barriers to cyclisation or dehydrogenation were not fully surmounted at this temperature. Interestingly, after one hour, a small yet consistent signal appeared at 7.36 ppm in the ^{1}H NMR spectrum and at 128 ppm in the ^{13}C NMR spectrum, indicating the presence of a traces amount of benzene. Although GC-MS did not identify additional aromatic products, the NMR signal for benzene implies that the initial stages of aromatisation, possibly involving the dehydrogenation of octene to octadiene, followed by cyclisation, may have already commenced, albeit with very low conversion rates. This observation aligns with existing literature regarding the thermal cracking and dehydrocyclisation of alkenes over other Ru-C catalysts at low hydrogen pressures.[40] Consequently, 200 °C signifies a mechanistic transition zone where isomerisation predominates, while precursors to aromatics start to form. These observations are consistent with the previous findings[40] which reported that temperatures exceeding 250 °C are generally required to promote carbocation-mediated cyclisation and complete aromatic transformation of C_8 olefins on metal–acid bifunctional catalysts.[104] At 300 °C, as shown in Figure 6-13, a notable shift in the reaction mechanism was observed and, while isomerisation persisted, with a *trans/cis* ratio of approximately 1.4–1.5, a significant quantity of monoaromatic compounds **4** was also formed, as major products. NMR and GC-MS data reveal that the aromatisation process initiates with dehydrogenation to generate octadiene intermediates, which subsequently undergo cyclisation followed by further dehydrogenation to form the aromatic ring (see mechanistic section). The marked selectivity for ethylbenzene and *o*-xylene is likely indicative of the stereoelectronic effects related to the arrangement of double bonds in the intermediate diene and the conformation of the transition state during ring closure. The minimal formation of *m*- and *p*-xylene suggests either steric

hindrance during the cyclisation step or a kinetic preference for proximal substitution patterns. These findings align with earlier mechanistic studies on cyclisation–aromatisation over metal-acid catalysts, which demonstrated that constrained transition states favour the production of *ortho*-substituted products.[105]

6.3.3.2. The redRu-C catalyst

The aromatisation reaction generates H_2; thus, the Ru catalyst operates under a H_2-rich atmosphere, which could reduce the supported cationic Ru into metallic Ru or further aggregated ensembles. To verify this, a second type of Ru-C, referred to as redRu-C, was prepared by hydrogenating oxRu-C at 300 ºC under a stream of H_2/N_2. The PXRD analysis of redRu-C, after exposure to air (Figure 6A-12; Appendix 6A-12), shows the absence of Ru particles larger than 3 nm, as determined by the Scherrer equation, with the same pattern and Ru average size as oxRu-C. HAADF-STEM characterisation (Figures 6A-13-14; Appendix 6A-13-14S) highlights the porous structure of the support before and after the hydrogenation treatment, shows a good correlation of histograms at increasing magnifications from 1.1Mx to >4.0Mx, an effective particle dispersion in both materials, and confirms the similar Ru cluster size in both samples (sizes and dispersion, approximately 1.0 to 1.5 ±0.5 nm, respectively).

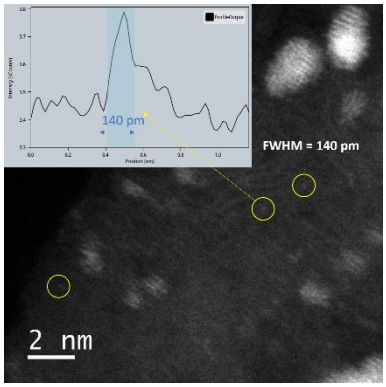

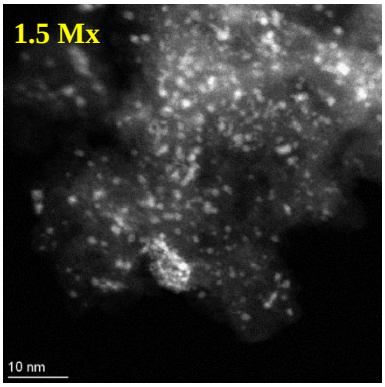

Total paricles: 167

Dispersion: 42.8 %

Average diameter: 1.17± 0.1 nm

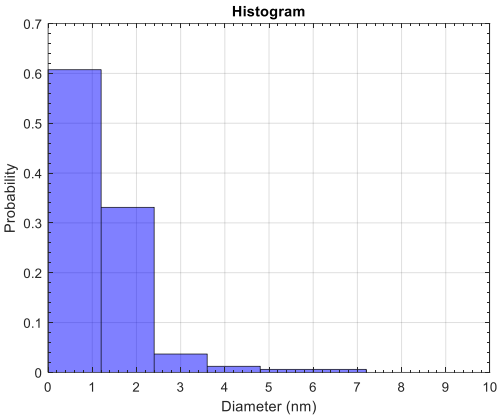

Figure 6-14 Aberration-corrected high angle annular dark field scanning transmission electron microscopy (AC-HAADF-STEM) image of redRu-C showing the presence of sub-nanometric and nanometric RuO_x clusters (circled). Intensity profiles were used to quantify the size of these subnanometric units and HAADF-STEM image (bottom) and the corresponding size analysis and histograms (right) of redRu-C, for increasing magnifications: 1.5.

However, the digital diffraction pattern (DDP) of redRu-C is typical of reduced Ru(0) nanoclusters (even after exposure to air) while the DDP of oxRu-C is indicative of RuOx nanoclusters. Energy dispersive spectroscopy (EDS) of the redRu-C sample further confirms the absence of RuOx nanoclusters after reduction, as the oxygen atoms detected by EDS are primarily associated with the carbon support. The XPS measurements for both samples (Figure 6A-15 A-B; Appendix 6A-15) show Ru (II-III) as the predominant surface species, with binding energies of 282.0 eV and 463.5 eV observed in the $Ru3d_{5/2}$ and $Ru3p_{3/2}$ XPS regions, respectively. These findings align with the known tendency for aerobic oxidation of small Ru clusters on the surface, even after reduction. The $O1_s$ XPS results (Figure 6A-15 C; Appendix 6A-15) further support evidence of oxidation of the supported Ru clusters on the surface of both catalysts. To explore this phenomenon in detail, the XPS measurement of the redRu-C sample was repeated while preventing any exposure to air, and the resulting data showed the expected lower binding energies for Ru(0), specifically 280.7 eV and 462.3 eV in the Ru $3d_{5/2}$ and Ru $3p_{3/2}$ XPS regions. The corresponding O1s XPS results also indicate the presence of Ru(0) as the main oxidation state in the redRu-C sample, as the binding energy for the oxygen atom decreased from 532.4 eV to 531.8 eV. These findings strongly suggest that the oxRu-C sample primarily contains Ru(II-III) oxide clusters, while the redRu-C sample features a core of Ru(0) surrounded by a layer of Ru(II-III) oxide upon exposure to air of the clusters. Therefore, it can be concluded that the only distinction between oxRu-C and redRu-C lies in the oxidation state of Ru, specifically (II) and (0), respectively (Figure 6-15).

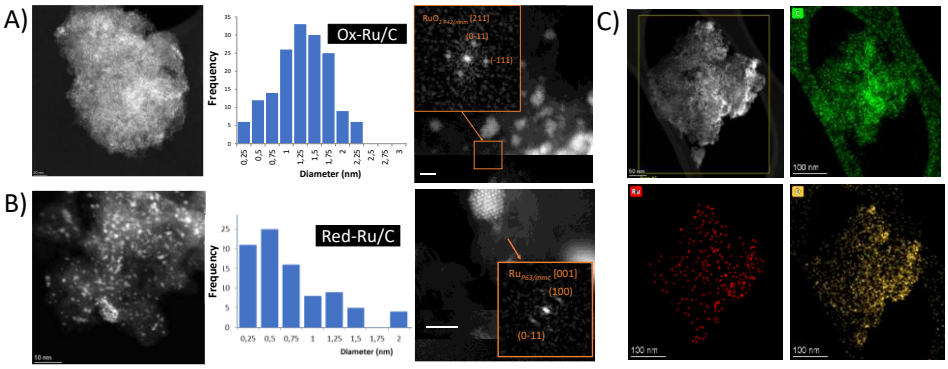

Figure 6-15 A) A representative HAADF–STEM image, histogram and digital diffraction pattern for oxRu-C. (B) Same analyses for redRu-C. C) EDS mapping of redRu-C, where the location of C, Ru and O atoms on the solid can be seen.

The catalytic results with redRu-C in the gas phase (Figure 6A-16, Appendix 6A-16) are very similar to oxRed-C (compare with Figure 6A-7), and the analysis of both samples by AC–HAADF–STEM after reaction does not show clear differences (Figures 6A-17-1; Appendix 6A-17-19). Both catalysts are composed, after reaction, of small Ru clusters and even isolated Ru atoms. However, a clearly different initial kinetic profile can be found not only in the gas phase (see initial points in Figures 6A-7 and 6A-16) but particularly in the liquid phase, where an induction time is observed for the redRu-C catalyst at all reaction temperatures. However, when the redRu-C catalyst is reused, the induction time disappears and the kinetic profile is now as that of oxRu-C. No leaching is not observed for the redRu-C catalyst, as with oxRu-C. The XPS signals for $Ru3d_{5/2}$, $Ru3p_{3/2}$ and $O1_s$ from the spent redRu-C and oxRu-C catalysts demonstrate similar values to the parent oxRu-C catalyst (or the exposed to air redRu-C catalyst). Notably, a new C1s signal appears at 288.7 eV, indicative of

adsorbed alkene compounds. These results strongly suggest that the Ru species supported on the oxRu-C catalyst, i.e. the Ru oxide clusters, are the true catalytically active species for the reaction, and that the redRu-C catalyst evolves to oxRu-C during reaction. Indeed, XANES and EXAFS experiments of the spent oxRu-C catalysts at different reaction temperatures (Figures 6A-20; Appendix 6A-20) show that Ru(0) is barely formed during reaction.

6.3.3.3. The Ru-zeolite catalysts

The good results with Ru-HUSY and Ru-HZMS5 found above in batch prompted catalytic exploration within the gas-phase continuous-flow system, which better reflects industrial conditions and offers advantages in scalability and product control. The Ru-HUSY catalyst was evaluated first, in a fixed-bed gas-phase reactor under the optimal conditions previously established for oxRu-C (300 °C in the reactor, 65 °C in the bubbler, and a flow rate of 5 mL min^{-1}). Due to material constraints and the limitations of the flow reactor, 50 mg of Ru-HUSY were physically blended with 50 mg of inert SiO_2, which allowed for the maintenance of a comparable catalyst bed mass while introducing acidity into the system. Under these experimental conditions, the conversion of 1-octene **1** remained high, with the majority of products comprising 2-octene isomers, predominantly in the *cis* configuration, signifying strong isomerisation activity. However, in contrast to oxRu-C, any aromatic products were not detected at any point under these reaction conditions (Figure 6-16).

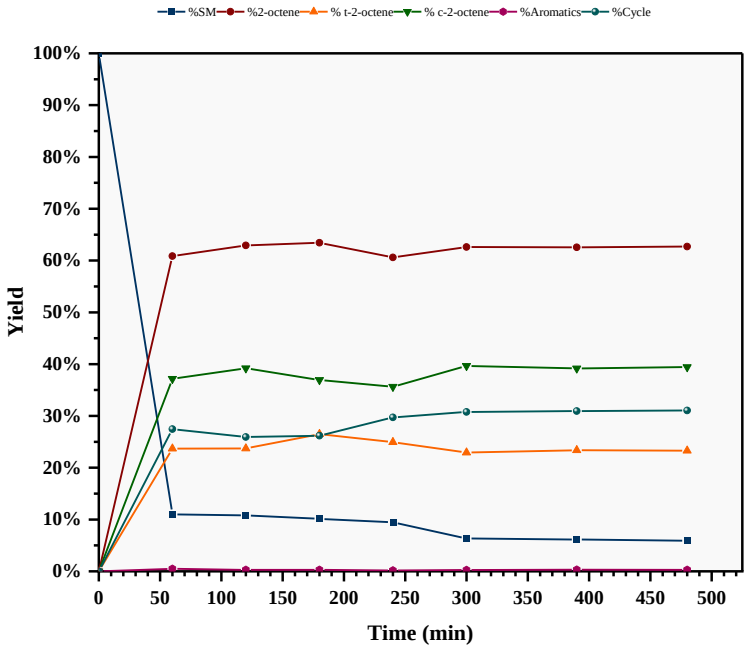

Figure 6-16 Kinetic profile for the reaction of 1-octene **1** using Ru-HUSY as a catalyst, under the optimal conditions for oxRu-C.

These results contrast sharply with those observed in the batch process. Several mechanistic and system-level factors may elucidate this discrepancy. First, the physical dilution of Ru sites due to the incorporation of SiO_2 likely diminished the density of these sites. Previous studies have demonstrated that close proximity between hydrogenation-dehydrogenation and acid functionalities is vital for facilitating skeletal rearrangement, cyclisation, and the final dehydrogenation to aromatic compounds.[106,107] Second, the residence time in the flow reactor was significantly shorter than in batch mode. As aromatisation occurs through

multiple sequential steps, including isomerisation, carbocation rearrangement, ring closure, and dehydrogenation, a shorter contact time may not suffice to complete this complex transformation.[108] It has been reported that aromatic yields over zeolites can be dramatically reduced under conditions where residence time limits intermediate evolution.[109] Third, the absence of hydrogen co-feeding may have indirectly influenced the lack of aromatic products. While hydrogen is not directly involved in the formation of aromatic rings from olefins, it plays a crucial role in stabilising intermediate species, influencing hydrogenation-dehydrogenation equilibria, and preventing metal sintering or coke formation. Hydrogen-rich atmospheres can enhance the stability and selectivity of metal-acid bifunctional catalysts under similar conditions.[110,111] Besides, using a smaller amount of active catalyst compared to the experiment with oxRu-C (50 vs 100 mg) likely led to a decreased overall availability. In the mixed bed with inert support, local heat and mass transfer gradients may have further influenced the reactivity profile, particularly for reactions necessitating synchronised bifunctional activity, such as aromatisation. Previous research on zeolite-based reforming and hydrocarbon upgrading systems has illustrated that catalyst dilution and bed packing directly impact product distribution.[112]

The Ru-HZSM-5 catalyst was then tested under flow reaction conditions. While the yield of aromatisation in batch conditions was modest, the significant production of cyclic intermediates, especially in the exchanged form of RuHZSM-5, indicated the potential for successfully completing the aromatisation process with the right conditions and residence time.

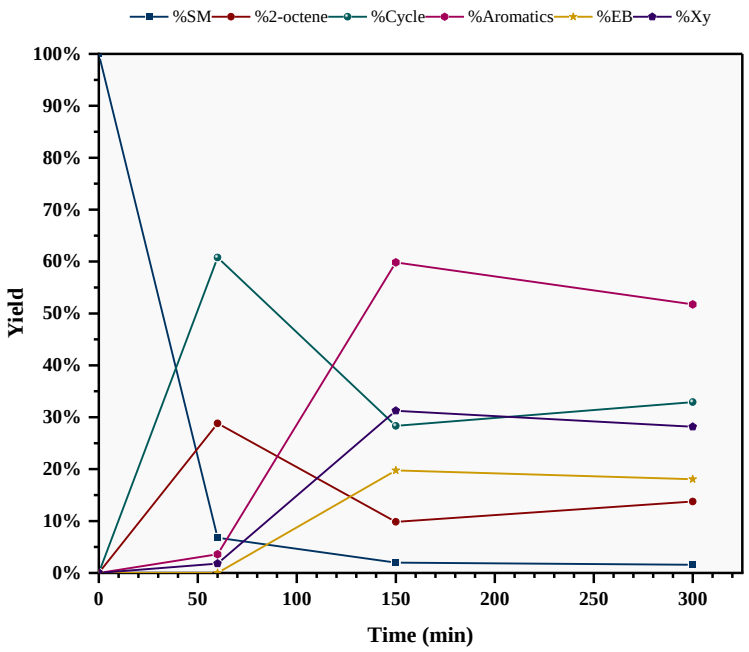

Figure 6-17 Kinetic profile for the reaction of 1-octene 1 with the Ru-HZSM-5 catalyst, under the optimal conditions for oxRu-C.

The results in Figure 6-17 show that, under the optimal conditions for oxRu-C, cyclized intermediates constituted approximately 60.78% of the total product distribution at early reaction stages (1 h), progressing into aromatic compounds to around 32.92% at 5 h. Furthermore, the formation of aromatic hydrocarbons increased significantly, reaching 59.82% at 2.5 h and stabilising at approximately 51.74% by 5 h. Among the identified aromatics, ethylbenzene and xylenes emerged as the dominant products, accounting for about 19.74% and 31.25% of the total product yield at 2.5 h, and approximately 18.06% and 28.17% at 5 h,

respectively. These figures correspond to roughly 33% ethylbenzene and 53% xylenes of the total aromatic yield, with the remainder potentially attributed to trace higher aromatics or minor alkylbenzenes.

The preference for xylenes over ethylbenzene in reactions involving the Ru-HZSM-5 zeolite highlights the significant rearrangement of molecular structure, potentially aided by hydride shifts and methyl group migrations. The lower yield of ethylbenzene indicates limited availability of the ethylation pathway, as bulkier alkylated benzenes face higher resistance to diffusion, resulting in potential trapping or secondary transformations. The batch process tends to yield more aromatics than the continuous-flow systems, as longer contact times enable cyclic intermediates to accumulate efficiently for desorption. In contrast, shorter residence times in flow systems can impede the desorption of bulkier aromatics, leading to diminished yields. To further explore this, two additional flow rates were tested: a reduced flow rate of 3 mL min^{-1}, intended to prolong the contact time between the reactants and the catalyst surface, and an increased flow rate of 7 mL min^{-1}, aimed at assessing how reduced residence time affects the progression of sequential reactions, particularly the transformation of cyclic intermediates into aromatics.

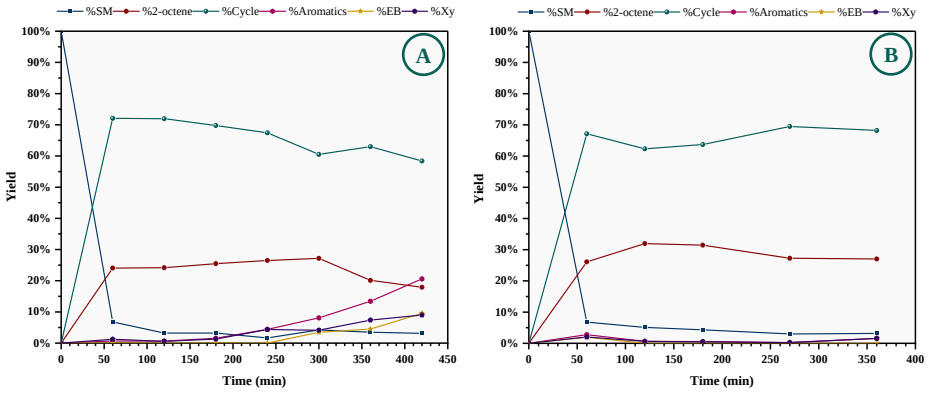

Figure 6-18 Kinetic profile for the reaction of 1-octene **1** under slower (3 mL min^{-1}, A) and faster (7 mL min^{-1}, B) flow rates compared to the optimal flow rate of 5 mL min^{-1}, using Ru-HZSM-5 as a catalyst.

The results (Figure 6-18) show that, on one hand, the longest residence time leads to nearly complete substrate conversion (over 95%) and high yields of cyclisation products (up to 72%) from the initial time points. The isomerisation products remained relatively substantial (approximately 20–27%), suggesting that prolonged contact with the acidic sites of Ru-HZSM-5 significantly promotes double-bond migration and ring closure. Initially, the aromatic compounds were low (<1% at 2 h), but they gradually increased over time, ultimately reaching around 21% at 7 h. This steady accumulation highlights the time-dependent nature of aromatisation, which is a slower, multistep process involving dehydrogenation, skeletal rearrangement, and hydride transfer, all of which require sustained interaction with the zeolite framework. In contrast to the results observed at 5 mL min^{-1}, where aromatic content exceeded 50% at 5 h, it is clear that while the same types of intermediates are formed at 3 mL min^{-1}, their

conversion into aromatics occurs at a considerably slower rate. On the other hand, the reaction operated under conditions of short residence time kept the conversion of 1-octene **1** high, but the product distribution was predominantly skewed towards unconverted cyclic olefins and a few isomerisation products. Aromatic compounds were infrequently observed, with the aromatic content consistently remaining <2% throughout the test duration. This clearly demonstrates that the contact time was inadequate for slower secondary reactions, such as ring dehydrogenation and methyl group rearrangement, to occur. Unlike cyclisation, which proceeds quickly through carbocation intermediates, aromatisation requires extended interaction with the catalytic sites and sufficient thermal activation, conditions that high flow rates do not allow. Consequently, even though the zeolite structure and Ru functionality remain unchanged, the residence time emerges as the limiting factor in accessing deeper reaction pathways that yield aromatics. The optimal flow rate of 5 $mL \cdot min^{-1}$ represents the best compromise between effective throughput and thorough conversion, enabling both cyclisation and aromatisation to occur within a reasonable time frame. This systematic approach provides a detailed assessment of how residence time influences the balance between isomerisation, cyclisation, and aromatisation over Ru-HZSM-5 under dynamic flow conditions.

To enhance the understanding of the catalytic performance observed at different flow rates, post-reaction AC-HAADF-STEM and iDPC imaging were conducted on the spent catalysts. The images in Figure 6-19 show a high similarity with the solid ancestor (Figure 6A-21; Appendix 6A-21), with a major fraction of Ru species remaining confined within the zeolite micropores, appearing as faint, highly dispersed features below 1 nm. XPS measurements confirm the integrity of the Ru oxide clusters inside the zeolite (Figure 6A-22; Appendix 6A-22).

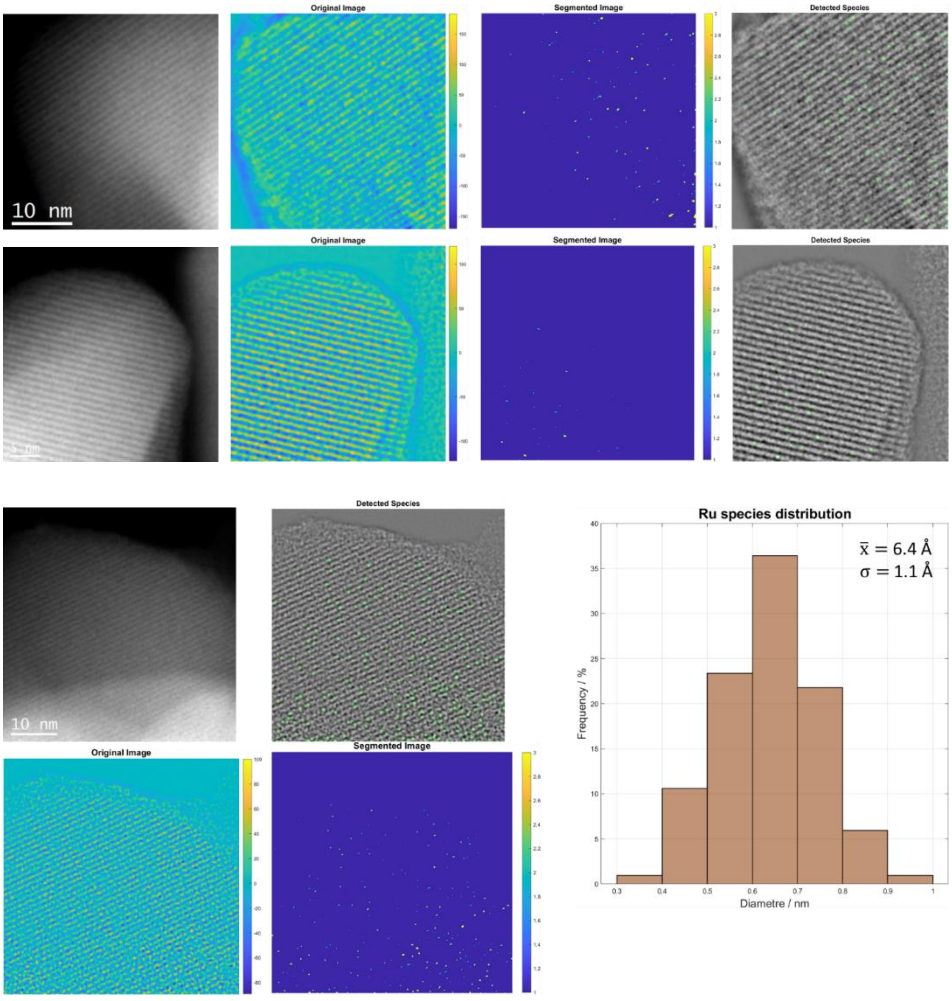

Figure 6-19 Representative aberration-corrected high-resolution HAADF-STEM (AC-HR-HAADF-STEM) images of the spent Ru-HZSM-5 zeolite after the in-flow reaction at 5 mL·min^{-1}, with the corresponding integrated differential phase contrast (iDPC) analysis (left), and histogram (taking into account more images). The observed Ru particles still show sizes between 0.5 and 1.5 nm, approximately.

6.3.4. Structural Evolution and Thermal Stability of Ru-Loaded Zeolites: Insights from Ex- and In-Situ HR-TEM

To evaluate the structural robustness of the ion-exchanged Ru-H-ZSM-5 catalyst under conditions pertinent to olefin aromatisation, high-resolution transmission electron microscopy (TEM) experiments were conducted at the SUperTEM facility at Université Paris Cité. The differential pumping system and MEMS heating chips of the instrument facilitated the examination of the same specimen in two distinct conditions: (i) under high vacuum during stepwise ex-situ annealing and (ii) in situ while subjected to a flowing 1-heptene/argon stream at the reaction temperature. This comprehensive investigation elucidates the effects of atmospheric conditions and thermal history on metal migration, particle growth, and the integrity of the catalyst framework.

6.3.4.1. Ex-situ TEM Heating: Thermally Induced Migration of Ru Species from Zeolite Channels

Systematic ex-situ heating of ion-exchanged Ru/H-ZSM-5 (Figure 6-20) under high vacuum (≈ 10^{-6} mbar) was used to visualise temperature-dependent metal mobility. HAADF-STEM micrographs recorded at RT, 150, 200, 250, 300 and 350 °C on two independent regions (see Figures 6-21 and 6-22) revealed a reproducible sequence of structural events that can be correlated with the catalytic temperature profile for 1-heptene upgrading.

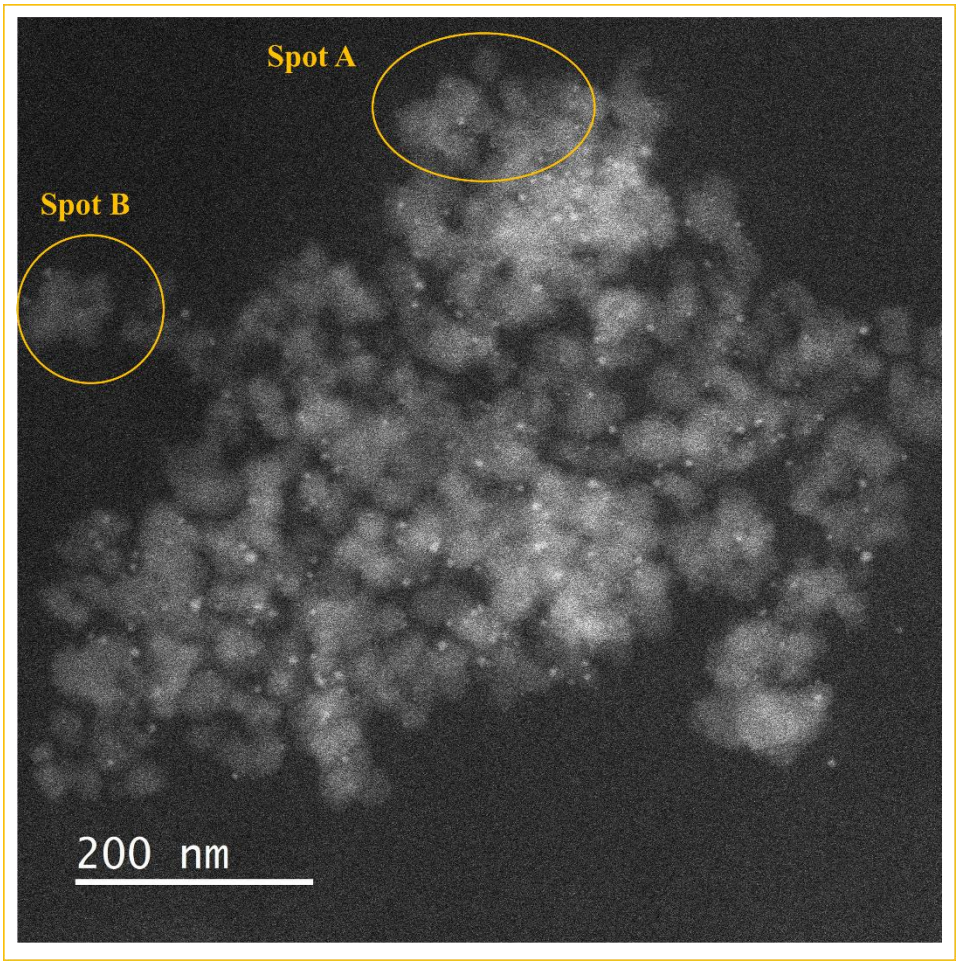

Figure 6-20 Low-magnification HAADF-STEM image of the Ru-H-ZSM-5 crystal, with two selected regions of interest (ROIs) indicated for detailed analysis in subsequent figures.

The first Ru-related contrast on the external crystal facets appeared at ≈ 200 °C, whereas intra-channel contrast diminished (Figure 6-21). This temperature coincides with the onset of olefin isomerisation and is attributed to partial

dehydroxylation of Brønsted acid sites (BAS). Density-functional calculations indicate that, once BAS are dehydrated, the diffusion barrier for single Ru atoms in MFI channels drops below 1.2 eV, enabling outward migration of sub-nanometre clusters.[68,113,114]

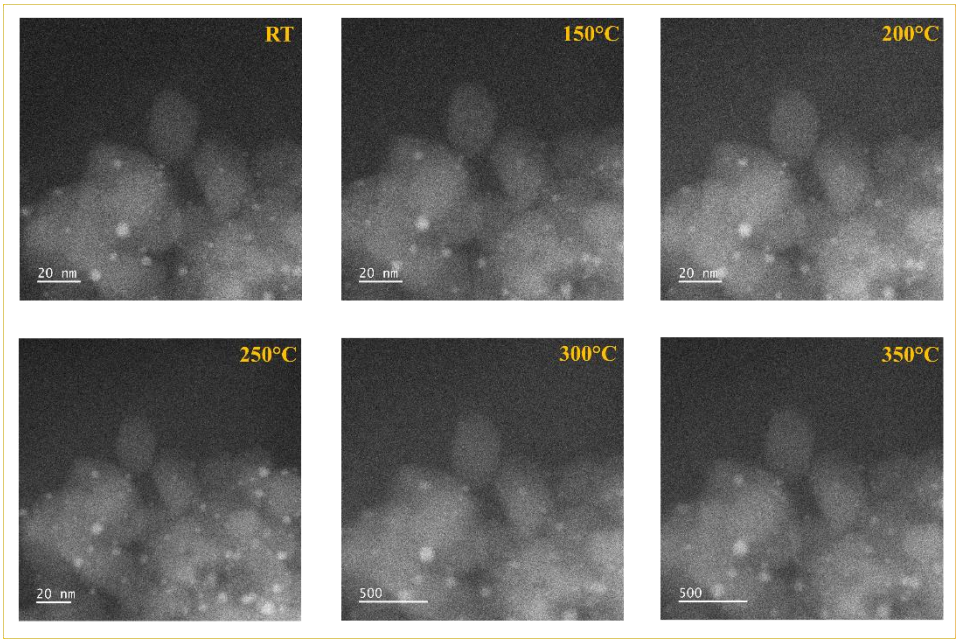

Figure 6-21 HAADF-STEM images of Spot A at increasing temperatures, illustrating the temperature-dependent migration behaviour of Ru nanoparticles during ex situ thermal treatment.

At 250 °C, an increase in the mobility of Ru species is observed, which coincides with the temperature typically associated with the onset of aromatisation catalysis. Under these conditions, Ru begins to form 1–2 nm nanoclusters

predominantly at the external surfaces of the zeolite crystals, accompanied by a noticeable decline in metal density within the internal pore structure. This redistribution suggests that thermal energy facilitates the migration of metal species, likely driven by progressive dehydroxylation of the zeolite framework, which lowers the energetic barriers for diffusion.[113–115]

At 300 °C, the growth of ruthenium particles remains markedly limited: even after outward migration from the zeolite channels, the average particle size does not exceed 3 nm. This size-confinement effect is attributed chiefly to the steric constraints imposed by the MFI framework, which restrict the coalescence of neighbouring clusters once they approach the pore mouth.[113,115]

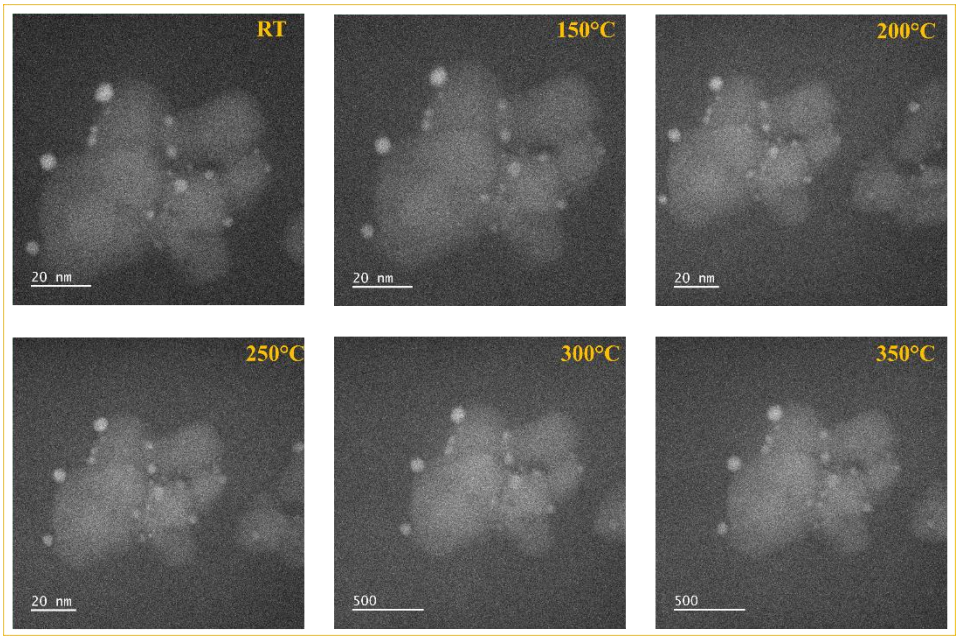

Figure 6-22 HAADF-STEM images of Spot B captured at successive temperatures, highlighting the gradual relocation of Ru nanoparticles as a function of thermal treatment during ex situ heating.

Several complementary stabilisation mechanisms further inhibit extensive agglomeration (Figure 6-22). First, Ru nanoparticles residing on the external crystal surfaces experience strong metal–support interactions that raise the energetic penalty for coalescence, thereby suppressing classical sintering pathways. Second, geometrical confinement within the zeolite micropores inherently resists particle growth; comparable behaviour has been reported for high-aluminium ZSM-5, where sub-nanometer Ru clusters (<1 nm) persist even after prolonged thermal exposure. Finally, the presence of Brønsted acid sites (BAS) plays an electronic role: partial electron transfer from framework AlO_4^- units stabilises cationic $Ru^{\delta+}$ species, anchoring them within the lattice and discouraging migration. Progressive dehydroxylation at elevated temperatures weakens this BAS–metal interaction, enabling limited diffusion, yet steric and interfacial factors continue to cap the ultimate particle size. Together, these effects ensure that, despite thermal activation, ruthenium remains highly dispersed and structurally robust within the H-ZSM-5 matrix under the conditions investigated.[68, 113–115]

6.3.4.2. In Situ HAADF-STEM Investigation of Ru Nanoparticle Stability Under Reactive Conditions

To investigate the structural evolution of Ru nanoparticles under conditions akin to those encountered during catalytic operations, in situ high-angle annular dark field scanning transmission electron microscopy (HAADF-STEM) measurements were conducted using the THEMIS microscope at the SUPER-TEM facility (Université Paris Cité). The Ru-H-ZSM-5 sample was incrementally heated from 280 °C to 300 °C while maintaining a flow of

hydrocarbons. Images (Figure 6-23) were captured over a five-hour period to monitor both temporal changes and variations in response to temperature.

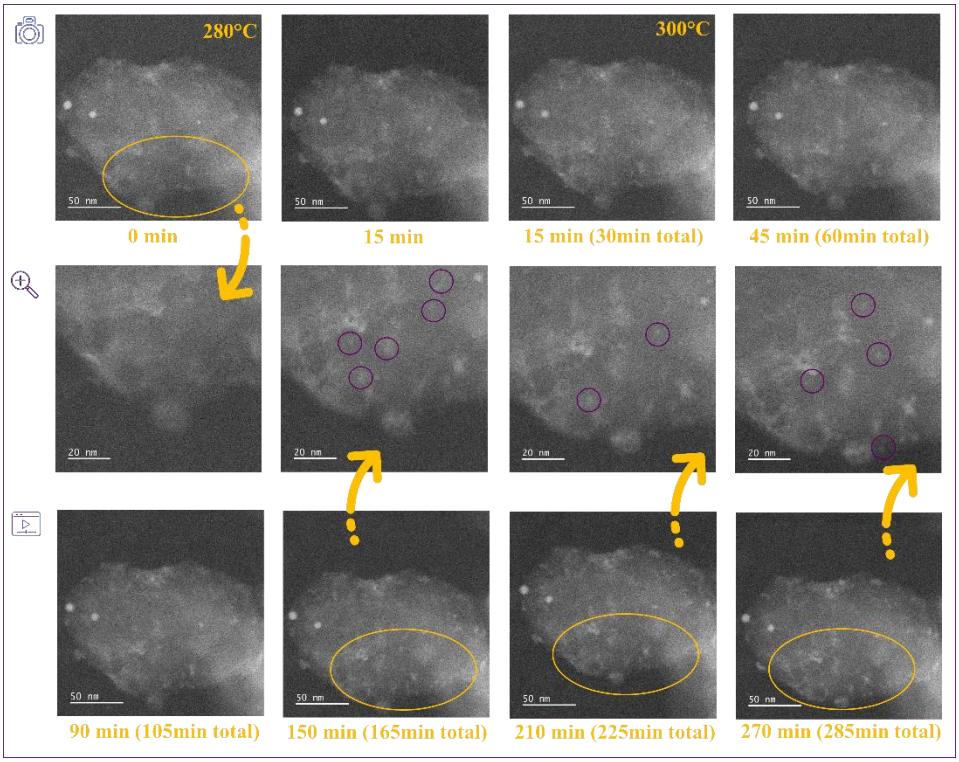

Figure 6-23 Time-resolved *in situ* HAADF-STEM analysis of Ru nanoparticles in H-ZSM-5 under reactive conditions, showing preservation of dispersion at 300 °C.

At 280 °C, initial HAADF–STEM imaging (0–15 min) revealed well-dispersed Ru nanoparticles, predominantly located on the external surface of the zeolite crystallites. Upon increasing the temperature to 300 °C, a series of images acquired at 15, 45, 90, 150, 210, and 270 minutes showed negligible particle

migration or agglomeration. Throughout the experiment, no significant particle growth or coalescence was observed, with the majority of Ru clusters remaining below 2–3 nm in diameter.

This remarkable stability stands in contrast to the temperature-induced migration observed under ex-situ vacuum conditions. The preservation of dispersion and confinement during in situ heating suggests that the presence of gas-phase adsorbates, particularly hydrocarbon intermediates, plays a stabilising role, suppressing both dehydroxylation and metal mobility. Recent studies have demonstrated that the nano-environment within zeolites, including the presence of retained hydrocarbon species, can significantly influence the behaviour and stability of encapsulated metal nanoparticles, preventing their migration and aggregation under reaction conditions.[116–118] For example, Xu *et al.* showed that the interaction between Ru and ZSM-5, as well as the chemical state of Ru, are crucial for maintaining high dispersion and catalytic performance, with the zeolite framework and adsorbed species inhibiting sintering even at elevated temperatures.[118] Moreover, the consistent HAADF contrast observed throughout the experiment indicates that Ru remained in a reduced and metallic state, further supporting the catalytic relevance of the observed structural configurations. These in situ observations affirm that under relevant reaction conditions, the Ru/H-ZSM-5 system maintains its structural integrity, which is crucial for sustaining activity and selectivity in reactions such as 1-heptene isomerisation and subsequent aromatisation. [118]

In summary, the literature supports the hypothesis that gas-phase adsorbates and the zeolite nano-environment are key factors in stabilising Ru nanoparticles during catalysis, in stark contrast to the migration and aggregation observed under vacuum or in the absence of stabilising species.

6.3.5. Mechanistic studies

To mechanistically validate the proposed aromatisation pathway of linear C_8 olefins over the Ru-HZSM-5 catalyst, a series of model reactions were conducted using 1-methyl-1-hexene **3a** as the feed molecule. This cyclic olefin was chosen as a plausible intermediate resulting from the skeletal isomerisation and intramolecular cyclisation of linear octenes, serving as a key probe for assessing the subsequent dehydrogenation step. The main objective of this study was to determine whether the transformation of cyclic olefins into aromatic compounds constitutes the rate-limiting step in the overall aromatisation mechanism and to quantify the influence of reaction temperature on this process.

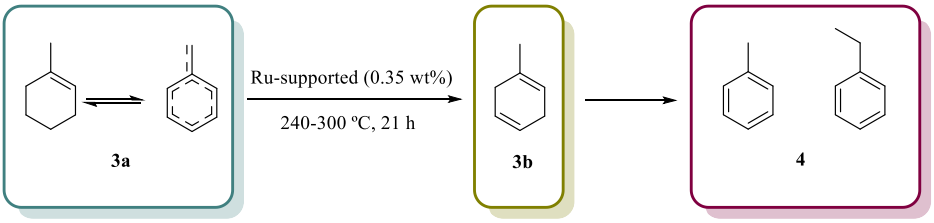

Figure 6-24 Reaction pathway for the aromatisation reaction of 1-methyl-1-hexene 3a as reactant over the Ru-HZSM-5 catalyst.

Catalytic tests were performed under controlled feed and pressure conditions, with temperature incrementally varied at 240 °C, 260 °C and 300 °C, using Ru-HZSM-5 as the solid catalyst. The product distributions obtained from the experiments shown in Figure 6-24 provided significant evidence of a temperature-sensitive transition in reaction pathways. At 240 °C, the yield of unconverted 1-methyl-1-hexene **3a** was notably high, 87.90%, with only trace amounts of aromatics (2.46%) present, predominantly toluene (1.76%).

Additionally, minor quantities of dienes (6.15%) and isomerised ketones (1.76%) were observed, suggesting limited skeletal rearrangement and minimal dehydrogenation activity at this temperature.[119] At 260 °C, a marked alteration in the product profile was evident. The conversion of the starting material **3a** increased, leading to a decline in the yield of unreacted olefin to 57.41%. Concurrently, aromatic production exhibited a more than sixfold increase, with toluene rising to 16.6%. The formation of dienes increased modestly to 8.90%, while isomerised ketones decreased slightly to below 1.50%. This indicates that the onset of enhanced dehydrocyclisation activity and partial olefin cracking is around 260 ºC.[77] At 300 °C, the reaction pathway further shifted towards aromatisation, with the conversion of 1-methyl-1-hexene **3a** reaching 69.13%, signifying heightened catalytic activity. Notably, isomerisation products remained low at 1.39%, and dienes decreased slightly to 7.87%. The majority of the product stream consisted of aromatic products 4, with toluene accounting for 29.43% of the total product yield. Trace amounts of ethylbenzene and benzene were also detected. The presence of these minor aromatics may imply the involvement of Friedel–Crafts alkylation and/or dealkylation reactions, facilitated by the Brønsted acid sites within the zeolite framework.[75] Under elevated temperatures, these sites are recognised for catalysing electrophilic substitution reactions, particularly when alkylcarbenium intermediates are stabilised on the catalyst surface.[120] Together, these findings demonstrate that aromatisation emerges as the predominant reaction pathway at elevated temperatures. This is driven by the synergistic interaction between Ru-mediated dehydrogenation functions and the acidic sites of the zeolite, which together facilitate complex rearrangements, cyclisation, and aromatising dehydrogenation reactions.[79] These empirical findings lend support to the hypothesis that the dehydrogenation of cyclic intermediates serves as the rate-limiting step in the

aromatisation pathway. While Ru-HZSM-5 effectively catalyses the initial processes of cyclisation and isomerisation under relatively mild conditions, dehydrogenation necessitates a higher input of thermal energy.[77,79–81,121]

The same mechanistic insights were then expanded to 1-hexene **7** and 1-heptene **9**. Both substrates lead to the formation of internal alkene isomers[77] and saturated and unsaturated cyclic hydrocarbons, such as methylcyclopentane and methylcyclohexene, which generate benzene and toluene.[122] Simultaneously, a parallel cracking pathway was observed, in which β-scission of long-chain alkenes (including the feed and intermediate isomers) generates smaller fragments. Among these, ethylene was found as a prominent product.[77] Although ethylene is a gaseous molecule often lost during reaction venting or workup, GC-MS analysis of the post-reaction organic extract (in $CDCl_3$) reveals a sharp peak at m/z = 28, confirming its presence in the reaction mixture (Figure 6A-23; Appendix 6A-23). The concurrent presence of benzene and ethylene within the acidic micropores of Ru-HZSM-5 would facilitate a secondary Friedel–Crafts-type alkylation, resulting in the formation of ethylbenzene. This compound is generated not through dehydrogenation pathways but rather from the in-situ alkylation of benzene by ethylene. Indeed, ^{1}H NMR analysis of the extracted organic phase reveals a distinct set of aromatic proton signals at δ ~7.36 ppm, corresponding to benzene, along with additional resonances, including a quartet centred at δ ~2.65 ppm that integrates for two protons. This is indicative of a benzylic –CH_2–group adjacent to an aromatic ring. These values align with reference spectra for ethylbenzene, thereby confirming its formation as a secondary product. The consistent identification of ethylbenzene via both ^{1}H NMR and GC-MS provides robust support for the Friedel–Crafts-type mechanistic pathway.[75,78,79] The sequence of transformations is summarised in

Figure 6-25 (top), which also shows the catalytic results for the transformation of 1-heptene **9** over the Ru-HZSM-5 catalyst (bottom).

1. Metal-catalysed isomerisation:

1-heptene ⇌ 2-heptene ⇌ 3-heptene

2. Beta-scission reactions generate ethylene.

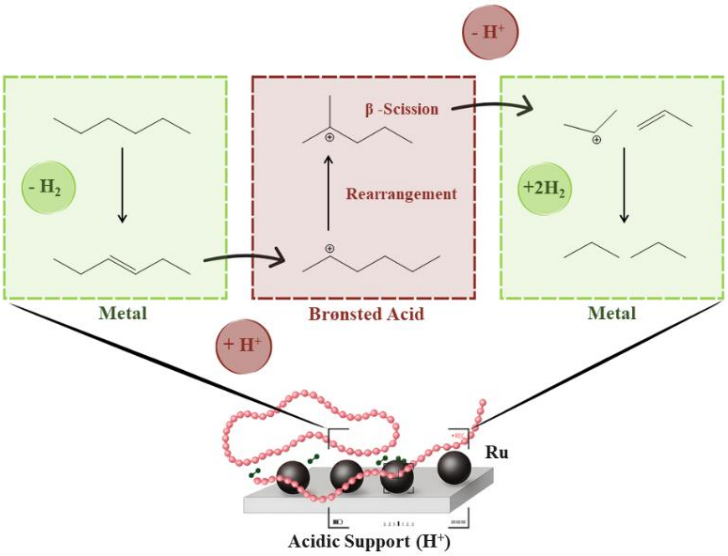

3. Catalysed cyclisation:

2-/3-heptene → methylcyclopentane / methylcyclohexene

4. Dehydrogenation to aromatics:

cyclic intermediates → benzene / ethylbenzene

5. Alkylation with ethylene:
benzene + ethylene → ethylbenzene
(Friedel–Crafts reaction)

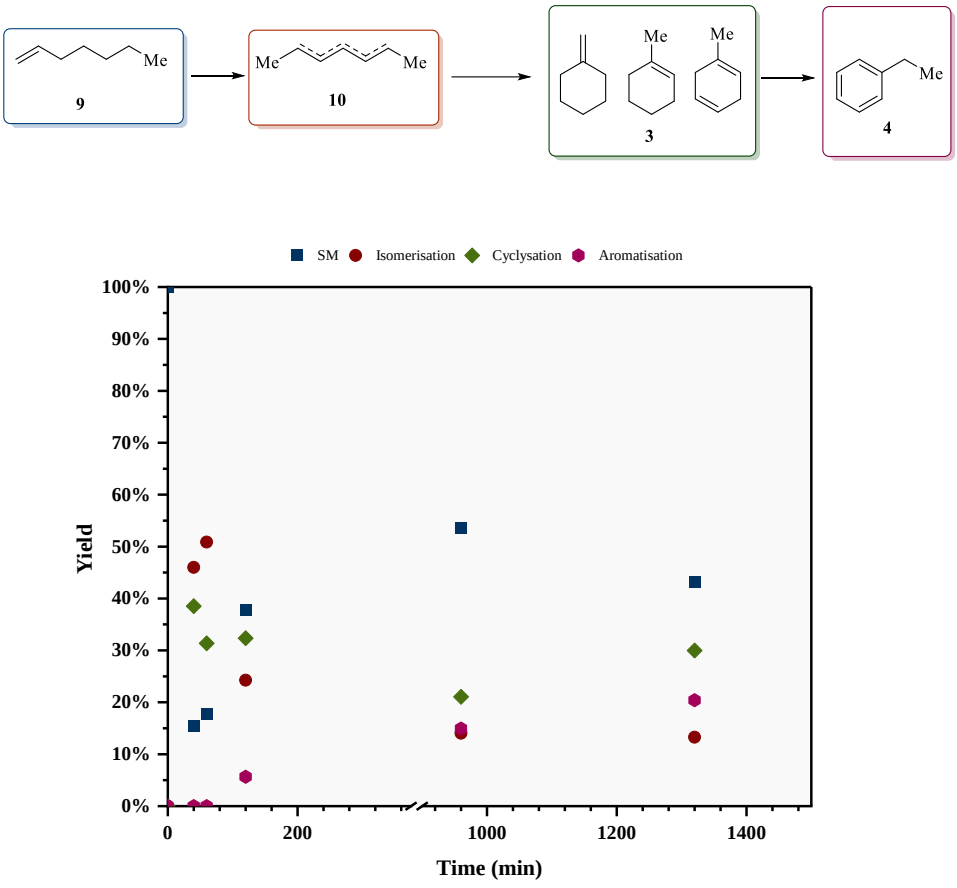

Figure 6-25 Reaction sequence and catalytic results for the transformation of 1-heptene over the Ru-HZSM-5 catalyst.

Parallel experiments were conducted using 1-hexene **7** as a substrate. It is important to note that 1-hexene lacks the additional methylene unit found in 1-heptene **9**, which could affect the kinetics of ring closure and the distribution of cracking products. However, under the same catalytic conditions with Ru-HZSM-5, a similar product spectrum was observed. Aromatics such as benzene and toluene were prominently detected in both GC-MS and NMR analyses.[75] Crucially, the characteristic signals for toluene were revealed by ^{1}H NMR analysis: a singlet near 2.36 ppm was noted, corresponding to the methyl group (-CH_3) attached to the benzylic carbon, and a multiplet between 7.0 and 7.2 ppm, integrating to five protons, was attributed to the aromatic protons of the monosubstituted benzene ring. Furthermore, the presence of a molecular ion at m/z = 92, corresponding to toluene, and another at m/z = 28, indicating ethylene, was confirmed by GC-MS. This evidence supports the conclusion that beta-scission and alkylation proceed concurrently, even when starting from a C6 precursor.[123] The formation of toluene from 1-hexene **7** strongly supports the occurrence of the beta-scission reaction to generate ethylene. Consequently, in-situ isomerisation, beta-scission, cyclisation, dehydrogenation, and alkylation reactions are applicable to linear olefins ranging from C_6 to C_{10}. For 1-hexene **7**, cyclisation through a six-membered transition state is regarded as more kinetically accessible compared to longer chains, facilitating the production of benzene precursors.[124] Moreover, the cracking of shorter olefins to produce ethylene is considered to be more efficient due to lower activation barriers. The significant formation of toluene and ethylbenzene in both 1-hexene **7** and 1-heptene **9** emphasises the role of ethylene as an alkylating agent and illustrates the dual function of Ru-HZSM-5 in rearranging hydrocarbon skeletons while upgrading through secondary alkylation.

At this point, the CO_2 was introduced as a co-reactant with both 1-hexene **7** and 1-heptene **9**, which significantly alters the reaction pathway by quenching the H_2 generated after the Ru-catalysed hydrogenation of CO_2 to methane (Table 6-4).[125–127]

Table 6-4 Comparative performance of Ru-HZSM-5 in the conversion of 1-hexene **7** and 1-heptene **9** with and without CO_2 co-feeding.

Feedstock	CO_2 Co-feed	Dominant Products	Main Pathway
1-Heptene 9	No	Ethylbenzene, benzene	Isomerisation → Cyclisation → Alkylation
1-Heptene 9	Yes	CH_4, C_2H_4, C_3H_6	CO_2-promoted deep cracking
1-Hexene 7	No	Ethylbenzene (major)	Cracking + Benzene formation + Ethylene alkylation

Under our optimised catalytic conditions, employing a CO_2/alkene molar ratio of 0.35 leads to the complete suppression of aromatic species formation. As a result, the product stream is dominated by low-molecular-weight alkanes and olefins, particularly methane, ethylene, and propylene (Figure 6A-24; Appendix 6A-24). As a result, the catalytic behaviour shifts toward enhanced C–C bond cleavage and cracking, resulting in minimal formation of condensed-phase hydrocarbons. These findings align with previous reports on CO_2-induced pathway switching in bifunctional systems and confirm its significant modulatory role. To distinguish catalytic activity from thermal effects, literature on the intrinsic thermal decomposition of 1-heptene **9** in the absence of a catalyst is referenced.[127] These studies, utilising mass spectrometric analysis, have identified two primary

degradation pathways: classical γ-scission and the diradical retro-ene mechanism. Commonly observed fragment ions at m/z = 42, 56, and 70 correspond to C_3, C_4, and C_5 hydrocarbons, respectively. The peak at m/z = 70 is indicative of the diradical retro-ene mechanism, wherein a hydrogen atom undergoes a concerted shift through a cyclic transition state, forming a diradical that subsequently undergoes β-scission, yielding ethylene and shorter-chain fragments. The peaks at m/z = 56 and 42, associated with butenes and propenes, arise from either pathway. Furthermore, the appearance of peaks at m/z = 41 and 57 supports the involvement of γ-C–C bond cleavage, yielding allyl and butyl radicals. Quantum chemical calculations further reinforce this dual-pathway model, with γ-scission bond dissociation energies reported in the range of 64.8 to 74.6 kcal/mol, indicating that both pathways are feasible at elevated temperatures.[128,129] These data, altogether, strongly indicate that CO_2 exerts an inhibitory effect on both the cyclisation-aromatisation and alkylation pathways.

In order to study the influence of the acidity and confinement provided by the Ru-HZSM-5 zeolite, the synthesis of basic and hierarchically structured ZSM-5 catalysts was carried out, aiming to overcome the well-known diffusion limitations associated with conventional microporous zeolites. Two modified catalysts were prepared: Ru-NaOH-ZSM-5, generated through alkaline desilication, and Ru-NaOH+TPAOH-ZSM-5, synthesised using a dual-template approach that combines base-assisted mesopore formation with organic structure direction. In the case of Ru-NaOH-ZSM-5, desilication was carried out by treating the parent zeolite with a 0.3M sodium hydroxide solution.[130,131] This basic treatment selectively removed silicon from the framework, resulting in the formation of disordered mesopores while preserving the crystallinity and Brønsted acidity of the zeolite. Although this approach significantly improved

the diffusion properties, the randomness of the mesopore network occasionally led to a slight loss in shape selectivity and a more varied product distribution, with enhanced formation of heavier alkylated aromatics and polycyclic species. To further refine the pore architecture and address this limitation, a dual-template strategy employing a mixture of 0.3 M NaOH and 0.25M tetrapropylammonium hydroxide (TPAOH) in a 1:1 volume ratio was performed. In the Ru-NaOH+TPAOH-ZSM-5 catalyst, NaOH facilitates silicon extraction and initial mesopore formation, while TPAOH, acting as a soft template and crystal growth modifier, guides the recrystallisation and stabilisation of the external surface, yielding a more uniform mesopore network. This tailored structure resulted in a catalyst with different textural properties, including increased mesopore volume and more accessible catalytic sites, while maintaining the intrinsic microporous features of Ru-ZSM-5. The dual-template treatment also subtly adjusted the acidity of the zeolite, typically lowering the overall Brønsted acid site density while increasing their accessibility, a factor known to influence reaction selectivity and reduce coke formation.

The PXRD patterns (Figure 6A-25; Appendix 6A-25) provide clear evidence of the structural consequences of different desilication strategies. Treatment with 0.3 M NaOH alone resulted in a slight loss of peak intensity and broadening, indicating partial degradation of the crystalline MFI framework. In contrast, the combined treatment with 0.3 M NaOH and 0.25 M TPAOH (1:1 volume ratio) preserved the intensity and sharpness of the characteristic MFI reflections, confirming that the microporous architecture was maintained. This indicates a more controlled and selective desilication process, where TPAOH acts to stabilise the framework during silicon removal. As a result, mesopores were likely introduced within an intact microporous matrix, successfully achieving

hierarchical porosity. Complementary, Fourier-transformed infrared (FT-IR) spectroscopy with pyridine adsorption further elucidated the impact of these treatments on acidity (Figure 6-26). Both Brønsted and Lewis acid sites were probed, with characteristic bands observed near 1545 cm^{-1} for Brønsted sites and around 1450 cm^{-1} for Lewis sites. The NaOH-treated sample exhibited a reduction in Brønsted acidity, likely due to partial dealumination or framework collapse. However, the sample treated with NaOH and TPAOH retained more Brønsted acid sites, indicating that the co-treatment preserved the acid functionality more effectively. The relative increase in Lewis acid features may reflect extra-framework Al species generated during desilication. Overall, these findings confirm that the NaOH–TPAOH treatment not only promotes the formation of mesopores but also maintains the essential structural and acidic properties of ZSM-5, making it more suitable for reactions involving bulky aromatic molecules where both accessibility and acidity are critical for performance.[81]

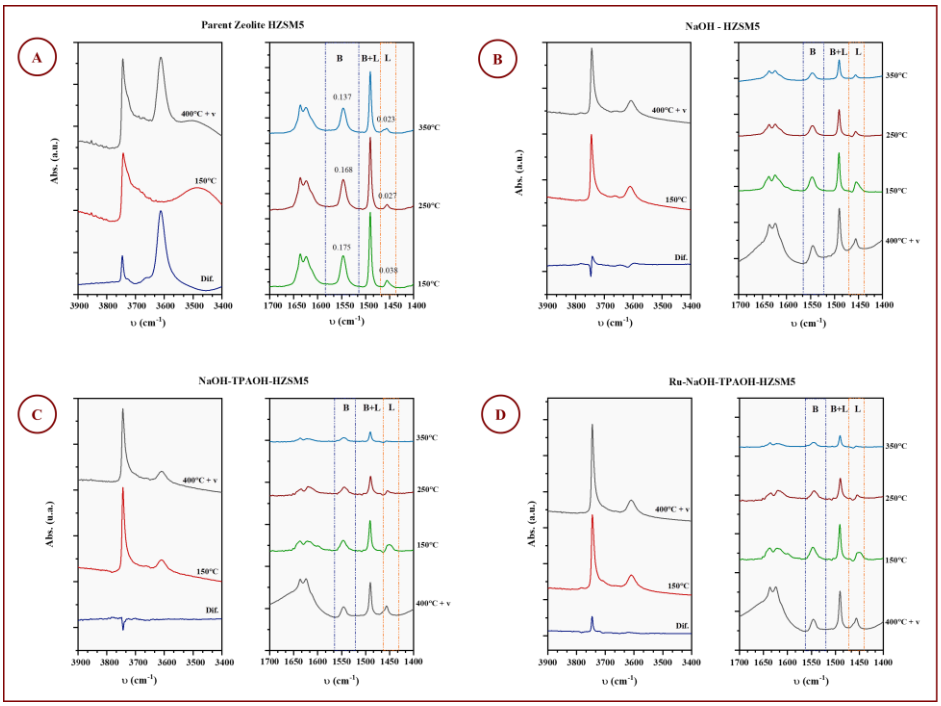

Figure 6-26 Fourier-transformed infrared (FT-IR) spectroscopy of adsorbed pyridine on MFI zeolites after desilication with NaOH and NaOH–TPAOH.

Ru-NaOH-ZSM-5 exhibited a marked decline in catalytic performance compared to Ru-ZSM-5, as evidenced by a decrease in conversion from 69.13% to 35.73% and a corresponding drop in total aromatic yield from 29.43% to 18.86%. Furthermore, there was a significant alteration in product distribution: ethylbenzene increased to 9.55%, xylenes rose to 2.71%, while toluene dropped to just 3.5%. This shift reflects, according to literature,[132,133] the partial degradation of the microporous structure and the emergence of irregular, non-uniform mesopores, which undermined the original shape selectivity. In contrast, Ru-NaOH+TPAOH-ZSM-5 resulted in a significant enhancement in catalytic

performance, with an excellent conversion of 81.62% and aromatic yield of 25.55%, with ethylbenzene (15.07%), toluene (5.45%) and xylenes (4.5%) as the predominant aromatic products. Apparently, the co-templated desilication approach benefits from TPAOH's role as a mesopore-directing agent, which also supports the stability of the zeolite framework during the hydroxide attack, to generate more uniform and interconnected mesopores while maintaining the integrity of the microporous MFI domains.[134]

6.4. Conclusion

This study successfully achieved its primary objective: the development of a selective and sustainable catalytic system for the transformation of linear olefins, such as 1-octene **1**, into valuable alkylated aromatics **4**, specifically xylenes and ethylbenzene, under relatively mild thermal conditions (300 ºC) and in the absence of strong acidic or basic promoters. A combination of catalyst design, optimisation of reaction conditions, and advanced characterisation techniques facilitated a comprehensive understanding of the interplay between catalyst structure and function.

Batch experiments demonstrated significant catalytic behaviour of various Ru-based solid catalysts, highlighting concurrent processes of isomerisation, cyclisation, and aromatisation. Among the materials evaluated, ion-exchanged Ru-HZSM-5 emerged as the most effective catalyst, achieving over 85% conversion and more than 60% selectivity toward cyclic and aromatic products. This high performance is attributed to the dispersion of ultrasmall (≈ 1 nm) Ru oxide clusters within the zeolite micropores, which is confirmed by a comprehensive characterisation of the solid catalyst before and after reaction. In contrast, oxRu-C exhibited high isomerisation activity but limited aromatisation capabilities in batch, underscoring the critical role of the support in catalytic performance. Time-resolved batch studies further corroborated that aromatic products are secondary products, forming after the accumulation of isomerised and cyclic intermediates. This observation supports a stepwise mechanism that begins with isomerisation, followed by cyclisation and dehydrogenation reactions.

In flow, oxoRu-C allowed us to identify the optimal operating conditions, which were subsequently applied to Ru-HUSY and Ru-HZSM-5, effectively exploiting its catalytic characteristics. These experiments confirmed the robustness of the ion-exchanged Ru-HZSM-5 zeolite catalyst, particularly at moderate flow rates (5 mL min^{-1}). Under these conditions, the catalyst retained a high aromatic yield (>50%) with good stability over time. Post-reaction analysis of the used catalysts confirmed the stability of the zeolite, with highly dispersed Ru oxide clusters confined within the zeolite micropores (less than 1 nm), thereby preserving catalytic activity.

Mechanistic reactive experiments with different alkenes confirmed the intermediacy of cycloalkene products **3** towards the desired aromatic products **4**, and the generation of both ethylene and benzene for the production of ethylene. A reactive sequence involving isomerisation, beta-scission, cyclisation, aromatisation, and Friedel-Crafts reactions is proposed based on the experimental data compiled here.

In summary, these findings validate that small Ru (II, III) oxide clusters dispersed within solid supports (carbon or zeolite frameworks) provide an efficient and tunable platform for converting linear alkenes, particularly relatively long-linear alkenes such as 1-octene **1**, into high-value aromatics **4**. The support's structure, porosity, and the electronics of Ru (II, III) oxide cluster sites were identified as key determinants of catalytic performance, while reaction engineering parameters offered an additional degree of control over product distribution. All in all, the research establishes a strong foundation for designing Ru-based solid catalysts for alkene aromatisation from renewable or fossil-derived olefins, supporting broader goals of sustainable and selective petrochemical production.

6.5. Appendix

a) 6A-1

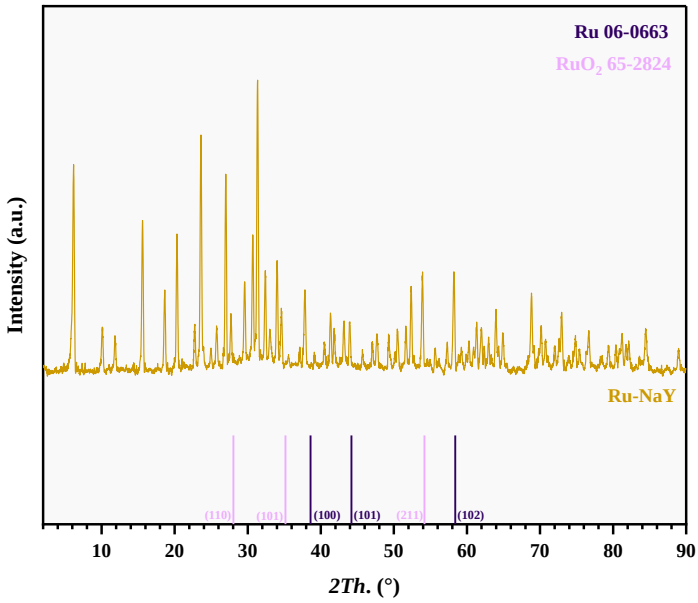

Figure 6A-1 Powder X-ray diffraction (PXRD) analysis of the NaY zeolite before and after incorporating the Ru (Ru-NaY).

b) 6A-2

Table 6A-2 Comparison of Structural and Catalytic Properties of HY and HZSM-5 Zeolites

Parameter	HY Zeolite	HZSM-5 Zeolite
Pore Size	Large (~0.74 nm)	Medium (~0.55 nm)
Acidity	Moderate Brønsted acidity	Strong Brønsted acidity
Shape-Selectivity	Low	High
Aromatics Yield (510 min)	2.40%	2.12%
Product Distribution	Broad, potential for over-cracking	Narrow, favouring monoaromatics

c) 6A-3

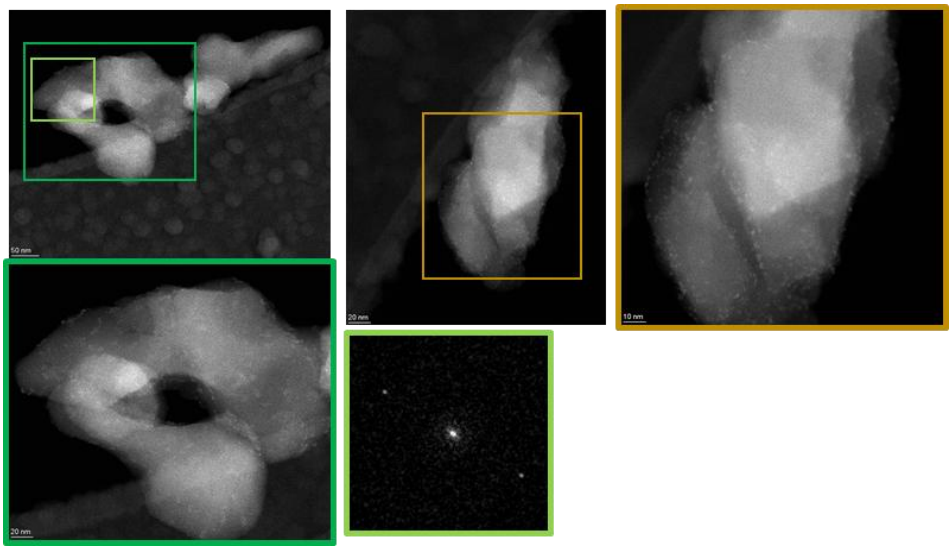

Figure 6A-3 High-magnification HAADF-STEM images of the Ru-HZSM-5 zeolite. Small Ru particles appear dispersed on the zeolite surface. In the left image, structural channels with dimensions of approximately 11.3 Å are visible.

d) 6A-4

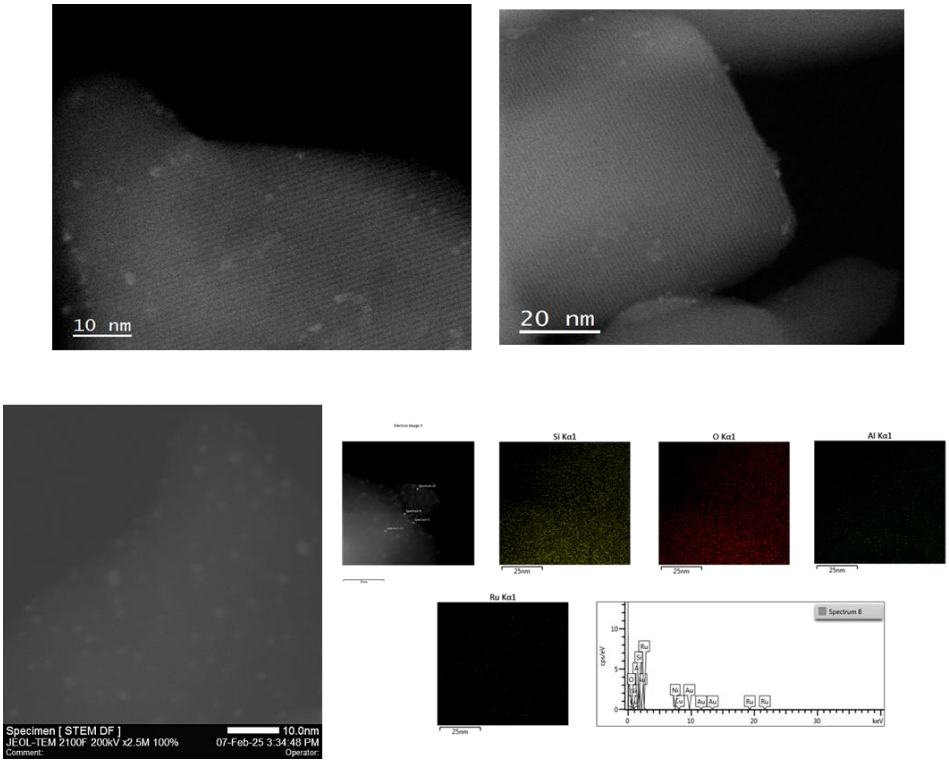

Figure 6A-4 Representative high-angle annular dark field scanning transmission electron microscopy (HAADF-STEM) images for the exchanged Ru-HZSM-5 catalyst (top), and also for the impregnated Ru-HZSM-5 catalyst (Ru-HZSM-5imp, bottom), together with the elemental mapping and EDX analysis.

e) 6A-5

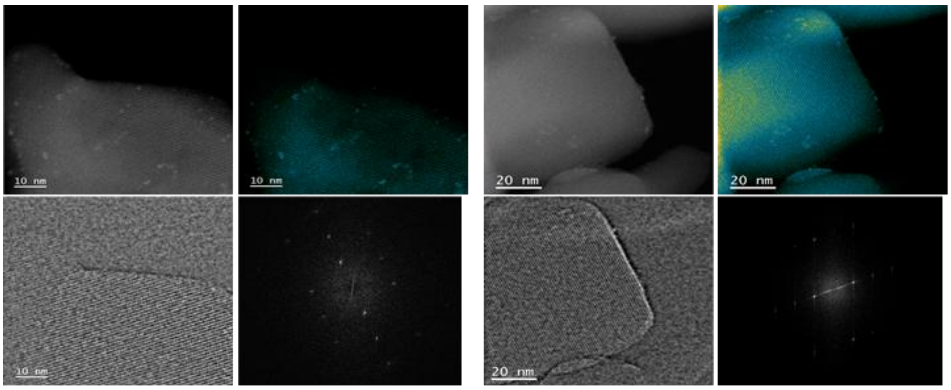

Figure 6A-5 Aberration-corrected high-resolution HAADF-STEM (AC-HR-HAADF-STEM, top) and aberration-corrected high-resolution transmission electron microscopy (AC-HR-TEM) images of the Ru-HZSM-5 zeolite, with the corresponding integrated differential phase contrast (iDPC) analysis and crystalline channel size recognition, respectively.

f) 6A-6

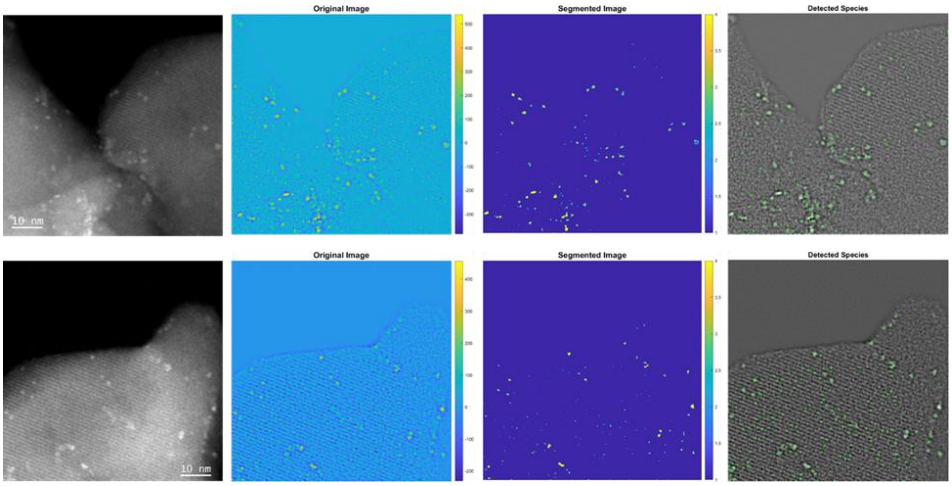

Figure 6A-6 Two representative aberration-corrected high-resolution HAADF-STEM (AC-HR-HAADF-STEM) images of the Ru-HZSM-5 zeolite, with the corresponding integrated differential phase contrast (iDPC) analysis to detect the small Ru oxide clusters.

g) 6A-7

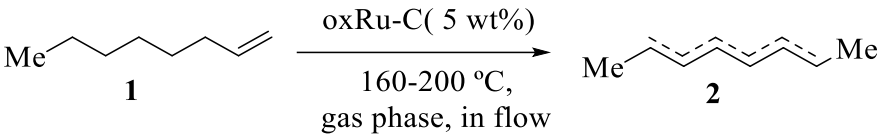

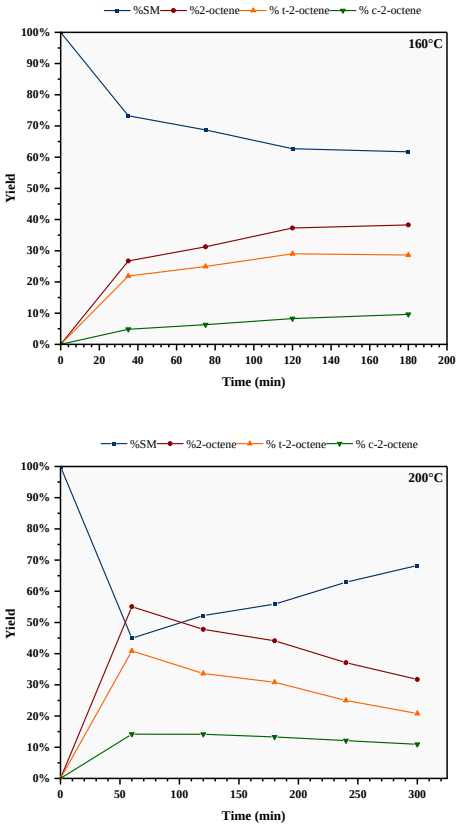

Figure 6A-7 Kinetic plots for the conversion of 1-octene **1** at 160 ºC (top) and 200°C (bottom) with the oxRu-C catalyst under flow reaction conditions.

h) 6A-8

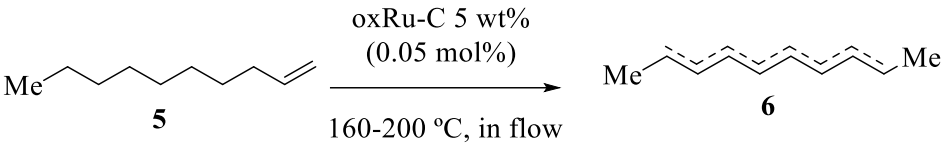
Me
5
oxRu-C 5 wt%
(0.05 mol%)
160-200 ºC, in flow
Me
Me
6

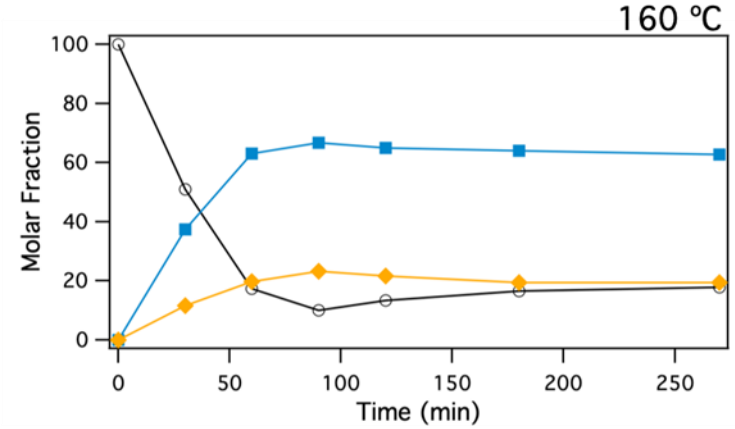
160 ºC
Molar Fraction
100
80
60
40
20
0
0
50
100
150
200
250
Time (min)

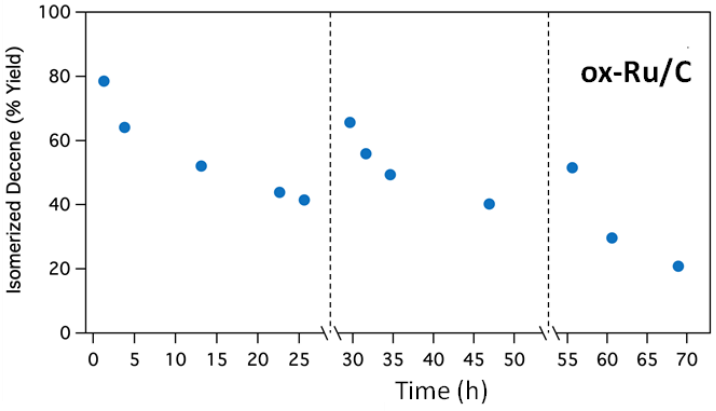
Isomerized Decene (% Yield)
ox-Ru/C
100
80
60
40
20
0
0
5
10
15
20
25
30
35
40
45
50
55
60
65
70
Time (h)

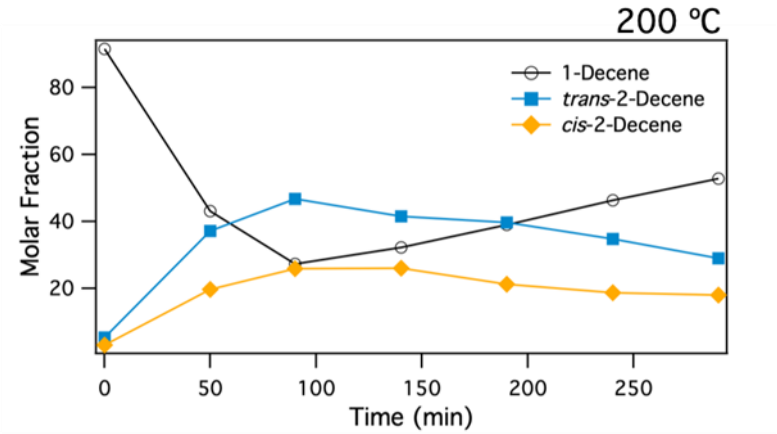

Figure 6A-8 Kinetic results for the isomerisation 1-decene **5** at 160-200 ºC and the corresponding internal alkenes **6** in the gas phase (short and long reaction times) under the indicated reaction conditions, catalysed by oxRu-C. Discontinuous lines indicate the stopping of the reaction and N_2 purge.

i) 6A-9

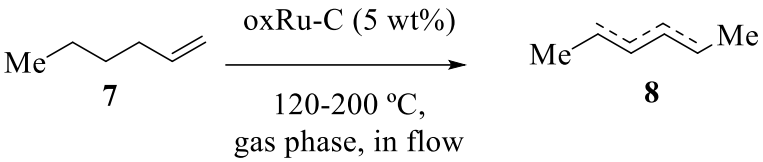
Me
7
oxRu-C (5 wt%)
120-200 ºC,
gas phase, in flow
Me
Me
8

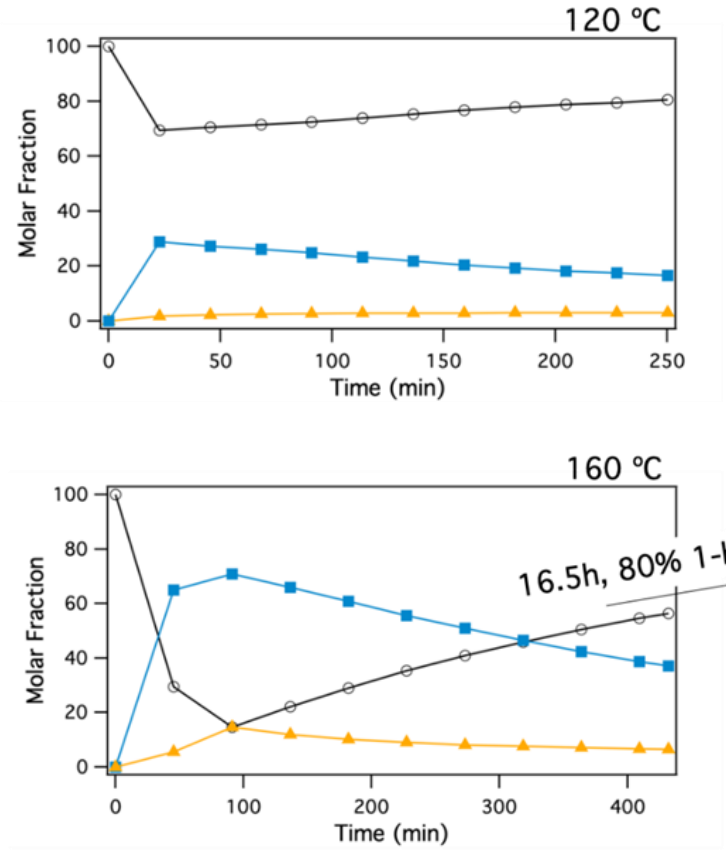
120 °C
Molar Fraction
Time (min)
160 °C
16.5h, 80% 1-hexene
Molar Fraction
Time (min)

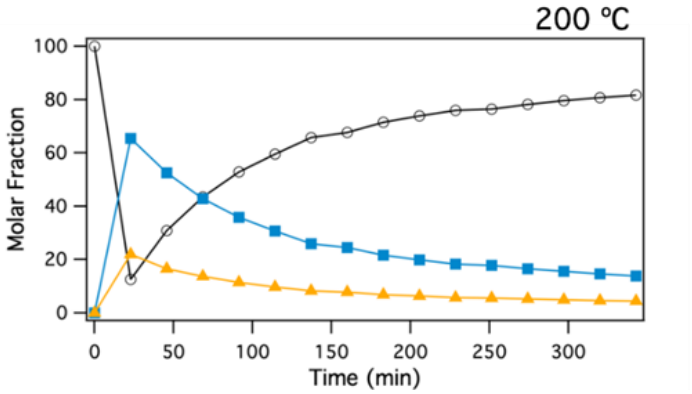

Figure 6A-9 Kinetic results for the isomerisation of 1-hexene **7** to the corresponding internal alkenes **8** in the gas phase, catalysed by oxRu-C at different reaction temperatures. Molar fraction refers to the yield of the corresponding internal alkene product, in %.

j) 6A-10

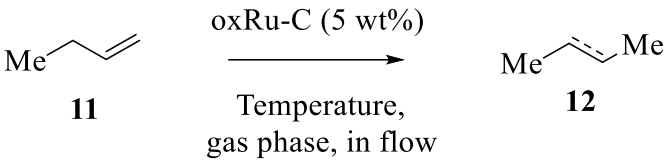

11 **12**

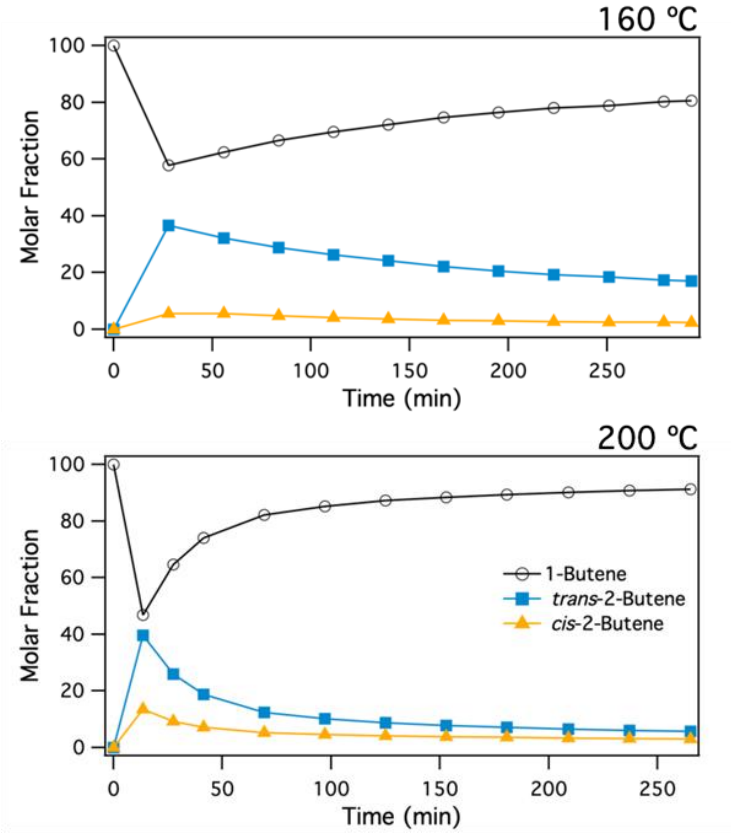

Figure 6A-10 Kinetic results for the isomerisation of 1-butene **11** to the corresponding internal alkenes **12** in the gas phase, catalyzed by oxRu-C at different reaction temperatures. Molar fraction refers to yield of the corresponding internal alkene product, in %.

k) 6A-11

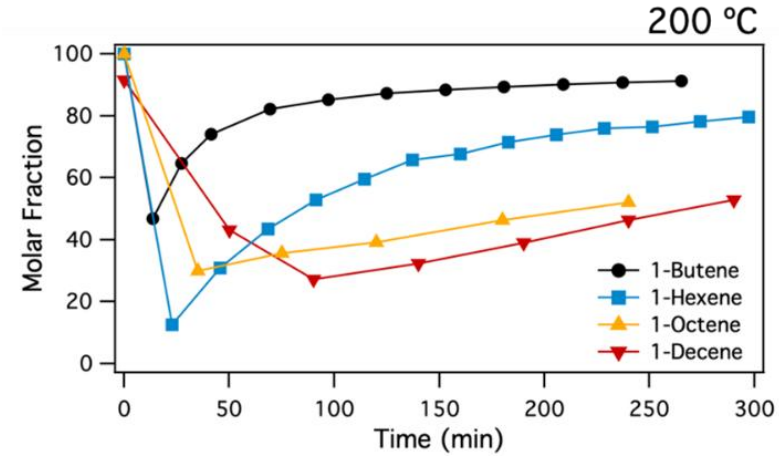

Figure 6A-11 Comparative kinetic results for the isomerisation of different linear terminal alkenes in the gas phase, catalysed by oxRu-C at 200 ºC. Molar fraction refers to the yield of the corresponding internal alkene product, in %.

l) 6A-12

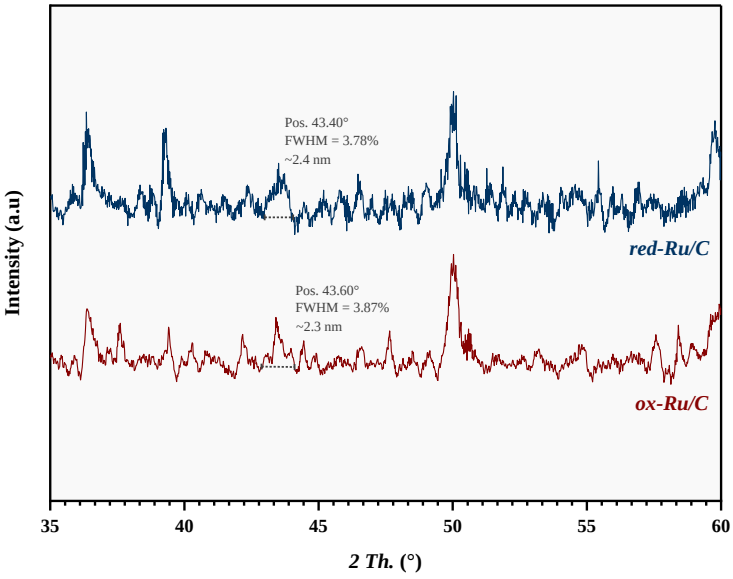

Figure 6A-12 Powder X-ray diffraction (PXRD) spectra of redRu-C exposed to air (top) compared to oxRu-C (bottom), and the corresponding nanoparticle size average according to the Scherrer equation using a shape factor of 0.9.

m) 6A-13

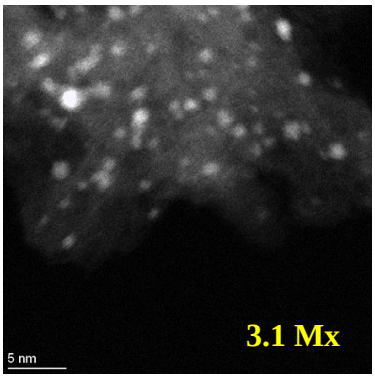

Total particles: 59
Dispersion: 37.9%
Average diameter: 1.85 ± 0.22 nm

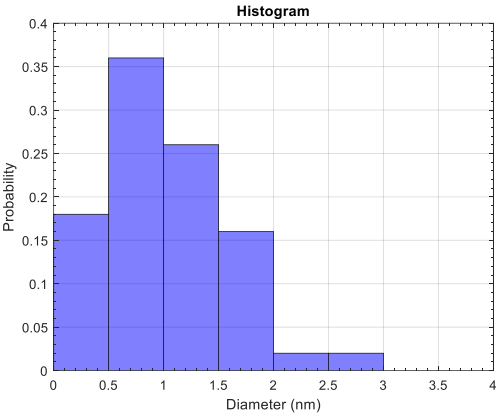

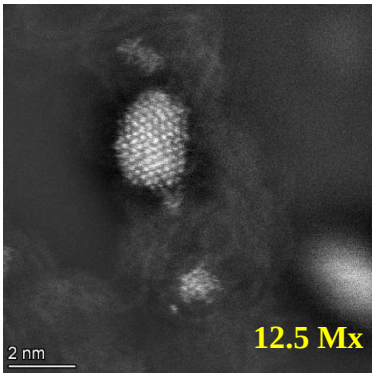

Total particles: 89
Dispersion: 78.8%
Average diameter: 0.83 ± 0.06 nm

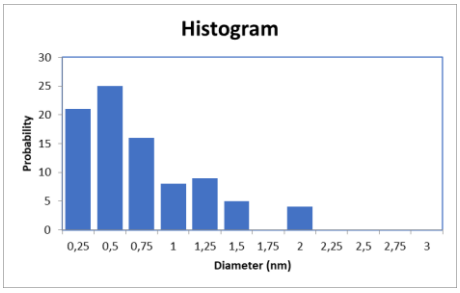

Figure 6A-13 Representative high angle annular dark field scanning transmission electron microscopy (HAADF-STEM) images (left) and the corresponding size analysis and histograms (right) of redRu-C, for increasing magnifications: 3.1 to 12.5 Mx (from top to bottom).

n) 6A-14

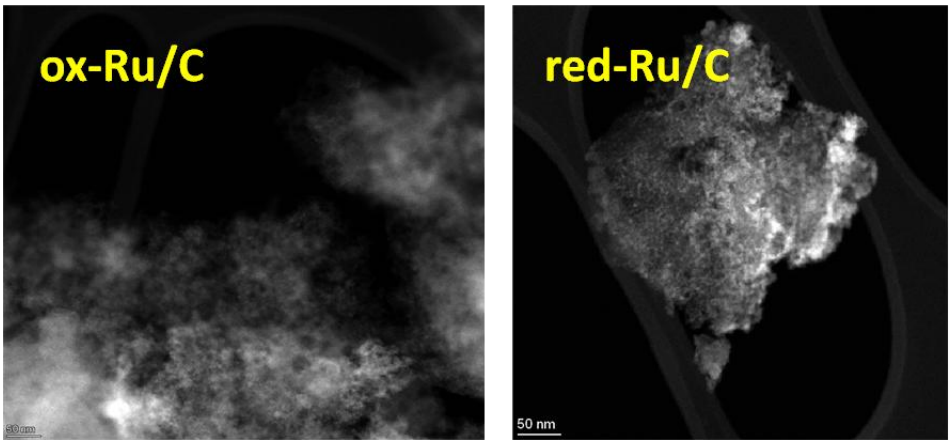

Figure 6A-14 Representative high angle annular dark field scanning transmission electron microscopy (HAADF-STEM) images of oxRu-C (left) and redRu-C (right) showing the porosity of the solid catalyst.

o) 6A-15

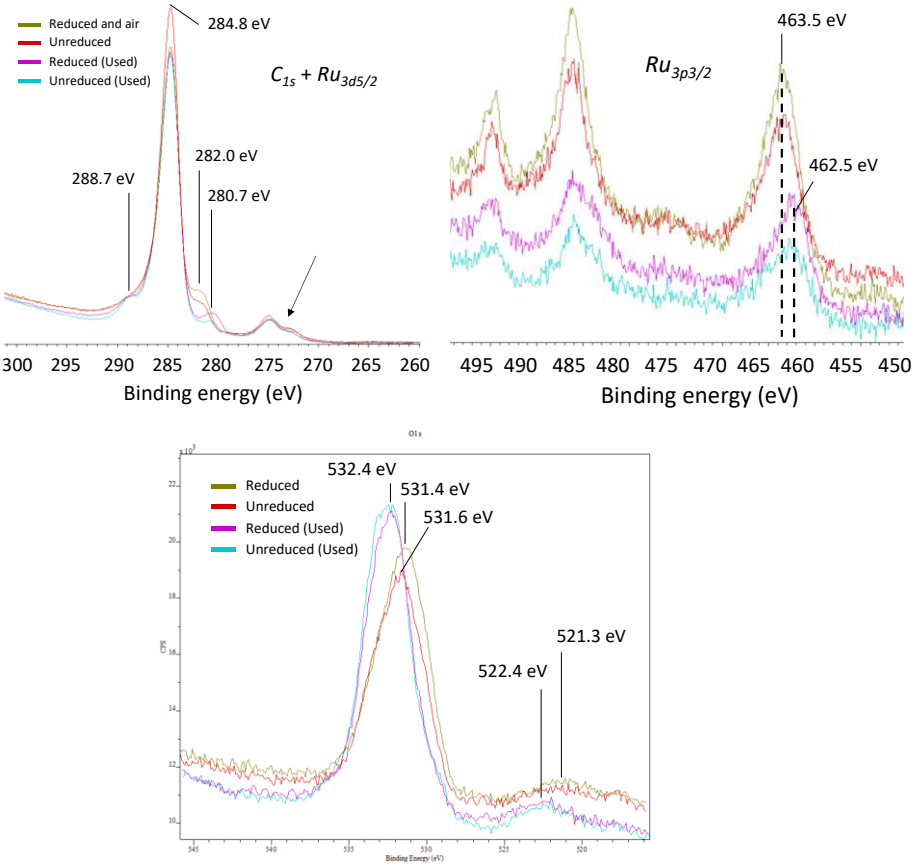

Figure 6A-15 X-ray photoelectron spectroscopy (XPS) comparison of red–Ru/C exposed to air and oxRu/C, both in fresh and used forms from gas-phase flow reactions. Spectra are shown for Ru3d$_{5/2}$ (top left), Ru3p$_{3/2}$ (top right), and O 1s regions (bottom) .

p) 6A-16

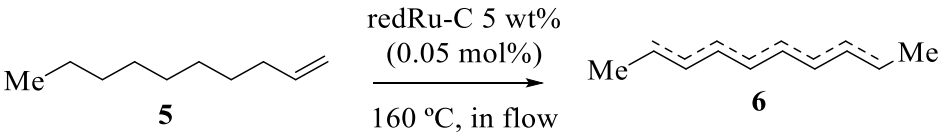

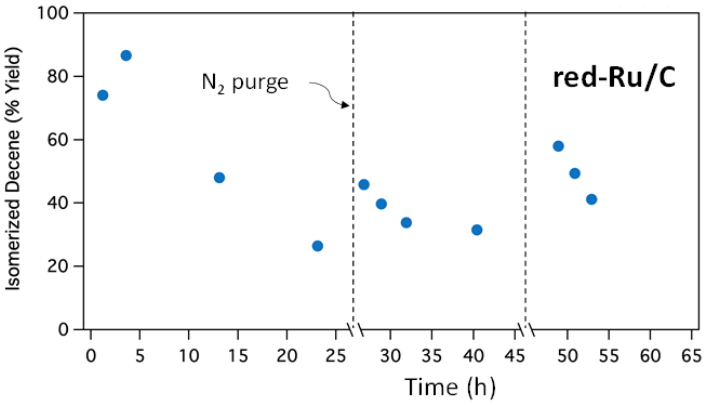

Figure 6A-16 Kinetic results for the isomerisation of 1-decene **5** to the corresponding internal alkenes **6** in the gas phase under the indicated reaction conditions, catalyzed by redRu/C. Discontinuous lines indicate the stopping of the reaction and the N_2 purge.

r) 6A-17

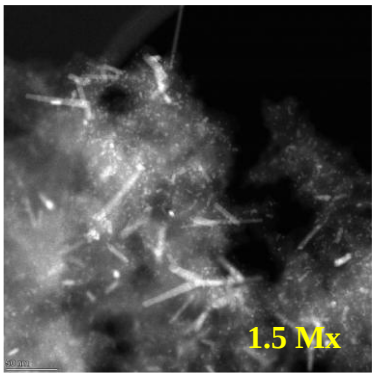

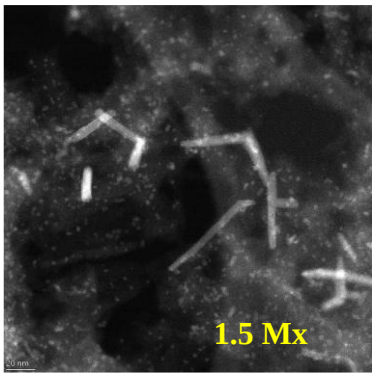

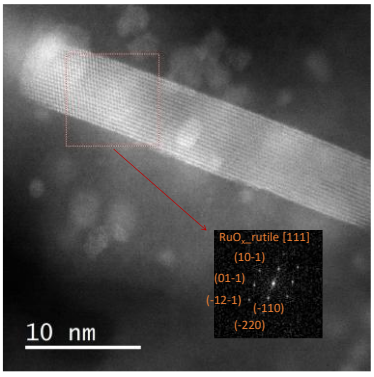

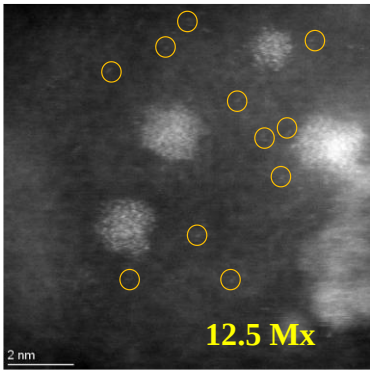

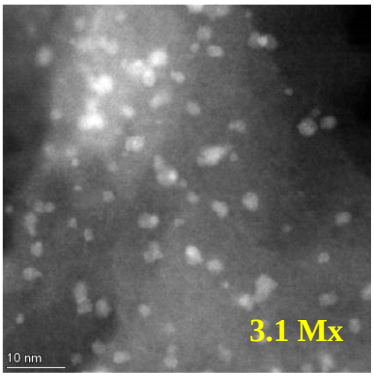

Total particles: 153
Dispersion: 43.9%
Average diameter: 2.05 ± 0.09 nm

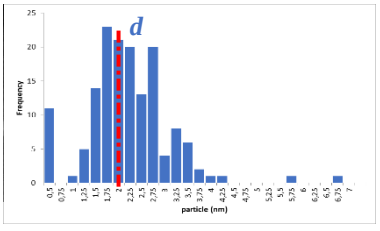

Figure 6A-17 HAADF-STEM images of the oxRu-C sample after reaction with increasing magnifications: 1.5 to 12.5 Mx (top, middle and bottom left). The corresponding EDX analysis shows the presence of rutile RuO_x nanoparticles (middle left). Single Ru atoms are circled in yellow. Size analysis and histogram of representative microimages are also shown (bottom right).

s) 6A-18

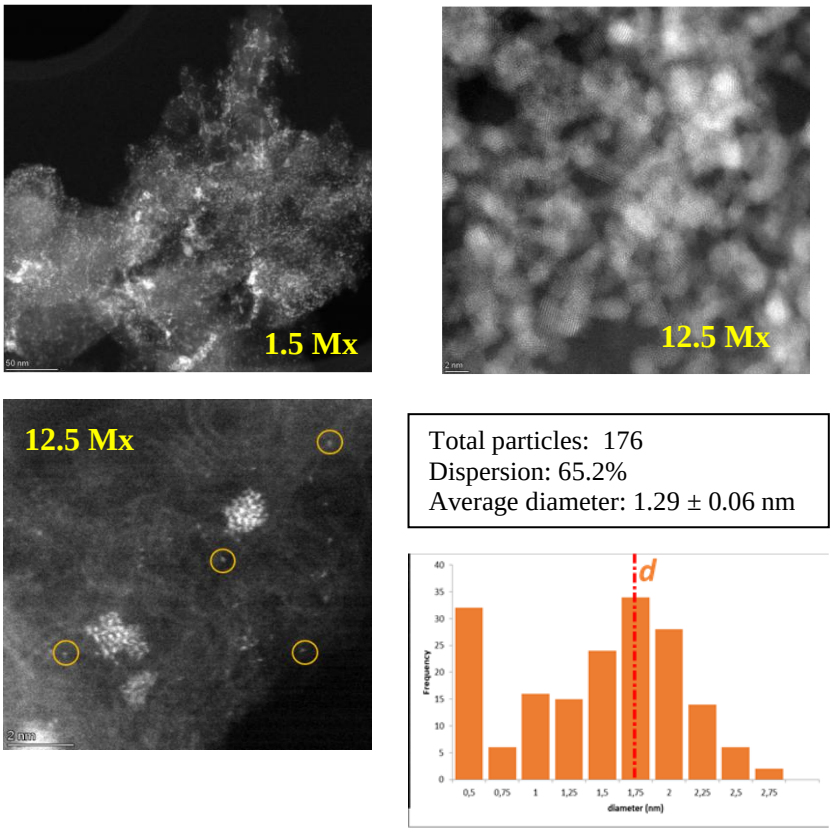

Figure 6A-18 HAADF-STEM images of the redRu-C sample after reaction with increasing magnifications: 1.5 to 12.5 Mx (top and bottom left). Single Ru atoms are circled in yellow. Size analysis and histogram of representative microimages are also shown (bottom right).

t) 6A-19

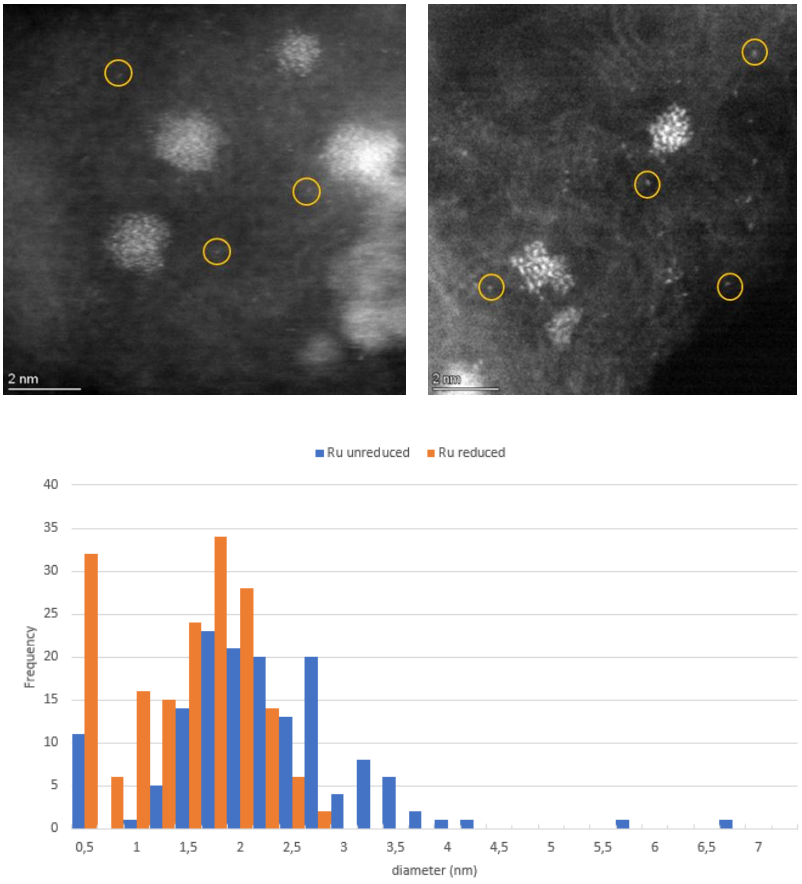

Figure 6A-19 Comparison of representative AC-HAADF–STEM images of redRu-C (top left) and oxRu-C (top right) after the isomerisation of 1-decene **5** to the corresponding internal alkenes **6** in the gas phase, in flow, and comparative histograms of the Ru-C catalysts after reaction. Single Ru atoms are circled in orange (circles are used as a guide to the eye).

u) 6A-20

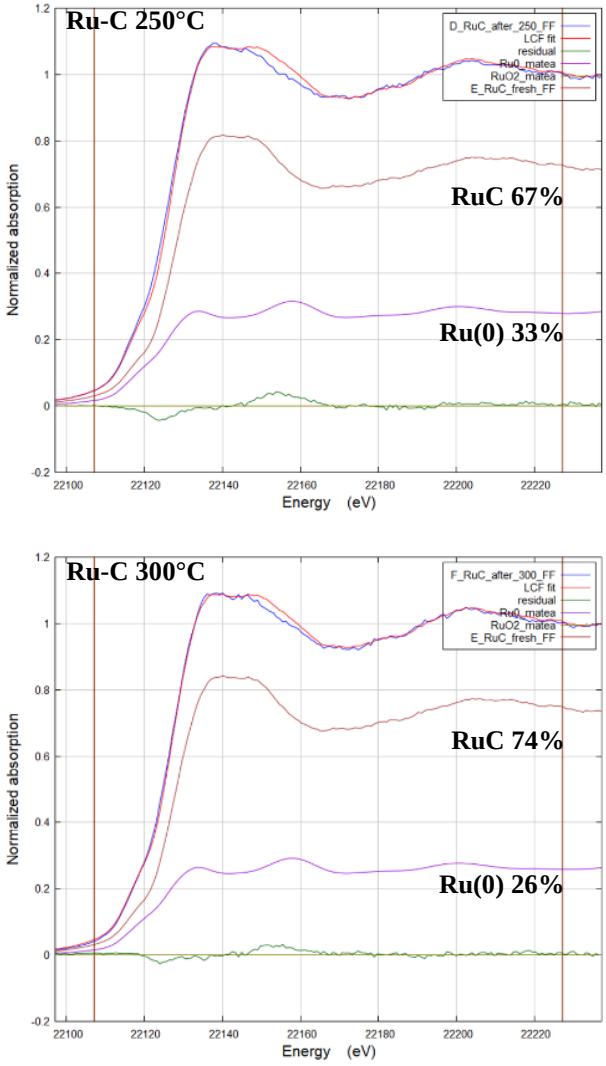

Figure 6A-20 Normalised X-ray absorption near-edge structure (XANES) spectrum for the fresh and used oxRu-C catalysts at different reaction temperatures, at the Ru K-edge, compared to RuO_2 and metallic Ru as references.

v) 6A-21

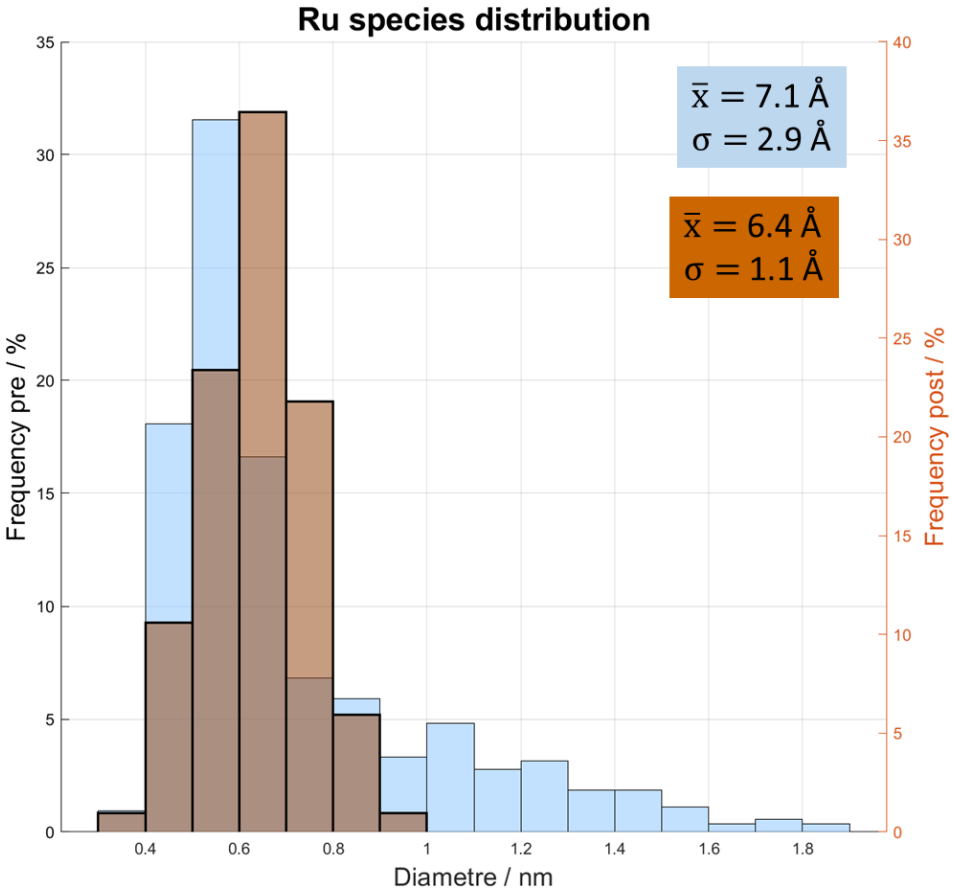

Figure 6A-21 Comparison of the Ru particle size distribution in Ru-HZSM-5 before (blue) and after (brown) the in-flow reaction.

w) 6A-22

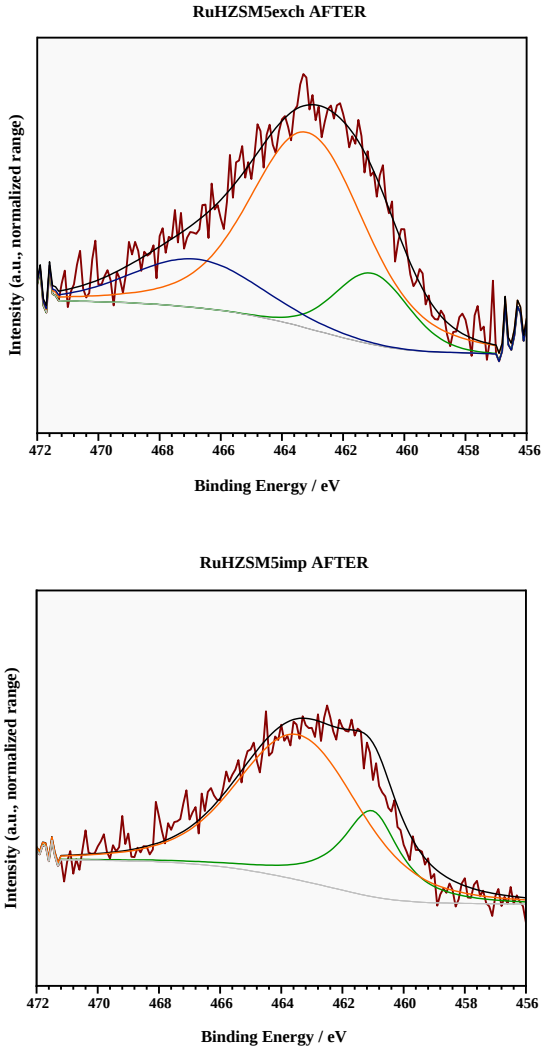

Figure 6A-22 X–ray photoelectron spectroscopy (XPS) spectra of the Ru $3p_{3/2}$ region for the exchanged (left) and impregnated (right) Ru-HZSM-5 catalyst after the in-flow reaction.

x) 6A-23

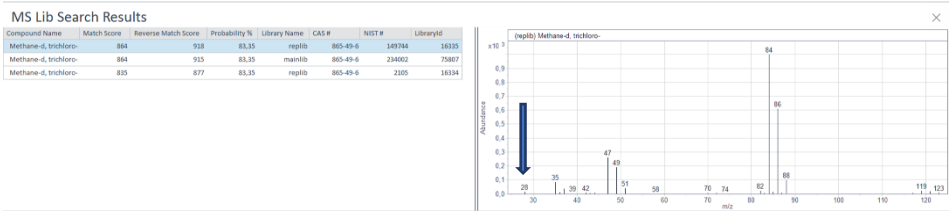

Figure 6A-23 GC-MS spectrum of the post-reaction organic extract (in $CDCl_3$) of 1-heptene with Ru-HZSM-5, showing a peak at m/z = 28 corresponding to ethylene.

y) 6A-24

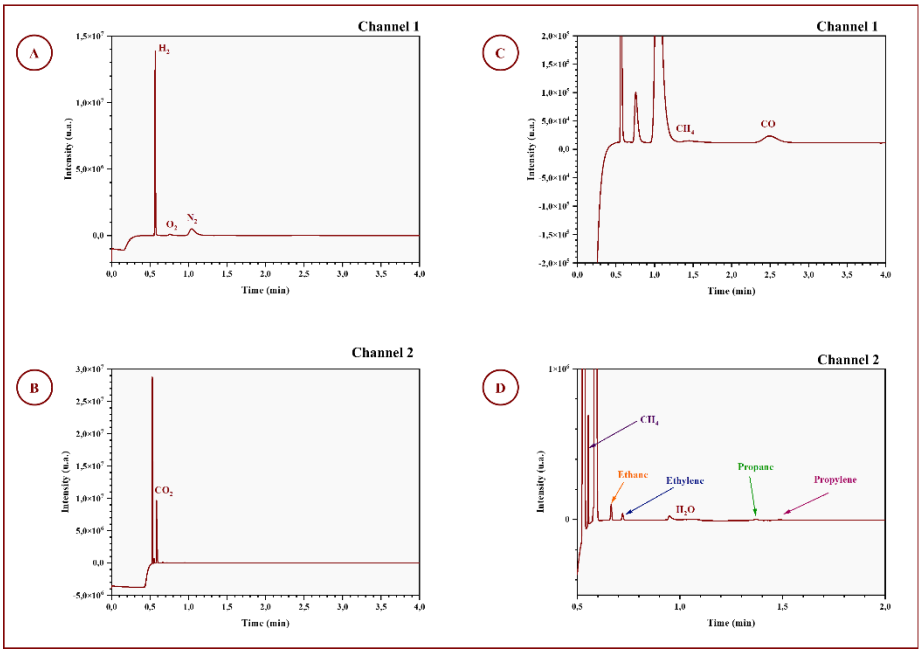

Figure 6A-24 Effect of CO_2 co-feeding on the product distribution during the 1-heptene **9** transformation over Ru-HZSM-5. GC analysis of gas- and hydrocarbon-phase products with and without CO_2 co-feed. Channel 1 (A, B) monitors permanent gases (H_2, N_2, O_2, CO_2), while Channel 2 detects hydrocarbon species.(C, D) Enlarged views of selected regions from (A) and (B), respectively, highlighting changes in hydrocarbon distribution under CO_2 co-feeding.

z) 6A-25

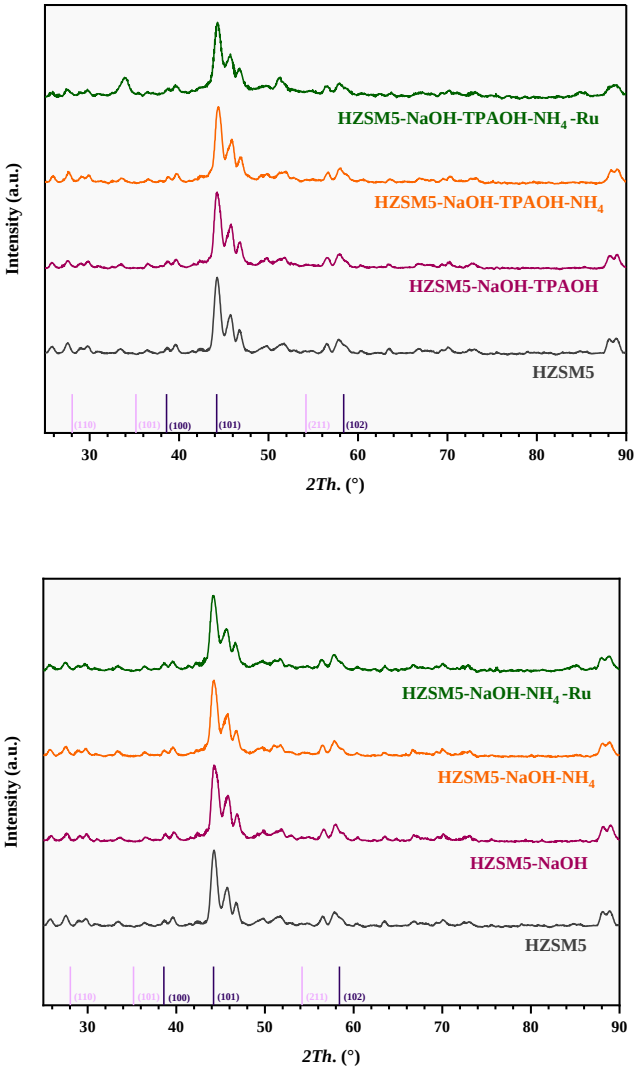

Figure 6A-25 Powder X-ray diffraction (PXRD) patterns of the MFI zeolites after desilication with NaOH and NaOH–TPAOH treatments.

6.6. References

1. Fan HX, Rajendran A, Li WY. *Ethylbenzene Dehydrogenation to Styrene*. Vol 3.; 2023. doi:10.1002/9783527827992.ch42

2. Wang D, Izawa Y, Stahl SS. Pd-catalyzed aerobic oxidative coupling of arenes: Evidence for transmetalation between two Pd(II)-aryl intermediates. *J Am Chem Soc*. 2014;136(28):9914-9917. doi:10.1021/ja505405u

3. Ames DEHJ, Chemical D, States U. Styrene. *Ind Org Chem Start Mater Intermed an Ullmann´s Encycl*. 1995;7:4417-4441. doi:10.1002/14356007.a25

4. Serna P, Corma A. Towards a zero-waste oxidative coupling of nonactivated aromatics by supported gold nanoparticles. *ChemSusChem*. 2014;7(8):2136-2139. doi:10.1002/cssc.201402061

5. Giakoumakis NS, Marquez C, de Oliveira-Silva R, Sakellariou D, De Vos DE. Upcycling of Polystyrene to Aromatic Polyacids by Tandem Friedel-Crafts and Oxidation Reactions. *J Am Chem Chen M, Ren S, Han D Recent Adv bimetallic small-pore zeolite Catal Ammon Sel Catal Reduct NO x Publ online 2025 doi1020517/cs202425al Soc*. 2024;146(50):34753-34762. doi:10.1021/jacs.4c13265

6. Jaiyeola A, Ako C. Aromatics Production By Paraffin Dehydrocyclization: Mechanism And The Kinetics Of nC 8 Dehydrocyclization Reaction On Acidic Pt/Al2O3 Catalyst. *West Indian J Eng*. 2008;30(2):24-35. https://sta.uwi.edu/eng/wije/vol3002_jan2008/documents/AromaticsProduction.pdf

7. Lee K, Choi M. Hierarchically micro-/mesoporous Pt/KL for alkane aromatization: Synergistic combination of high catalytic activity and suppressed hydrogenolysis. *J Catal*. 2016;340:66-75. doi:10.1016/j.jcat.2016.05.010

8. Dębek R, Radlik M, Motak M, et al. Ni-containing Ce-promoted hydrotalcite derived materials as catalysts for methane reforming with carbon dioxide at low temperature - On the effect of basicity. *Catal Today*. 2015;257(P1):59-65. doi:10.1016/j.cattod.2015.03.017

9. Dasireddy VDBC, Singh S, Friedrich HB. Oxidative dehydrogenation of n-octane using vanadium pentoxide-supported hydroxyapatite catalysts. *Appl Catal A Gen*. 2012;421-422:58-69. doi:10.1016/j.apcata.2012.01.034

10. Fadlalla MI, Friedrich HB. The effect of the oxidation environment on the activity and selectivity to aromatics and octenes over cobalt molybdate in the oxidative dehydrogenation of n-octane. *Catal Sci Technol*. 2014;4(12):4378-4385. doi:DOI https://doi.org/10.1039/C4CY00812J

11. Long H, Wang X, Sun W. Study of n-octene aromatization over nanoscale HZSM-5 zeolite. *Microporous Mesoporous Mater*. 2009;119(1-3):18-22. doi:10.1016/j.micromeso.2008.09.032

12. Amsley-Benzie S, Fegade S, Tande B, Kubátová A, Kozliak E, Seames W. An Initial Study of the Catalytic Reforming of Crop Oil-Derived 1-Alkenes with HZSM-5 to Aromatic Hydrocarbons. *JAOCS, J Am Oil Chem Soc*. 2018;95(9):1201-1211. doi:10.1002/aocs.12125

13. Lin W, Song Y, Han L, Yang X, Liu J, Peng B. Dehydrogenative aromatization of 1-octene over multifunctional Ni/ZSM-5-P-Fe catalyst. *Fuel*. 2021;299(February):120890. doi:10.1016/j.fuel.2021.120890

14. Oeffelen RCBBJLPJSSAG Van. US6509180B1 - Process for producing ethanol - Google Patents. https://patents.google.com/patent/US6509180B1/en

15. Mougel V, Chan KW, Siddiqi G, et al. Low temperature activation of supported metathesis catalysts by organosilicon reducing agents. *ACS Cent Sci*. 2016;2(8):569-576. doi:10.1021/acscentsci.6b00176

16. Narayanappa M, Dasireddy VDBC, Friedrich HB. Catalytic oxidation of n-octane over cobalt substituted ceria (Ce 0.90Co0.10O2-δ) catalysts. *Appl Catal A Gen*. 2012;447-448:135-143. doi:10.1016/j.apcata.2012.09.013

17. Sanz-Navarro S, Ballesteros-Soberanas J, Martínez-Castelló A, et al. Evidence for Ruthenium(II) Peralkene Complexes as Catalytic Species during the Isomerization of Terminal Alkenes in Solution. *Inorg Chem*. 2023;62(28):10984-10992. doi:10.1021/acs.inorgchem.3c00967

18. Sanz-Navarro S, Mon M, Doménech-Carbó A, et al. Parts–per–million of ruthenium catalyze the selective chain–walking reaction of terminal alkenes. *Nat Commun*. 2022;13(1):1-9. doi:10.1038/s41467-022-30320-9

19. Conejero Marta MonPérez Antonio LeyvaMeseguer Judit Oliver. ES2929364A1 - PROCEDURE FOR OBTAINING LONG-CHAIN LINEAR ALKENES - Google Patents.

20. Webber MS, Watson J, Zhu J, et al. Lignin deoxygenation for the production of sustainable aviation fuel blendstocks. *Nat Mater*. 2024;23(12):1622-1638. doi:10.1038/s41563-024-02024-6

21. Paul N Rylander JGK. US3150192A - Hydrogenation of aldehydes using ruthenium catalyst - Google Patents.

22. Klinkenberg JL, Lawry KP. Sterically Encumbered and Poorly Electron-Donating Oxaphosphaadamantane Ligands for the Pd-Catalyzed Telomerization of Butadiene with Methanol. *Org Process Res Dev*. 2019;23(8):1654-1658. doi:10.1021/acs.oprd.9b00018

23. Yadav G, Singh A, Dutta A, et al. Techno-economic analysis and life cycle assessment for catalytic fast pyrolysis of mixed plastic waste. *Energy Environ Sci*. 2023;16(9):3638-3653. doi:10.1039/d3ee00749a

24. Windels S, Seynaeve N, Stuyck W, De Vos DE. Catalytic revalorization of plastic

waste phthalate plasticizers into simple aromatics and alkenes. *Front Chem Eng*. 2024;6(September):1-9. doi:10.3389/fceng.2024.1463638

25. Matsuura R, Karunananda MK, Liu M, Nguyen N, Blackmond DG, Engle KM. Mechanistic Studies of Pd(II)-Catalyzed E/ Z Isomerization of Unactivated Alkenes: Evidence for a Monometallic Nucleopalladation Pathway. *ACS Catal*. 2021;11(7):4239-4246. doi:10.1021/acscatal.1c00783

26. Musolino MG, De Maio P, Donato A, Pietropaolo R. Hydrogenation versus isomerization in α,β-unsaturated alcohols reactions over Pd/TiO2 catalysts. *J Mol Catal A Chem*. 2004;208(1-2):219-224. doi:10.1016/j.molcata.2003.07.008

27. Al-Amin M, Roth KE, Blum SA. Mechanistic studies of gold and palladium cooperative dual-catalytic cross-coupling systems. *ACS Catal*. 2014;4(2):622-629. doi:10.1021/cs400641k

28. McEwan L, Julius M, Roberts S, Fletcher JCQ. A review of the use of gold catalysts in selective hydrogenation reactions. *Gold Bull*. 2010;43(4):298-306. doi:10.1007/bf03214999

29. Ku YP, Kumar K, Hutzler A, et al. Impact of Carbon Corrosion and Denitrogenation on the Deactivation of Fe-N-C Catalysts in Alkaline Media. *ACS Catal* . 2024;14(11):8576-8591. doi:10.1021/acscatal.4c01219

30. Wedal JC, Virtue KB, Bernskoetter WH, Hazari N, Mercado BQ. Iron Catalysts Supported by a PNP Ligand with an Additional Hemilabile Donor for CO2 Hydrogenation. *ACS Catal*. Published online 2024:13903-13914. doi:10.1021/acscatal.4c04127

31. Gorgas N, Kirchner K. Isoelectronic Manganese and Iron Hydrogenation/Dehydrogenation Catalysts: Similarities and Divergences. *Acc Chem Res*. 2018;51(6):1558-1569. doi:10.1021/acs.accounts.8b00149

32. Woof CR, Durand DJ, Fey N, Richards E, Webster RL. Iron Catalyzed Double

Bond Isomerization: Evidence for an FeI/FeIII Catalytic Cycle. *Chem - A Eur J*. 2021;27(19):5972-5977. doi:10.1002/chem.202004980

33. Geng L, Gong J, Qiao G, et al. Effect of metal precursors on the performance of Pt/SAPO-11 catalysts for n-dodecane hydroisomerization. *ACS Omega*. 2019;4(7):12598-12605. doi:10.1021/acsomega.9b01216

34. Chianese AR, Lee SJ, Gagné MR. Electrophilic activation of alkenes by platinum(II): So much more than a slow version of palladium(II). *Angew Chemie - Int Ed*. 2007;46(22):4042-4059. doi:10.1002/anie.200603954

35. Chang ASM, Kascoutas MA, Valentine QP, How KI, Thomas RM, Cook AK. Alkene Isomerization Using a Heterogeneous Nickel-Hydride Catalyst. *J Am Chem Soc*. 2024;146(22):15596-15608. doi:10.1021/jacs.4c04719

36. Okumura M, Nakamura S, Tsubota S, Toshiko N, Azuma M, Haruta M. Chemical vapor deposition of gold on Al_2O_3,SiO_2,and TiO_2 for the oxidation of CO and of H_2. *Catal Letters*. 1998;51(1-2):53-58. http://www.journal.csj.jp/doi/10.1246/cl.1998.315

37. Hammer B, Norskov JK. Why gold is the noblest of all the metals. *Nature*. 1995;376(6537):238-240. doi:10.1038/376238a0

38. Lastra-Barreira B, Francos J, Crochet P, Cadierno V. Ruthenium(IV) catalysts for the selective estragole to trans-anethole isomerization in environmentally friendly media. *Green Chem*. 2011;13(2):307-313. doi:10.1039/c0gc00417k

39. Manzini S, Poater A, Nelson DJ, Cavallo L, Nolan SP. How phenyl makes a difference: Mechanistic insights into the ruthenium(ii)-catalysed isomerisation of allylic alcohols. *Chem Sci*. 2014;5(1):180-188. doi:10.1039/c3sc52612g

40. Sarma BB, Kim J, Amsler J, et al. One-Pot Cooperation of Single-Atom Rh and Ru Solid Catalysts for a Selective Tandem Olefin Isomerization-Hydrosilylation Process. *Angew Chemie - Int Ed*. 2020;59(14):5806-5815.

doi:10.1002/anie.201915255

41. Kočí P, Bártová Š, Mráček D, et al. Effective model for prediction of N2O and NH3 formation during the regeneration of NO x storage catalyst. *Top Catal*. 2013;56(1-8):118-124. doi:10.1007/s11244-013-9939-y

42. Platinum_Ruthenium Price Today _ Platinum_Ruthenium Spot Price Chart _ Historical Price of Platinum_Ruthenium - Shanghai Metal Market.

43. Zhao H, Li J, Zou J, et al. Fine-tuning surface oxidation states of ruthenium nanoparticles to enhance hydrogen electrode reactions. *J Mater Chem A*. 2023;11(34):18262-18271. doi:10.1039/D3TA02313C

44. Gimferrer M, Salvador P, Poater A. Computational Monitoring of Oxidation States in Olefin Metathesis. *Organometallics*. 2019;38(24):4585-4592. doi:10.1021/acs.organomet.9b00591

45. Duan L, Araujo CM, Ahlquist MSG, Sun L. Highly efficient and robust molecular ruthenium catalysts for water oxidation. *Proc Natl Acad Sci U S A*. 2012;109(39):15584-15588. doi:10.1073/pnas.1118347109

46. Yin SF, Xu BQ, Zhu WX, Ng CF, Zhou XP, Au CT. Carbon nanotubes-supported Ru catalyst for the generation of CO x-free hydrogen from ammonia. *Catal Today*. 2004;93-95:27-38. doi:10.1016/j.cattod.2004.05.011

47. Wang Y, Wildfire C, Khan TS, et al. Effects of support and promoter on Ru catalyst activity in microwave-assisted ammonia synthesis. *Chem Eng J*. 2021;425(March):1-11. doi:10.1016/j.cej.2021.130546

48. Peng S, Pan B, Hao H, Zhang J. Hollow Mesoporous Silica Supported Ruthenium Nanoparticles: A Highly Active and Reusable Catalyst for H2 Generation from the Hydrolysis of NaBH4. *J Nanomater*. 2015;2015(C). doi:10.1155/2015/249180

49. Zhang Y, Judkins EC, McMillin DR, Mehta D, Ren T. Mesoporous silica-supported ruthenium oxide nanoparticulates as efficient catalysts for photoinduced water oxidation. *ACS Catal*. 2013;3(11):2474-2478. doi:10.1021/cs4006106

50. Araujo-Barahona G, Shcherban N, Eränen K, et al. Ruthenium supported on silicate and aluminosilicate mesoporous materials applied to selective sugar hydrogenation: Xylose to xylitol. *Chem Eng J*. 2024;485(February). doi:10.1016/j.cej.2024.150019

51. Maina SCP, Vilella IMJ, Ballarini AD, de Miguel SR. Performance of Modified Alumina-Supported Ruthenium Catalysts in the Reforming of Methane with CO2. *Catalysts*. 2023;13(2). doi:10.3390/catal13020338

52. Betancourt P, Rives A, Hubaut R, Scott CE, Goldwasser J. A study of the ruthenium-alumina system. *Appl Catal A Gen*. 1998;170(2):307-314. doi:10.1016/S0926-860X(98)00061-1

53. Khalil I, Rigamonti MG, Janssens K, et al. Atomically dispersed ruthenium hydride on beta zeolite as catalysts for the isomerization of muconates. *Nat Catal*. 2024;7(8):921-933. doi:10.1038/s41929-024-01205-5

54. Garnes-Portolés F, Greco R, Oliver-Meseguer J, et al. Regioirregular and catalytic Mizoroki–Heck reactions. *Nat Catal*. 2021;4(4):293-303. doi:10.1038/s41929-021-00592-3

55. Solymosi F, Pásztor M. An infrared study of the influence of CO chemisorption on the topology of supported rhodium. *J Phys Chem*. 1985;89(22):4789-4793. doi:10.1021/j100268a026

56. Jiao D, Wang Y, Zhang Z, Zhang J, Lei L, Wang F. Catalysis of Positively Charged Ru Species Stabilized by Hydroxyapatite in Amine Formylation. *ChemCatChem*. 2021;13(19):4159-4163. doi:10.1002/cctc.202100937

57. Turnell-Ritson RC, Frederiksen LEK, Romano-DeGea J, et al. Single-site ruthenium catalyst supported on zeolite for CO2 hydrogenation to methyl formate. *Sci Adv* . 2025;11(16). doi:10.1126/sciadv.adu2857

58. Petcuta OA, Guzo NC, Bordeiasu M, Nicolaev A, Parvulescu VI, Coman SM. Ru/Beta Zeolite Catalysts for Levulinic Acid Hydrogenation: The Importance of Catalyst Synthesis Methodology. *Catalysts*. 2025;15(1). doi:10.3390/catal15010080

59. Ogino I, Gates BC. Molecular chemistry in a zeolite: Genesis of a zeolite y-supported ruthenium complex catalyst. *J Am Chem Soc*. 2008;130(40):13338-13346. doi:10.1021/ja804265r

60. Cheng K, Kang J, Huang S, et al. Mesoporous beta zeolite-supported ruthenium nanoparticles for selective conversion of synthesis gas to C 5-C 11 isoparaffins. *ACS Catal*. 2012;2(3):441-449. doi:10.1021/cs200670j

61. Kato K, Fa S, Ohtani S, Shi T, Brouwer AM, Ogoshi T. Noncovalently bound and mechanically interlocked systems using pillar[n]arenes. *Chem Soc Rev*. 2022;51(9):3648-3687. doi:10.1039/D2CS00169A

62. Lang Q, Lu P, Yang X, Valtchev V. Zeolites for the environment. *Green Carbon*. 2024;2(1):12-32. doi:10.1016/j.greenca.2024.02.007

63. Chica A. Zeolites: Promised Materials for the Sustainable Production of Hydrogen. *ISRN Chem Eng*. 2013;2013(1):1-19. doi:10.1155/2013/907425

64. Ho PH, Yao D, Creaser D, Olsson L. Advantages of High-Siliceous Zeolites in the Reactivity and Stability of Diesel Oxidation Catalysts. *ACS Eng Au*. 2022;2(3):219-235. doi:10.1021/acsengineeringau.1c00035

65. Zheng Y, Vidal-Moya A, Hernández-Garrido JC, Mon M, Leyva-Pérez A. Silver-Exchanged Zeolite Y Catalyzes a Selective Insertion of Carbenes into C-H and O-H Bonds. *J Am Chem Soc*. Published online 2023. doi:10.1021/jacs.3c08317

66. Zheng Y, Espinosa M, Mon M, Leyva–Pérez A. Dealuminated H–Y zeolites generate, stabilize and catalytically insert carbenes from diazocarbonyl compounds. *J Catal*. 2024;440(July). doi:10.1016/j.jcat.2024.115835

67. Oliver-Meseguer J, Leyva-Pérez A. Counterbalancing Cations in Ru(III)-Zeolites to Fine-Tune the Catalytic Activity during the Dehydrogenative Aerobic Imination of Benzyl Alcohols. *ACS Sustain Chem Eng*. 2025;(Iii). doi:10.1021/acssuschemeng.5c01742

68. Otani A, Kuroda M, Suganuma S, Tsuji E, Katada N. MFI zeolite-supported Ru nanoparticles for efficient conversion of pyroglutamic acid to 2-pyrrolidone. *React Chem Eng*. 2021;6(10):1920-1927. doi:10.1039/D1RE00186H

69. Chen M, Ren S, Han D. Recent advances in bimetallic small-pore zeolite catalysts for ammonia-assisted selective catalytic reduction of NO x. *Chem Synth*. 2025;5:33. doi:10.20517/cs.2024.25

70. Deng C, Zhang J, Dong L, et al. The effect of positioning cations on acidity and stability of the framework structure of y zeolite. *Sci Rep*. 2016;6(March):1-13. doi:10.1038/srep23382

71. Yu J, Wang K, Shao S, et al. Effect of ionic radius and valence state of alkali and alkaline earth metals on promoting the catalytic performance of La2O3 catalysts for glycerol carbonate production. *Chem Eng J*. 2023;458(January):141486. doi:10.1016/j.cej.2023.141486

72. Liutkova A, Zhang H, Simons JFM, et al. Ca Cations Impact the Local Environment inside HZSM-5 Pores during the Methanol-to-Hydrocarbons Reaction. *ACS Catal*. 2023;13(6):3471-3484. doi:10.1021/acscatal.3c00059

73. Ge S, Hu Z, Xie H, Gao S, Zhang Z, Wu Z. Shape selection of alkane hydroisomerization over one-dimensional zeolite supported Pt catalyst: Pt/ZSM-48 versus Pt/ZSM-22. *Microporous Mesoporous Mater*.

2024;376(March):113179. doi:10.1016/j.micromeso.2024.113179

74. Wang L, Liu J, Lin C, et al. Effects of different alkali metal cations in FAU zeolites on the separation performance of CO2/N2O. *Chem Eng J*. 2022;431(P3):134257. doi:10.1016/j.cej.2021.134257

75. Zhang L, Zhang H, Chen Z, et al. Insight into the impact of Al distribution on the catalytic performance of 1-octene aromatization over ZSM-5 zeolite. *Catal Sci Technol*. 2019;9(24):7034-7044. doi:10.1039/C9CY01672D

76. De Lucas A, Sánchez P, Fúnez A, Ramos MJ, Valverde JL. Liquid-phase hydroisomerization of n-octane over platinum-containing zeolite-based catalysts with and without binder. *Ind Eng Chem Res*. 2006;45(26):8852-8859. doi:10.1021/ie060388s

77. Rorrer JE, Ebrahim AM, Questell-Santiago Y, et al. Role of Bifunctional Ru/Acid Catalysts in the Selective Hydrocracking of Polyethylene and Polypropylene Waste to Liquid Hydrocarbons. *ACS Catal*. 2022;12(22):13969-13979. doi:10.1021/acscatal.2c03596

78. Meng B, Ren S, Zhang X, et al. Enhancement of the strong Brønsted acidity and mesoporosity: Zr4+ promoted framework modification of Zeolite Y. *Microporous Mesoporous Mater*. 2022;335(December 2021):111849. doi:10.1016/j.micromeso.2022.111849

79. Kumar A, Kumar A, Santosa DM, et al. Engineered Ru on HY zeolite catalyst for continuous and selective hydrodeoxygenation of lignin phenolics to cycloalkanes under moderate conditions. *Appl Catal A Gen*. 2024;676(February):119649. doi:10.1016/j.apcata.2024.119649

80. Zhang L, Liu N, Dai C, et al. Recent advances in shape selectivity of MFI zeolite and its effect on the catalytic performance. *Chem Synth*. 2023;3(1):1-26. doi:10.20517/cs.2022.31

81. Corma A. From Microporous to Mesoporous Molecular Sieve Materials and Their Use in Catalysis. *Chem Rev*. 1997;97(6):2373-2419.

82. Kattel S, Ramírez PJ, Chen JG, Rodriguez JA, Liu P. Active sites for CO 2 hydrogenation to methanol on Cu/ZnO catalysts Downloaded from. *Science (80-).* 2017;355(March):24. http://science.sciencemag.org/

83. Biesinger MC. Advanced analysis of copper X-ray photoelectron spectra. *Surf Interface Anal*. 2017;49(13):1325-1334. doi:10.1002/sia.6239

84. Deng X, Petitjean M, MA T, et al. Similarities and differences in the biochemical and enzymological properties of the four isomaltases from Saccharomyces cerevisiae. *FEBS Open Bio*. 2014;4:200-212. doi:10.1016/j.fob.2014.02.004

85. Morgan DJ. Resolving ruthenium : XPS studies of common ruthenium materials. 2015;(August):1072-1079. doi:10.1002/sia.5852

86. Treacy MMJ. *Collection of Simulated XRD Powder Patterns for Zeolites Editors*. (Treacy MMJ, Higgins JB, eds.). Elsevier; 2001.

87. O.U. Valdés-Martínez;, C. E. Santolalla-Vargas;, Santes V, J. A. de los Reyes, Pawelec B, J.L.G. Fierro. Influence of calcination on metallic dispersion and support interactions for NiRu / TiO 2 catalyst in the hydrodeoxygenation of phenol. *Catal Today*. 2019;329:149-155. doi:10.1016/j.cattod.2018.11.007

88. Quindimil A, De-la-torre U, Pereda-ayo B, Davó-quiñonero A. E ff ect of metal loading on the CO 2 methanation : A comparison between alumina supported Ni and Ru catalysts. 2020;356(January 2019):419-432. doi:10.1016/j.cattod.2019.06.027

89. Fechete I, Wang Y, Védrine JC. The past , present and future of heterogeneous catalysis. *Catal Today*. 2012;189(1):2-27. doi:10.1016/j.cattod.2012.04.003

90. Vaher M, Helmja K, Käsper A, Kuraˇ M, Väljamäe P, Kudrjaˇ M. Capillary

electrophoretic monitoring of hydrothermal pre-treatment and enzymatic hydrolysis of willow : Comparison with HPLC and NMR. *Catal Today*. 2012;196:34-41. doi:10.1016/j.cattod.2012.02.047

91. Imran M, Assiri MA. Toxicological evaluation of bisphenol analogues : preventive measures and therapeutic interventions. Published online 2023:21613-21628. doi:10.1039/d3ra04285e

92. Guisnet M, Magnoux P. Organic chemistry of coke formation. *Appl Catal A Gen*. 2001;212:83-96. doi:https://doi.org/10.1016/S0926-860X(00)00845-0

93. Zhou J, Zhao J, Zhang J, Zhang T, Ye M, Liu Z. Regeneration of catalysts deactivated by coke deposition : A review. *Chinese J Catal*. 2020;41(7):1048-1061. doi:10.1016/S1872-2067(20)63552-5

94. Qin L, Li J, Zhang S, Liu Z, Li S, Luo L. Catalytic performance of Ni – Co / HZSM-5 catalysts. Published online 2023:7694-7702. doi:10.1039/d2ra07706j

95. Xu Y, Wang J, Suzuki Y, Zhang Z. Applied Catalysis A : General Effect of transition metal additives on the catalytic stability of Mo / HZSM-5 in the methane dehydroaromatization under periodic CH 4 – H 2 switch operation at 1073 K. *"Applied Catal A, Gen*. 2011;409-410:181-193. doi:10.1016/j.apcata.2011.10.003

96. US6900151B2 - In situ catalyst regeneration_activation process - Google Patents.

97. Rorrer JE, Beckham GT, Roma Y. Conversion of Polyole fi n Waste to Liquid Alkanes with Ru-Based Catalysts under Mild Conditions´. *JACS Au*. Published online 2021:8-12. doi:10.1021/jacsau.0c00041

98. Bligaard T, Nørskov JK, Dahl S, Matthiesen J, Christensen CH, Sehested J. The Brønsted–Evans–Polanyi relation and the volcano curve in heterogeneous catalysis. *J Catal*. 2004;224(1):206-217. doi:https://doi.org/10.1016/j.jcat.2004.02.034

99. Devaraj A, Vijayakumar M, Bao J, Guo MF, Derewinski MA. Discerning the Location and Nature of Coke Deposition from Surface to Bulk of Spent Zeolite Catalysts. *Nat Publ Gr*. 2016;(October):1-11. doi:10.1038/srep37586

100. Nazarova GY, Ivashkina EN, Ivanchina ED, Mezhova MY. A Model of Catalytic Cracking : Catalyst Deactivation Induced by Feedstock and Process Variables. *Catalysts*. 2022;12(98). doi:https:// doi.org/10.3390/catal12010098

101. Bresó-Femenia E, Chaudret B, Castillón S. Selective catalytic hydrogenation of polycyclic aromatic hydrocarbons promoted by ruthenium nanoparticles. *Catal Sci Technol*. 2015;5(5):2741-2751. doi:10.1039/C4CY01758G

102. Engel J, Smit W, Foscato M, Occhipinti G, Törnroos KW, Jensen VR. Loss and Reformation of Ruthenium Alkylidene: Connecting Olefin Metathesis, Catalyst Deactivation, Regeneration, and Isomerization. *J Am Chem Soc*. 2017;139(46):16609-16619. doi:10.1021/jacs.7b07694

103. Liu X, An W, Turner CH, Resasco DE. Hydrodeoxygenation of m-cresol over bimetallic NiFe alloys: Kinetics and thermodynamics insight into reaction mechanism. *J Catal*. 2018;359:272-286. doi:10.1016/j.jcat.2018.01.006

104. del Campo P, Martínez C, Corma A. Activation and conversion of alkanes in the confined space of zeolite-type materials. *Chem Soc Rev*. 2021;50(15):8511-8595. doi:10.1039/D0CS01459A

105. Pastrana-Martínez LM, Morales-Torres S, Maldonado-Hódar FJ. A Comparative Study of Aromatization Catalysts: The Advantage of Hybrid Oxy/Carbides and Platinum-Catalysts Based on Carbon Gels. *C*. 2021;7(1):21. doi:10.3390/c7010021

106. Zhang Y, Yang Y, Hou Q, et al. Metal–Acid Bifunctional Catalysts toward Tandem Reaction: One-Step Hydroalkylation of Benzene to Cyclohexylbenzene. *ACS Appl Mater Interfaces*. 2022;14(28):31998-32008.

doi:10.1021/acsami.2c07074

107. Bukhtiyarova M V, Nuzhdin AL, Bukhtiyarova GA. Comparative Study of Batch and Continuous Flow Reactors in Selective Hydrogenation of Functional Groups in Organic Compounds: What Is More Effective? *Int J Mol Sci*. 2023;24(18). doi:10.3390/ijms241814136

108. Zhang L, Liu H, Li X, et al. Differences between ZSM-5 and ZSM-11 zeolite catalysts in 1-hexene aromatization and isomerization. *Fuel Process Technol*. 2010;91(5):449-455. doi:https://doi.org/10.1016/j.fuproc.2009.12.003

109. Meusinger J, Corma A. Activation of Hydrogen on Zeolites: Kinetics and Mechanism of n-Heptane Cracking on H-ZSM-5 Zeolites Under High Hydrogen Pressure. *J Catal*. 1995;152(1):189-197. doi:https://doi.org/10.1006/jcat.1995.1072

110. Reif P, Gupta NK, Rose M. Liquid phase aromatization of bio-based ketones over a stable solid acid catalyst under batch and continuous flow conditions. *Catal Commun*. 2022;163:106402. doi:https://doi.org/10.1016/j.catcom.2022.106402

111. Kumar A, Kumar A, Santosa DM, et al. Engineered Ru on HY zeolite catalyst for continuous and selective hydrodeoxygenation of lignin phenolics to cycloalkanes under moderate conditions. *Appl Catal A Gen*. 2024;676:119649. doi:https://doi.org/10.1016/j.apcata.2024.119649

112. Nandapurkar PJ, Ruckenstein E. Effect of dilution on the activity of diluted porous catalysts. *Chem Eng Sci*. 1984;39(2):371-380. doi:https://doi.org/10.1016/0009-2509(84)80035-4

113. Yang J, He Y, He J, et al. Enhanced Catalytic Performance through In Situ Encapsulation of Ultrafine Ru Clusters within a High-Aluminum Zeolite. *ACS Catal*. 2022;12(3):1847-1856. doi:10.1021/acscatal.1c05012

114. Zhou L, Lin W, Wang X, et al. Influence of Brønsted acid sites on the product

distribution in the hydrodeoxygenation of methyl laurate over supported Ru catalysts. *Catal Sci Technol*. 2022;12(8):2578-2588. doi:10.1039/D2CY00011C

115. Li A, Zhang Y, Heard CJ, et al. Encapsulating Metal Nanoparticles into a Layered Zeolite Precursor with Surface Silanol Nests Enhances Sintering Resistance. *Angew Chemie Int Ed*. 2023;62(1):e202213361. doi:https://doi.org/10.1002/anie.202213361

116. Liu M, Miao C, Wu Z. Recent advances in the synthesis, characterization, and catalytic consequence of metal species confined within zeolite for hydrogen-related reactions. *Ind Chem Mater*. 2024;2(1):57-84. doi:10.1039/d3im00074e

117. Liutkova A, Zhang H, Simons JFM, et al. Ca Cations Impact the Local Environment inside HZSM-5 Pores during the Methanol-to-Hydrocarbons Reaction. *ACS Catal*. 2023;13(6):3471-3484. doi:10.1021/acscatal.3c00059

118. Xu S, Dugkhuntod P, Ding S, et al. Product selectivity controlled by the nano-environment of Ru/ZSM-5 catalysts in nonthermal plasma catalytic CO2 hydrogenation. *Appl Catal B Environ Energy*. 2024;348:123826. doi:https://doi.org/10.1016/j.apcatb.2024.123826

119. de Lucas A, Sánchez P, Fúnez A, Ramos MJ, Valverde JL. Liquid-Phase Hydroisomerization of n-Octane over Platinum-Containing Zeolite-Based Catalysts with and without Binder. *Ind Eng Chem Res*. 2006;45(26):8852-8859. doi:10.1021/ie060388s

120. Meng B, Ren S, Zhang X, et al. Enhancement of the strong Brønsted acidity and mesoporosity: Zr4+ promoted framework modification of Zeolite Y. *Microporous Mesoporous Mater*. 2022;335:111849. doi:https://doi.org/10.1016/j.micromeso.2022.111849

121. Dong H, Zhang L, Fang Z, et al. Acidic hierarchical zeolite ZSM-5 supported Ru catalyst with high activity and selectivity in the seleno-functionalization of

alkenes. *RSC Adv*. 2017;7(36):22008-22016. doi:10.1039/c7ra01732d

122. Navarro de Miguel JC, Chung S-H, Dikhtiarenko A, Li T, Patarroyo J, Ruiz-Martínez J. Brønsted Acid-Site Density Controls the Mechanistic Cycle and Product Selectivity in the Methanol-to-Hydrocarbons Reaction in BEA Zeolite. *ACS Catal*. 2024;14(8):5989-6000. doi:10.1021/acscatal.3c06077

123. Li LL, Janik MJ, Nie XW, Song CS, Guo XW. Reaction mechanism of toluene methylation with dimethyl carbonate or methanol catalyzed by H-ZSM-5. *Wuli Huaxue Xuebao/ Acta Phys - Chim Sin*. 2013;29(7):1467-1478. doi:10.3866/PKU.WHXB201304262

124. Montalvo-Castro H, DeLuca M, Kilburn L, Hibbitts D. Mechanisms and Kinetics of the Dehydrogenation of C6–C8 Cycloalkanes, Cycloalkenes, and Cyclodienes to Aromatics in H-MFI Zeolite Framework. *ACS Catal*. 2023;13(1):99-112. doi:10.1021/acscatal.2c03360

125. Chen X, Chen Y, Song C, et al. Recent Advances in Supported Metal Catalysts and Oxide Catalysts for the Reverse Water-Gas Shift Reaction. *Front Chem*. 2020;8:709. doi:10.3389/fchem.2020.00709

126. Song Z, Wang X, Chen C, et al. Stability and kinetics study of direct CO2 hydrogenation to aromatics over Cu-Fe2O3/HZSM-5-P bifunctional catalysts. *Fuel*. 2025;389:134585. doi:https://doi.org/10.1016/j.fuel.2025.134585

127. Liu Y, Ma B, Tian J, Zhao C. Coupled conversion of polyethylene and carbon dioxide catalyzed by a zeolite-metal oxide system. *Sci Adv*. 2024;10(15):eadn0252. doi:10.1126/sciadv.adn0252

128. Kusmiyati K, Amin NAS, Siswanto WA. Highly Active W-H2SO4/HZSM-5 Catalyst for Direct Conversion of Methane into Aromatic. *Bull Chem React Eng Catal*. 2007;2(2-3):32-36. doi:10.9767/bcrec.2.2-3.7.32-36

129. Mahnaz F, Mangalindan JR, Dharmalingam BC, et al. Intermediate Transfer

Rates and Solid-State Ion Exchange are Key Factors Determining the Bifunctionality of In2O3/HZSM-5 Tandem CO2 Hydrogenation Catalyst. *ACS Sustain Chem Eng*. 2024;12(13):5197-5210. doi:10.1021/acssuschemeng.3c08250

130. Chaihad N, Situmorang YA, Anniwaer A, et al. Preparation of various hierarchical HZSM-5 based catalysts for in-situ fast upgrading of bio-oil. *Renew Energy*. 2021;169:283-292. doi:https://doi.org/10.1016/j.renene.2021.01.013

131. Svelle S, Sommer L, Barbera K, et al. How defects and crystal morphology control the effects of desilication. *Catal Today*. 2011;168(1):38-47. doi:https://doi.org/10.1016/j.cattod.2010.12.013

132. Groen JC, Moulijn JA, Pérez-Ramírez J. Desilication: On the controlled generation of mesoporosity in MFI zeolites. *J Mater Chem*. 2006;16(22):2121-2131. doi:10.1039/b517510k

133. Pérez-Ramírez J, Christensen CH, Egeblad K, Christensen CH, Groen JC. Hierarchical zeolites: Enhanced utilisation of microporous crystals in catalysis by advances in materials design. *Chem Soc Rev*. 2008;37(11):2530-2542. doi:10.1039/b809030k

134. Ogura M, Shinomiya S, Tateno J, et al. Alkali-treatment technique — new method for modification of structural and acid-catalytic properties of ZSM-5 zeolites. *Appl Catal A Gen*. 2001;219(1):33-43. doi:https://doi.org/10.1016/S0926-860X(01)00645-7

Chapter 7.

Conclusions

7.1. General Conclusions

This thesis investigates three catalytic systems designed to enhance the sustainability and efficiency of the petrochemical industry through the valorisation of hydrocarbon feedstocks. It emphasises the transformation of naphtha-derived intermediates, specifically KA oil, acetylene, and 1-octene, into high-value chemicals while providing insights for the development of effective catalytic processes.

Chapter 4 presents a solvent-free, hydrogen-borrowing coupling reaction utilising KA oil and bio-based alcohols, catalysed by Pd/C with KOH. This method produces hydrocarbon-rich mixtures suitable for sustainable aviation fuel (SAF) under mild conditions. The system is notable for its recyclability, ease of operation, and alignment with green chemistry principles, marking it as a promising alternative for renewable jet fuel production.

Chapter 5 examines the semihydrogenation of acetylene to ethylene, a crucial purification step in polyethylene production. It evaluates the performance of Pd- and Pd-Au-based catalysts supported on metal-organic frameworks (MOFs) and zeolites. While MOF-supported catalysts provide in-depth mechanistic insights, zeolite-supported catalysts achieve a more favourable balance of conversion, selectivity, and stability, underscoring the importance of support characteristics on catalytic performance.

Chapter 6 focuses on converting terminal olefins, such as 1-octene, into BTX aromatics using Ru-based solid catalysts. The findings reveal a stepwise mechanism involving isomerisation, cyclisation, and aromatisation, with Ru-HZSM5 displaying enhanced activity and selectivity due to the unique properties

of its support. This highlights the role of support acidity and metal distribution in shaping catalytic effectiveness.

Collectively, these studies demonstrate that strategic catalyst design, including alloy composition and support selection, can significantly influence product outcomes and reaction efficiency. While each process targets different applications, they share a unified foundation in transforming naphtha-derived intermediates using noble metal catalysis in an environmentally responsible manner.

This thesis ultimately contributes to a vision of a sustainable petrochemical industry by integrating catalytic science with practical industrial considerations. It highlights the potential for innovations in catalyst development and reaction engineering to create new reaction pathways, minimise carbon emissions, and enhance the utilisation of renewable feedstocks. Given the pressing demands of the modern world, the findings reinforce the transformative capacity of catalysis to drive industrial processes toward greater sustainability and economic viability, making significant strides toward achieving long-term environmental goals within the petrochemical sector.

Publications

1. List of Publications and Patents Related to the Current Thesis:

- Ballesteros-Soberanas, J., Martín, N., **Bacic, M.** *et al.* A MOF-supported Pd1–Au1 dimer catalyses the semihydrogenation reaction of acetylene in ethylene with a nearly barrierless activation energy. *Nat Catal* 7, 452–463 (2024)

- **Bacic, M.,** Oliver-Meseguer, J., Leyva-Pérez, A. Palladium on carbon-catalysed carbon-carbon coupling reactions of cyclohexanone (KA oil) and alkyl alcohols for the synthesis of zero net emission jet fuels. *Appl. Catal. A Gen.* **674**, 119632 (2024)

- **Bacic, M**., Soberanas, J. B., Manzorro, R., Hernández-Garrido, J. C., Martin-Diaconescu, V.; Oliver-Meseguera, J., Leyva–Pérez, A., Few-atom Ru oxide clusters catalyse the aromatisation of linear alkenes at 300 ºC. (in revision - NATCATAL-25071561)

- **Bacic, M**.; Leyva Perez, A.; Mon Conejero, M. *Aromatización de alquenos terminales y lineales de cadena larga catalizada por rutenio soportado en sólidos*; Spanish Patent Application P202330801, filed September 26, 2023.

- Pardo Marín, E. J.; Ferrando Soria, J.; Leyva Pérez, A.; Ballesteros Soberanas, J.; **Bacic, M**. *Catalizador dímero heterometálico estabilizado en una red metalorgánica con metilcisteína y su uso en semi-hidrogenación de acetileno*; Spanish Patent Application, filed July 14, 2023.

2. Other Scientific Publications:

- **Bacic, M.,** Tejeda-Serrano, M., Zheng, Y., Oliver-Meseguer, J., Leyva-Pérez, A. HY zeolite catalyzes the ortho–methylation of 1–naphthol. *Appl. Surf. Sci. Adv.* **21**, 100598 (2024)

- Lumbreras-Teijeiro, A., **Bacic, M**., Oliver-Meseguer, J., Leyva-Pérez, A. A Cascade Sonogashira Cross-Coupling-Substitution-Elimination Reaction for the Synthesis of Linear Conjugated Dienynes. *Chem. Eur. J.* **28**, e202202421 (2022)

- Leyva-Pérez, A., Bilanin, C., **Bacic, M.,** Greco, R. Acid and Base Water Coexists in a Micro-Structured Ionic Liquid and Catalyzes Organic Reactions in One-Pot. *ChemCatChem* **14**, 2718–2723 (2022)

- Mlakić, M., Šalić, A., **Bačić, M.,** Zelić, B., Šagud, I., Horváth, O., & Škorić, I. Photocatalytic Oxygenation of Heterostilbenes—Batch versus Microflow Reactor. *Catalysts* **11**, 395 (2021)

- **Bačić, M.,** Ljubić, A., Gojun, M., Šalić, A., Jurinjak Tušek, A., & Zelić, B. Continuous Integrated Process of Biodiesel Production and Purification—The End of the Conventional Two-Stage Batch Process? *Energies* **14**, 403 (2021)

- Gojun, M., Ljubić, A., **Bačić, M.,** Jurinjak Tušek, A., Šalić, A., Zelić, B. Model-to-model: Comparison of mathematical process models of lipase catalysed biodiesel production in a microreactor. *Comput. Chem.*

Eng. **145**, 107200 (2021).

- Gojun, M., **Bačić, M.,** Ljubić, A., Šalić, A., Zelić, B. Transesterification in Microreactors—Overstepping Obstacles and Shifting Towards Biodiesel Production on a Microscale. *Micromachines* **11**, 457 (2020)

“It always seems impossible until it’s done.”

Nelson Mandela

“Fais de ta vie un rêve et d’un rêve une réalité”

Antoine de Saint-Exupéry